

Numerical Simulations of Turbulent Mixing in Complex Flows

Elizaveta Ivanova

Deutsches Zentrum für Luft- und Raumfahrt
Institut für Verbrennungstechnik
Stuttgart



DLR

Deutsches Zentrum
für Luft- und Raumfahrt



Herausgeber

Deutsches Zentrum
für Luft- und Raumfahrt

**Institut für
Verbrennungstechnik**

Pfaffenwaldring 38-40
70569 Stuttgart

Telefon
Telefax

(0 7 11) 68 62 - 3 08
(0 7 11) 68 62 - 5 78

Als Manuskript gedruckt.
Abdruck oder sonstige Verwendung
nur nach Absprache mit dem Institut gestattet

D93, Stuttgart

Numerical Simulations of Turbulent Mixing in Complex Flows

A thesis accepted by the Faculty of Aerospace Engineering and Geodesy of the
Universität Stuttgart in partial fulfilment of the requirements for the degree of
Doctor of Engineering Sciences (Dr.-Ing.)

by

Elizaveta Ivanova

born in Leningrad

main referee: Prof. Dr.-Ing. Manfred Aigner

co-referee: Prof. James J. McGuirk D. Sc.

Date of defence: 26/July/2012

Institute of Combustion Technology for Aerospace Engineering
University of Stuttgart

2012

Acknowledgments

This work was conducted during my employment at the Institute of Combustion Technology of the German Aerospace Center (DLR) in Stuttgart, Germany.

I would like to thank the director of the Institute and my main referee Professor Manfred Aigner for his support, encouragement, and the pleasant working conditions. I would also like to thank Professor James J. McGuirk for his agreement to be my co-referee, the time and effort that he spent reading my thesis, and his insightful and beneficial comments and recommendations.

I want to express my heartfelt gratitude to my department head and advisor Dr.-Ing. habil. Berthold Noll for his mentorship, technical advice, fruitful discussions, and his continuous moral support. I also greatly appreciate the creative freedoms that he gave me during this work making it enjoyable yet challenging and greatly beneficial for my professional development.

My special thanks goes to Dr.-Ing. Massimiliano Di Domenico. He assisted me starting from my first day at the Institute. His help with the THETA-code was absolutely crucial. Our technical discussions always helped me to look critically at my results, and he provided thoughtful input for my future research. I also want to acknowledge Guido Schmitz for his help in generating the grids as well as Peter Habisreuther and Flavio Galeazzo (Engler-Bunte-Institute, Karlsruhe Institute of Technology) for the provision of excellent experimental data and related discussions about the jet in crossflow test case.

There are many people whom I would like to thank not only for the professional discussions and support but also for the memorable time in the Institute and outside of its walls. That are Axel Widenhorn, Bernd Mühlbauer, Daniele Panara, Thomas Monz, Markus Kindler, Rajesh Sadanandan, Holger Ax, Michel Lourier, Christian Eberle, Peter Ess, Andreas Jeromin, Stefan Voigt, and many others. My office mate for the last three years Georg Eckel deserves a particular recognition for being an immediate dialog partner at any time and occasion.

Finally, I would like to thank all members of my family for their love and indispensable support especially my dad who encouraged my choice of profession and helped me to take the very first steps leading to this dissertation.

Contents

Nomenclature	7
Zusammenfassung	13
Abstract	15
1 Introduction	17
1.1 Motivation	17
1.2 Previous work on numerical simulations of complex jet flows	19
1.2.1 Jet in crossflow	19
1.2.2 Confined swirling and non-swirling jets	23
1.3 Goals and outline of this work	24
1.3.1 Goals and outline	24
1.3.2 Structure	26
2 Modeling of turbulence and turbulent scalar mixing	27
2.1 Basic equations and turbulence theory	27
2.1.1 Basic assumptions and governing equations	27
2.1.2 Scales of the turbulent motion and challenge of the direct numerical simulation	28
2.1.3 Reynolds averaging	31
2.1.4 Filtering	33
2.2 RANS modeling	35
2.2.1 Turbulent viscosity modeling	37
2.2.2 Turbulent scalar diffusivity modeling	67
2.3 LES and hybrid RANS/LES modeling	85
2.3.1 Velocity field modeling	85
2.3.2 Scalar transport modeling	89
2.4 Numerical realization	90
3 Study on the accuracy of RANS modeling using experimental and LES data	93
3.1 Jet in crossflow	93
3.1.1 Description of the basis test case and computational setup	94
3.1.2 Velocity field modeling	96

3.1.3	Scalar mixing modeling	130
3.2	Confined coaxial jets	151
3.2.1	Description of the test cases and computational setup	151
3.2.2	Velocity field modeling	153
3.2.3	Scalar mixing modeling	177
3.3	Concluding remarks	193
4	Application of alternative unsteady vortex-resolving methods	195
4.1	Scale-Adaptive Simulations (SAS)	195
4.2	Unsteady RANS simulations (URANS) of jet in crossflow	202
4.3	Practical application: self-ignition simulation in jet in crossflow	207
4.3.1	Test case description	208
4.3.2	Details of the numerical simulation.	209
4.3.3	Results	210
4.4	Concluding remarks	213
5	Summary and conclusions	215
	Bibliography	219

Nomenclature

Roman symbols

C	transported scalar
\overline{C}_0	mean transported scalar value on the jet centerline
c'	turbulent scalar fluctuation
CD	cross-diffusion
C_{jet}	mean transported scalar concentration on the jet exit
$C_\mu, C_{\varepsilon 1}, C_{\varepsilon 2}, C_{\varepsilon 3}$	modeling constants of k - ε models
$C_\lambda, C_{d1}, C_{d2}, C_{p1}, C_{p2}$	modeling constants of $\overline{c'^2}$ - ε_c and $\overline{c'^2}$ - ω_c models
c_p	heat capacity
C_w	modeling constant in the law of the wall
d	jet diameter in the jet in crossflow test case
\mathcal{D}	sum of the pressure diffusion and of the turbulent diffusion of the turbulent kinetic energy
\mathcal{D}_p	pressure diffusion of the turbulent kinetic energy
\mathcal{D}_t	turbulent diffusion of the turbulent kinetic energy
E	energy spectrum function (energy spectral density)
\mathbf{e}_i	unit vector in the i^{th} -direction
F_1, F_2	blending functions of the SST k - ω model
$f_\lambda, f_{d1}, f_{d2}, f_{p1}, f_{p2}$	near-wall damping functions of $\overline{c'^2}$ - ε_c models
$f_\mu, f_{\varepsilon 1}, f_{\varepsilon 2}$	damping functions of low-Re k - ε models
J	jet to crossflow momentum ratio, $J = \rho_{jet} U_{jet}^2 / \rho_{crossflow} U_{crossflow}^2$
k	turbulent kinetic energy, $k = \frac{1}{2} \overline{u'_i u'_i}$, ($i = 1 - 3$)

Nomenclature

k_{mod}	modeled part of the turbulent kinetic energy
k_{res}	resolved part of the turbulent kinetic energy
L	integral length scale
L	mixing section side length in the jet in crossflow test case
\mathcal{L}	characteristic length scale in the mixing length hypothesis
\mathcal{L}_c	characteristic length scale of turbulent scalar mixing
\mathcal{P}	production rate of the turbulent kinetic energy
\mathcal{P}_c	production rate of the turbulent scalar variance
P	pressure
\mathbf{P}	modified pressure in RANS or LES equations, $\mathbf{P} = \overline{P} + \frac{2}{3}\rho k$
p'	pressure fluctuation
Q	second invariant of the velocity gradient tensor
q_w	wall heat flux
r	radial coordinate
R	ideal gas constant
R	radius of the mixing section in confined coaxial jets test cases
Re	Reynolds number, $Re = \frac{UL}{\nu}$
Re_t	turbulent Reynolds number, $Re_t = \frac{\sqrt{k}L}{\nu}$
Re_y	dimensionless wall distance based on $k^{1/2}$, $Re_y = \frac{k^{1/2}y}{\nu}$
Re_T	turbulent Reynolds number in the near-wall damping functions, $Re_T = \frac{k^2}{\varepsilon\nu}$
\mathcal{R}	ratio of the turbulent scalar time scale to the turbulent velocity time scale, $\mathcal{R} = \tau_c/\tau_d$
S_{ij}	strain-rate tensor $S_{ij} = \frac{1}{2} \left(\frac{\partial U_i}{\partial x_j} + \frac{\partial U_j}{\partial x_i} \right)$, $(i = 1 - 3, j = 1 - 3)$
\mathcal{S}	swirl number
t	time
T	temperature
t_L	integral time scale

Nomenclature

\overline{U}_0	mean axial velocity value on the jet centerline
$U_{abs\ xy}$	mean xy -velocity in the jet in crossflow test case, $U_{abs\ xy} = \sqrt{\overline{U}_x^2 + \overline{U}_y^2}$
$U_{abs\ xz}$	mean xz -velocity in the jet in crossflow test case, $U_{abs\ xz} = \sqrt{\overline{U}_x^2 + \overline{U}_z^2}$
$U_{crossflow}$	mean crossflow velocity
U_i	i^{th} -component of the velocity vector ($i = 1 - 3$)
u'_i	turbulent fluctuation of the i^{th} -component of the velocity vector ($i = 1 - 3$)
U_{jet}	mean jet velocity
u_η	dissipation (Kolmogorov) velocity scale $u_\eta = (\nu\varepsilon)^{1/4}$
u_L	integral velocity scale
u_τ	wall friction velocity, $u_\tau = \sqrt{\frac{\tau_w}{\rho}}$
\mathbb{U}	characteristic mean flow velocity
\mathcal{U}	characteristic velocity scale in the mixing length hypothesis
\mathbf{x}	position in the Cartesian coordinate system
x_0	virtual origin of the free round jet
x_a	absolute axial coordinate for the free round jet $x_a = x - x_0$
x_i	i^{th} -component of the Cartesian coordinate system ($i = 1 - 3$)
x, y, z	components of the Cartesian coordinate system
Y_k	specific mass fraction of k -component of a mixture
y	absolute distance from the wall
y^*	dimensionless distance from the wall based on the Kolmogorov velocity scale, $y^* = u_\eta y / \nu$

Greek symbols

α	molecular diffusivity of the transported scalar
α_t	turbulent scalar diffusivity
β_k, β_ω	modeling constants of k - ω models
χ_p, χ_ω	non-dimensional vortex stretching measure
$\delta'_{0.5}$	spreading rate of the free round jet

Nomenclature

ε	dissipation rate of the turbulent kinetic energy
ε_c	dissipation of the turbulent scalar variance
η	dissipation (Kolmogorov) length scale
η_B	Batchelor length scale
γ	modeling constant of k - ω models
κ	von Karman constant
κ	reciprocal of the eddy characteristic length
μ	molecular dynamic viscosity, $\mu = \rho\nu$
μ_t	turbulent dynamic viscosity, $\mu_t = \rho\nu_t$
ν	molecular kinematic viscosity
ν_t	turbulent kinematic viscosity
Ω_{ij}	vorticity tensor $\Omega_{ij} = \frac{1}{2} \left(\frac{\partial U_i}{\partial x_j} - \frac{\partial U_j}{\partial x_i} \right)$, ($i = 1 - 3$, $j = 1 - 3$)
ω	specific dissipation rate
ω_c	specific dissipation rate of the turbulent scalar variance
ω_u	reciprocal turbulent velocity time scale
ρ	density
σ_h, σ_ϕ	modeling constants of $\overline{c'^2}$ - ε_c and $\overline{c'^2}$ - ω_c models
σ	molecular Prandtl or Schmidt number, $\sigma = \nu/\alpha$
σ_t	turbulent Prandtl or Schmidt number, $\sigma_t = \nu_t/\alpha_t$
$\sigma_k, \sigma_\varepsilon$	k and ε diffusion modeling constants of k - ε models
σ_k, σ_ω	modeling constants of k - ω models
τ	dissipation (Kolmogorov) time scale
τ_c	turbulent scalar time scale, $\tau_c = \overline{c'^2}/2\varepsilon_c$
τ_d	turbulent velocity time scale, $\tau_d = k/\varepsilon$
τ_λ	time scale in two-equation turbulent scalar mixing models
τ_w	surface shear stress

Nomenclature

θ_w wall friction temperature, $\theta_w = q_w / \rho c_p u_\tau$

Superscripts

$\overline{\phi}$ averaged or filtered variable

ϕ^+ dimensionless variable normalized using u_τ , ν , or θ_w

Abbreviations

2D two-dimensional

3D three-dimensional

AKN turbulent viscosity or turbulent scalar diffusivity model of Abe et al. [1] and [2]

BSL baseline turbulent viscosity model of Menter [83]

CFD Computational Fluid Dynamics

CFL Courant-Friedrichs-Lewy number

curv. c. streamline curvature correction of Hellsten [46]

DNS Direct Numerical Simulation

DWX turbulent scalar diffusivity model of Deng et al. [21]

exp. experimental

GT gas turbine

HB turbulent scalar diffusivity model of Huang and Bradshaw [48]

LB turbulent viscosity model of Lam and Bremhorst [71]

LES Large Eddy Simulation

LIF Laser-Induced Fluorescence

lim. limiter

NK turbulent scalar diffusivity model of Nagano and Kim [89]

PDF Probability Density Function

PIV Particle Image Velocimetry

RANS Reynolds-Averaged Navier-Stokes

ref. reference

Nomenclature

refs. references

r. j. c. round jet correction

RMS root mean square

SAS Scale-Adaptive Simulation

SGS subgrid scale

SIMPLE Semi-Implicit Pressure-Linked Equations

SST Shear-Stress Transport turbulent viscosity model of Menter [83]

std. standard

URANS Unsteady Reynolds-Averaged Navier-Stokes

vol. volume

Zusammenfassung

Für eine genaue numerische Simulation der Gasturbinenverbrennung ist die Qualität der Abbildung von Geschwindigkeits-, Temperatur-, und Konzentrationsfeldern entscheidend. Typische Strömungsfelder der Gasturbinenbrennkammer sind äußerst komplex und bestehen aus Elementen die miteinander interagieren. Die numerische Abbildung der Turbulenz und der Mischungsprozesse in solchen Strömungen ist daher herausfordernd. In der vorliegenden Dissertation werden unterschiedliche Aspekte der Modellierung der Strömung und der turbulenten skalaren Mischung in komplexen Strahlkonfigurationen betrachtet.

Im Rahmen der vorliegenden Arbeit werden für detaillierte Studien drei Grundtestfälle ausgewählt: Strahl in einer Querströmung, eingeschlossene verdrallte koaxiale Strahlströmung, und eingeschlossene koaxiale Strahlströmung ohne Drall. Im Kapitel 1 werden die bekannten numerischen Untersuchungen solcher Strömungen in einer Literaturstudie zusammengestellt und diskutiert: von den Direkten Numerischen Simulationen (DNS) bis zur Reynolds-Averaged Navier-Stokes (RANS) Modellierung. Es werden drei Hauptziele dieser Arbeit genannt. Das erste Ziel ist ein kritischer Vergleich der hocheffizienten RANS Modelle für Turbulenz und Mischung für die ausgewählten Testfälle. Das zweite Ziel ist eine detaillierte Auswertung der Daten, die in einer Large Eddy Simulation (LES) für die betrachteten Testfälle generiert werden. Dabei können in einer LES Auswertung auch Variablen beschafft werden, die im Experiment nicht zugänglich sind. Damit soll eine umfassende Datenbasis für die Validierung der RANS Modelle zur Verfügung stehen. Das dritte Ziel dieser Arbeit ist die Untersuchung des Potentials der Scale-Adaptive Simulation (SAS) und der instationären RANS (URANS) für die Mischungsmodellierung in den betrachteten Konfigurationen. Hier soll auch geklärt werden, wie gut die unterschiedlichen Simulationsmethoden die Flammenausbreitung nach der Selbstzündung in einem Vormischkanal mit Querstrahleinblasung wiedergeben können.

Im Kapitel 2 wird der theoretische Hintergrund dieser Arbeit beleuchtet. Die Konzepte der RANS und LES werden vorgestellt, wobei insbesondere auf weitverbreitete Modelle eingegangen wird. Die wichtigsten Probleme und offene Fragen werden basierend auf einer Literaturstudie beschrieben. Ein besonderes Augenmerk wird auf die RANS Modellierung gerichtet. Es werden mehrere Zweigleichungsmodelle und Modellkorrekturen, sowie Konzepte für die Modellierung der turbulenten skalaren Diffusivität beschrieben und diskutiert. Die Modelldiskussion wird mit der Präsentation der Ergebnisse für eine ebene Kanalströmung und für einen Freistrahle begleitet. Auf diese Weise werden die Stärken und Schwächen unterschiedlicher RANS Modelle in akademischen Standardtestfällen und in komplexen Strahlströmungen ermittelt.

Im Kapitel 3 werden RANS Studien und die Auswertung von LES Daten für drei Haupttest-

fälle präsentiert. Die RANS Ergebnisse für die Mittel- und Fluktuationswerte der Geschwindigkeitsfelder und der skalaren Konzentrationsfelder werden experimentellen Daten und LES Ergebnissen gegenüber gestellt. Die LES ergibt meistens die beste Übereinstimmung mit den experimentellen Daten. Viele der untersuchten RANS Modelle zeigen eine klare Tendenz zur Unterschätzung der Turbulenz- und Mischungsintensität in den komplexen Strahlströmungen. Der Einfluss unterschiedlicher Gleichungsterme und Korrekturen auf die Genauigkeit der RANS Modelle wird untersucht. Für eine umfassendere Studie werden LES Daten für die Auswertung der turbulenten Viskositäten, turbulenten skalaren Diffusivitäten, Budgetterme der Transportgleichungen für die turbulente kinetische Energie und die turbulente skalare Varianz eingesetzt. Mit Hilfe dieser Daten wird auch die praktisch relevante Information über die Werte der turbulenten Schmidtzahl in den betrachteten Testfällen gewonnen. Die mittleren turbulenten Schmidtzahlen aus der LES Auswertung liegen um 0.5 für den quereingedüsten Strahl und bei 0.6 – 0.9 für die beiden eingeschlossenen koaxialen Strahlströmungen. Es wurden weitere Größen (das Verhältnis der Produktions- und Dissipationsraten, der Modellierungskoeffizient der Gleichung für die turbulente Viskosität, das Verhältnis zwischen der Skalaren und der dynamischen Zeitskala) ausgewertet, die wichtig für die Validierung der verbreiteten RANS Modellierungsannahmen sind. So wird eine umfassende Datenbasis geschaffen, die für die weitere Verfeinerung der RANS Modelle im Hinblick auf die Gasturbinenapplikationen genutzt werden kann. Weiterhin wird eine detaillierte Diskussion über die Auswertungsmethoden und die gewonnenen Ergebnisse angeführt.

Im Kapitel 4 sind URANS und SAS Rechnungen der betrachteten Testfälle präsentiert. Die Genauigkeit der SAS Ergebnisse wird mit RANS und LES Ergebnissen für die drei Haupttestfälle verglichen. Eine weitgehende Vergleichstudie zwischen SAS und URANS wird für die Querstrahlkonfiguration durchgeführt. Die Validierung der Rechenmethoden mit experimentellen Daten wird mit einer Visualisierung der aufgelösten Wirbelstrukturen begleitet. Desweiteren wird der Vorgang von Selbstzündung und Flammenausbreitung für die Konfiguration eines quereingedüsten Strahls mit Hilfe von URANS und SAS modelliert. Qualitative Differenzen in der Flammenfrontausbreitung werden besprochen und die Überlegenheit der SAS Methode für solche Simulationen aufgezeigt.

Abstract

For an accurate gas turbine combustion simulation the quality of the mean and fluctuating velocity, temperature, and species concentration field predictions is of critical importance. A typical flow pattern of a gas turbine combustion chamber comprises several complex jet configurations intricately interacting. Numerical representation of turbulence and mixing in such flows is a challenging task. Different aspects of modeling the turbulence and turbulent scalar mixing in complex jets are considered in this dissertation.

Three complex jet test cases are selected for a systematic investigation in the present work: jet in crossflow, confined coaxial swirling jets, and confined coaxial jets without swirl. A comprehensive literature overview on the previous numerical investigations of these flows ranging from Direct Numerical Simulations (DNS) to Reynolds-Averaged Navier-Stokes (RANS) modeling is given in chapter 1. Three main goals of the present work are formulated. The first one is the critical assessment of the widespread turbulent viscosity and turbulent scalar diffusivity RANS approaches in application to the flow and mixing modeling in the selected test cases. The second aim is a thorough evaluation of the statistical data obtained in Large Eddy Simulations (LES) of three main test cases. This goal is set in order to provide a more comprehensive database for validating RANS models and to obtain variables of interest which cannot be determined easily in experiments due to measurement instrumentation limitations. The third aim of the present work is to understand the potential of the Scale-Adaptive Simulation (SAS) method and of the Unsteady RANS (URANS) approach for the mixing modeling in the considered flows. The most important question here is the clarification of the ability of different methods to correctly predict the flame propagation processes in the practically relevant case of autoignition in a jet in crossflow. All goals are achieved in this work and the respective studies are presented.

Chapter 2 develops the theoretical framework of this dissertation. RANS and LES concepts are introduced and common modeling closure approaches for both methods are discussed. The most important problems and open questions are outlined based on a literature study. Especially high attention is paid to the challenges of modeling turbulence and mixing within the RANS formalism. Chapter 2 describes several widespread two-equation turbulent viscosity models and their additional corrections, and several turbulent scalar diffusivity modeling approaches. A discussion on the advantages and weaknesses of different models is provided. The model discussion is accompanied by the presentation of the results obtained for a plane channel flow and for a free round jet test case respectively. This is included to better illustrate the relative advantages and weaknesses of different RANS models in standard academic test

cases, and to provide the foundation for analyzing complex jet flows which are the primary configurations of interest of this dissertation.

Chapter 3 is devoted to the study of the accuracy of RANS in three main test cases and to LES data evaluation. The results of RANS mean and fluctuating velocity and scalar field simulations are validated against experimental data and the outcome of accompanying LES calculations. The LES results, for the most part, agree better with the respective experimental data. Many of the tested RANS models show a clear trend of the underestimation of turbulence and mixing in the considered complex jet configurations. The influence of different equation terms and corrections on the RANS model accuracy is investigated. For a more thorough study, the resolved data fields from LES are used for the evaluation of the Reynolds-averaged turbulent viscosities, turbulent scalar diffusivities, and the main budget terms of the turbulent kinetic energy and the turbulent scalar variance transport equations. This data is also used to extract practically important information on the turbulent Schmidt numbers in the considered flows. The turbulent Schmidt numbers given by LES data evaluation fluctuate around 0.5 for the jet in crossflow case and 0.6 – 0.9 for both confined coaxial jet cases. Other important quantities needed for the validation of the common RANS modeling assumptions, such as production to dissipation ratios, modeling coefficients of the turbulent viscosity equation, turbulent scalar to velocity time scale ratios, are evaluated from LES data as well. This builds a comprehensive database useful for the further refinement of RANS modeling in gas turbine applications. A detailed discussion on the evaluation methods and on the obtained results is provided.

In chapter 4 URANS and SAS calculations of the considered complex jet flows are presented. The accuracy of SAS is assessed on all three main test cases by comparing against the RANS and the LES data. For a comparative study of SAS and URANS, the jet in crossflow configuration is selected. The quantitative validation of the results against experimental data is supplemented by the visualization of the vortex structures resolved by both methods. Furthermore, the autoignition and the flame propagation in a jet in crossflow configuration is modeled using both URANS and SAS and qualitative differences in the flame front propagation predictions are assessed.

1 Introduction

1.1 Motivation

The importance of Computational Fluid Dynamics (CFD) in engineering has constantly grown over the last decades. The tools of CFD have become an essential link in every development chain in the aerospace and turbomachinery industry as well as in numerous other fields. CFD methods used for practical applications should fulfill the requirements of reliability and of time efficiency. Those requirements can present a challenge, especially in simulations of complex multi-physics processes, such as gas turbine (GT) combustion.

Even not considering the topics of spray and chemical reaction modeling, an accurate reproduction of the flow fields and mixing processes in a GT combustion chamber is a demanding task. The reason for this is that GT combustor flows are characterized by a high level of complexity (figure 1.1.1). A typical flow pattern comprises swirling and non-swirling confined jets and jets in crossflows interacting in intricate ways. For an accurate combustion simulation, the employed turbulence and turbulent scalar mixing models should be able to correctly reproduce the mean and fluctuating velocity, temperature, and species concentration fields. Different aspects of the computational modeling of these quantities with emphasis on GT combustor flows are considered in this dissertation.

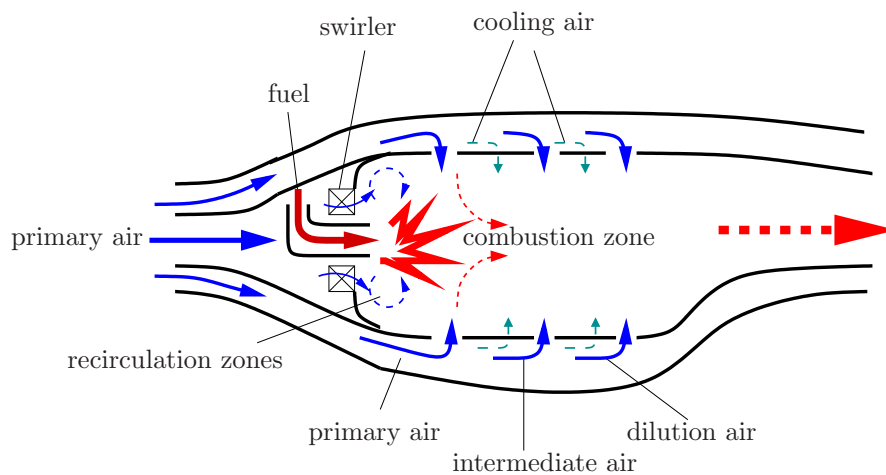


Figure 1.1.1: Schematic representation of the air distribution in a typical gas turbine combustor according to Lefebvre [73]

Reynolds-Averaged Navier-Stokes (RANS) turbulence modeling methods are well suited for design optimization calculations due to their low computational cost. Unfortunately, they can

be inaccurate for complex flows. This is a consequence of the RANS formalism. Its fundamental idea is to model the effects of all scales of the turbulence, even the largest eddies. The simulation output is the ensemble- or time-averaged flow field. Consequently, if the modeled flow pattern is characterized by the presence of anisotropic, highly unsteady, large-scale structures, the reproduction of their physics by a RANS model presents a challenge. The first topic of this work is to highlight particular difficulties connected with the application of widespread RANS turbulence and mixing closures for complicated jet flows typical for GT combustion. A supporting aim of this dissertation is the exploration of possible improvements of current RANS methods.

In order to avoid the modeling of complex large-scale turbulent structures, unsteady vortex-resolving methods such as Large Eddy Simulation (LES) or even Direct Numerical Simulation (DNS) can be used instead of RANS. In DNS the discretized momentum and scalar transport equations are solved by a numerical method without any additional modeling of the turbulent content. This is without doubt the most straight-forward and accurate way of simulation, but it implies that the full range of the length and time scales of the flow must be resolved. In actual technical applications, often characterized by high Reynolds numbers, the range between the largest and the smallest scales can be significant. The computational cost of DNS grows with the turbulent Reynolds number as Re_t^3 [101] (see section 2.1.2). Thus, even the academic DNS of complex jet flows relevant in the context of the current work are a rarity [37, 88]; furthermore, such simulations are typically characterized by unrealistically low Reynolds numbers (around 5000). A DNS of a real combustor is and will be computationally out of reach for decades [99, 102].

In Large Eddy Simulations (LES), large to intermediate turbulent flow structures are resolved, and the effects of the smaller eddies are modeled. Consequently, this approach allows a relatively accurate representation of the flow physics at lower computational cost than DNS. In direct comparison with RANS, well-resolved LES gives better results in most cases. Unfortunately, from the point of view of practical engineering simulations, LES methods are still too expensive to be employed in design optimization calculations. But due to their high accuracy and the vortex-resolving ability, this class of techniques can be extremely useful for thorough numerical studies of realistic high-Reynolds number flows. The data obtained in LES can provide an insight into the unsteady physics of turbulence and mixing in the cases when such knowledge can not be easily gained from experiment due to measurement instrumentation limitations or from DNS due to computational cost restrictions. The present work employs LES to recover practically relevant statistical information about the turbulence and mixing characteristics in complex jet flows that can facilitate RANS model improvement.

A pragmatic alternative to LES in cases when an unsteady vortex-resolving solution is needed, but the computational cost restrictions are severe, can be the application of hybrid RANS/LES methods. These approaches allow the variation of the spectral resolution (from RANS to LES) in the flow field depending on the importance of accuracy in certain regions, essential unsteadiness of the flow, and grid resolution. Over the last decade hybrid methods have become

immensely popular and are one of the most intensive fields of engineering turbulence modeling development. The computational cost reduction compared to LES can be of several orders of magnitude [114]. The argument for applying such methods in lieu of RANS is their improved accuracy due to the resolution of complex vortical structures by LES-like calculations. The quality of RANS modeling, however, still plays an important role in hybrid models, and the computational cost of “pure” RANS will always be lower. Hence, successful development of the hybrid methods does not imply that further work on RANS modeling should be slowed down. In GT combustion computations hybrid RANS/LES methods can be indispensable for the simulation of fundamentally unsteady processes, such as self-ignition or flame propagation. Such processes cannot be recovered by a steady-state simulation, even if a perfectly accurate RANS model would exist. For this reason the present work considers the application of a hybrid RANS/LES approach for the flame propagation modeling in a jet in crossflow configuration. Furthermore, a study on the relative accuracy of different turbulence simulation methods (RANS, LES, hybrid RANS/LES) in the GT-related jet flows is presented.

1.2 Previous work on numerical simulations of complex jet flows

Jets in crossflow, confined swirling jets, and confined non-swirling jets represent important configurations often implemented for mixing enhancement and flame stabilization in GT combustion applications. Consequently, the accuracy of the turbulence and mixing modeling for these jet flows directly affects the accuracy of the simulation of all processes occurring in a combustor. This section presents a review on previous numerical studies devoted to these flows. Detailed theoretical background on all modeling approaches mentioned in this section can be found in chapter 2.

1.2.1 Jet in crossflow

Jets in crossflow, also known as transverse jets, are widely used to achieve enhanced mixing in many industrial applications as well as for flight control purposes in aerospace vehicles. In gas turbine technology, important examples include the flows in the premixing and dilution zones of gas turbine combustion chambers. Targeting this application area, current work focuses primarily on the transverse jets with relatively high jet to crossflow momentum ratios $J \approx 5$ to $J \approx 100$ with J defined as

$$J = \frac{\rho_{jet} U_{jet}^2}{\rho_{crossflow} U_{crossflow}^2}. \quad (1.2.1)$$

Jets with lower momentum ratios more typical for cooling applications, are not considered here since wall proximity effects play an important role in these cases, and the flow physics can differ comparatively to flows with high momentum ratios.

A comprehensive review of the research on transverse jets carried out by early 1990s can be found in the publication of Marganson [82]. The studies (mostly of experimental nature) reviewed in ref. [82] build a basis for all later jet in crossflow research, but for the current work

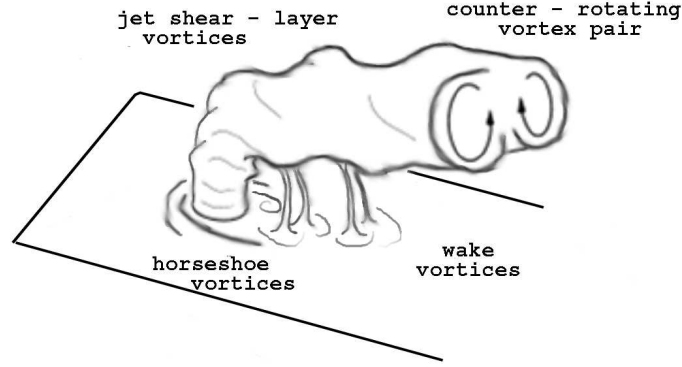


Figure 1.2.1: Vortical structures in the near field of transverse jet according to Fric and Roshko [38]

the numerical and experimental investigations published since the mid-1990s and discussed below are more relevant.

The experimental work of Fric and Roshko [38] made important contributions to the jet in crossflow research by elucidating the inner vortical structure and by indicating the main types of the coherent vortices that dominate transverse jets. It is shown by the authors that the flow field of a jet in crossflow is characterized by its high degree of unsteadiness and by at least four different types of the large-scale coherent vortical structures indicated in figure 1.2.1. The presence of these vortices can explain the severe challenges in the RANS simulations of transverse jets reported by different authors [5, 53, 54, 51, 80, 42]. In such simulations the effects of the anisotropic, highly unsteady, large-scale structures have to be reproduced by a steady-state turbulence model, which often additionally assumes local isotropy of the turbulent viscosity.

Alvarez et al. [5] compared the mean and the fluctuating velocity and temperature fields predicted by RANS using two different methods: the standard $k-\epsilon$ model in combination with the constant turbulent Prandtl or Schmidt number hypothesis (the turbulent Prandtl number value was 1.0), and a second moment closure (direct Reynolds stress and turbulent scalar flux modeling not involving the turbulent viscosity concept). The results given by the second moment closure were slightly better than those from the $k-\epsilon$ model, but the mixing predictions were especially unsatisfactory in both cases. He et al. [45] also applied the standard $k-\epsilon$ model for jet in crossflow turbulence and mixing simulations, but they varied the values of the turbulent Schmidt number. The most accurate mixing results were obtained in ref. [45] at $\sigma_t = 0.2$; furthermore, this and similar values (0.25 – 0.3) were also found to give the best agreement with experimental data in a number of publications [53, 54, 51, 42]. In these works, besides of the standard $k-\epsilon$ model, the SST $k-\omega$ model of Menter was applied for turbulence modeling. A more thorough RANS simulation analysis made in preparation of this dissertation, however, shows [51] that such low values of the turbulent Prandtl or Schmidt number are not justified physically. These values help to artificially increase the level of the turbulent scalar diffusivity, that would be under predicted when using higher turbulent Prandtl or Schmidt

number values, since generally the level of turbulent kinetic energy and turbulent viscosity is under predicted by the turbulence models employed in the calculations [51]. Continuing investigations of this subject will be one of the topics of the present work.

The unsteady methods ranging from DNS to unsteady RANS (URANS) applied for the jet in crossflow modeling show, in general, a higher degree of accuracy than the steady-state RANS simulations, but direct comparisons are rare. Muppidi and Mahesh [88, 87] conducted DNS for a transverse jet characterized by a relatively low Reynolds number based on the jet diameter and velocity ($Re = 5000$). The flow structure analysis can be found in refs. [88, 87] as well as important data on the budget terms of the turbulent kinetic energy balance equation in transverse jets. Such data can not be obtained in experiments due to limitations of the measurement techniques, but are extremely useful for a detailed validation of the RANS modeling equations. Unfortunately, the low value of the Reynolds number used in these calculations cannot be significantly raised due to the limited computational resources. At present, DNS-based investigations of jets in crossflow at practically relevant Reynolds numbers are almost impossible.

As a consequence of its lower computational cost combined with the ability to resolve a wide range of spatiotemporal scales present in the flow physics, LES is much more popular than DNS for the transverse jet simulations [130, 111, 79, 109, 120, 42, 63]. Yuan et al. [130] simulated round transverse jets with momentum ratios of $J = 4$ and $J = 9.9$ and Reynolds numbers of $Re = 1050$ and $Re = 2100$ (based on the crossflow velocity and jet diameter) employing a dynamic subgrid scale (SGS) model. This publication (ref. [130]) is focused primarily on flow visualization and on the study of the main coherent vortical structures of a jet in a crossflow. Only a few comparisons of LES results with the statistical experimental data are made in ref. [130]. Additionally, the experimental data used for this comparison were obtained for a flow characterized by higher Reynolds numbers than the flow simulated by LES. Thereby, clear conclusions about the LES prediction accuracy are not possible. Schlüter and Schönfeld [111] in their simulations employing a Smagorinsky-type SGS models made a more comprehensive validation of the LES flow and mixing predictions against experimental data (mean flow velocity, turbulent kinetic energy, mean scalars). The simulations were carried out at industry-relevant Reynolds numbers ($Re = 82000$ and $Re = 16400$). The agreement between the LES and the experimental data was satisfactory. Additionally, in ref. [111] practically relevant grid resolution and molecular Schmidt number dependence studies can be found as well as analysis of the interaction mechanism of two transverse jets injected in a parallel arrangement. Majander and Siikonen [79] used the Smagorinsky SGS model for their simulations of a jet in crossflow with the Reynolds number of $Re = 46700$ based on the jet velocity and diameter and the momentum ratio of $J = 4.9$. Their study presents a deep investigation on the LES scalar and velocity field modeling quality depending on the jet exit boundary conditions (steady and fluctuating). Reference [79] also contains some discussion on the influence of the numerical discretization scheme and of the grid resolution on the mixing predictions. Salewski et al. [109] performed an analysis regarding the dependence of the mixing characteristics on the jet

nozzle geometry based on the results of LES simulations in combination with experimental data. Furthermore, in this publication [109], the problem of counter-gradient transport in a jet in crossflow is briefly discussed. Based on the numerical and experimental data, it is shown that in several flow regions the turbulent scalar diffusivity α_t in the gradient diffusion hypothesis, $-\overline{c'u'_j} = \alpha_t \partial \overline{C} / \partial x_j$, becomes negative, whereas in the traditional RANS modeling it is always assumed positive. Galeazzo et al. [42] compared the results of LES simulations using the Smagorinsky model with the results of RANS modeling using the standard k - ε and the SST k - ω models for a jet with $Re = 20000$ and $J = 16$. It is shown in ref. [42] that the LES predictions, despite of some problems, are superior in comparison to RANS using turbulent viscosity models and the constant turbulent Schmidt number approach. Finally, in the preparation of this dissertation [50] high quality LES results were obtained by employing the WALE SGS model [92] for the jet in crossflow with $Re = 20000$ and $J = 36$.

Despite the growing popularity of LES in academic applications, this method is still computationally too expensive to be applied in engineering routine and cheaper alternatives such as hybrid RANS/LES or URANS methods are needed. As it was shown in the publications [47, 54, 51], URANS, which give an unsteady solution by application of RANS models, is feasible in the case of transverse jets. The reason for this will be discussed in chapter 4. A first attempt to apply a URANS method for the jet in crossflow simulations employing the standard k - ε model was made by Hsu et al. [47]. As preparatory work for this dissertation URANS calculation of jets in crossflow made using the SST k - ω model of Menter were presented in refs. [54, 51]. It was shown in all cited publications that URANS can improve the flow and mixing prediction accuracy in comparison to steady-state RANS simulations. However, refs. [51, 50] also revealed that the scalar mixing predictions could be improved only slightly and the dependence on the RANS mixing models was exceptionally strong. Dependence of the URANS predictions on the RANS turbulence and mixing models is more thoroughly investigated in the present work.

Regarding hybrid URANS/LES methods, not many examples of their application to jet in crossflow simulations exist [55, 51, 54, 106], which is due to their relative novelty. Rush [106] used the Scale-Adaptive Simulation method (SAS) for the simulation of a buoyant jet in crossflow with results superior to those of URANS. Investigations made in preparation of this dissertation [51] showed that results of the SAS mixing simulations of a jet in crossflow are generally much less dependent on the scalar mixing model than the URANS results due to resolving a much larger part of the turbulent kinetic energy. Furthermore, in ref. [55] the SAS method was successfully applied for the modeling of self-ignition in a practically relevant jet in crossflow configuration. Direct comparisons of the SAS and the RANS results in both reacting and non-reacting cases revealed the superiority of SAS. In this dissertation the results of the SAS self-ignition simulations are compared with URANS results in order to understand the importance of the relative resolution depth of the turbulent vortical structures in an unsteady simulation for the accuracy of self-ignition and flame propagation simulations.

1.2.2 Confined swirling and non-swirling jets

Whereas jets in crossflow considered in the previous section are used mostly in the premixing or in the dilution zones of a typical combustor, the primary fuel-oxidizer mixing often occurs in swirling or non-swirling coaxial jet configurations. Consequently, consideration of these flow patterns is important for a comprehensive review on the turbulence and mixing modeling challenges in GT combustion applications.

There is a large number of experimental studies on these flow patterns. Most of them are devoted to the investigation of the physical processes governing the mixing behavior. From the perspective of a validation database for numerical simulations, the experimental works of Roback and Johnson [104] and Ahmed and So [3] should be mentioned with regards to the swirling confined jet configuration. For the non-swirling coaxial jet mixing, detailed experimental investigations with a large amount of validation data can be found in refs. [132, 58, 76, 3]. In all these works mean and fluctuating velocity and scalar field measurements are presented for constant [104, 132, 58, 76] and variable density [3] flows.

Regarding the numerical simulations, a large amount of studies using different turbulence modeling approaches can be found for the confined swirling and non-swirling jets. One of the rare examples of DNS of a swirling confined jet configuration at relatively low Reynolds number ($Re = 5000$) can be found in ref. [37]. A thorough analysis of the turbulent one- and two-point correlations for both the velocity and the scalar field is presented in this publication. The influence of the large-scale coherent vortical structures on the mixing behavior is investigated. Unfortunately, unlike in the previously mentioned DNS simulations of transverse jets [88, 87], a practically relevant evaluation of the budget terms of the turbulent kinetic energy balance equation is not presented in ref. [37]. An additional disadvantage is that computational cost restrictions do not allow the simulation at practically relevant higher values of the Reynolds numbers.

Considering LES applications of swirling and non-swirling confined jets, a larger quantity of studies can be found in the literature. The study of Akselvoll and Moin [4] represents, to the author's knowledge, the first attempt of applying LES methods to simulate the flow and mixing in a confined non-swirling jet. Dynamic SGS models for the velocity and scalar fields were used. The results were validated against the experiments of Johnson and Bennett [58]. Dianat et al. [26, 25] conducted LES simulations at the experimental conditions given in ref. [76] using the Smagorinsky SGS model for the velocity field and the constant SGS Schmidt number for the scalar mixing modeling. In this publication good accuracy of the LES data was reported as well as their superiority over the RANS modeling results. For the RANS simulations the standard $k-\varepsilon$ model in conjunction with the constant turbulent Schmidt number hypothesis was applied in ref. [26, 25]. Another comparison between the velocity and scalar field predictions made by several widespread RANS turbulence models and the respective LES results obtained using the Smagorinsky SGS model for a non-swirling confined jet can be found in ref. [116]. LES, generally, displays higher accuracy than most RANS approaches. In the context of this

dissertation, the LES studies of Dianat et al. [26, 25] are interesting since in those papers an attempt to evaluate the turbulent Schmidt number from the time-averaged LES velocity and scalar fields is presented. This is one of the rare examples of the usage of LES data in order to obtain the knowledge potentially useful for the improvement of RANS modeling. In the present work not only the turbulent Schmidt numbers but also further statistical data of interest such as budget terms of the turbulent kinetic energy transport equation are evaluated for all considered flow configurations.

The LES studies on the modeling of a swirling jet [98, 121, 110, 40] are mostly of the same character and structure as the non-swirling confined jet investigations discussed above. Again, LES results, although not ideal in some cases, are normally more accurate than the results based on RANS modeling. In the RANS studies [9, 56, 77, 118, 122], a large variety of different modeling approaches can be found. Whereas refs. [9, 77, 118] are devoted to the application of the common two-equation turbulence models used in conjunction with the constant turbulent Schmidt number hypothesis, the refs. [56, 122] used the turbulent Reynolds stress and scalar flux models. The attempts of direct Reynolds stress and scalar flux modeling are motivated by the poor turbulence and mixing prediction that often can be observed in swirling jet studies employing two-equation RANS models [9, 56, 77, 118, 122, 52]. Particularly remarkable is the under prediction of the level of turbulence and mixing which has been reported in ref. [52] in preparation of this dissertation as well as by other authors [118]. Specially designed Reynolds stress and scalar flux models help to improve the mixing predictions in swirling jets [56, 122], but, generally, this approach is unpopular in engineering computations due to its complexity, a large number of transport equations and many free parameters, resulting in a highly empirical model and thus sometimes a poor degree of universality. Continuous work on the refinement of RANS modeling is needed here as in the configurations discussed previously.

Only a few examples of the application of hybrid RANS/LES methods for the confined jet simulations exist in the literature [123, 124, 23]. These works are devoted to the simulation of reacting, industry-relevant flows, and the results presented in refs. [123, 124, 23] are encouraging. Direct comparisons with the RANS modeling results shown in ref. [123] illustrates the high accuracy of the data obtained by the hybrid Scale-Adaptive Simulation (SAS) method used in this publication. Additional studies involving model validation and comparison with RANS and LES results for non-reacting flows for both swirling and non-swirling jets would be beneficial; consequently, such a study is presented in the current dissertation among other investigations.

1.3 Goals and outline of this work

1.3.1 Goals and outline

The literature review presented in the previous section reveals significant weaknesses in the widespread RANS turbulence and mixing models applied to complex jet simulations. These deficiencies are the main impetus for the current work. In order to explore possible directions

to refine existing RANS approaches, several investigations related to different modeling aspects were carried out in the present dissertation.

First, along with the theoretical consideration of the most common turbulent viscosity and turbulent scalar diffusivity RANS models, examples of their application on two basic “academic” test cases (2D channel flow and free round jet) will be provided. The aim is to have a reference regarding attainable accuracy of the RANS models for simple flows used widely for validation purposes. Such a reference will assist in highlighting the additional challenges that arise when applying the tested approaches on realistic engineering flows.

The assessment of all RANS models considered in this work on GT relevant complex jet configurations (jet in crossflow, confined coaxial swirling jets, confined coaxial non-swirling jets) will follow. The validation of the RANS results by experimental data and a comparison with the results of LES for the same test cases will be shown. This will help to improve the understanding about the relative accuracy of various approaches and to contrast the differences between the possible levels of precision achievable by the steady-state RANS methods and unsteady vortex-resolving methods represented by LES.

Next, a study on the relative influence of different RANS model equation terms and corrections will be given. For this study models were considered that take into account the effects potentially important for the flows under investigation (e.g. round jet vortex stretching, streamline curvature). The goal of this study is to ascertain which corrections help to improve the simulation accuracy and to promote promising ideas that could advance model development.

A further step directed towards a more complete understanding of the statistical turbulence and mixing properties in the considered flows is a comprehensive evaluation of the LES data. In this evaluation, budget terms of the Reynolds-averaged turbulent kinetic energy and turbulent scalar variance transport equations, turbulent viscosities and turbulent scalar diffusivities, and the effective turbulent Schmidt numbers in all considered flows will be obtained. Knowledge about the actual behavior of these statistical variables and a direct validation of the terms of different RANS models against this data is essential for the development of an improved closure for RANS equations.

The construction of all RANS approaches is based on the statistical analysis of the behavior of complex model equation terms under different conditions. Mostly, data from experiments or DNS in several simplified “academic” configurations (2D channel or pipe flows, free round or plane jets) are used to refine the models, but the statistical properties of turbulence and mixing in complex jet flows, such as those considered here, can be quite different. For these flows appropriate experimental databases are not available. Only sporadic DNS data on the variables of interest in realistic jet configurations can be found (see section 1.2). However, data on the actual trends shown by the turbulent Schmidt numbers and by the budget terms of the turbulent kinetic energy and the turbulent scalar variance transport equations in complex jet flows would help significantly to refine the existing RANS modeling approaches.

In the present work, LES is used to obtain missing statistical data that can facilitate the improvement of RANS modeling. LES results are, generally, not as accurate as DNS data.

However, from the pragmatic engineering point of view, the increased understanding that results from LES data analysis can be significant. Several examples of the successful application of LES for high-Reynolds number jet flows analysis and evaluation of the variables relevant for RANS model improvement became recently available in the literature [20, 8, 25, 26], but such works are still rare. To the author's knowledge, the jet in crossflow and the swirling confined jet configurations, which are especially important in the GT application context, have not been considered yet in such studies. The non-swirling confined jet mixing is analyzed in the LES studies of Dianat et al. [25, 26], but in these publications only the turbulent Schmidt numbers for the considered configuration are obtained. A thorough investigation that includes the analysis of the main budget terms of the turbulent kinetic energy and the turbulent scalar variance transport equations, comparison of their values evaluated from LES and given by the RANS modeling, and evaluation of the turbulent Schmidt numbers for a variety of jet flows is still not readily available. The present work will fill this gap.

The last aspect of turbulence and mixing simulations in complex jet flows studied in this work is the application of the Scale-Adaptive Simulation (SAS) and of the Unsteady RANS (URANS) approaches. To highlight the comparative advantages and weaknesses of both techniques, they are applied to the same test cases as used for the RANS and LES calculations. The results obtained with all considered methods are compared. Furthermore, the degree of the resolution of the turbulent fluctuating motions in both methods will be studied. The implication of the resolution degree to simulation quality will be shown for a non-reacting jet in crossflow and in the, practically relevant, self-ignition case.

1.3.2 Structure

This dissertation is organized as follows. In chapter 2 an overview of the most widespread engineering techniques for turbulent flow and scalar mixing simulations is presented. The theoretical background of RANS, LES, and hybrid modeling is discussed. Based on the literature review and the validation computations of the academic test cases (2D channel flow, round jet flow), the advantages and challenges of the considered modeling methods are analyzed. In chapter 3, the results of RANS and LES simulations for three test cases - jet in crossflow, confined coaxial swirling jets, and confined coaxial jets without swirl are presented. A comprehensive LES-based study on the budget terms of the turbulent kinetic energy and the turbulent scalar variance balance equations, turbulent viscosities and turbulent scalar diffusivities, and the turbulent Schmidt numbers in the considered flows can be found in this chapter. Moreover, RANS studies on the influence of different equation terms and corrections are included in this chapter. Chapter 4 discusses the results of the SAS and URANS computations. Finally, in chapter 5 the conclusions of this dissertation are summarized and discussed.

2 Modeling of turbulence and turbulent scalar mixing

This chapter develops the theoretical framework of the dissertation. First the governing Navier-Stokes and scalar transport equations are listed and basic turbulence background is outlined. Then RANS and LES concepts are introduced and common closure approaches for the Reynolds-averaged and filtered momentum and scalar transport equations are discussed. Special attention is paid to the modeling of turbulent mixing within the RANS framework. The most important problems and open questions are outlined and discussed based on a literature study. Models used in the present work are specified. A discussion on the advantages and weaknesses of different models using the results obtained for academic test cases such as 2D channel flow and free round jet is provided.

2.1 Basic equations and turbulence theory

2.1.1 Basic assumptions and governing equations

The following assumptions about the flow conditions are made for the theoretical considerations of the present work:

- high-Reynolds number (fully developed turbulence),
- low-Mach number (effects of pressure-based compressibility are neglected).

These conditions are typical for gas turbine combustors for both propulsion and power generation applications.

Due to combustion processes large density and temperature gradients are natural for the target applications. However, in the numerical simulation of a flow characterized by variable density, the modeling effects on the turbulence and on the scalar mixing are coupled. It is rather difficult in such cases to isolate and understand the individual impact of each of the modeled equations and their terms on the overall mixing predictions. The clarification of the individual accuracy of the turbulence and of the mixing models tested in this work is one of the main subjects of the studies performed here. For this reason all the main test cases considered here are constant density cases and this deviation from reality is consciously accepted. The equations presented in this chapter are derived using the constant density assumption. Therefore, buoyancy effects can be neglected, density fluctuations can be neglected in averaging or filtering, transported scalars such as species concentrations or temperatures are passive.

For the self-ignition test case studied in chapter 4 the constant density equations cannot be used. Favre-averaged variable density equations employed in the self-ignition test case calculations can be found in refs. [99, 43, 22]. The derivation of these equations is not given here since it is not essential for the main theoretical considerations of this dissertation.

Under the assumptions listed above the main equations governing the fluid motion in the considered systems can be written in the following form [30]:

- continuity equation

$$\frac{\partial U_j}{\partial x_j} = 0, \quad j = 1 - 3, \quad (2.1.1)$$

- Navier-Stokes (momentum) equations

$$\frac{\partial U_i}{\partial t} + U_j \frac{\partial U_i}{\partial x_j} = -\frac{1}{\rho} \frac{\partial P}{\partial x_i} + \frac{\partial}{\partial x_j} \left[\nu \left(\frac{\partial U_i}{\partial x_j} + \frac{\partial U_j}{\partial x_i} \right) \right], \quad i, j = 1 - 3. \quad (2.1.2)$$

Here x_i is the i^{th} -component of the Cartesian coordinate system, U_i is the instantaneous value of the flow velocity in the i^{th} -direction, ν is the kinematic viscosity, and P is the instantaneous value of pressure. Hereafter the summation over repeating indices is applied. The transport equation for a passive conservative scalar (no source terms) C is [30]:

$$\frac{\partial C}{\partial t} + U_j \frac{\partial C}{\partial x_j} = \frac{\partial}{\partial x_j} \left[\alpha \frac{\partial C}{\partial x_j} \right], \quad j = 1 - 3, \quad (2.1.3)$$

where α is the molecular diffusivity of the transported scalar.

2.1.2 Scales of the turbulent motion and challenge of the direct numerical simulation

The equations 2.1.1, 2.1.2, and 2.1.3 listed above describe flow and mixing under the chosen conditions entirely and are true for both laminar and turbulent flow regimes. The transition from a laminar to a turbulent state occurs when the non-linear convective terms of the momentum equations 2.1.2 become much larger than viscous terms (i.e. Reynolds numbers, $Re = \frac{\overline{UL}}{\nu}$, exceed the critical values). In this case minor flow instabilities cannot be damped by viscous forces and start to grow. Large unstable vortices are created. The size of these vortical structures can be up to the order of the characteristic geometrical parameters of the considered flow pattern.

The large-scale whirls remove the energy from the mean flow motion. Due to instability of the large-scale structures, a continuous breakdown of larger vortices into smaller ones occurs, and similarly the kinetic energy is also continuously transferred from larger to smaller scales of turbulence (energy cascade) [101, 29]. With the reduced size of the vortical structures, the viscous effects become more important. Finally, at the level of the smallest turbulent scales

(Kolmogorov-scales) all instabilities are damped out by the viscosity forces and the energy is dissipated.

Although there is no strict scale separation in the turbulent flows, the following approximate classification of turbulent scales can be applied [101, 128, 39]:

- **energy-containing range** - largest scales, generation of the turbulent kinetic energy,
- **inertial range** - transfer of the turbulent kinetic energy from the large scales to the small ones,
- **dissipation range** - smallest structures, energy dissipation.

The distribution of the turbulent kinetic energy k over different vortical scales in a high-Reynolds number fully developed homogeneous isotropic turbulent flow is indicated in figure 2.1.1 by the energy spectrum function (energy spectral density) $E(\kappa)$, and k and $E(\kappa)$ are related according to

$$k = \int_0^{\infty} E(\kappa) d\kappa, \quad (2.1.4)$$

where κ is the wave number (reciprocal of the eddy size). In the inertial subrange the spectrum obeys the Kolmogorov law [101]

$$E(\kappa) \sim \varepsilon^{2/3} \kappa^{-5/3}, \quad (2.1.5)$$

where ε is the rate of energy dissipation.

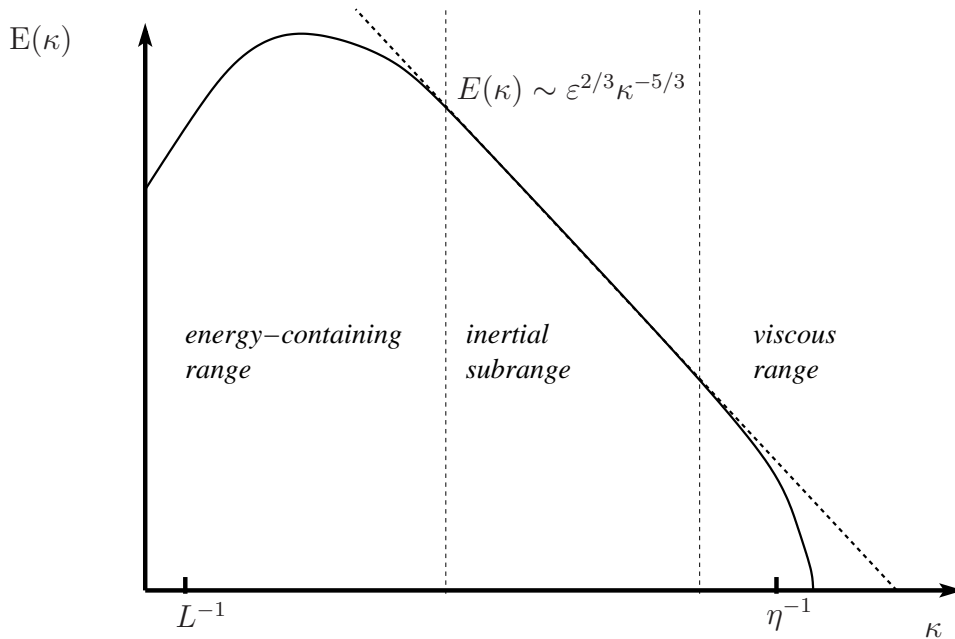


Figure 2.1.1: Energy spectrum of a turbulent flow (log-log scales).

The length scales L of the energy-containing vortices (also called integral length scales) can be defined as the distance at which two points separated in space show statistical correlations

(correlation length) [101]*. The length and time scales, (η and τ respectively), of the dissipation range can be defined using dimensional analysis in the following manner [101]:

$$\eta = \left(\frac{\nu^3}{\varepsilon} \right)^{1/4} \text{ and } \tau = \left(\frac{\nu}{\varepsilon} \right)^{1/2}, \quad (2.1.8)$$

where ε is the dissipation rate and ν the kinematic viscosity. The velocity scale is then $u_\eta = \eta/\tau = (\nu\varepsilon)^{1/4}$. Both length and time scales become smaller with decreasing viscosity. Furthermore, both scales decrease with increasing dissipation rate. The dissipation rate depends upon the energy supply from the largest scales. If L is the integral length scale and u_L the integral velocity scale, the time scale is approximated as $t_L = L/u_L$. For the velocity scale it can be assumed $u_L = \mathcal{O}((2/3k)^{1/2})$ [101], and for the dissipation rate $\varepsilon = \mathcal{O}(u_L^3/L)$ [101], thus $L = k^{3/2}/\varepsilon$. Therefore, the relationship between the smallest and the largest scales of the turbulent flow can be expressed in terms of their dependence on the turbulent Reynolds number ($Re_t = \frac{\sqrt{k}L}{\nu}$) as [101]

$$\frac{\eta}{L} = \mathcal{O}(Re_t^{-3/4}) \text{ and } \frac{\tau}{t_L} = \mathcal{O}(Re_t^{-1/2}). \quad (2.1.9)$$

The separation between the smallest and largest scales grows with increasing turbulent Reynolds number.

For a direct numerical solution of the discretized Navier-Stokes equations (equations 2.1.2), the computational grids and time steps must resolve the smallest scales of the turbulent motion, η and τ . The number of grid points required for η resolution in such a calculation scales as [101]

$$N_{xyz} \sim N_i^3 \sim Re_t^{9/4}. \quad (2.1.10)$$

Considering that for explicit time integration schemes where the time steps must be reduced proportionally to the decrease in space grid element size, the overall computational cost scales with the turbulent Reynolds number as [101]

$$N \sim N_{xyz} \cdot N_i \sim Re_t^3. \quad (2.1.11)$$

To estimate the computational cost of scalar transport calculations, the dependence of the smallest scales of the turbulent scalar fluctuations on the molecular scalar diffusivity α has to

* The two-point correlation is defined as

$$R_{ij}(\mathbf{r}, \mathbf{x}, t) \equiv \overline{u'_i(\mathbf{x}, t) u'_j(\mathbf{x} + \mathbf{r}, t)}, \quad (2.1.6)$$

and here various integral length scales can be built, for example:

$$L_{11}(\mathbf{x}, t) \equiv \frac{1}{R_{11}(0, \mathbf{x}, t)} \int_0^\infty R_{11}(\mathbf{e}_{x1}\mathbf{r}, \mathbf{x}, t) dr, \quad (2.1.7)$$

where \mathbf{e}_{x1} is the unit vector in the x_1 -direction, \mathbf{x} is the position in the Cartesian coordinate system, t -point in time, \mathbf{r} -distance [101].

be taken into account. An estimation of the relation between the smallest scales of turbulence and of turbulent scalar mixing can be obtained after the introduction of the Prandtl or Schmidt number $\sigma = \nu/\alpha$. This is a characteristic dimensionless measure of the relation between the momentum and scalar molecular diffusion transport (Prandtl number if the transported scalar is temperature or Schmidt number if the transported scalars are species). For $\sigma < 1$, the small scale scalar fluctuations are damped stronger than the small scale velocity fluctuations. If $\sigma > 1$, the smallest scales of the scalar fluctuations are finer than the smallest scales of the velocity fluctuations. The length scale of those fluctuations is $\eta_B = \sigma^{-1/2}\eta$ (Batchelor length scale) [27, 39]. This scaling represents an additional challenge for DNS of turbulent scalar mixing in fluids characterized by $\sigma > 1$.

In a typical gas turbine combustor, the Reynolds numbers at the diffuser inlets can easily exceed 10^5 [73] and turbulence intensities are quite high. Thus, direct numerical simulations of such flows are and will be for decades out of reach even with the promising trends in development of hardware and numerical algorithms. For this reason in practical simulations of high Reynolds number flows, the turbulent spectrum is normally not fully resolved but is partly or completely represented by a model. Reynolds-averaged Navier-Stokes (RANS) and large eddy simulation (LES) methods represent two different techniques to overcome the computational cost limitations arising in DNS. As mentioned in the introduction, in the first case the turbulence is completely modeled including even the largest scales, and in the second case large scales of the turbulent motion are resolved whereas the effects of the smallest scales are represented by a model. This is schematically depicted in figure 2.1.2. These approaches and their relative advantages and weaknesses in application to the considered problems are discussed in the next sections.

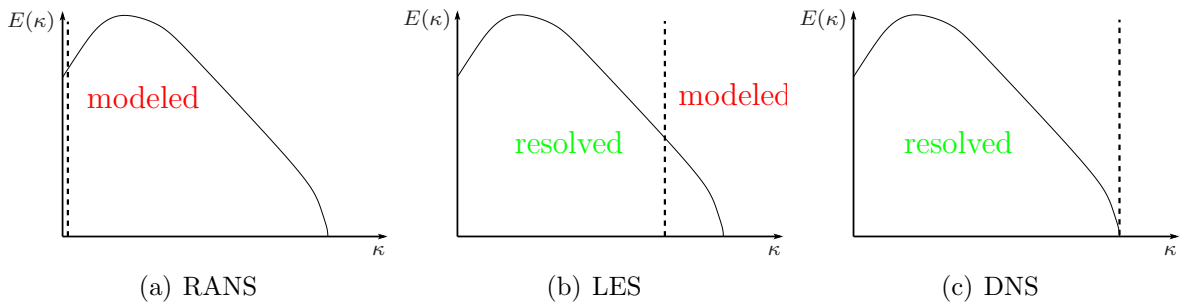


Figure 2.1.2: Turbulence energy spectrum as a function of wave numbers (log-log scales). Resolved and modeled parts in RANS, LES, and DNS.

2.1.3 Reynolds averaging

From the perspective of engineering design optimization simulations of GT combustors, in most cases the information about the time- or ensemble-averaged velocity, temperature, and species concentration fields is sufficient, and there is no need for the deep time- and space-resolution of the turbulent structures. Additionally, the computational costs of such simulations should be as low as possible to facilitate the conduction of a large number of simulations within a short

time. Therefore in such cases the application of RANS methods, which are based on the idea of the direct modeling of the ensemble- or time-averaged flow field so to avoid resolving the turbulent spectrum, seems to be the optimal choice.

The governing equations for the flow modeling within a RANS approach are obtained by the splitting of a general instantaneous turbulent flow variable Φ into a statistically mean value $\bar{\Phi}$ and a stochastic part ϕ' which fluctuates around the mean value and satisfies $\overline{\phi'} = 0$ [29],

$$\Phi = \bar{\Phi} + \phi'. \quad (2.1.12)$$

The main characteristics of this operation called Reynolds-averaging are:

- $\overline{\lambda \Phi + \Theta} = \lambda \bar{\Phi} + \bar{\Theta}$ if λ is a constant,
- $\overline{\bar{\Phi}} = \bar{\Phi}$,
- $\overline{\bar{\Phi} \Theta} = \bar{\Phi} \bar{\Theta}$.

The most widespread Reynolds averaging methods are based on [29]:

- **Time averaging.** The mean value is obtained by averaging over a time interval Δt , where Δt has to be large enough compared to the characteristic time scales of turbulent motions. This averaging method is primarily intended for the application to statistically steady flows (no large-scale coherent structures or pulsations, steady-state calculations)

$$\overline{\Phi(x_i)_T} = \lim_{\Delta t \rightarrow \infty} \frac{1}{\Delta t} \int_0^{\Delta t} \Phi(x_i, t) dt. \quad (2.1.13)$$

- **Ensemble averaging.** If the flow is unsteady in the sense of large-scale coherent unsteadiness or pulsations which can be depicted by a peak in the low wavenumber region of the turbulent spectrum as shown in figure 2.1.3(b), time averaging is replaced by the ensemble averaging [29, 93]. Ensemble averaging means that the values of the variable of interest at the same relative time and space location are averaged over all members of an ensemble. For instance, the measurements of N experiments with the same initial boundary condition form an ensemble

$$\overline{\Phi(x_i, t)_E} = \lim_{N \rightarrow \infty} \frac{1}{N} \sum_{n=1}^N \Phi^n(x_i, t). \quad (2.1.14)$$

It should be noted that the time averaging procedure is equal to the ensemble averaging only in the case of a statistically steady flow [29]. If RANS simulations are conducted in the unsteady mode (URANS), then the ensemble averaging is assumed. It should be clear that in URANS only the deterministic motions, often representing a small part of the turbulent energy spectrum, can be resolved as indicated in figure 2.1.3. The largest part including the inertial subrange is

still represented by a model in contrast to the LES approach which is the subject of the next section.

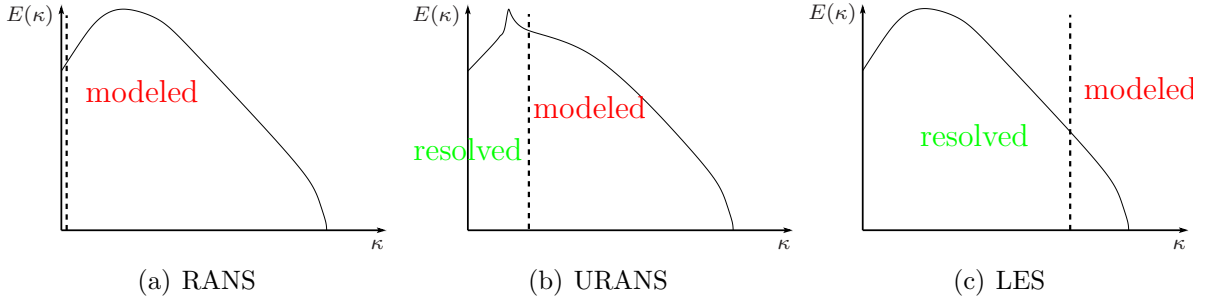


Figure 2.1.3: Turbulence energy spectrum as a function of wave numbers (log-log scales). Resolved and modeled parts in RANS, URANS, and LES.

After the application of the Reynolds-averaging procedure to the equations 2.1.1, 2.1.2, and 2.1.3 and assuming the density is constant, the following equations can be obtained [128, 29]:

$$\frac{\partial \bar{U}_j}{\partial x_j} = 0, \quad j = 1 - 3, \quad (2.1.15)$$

$$\frac{\partial \bar{U}_i}{\partial t} + \bar{U}_j \frac{\partial \bar{U}_i}{\partial x_j} = -\frac{1}{\rho} \frac{\partial \bar{P}}{\partial x_i} + \frac{\partial}{\partial x_j} \left[\nu \left(\frac{\partial \bar{U}_i}{\partial x_j} + \frac{\partial \bar{U}_j}{\partial x_i} \right) - \overline{u'_i u'_j} \right], \quad i, j = 1 - 3, \quad (2.1.16)$$

$$\frac{\partial \bar{C}}{\partial t} + \bar{U}_j \frac{\partial \bar{C}}{\partial x_j} = \frac{\partial}{\partial x_j} \left(\alpha \frac{\partial \bar{C}}{\partial x_j} - \overline{c' u'_j} \right), \quad j = 1 - 3. \quad (2.1.17)$$

As a result of applying the averaging procedure to the non-linear convective terms, new unknown correlations $\overline{u'_i u'_j}$ and $\overline{c' u'_j}$ appear in the equations. These correlations represent the turbulent transport of momentum and scalar and are called Reynolds stresses and turbulent scalar fluxes. A set of four equations 2.1.15 and 2.1.16 contains ten unknowns: \bar{U}_i , \bar{P} and $\overline{u'_i u'_j}$. To close these equations a semi-empirical formulation for six Reynolds stresses $\overline{u'_i u'_j}$ is needed. Equation 2.1.17 consists of four unknowns: \bar{C} and $\overline{c' u'_j}$ and here additional modeling of the turbulent scalar fluxes is necessary. The closure problem for the equations 2.1.15 - 2.1.17 is discussed in detail in section 2.2.

2.1.4 Filtering

As pointed out in the previous section, the application of the Reynolds-averaging operator to the equations 2.1.1 - 2.1.3 creates a set of equations 2.1.15 - 2.1.17 that are not capable of a deep resolution of the turbulent spectrum. However, even in industrial simulations time- and space-resolution of all large and intermediate turbulent structures, including those in the inertial sub-range, is often necessary for a better understanding of the fundamental flow, mixing,

and combustion phenomena. In this case an operator different than the Reynolds-averaging should be used that would allow the artificial decomposition of the scales of the turbulent motion into the resolved ones (large to intermediate) and the modeled ones (small). In the LES methods such a scale separation is realized by the application of a filtering procedure in spectral space (components greater than a given cut-off frequency are suppressed) or in physical space (weighted average over a given volume). The filtered quantity $\bar{\Phi}$ is defined as [39, 99, 108]

$$\bar{\Phi}(\mathbf{x}) = \int_{\mathbb{R}^3} G(\mathbf{x} - \mathbf{y}, \Delta(\mathbf{x})) \Phi(\mathbf{y}) d\mathbf{y}, \quad (2.1.18)$$

where $\mathbf{x} \in \mathbb{R}^3$, G is the filter, and Δ is the filter width. The filter G should conform to the relationship [39, 99, 108]

$$\int_{\mathbb{R}^3} G(\mathbf{x} - \mathbf{y}, \Delta(\mathbf{x})) d\mathbf{y} = 1. \quad (2.1.19)$$

The filtering operation differs from the Reynolds-averaging operation described in the previous section as follows. An averaging operation is “completed”, i.e. a time-averaged variable does not depend on time and a space-averaged variable does not depend on a coordinate [39]. After applying the filtering operation in time or space, a time or coordinate dependence still exists. A completed averaging operation is obtained in the limiting case of the infinite filter width [39]; furthermore, contrary to RANS averaging, the filtered value of a LES perturbation is not zero [39, 99, 108]

$$\overline{\phi'} \neq 0, \quad (2.1.20)$$

and filtered and double filtered values are not equal in general [39, 99, 108]

$$\overline{\bar{\Phi}} \neq \bar{\Phi}. \quad (2.1.21)$$

The advantage of filtering is that depending on the filter width the structures of different size can be “covered”, which better represents the multiscale nature of turbulence and can be used at the construction of the fine-scale models [39, 99, 108].

Filtering the instantaneous balance equations leads to the following equations formally similar to the Reynolds averaged balance equations derived in the previous subsection [39]:

$$\frac{\partial \bar{U}_j}{\partial x_j} = 0, \quad (2.1.22)$$

$$\frac{\partial \bar{U}_i}{\partial t} + \bar{U}_j \frac{\partial \bar{U}_i}{\partial x_j} = -\frac{1}{\rho} \frac{\partial \bar{P}}{\partial x_i} + \frac{\partial}{\partial x_j} \left[\nu \left(\frac{\partial \bar{U}_i}{\partial x_j} + \frac{\partial \bar{U}_j}{\partial x_i} \right) - (\overline{U_i U_j} - \bar{U}_i \bar{U}_j) \right], \quad (2.1.23)$$

$$\frac{\partial \bar{C}}{\partial t} + \bar{U}_j \frac{\partial \bar{C}}{\partial x_j} = \frac{\partial}{\partial x_j} \left(\alpha \frac{\partial \bar{C}}{\partial x_j} - (\overline{C U_j} - \bar{C} \bar{U}_j) \right). \quad (2.1.24)$$

Here, as in the RANS equations 2.1.15 - 2.1.17, new unclosed quantities appear which require additional modeling. In the LES terminology those quantities are called subfilter or more often subgrid scale (SGS) variables since the filter size is typically chosen to be equal to the grid cell size. The unclosed variables are:

- unresolved (SGS) Reynolds stresses $\overline{u_i' u_j'} - \overline{u_i} \overline{u_j}$,
- unresolved (SGS) scalar fluxes $\overline{C u_j} - \overline{C} \overline{u_j}$.

From a theoretical point of view, LES modeling should be less demanding than RANS. The reason is that the small scales that are represented by the unclosed terms in the LES equations have a more universal character than the big ones which are taken into account in the Reynolds-averaged equations. Possible approaches for the modeling of the SGS Reynolds stresses and scalar fluxes are discussed in the section 2.3.1.1 and in refs. [39, 99, 108].

As pointed out above the equation sets 2.1.15-2.1.17 and 2.1.22-2.1.24 have a similar form. Taking into account the main characteristics of the Reynolds-averaging operator, the Reynolds stresses $\overline{u_i' u_j'}$ and the turbulent scalar fluxes $\overline{C u_j'}$ in equations 2.1.15-2.1.17 can be rewritten as $\overline{u_i' u_j'} = \overline{u_i u_j} - \overline{u_i} \overline{u_j}$ and $\overline{C u_j'} = \overline{C u_j} - \overline{C} \overline{u_j}$. This allows considering these two sets of equations as particular cases of a general equation set where the symbol $\overline{(\quad)}$ denotes the application of a general scale separation operator without special assumptions carried out about the nature of this operator [108]. This similarity of the Reynolds-averaged and filtered equations motivates the development of a coupling between these two approaches and the construction of hybrid strategies which can potentially combine the advantages of both of them [108]. Such hybrid approaches will be discussed in section 2.3.1.2.

2.2 RANS modeling

In this section the widespread approaches for the closure of the Reynolds-averaged equations 2.1.16 and 2.1.17 obtained in section 2.1.3 are considered. The most direct method for such a closure is the construction of the additional transport equations for the Reynolds stress tensor and the turbulent scalar flux vector. The derivation of the exact transport equations is described in the works [29, 128]. The resulting equations are:

$$\begin{aligned} \frac{\partial \overline{u_i' u_j'}}{\partial t} + \overline{u_l} \frac{\partial \overline{u_i' u_j'}}{\partial x_l} = & \underbrace{-\overline{u_j' u_l'} \frac{\partial \overline{u_i}}{\partial x_l} - \overline{u_i' u_l'} \frac{\partial \overline{u_j}}{\partial x_l}}_{\text{production}} \underbrace{- 2\nu \frac{\partial \overline{u_i'}}{\partial x_l} \frac{\partial \overline{u_j'}}{\partial x_l}}_{\text{molecular dissipation}} \\ & - \underbrace{\frac{1}{\rho} \left(\overline{u_j' \frac{\partial p'}{\partial x_i}} + \overline{u_i' \frac{\partial p'}{\partial x_j}} \right)}_{\text{redistribution}} \underbrace{- \frac{\partial}{\partial x_l} \overline{u_l' u_i' u_j'}}_{\text{turbulent diffusion}} \underbrace{+ \nu \frac{\partial^2}{\partial x_l^2} \overline{u_i' u_j'}}_{\text{molecular diffusion}} , \end{aligned} \quad (2.2.1)$$

$$\begin{aligned}
 \frac{\partial \overline{c'u'_i}}{\partial t} + \overline{U}_j \frac{\partial (\overline{c'u'_i})}{\partial x_j} = & \underbrace{-\overline{u'_i u'_j} \frac{\partial \overline{C}}{\partial x_j}}_{\text{production}} - \underbrace{\overline{c'u'_j} \frac{\partial \overline{U}_i}{\partial x_j}}_{\text{dissipation}} - (\alpha + \nu) \underbrace{\overline{\frac{\partial u'_i}{\partial x_j} \frac{\partial c'}{\partial x_j}}}_{\text{molecular diffusion}} \\
 & \underbrace{-\frac{1}{\rho} \overline{c' \frac{\partial p'}{\partial x_i}}}_{\text{redistribution}} \underbrace{- \frac{\partial}{\partial x_j} \overline{u'_j u'_i c'}}_{\text{turbulent diffusion}} + \underbrace{\frac{\partial}{\partial x_j} \left(\overline{\alpha u'_i \frac{\partial c'}{\partial x_j}} + \overline{\nu c' \frac{\partial u'_i}{\partial x_j}} \right)}_{\text{molecular diffusion}}, \quad (2.2.2)
 \end{aligned}$$

where $i, j, l = 1 - 3$. The interpretation of each particular term on the right-hand side of these equations is denoted above.

It can be seen that the exact equations are not closed but contain additional terms such as third order moments, $\overline{u'_l u'_i u'_j}$ and $\overline{u'_j u'_i c'}$ as well as the velocity-pressure gradient $\overline{u'_i \frac{\partial p'}{\partial x_j}}$ and scalar-pressure gradient $\overline{c' \frac{\partial p'}{\partial x_i}}$ correlations; consequently, the solution of equations 2.2.1 and 2.2.2 is impossible without additional models for these terms. Attempts to form the exact equations for third-order moments lead to appearance of unclosed moments of higher order, thus successive formation of the transport equations for higher moments does not achieve closure [29]. Additionally, the velocity-pressure gradient correlation implicitly introduces the two-point velocity correlation and non-locality to the equation [29]. The two-point correlation $\overline{u'_i(x) u'_j(x^*)}$ is generally a function of six coordinates (x_l, x_k^*) , $l = 1 - 3, k = 1 - 3$. This dependence should be reflected in the model, which would be is a difficult task. Thus using the Reynolds stress and turbulent scalar flux equations for the closure of equations 2.1.16 and 2.1.17 adds at least nine further equations to the system and produces a non-trivial modeling effort.

For this reason, in practical applications, a much more popular approach for constructing closures of equations 2.1.16 and 2.1.17 is through eddy viscosity and eddy scalar diffusivity hypotheses. The eddy viscosity hypothesis (Boussinesq approximation) assumes that the Reynolds stresses can be algebraically expressed in terms of the mean velocity strain-rate tensor and of a turbulent viscosity ν_t , analogous to how viscous stresses in Newtonian fluids are expressed in terms of the strain-rate tensor and the molecular viscosity ν . In contrast to ν , the eddy viscosity ν_t , however, is not a material property but rather a local function of the flow field. Neglecting the density variation effects this hypothesis can be written as [128, 29]:

$$-\overline{u'_i u'_j} = -\frac{2}{3} k \delta_{ij} + \nu_t \left(\frac{\partial \overline{U}_i}{\partial x_j} + \frac{\partial \overline{U}_j}{\partial x_i} \right) = -\frac{2}{3} k \delta_{ij} + 2\nu_t \overline{S}_{ij}, \quad (2.2.3)$$

where \overline{S}_{ij} is the mean strain-rate tensor defined as

$$\overline{S}_{ij} = \frac{1}{2} \left(\frac{\partial \overline{U}_i}{\partial x_j} + \frac{\partial \overline{U}_j}{\partial x_i} \right). \quad (2.2.4)$$

The turbulent kinetic energy k is defined as

$$k = \frac{1}{2} \overline{u'_l u'_l} \quad (2.2.5)$$

with $l = 1-3$ and has been added in equation 2.2.3 to avoid an inconsistency with the continuity equation.

The turbulent scalar diffusivity hypothesis states that the turbulent scalar fluxes are linearly related to the mean scalar gradient [29]

$$-\overline{c' u'_j} = \alpha_t \frac{\partial \overline{C}}{\partial x_j}. \quad (2.2.6)$$

Here α_t is the turbulent scalar diffusivity. This hypothesis is an analogy to Fick's law (molecular diffusive scalar flux is linearly related to the mean scalar gradient). As in the case of the turbulent viscosity ν_t , the turbulent scalar diffusivity α_t is not a property of the fluid itself but mimics the characteristics of the turbulent transport under the given local flow conditions and the local scalar distribution.

Using both the eddy viscosity as well as the eddy diffusivity hypotheses the Reynolds-averaged momentum and scalar transport equations can be written as:

$$\frac{\partial \overline{U}_i}{\partial t} + \overline{U}_j \frac{\partial \overline{U}_i}{\partial x_j} = -\frac{1}{\rho} \frac{\partial \mathbf{P}}{\partial x_i} + \frac{\partial}{\partial x_j} \left[(\nu + \nu_t) \left(\frac{\partial \overline{U}_i}{\partial x_j} + \frac{\partial \overline{U}_j}{\partial x_i} \right) \right], \quad (2.2.7)$$

$$\frac{\partial \overline{C}}{\partial t} + \overline{U}_j \frac{\partial \overline{C}}{\partial x_j} = \frac{\partial}{\partial x_j} \left[(\alpha + \alpha_t) \frac{\partial \overline{C}}{\partial x_j} \right], \quad (2.2.8)$$

where $\mathbf{P} = \overline{P} + \frac{2}{3} \rho k$ is the modified pressure. To close these equations, modeling assumptions for ν_t and α_t have to be made. The most widespread ones are discussed in the next sections.

2.2.1 Turbulent viscosity modeling

2.2.1.1 The k and ε equations, standard k - ε model

The mixing length hypothesis introduced by L. Prandtl in 1925 leads to a representation of the turbulent viscosity ν_t as a product of the characteristic length and velocity scales [29]

$$\nu_t = \mathcal{L} \mathcal{U}. \quad (2.2.9)$$

The velocity scale can be defined using the mean turbulent kinetic energy of the flow

$$\mathcal{U} \sim \sqrt{k}. \quad (2.2.10)$$

The exact transport equation for k can be obtained from equation 2.2.1 by taking $i = j$, summing over i , and dividing by 2 [29, 128]. This results in

$$\frac{\partial k}{\partial t} + \overline{U}_l \frac{\partial k}{\partial x_l} = \underbrace{-\overline{u'_i u'_l} \frac{\partial \overline{U}_i}{\partial x_l}}_{\text{production}} - \underbrace{\nu \frac{\partial u'_i}{\partial x_l} \frac{\partial u'_i}{\partial x_l}}_{\text{dissipation}} - \underbrace{\frac{1}{\rho} \frac{\partial p' u'_l}{\partial x_l}}_{\text{pressure diffusion}} - \underbrace{\frac{1}{2} \frac{\partial \overline{u'_i u'_l u'_l}}{\partial x_l}}_{\text{turbulent diffusion}} + \underbrace{\nu \frac{\partial^2 k}{\partial x_l^2}}_{\text{molecular diffusion}}. \quad (2.2.11)$$

The first term on the right-hand side of this equation (production term) is the rate at which the turbulence is supplied with the energy taken from the mean flow

$$\mathcal{P} = -\overline{u'_i u'_l} \frac{\partial \overline{U}_i}{\partial x_l}. \quad (2.2.12)$$

Typical sources of turbulent kinetic energy generation are the flow instabilities caused by the mean shear. Another source may be stretching and intensification of the turbulent vortices by the mean rate of strain. Normally the average energy flow occurs in one direction from orderly mean flow to the disorderly turbulence. This implies that $\mathcal{P} \geq 0$; however, in some cases under the influence of strongly stabilized forces, such as centrifugal acceleration, \mathcal{P} can also become negative. This term can be easily closed using the Boussinesq hypothesis (equation 2.2.3).

The transport term $\frac{1}{2} \frac{\partial \overline{u'_i u'_l u'_l}}{\partial x_l}$ redistributes energy in space (no creation or destruction). To close the k transport equation, the triple-correlation and pressure diffusion terms are usually grouped together and approximated by a gradient transport model

$$\mathcal{D} = \mathcal{D}_t + \mathcal{D}_p = -\frac{\partial}{\partial x_l} \left[\frac{1}{2} \overline{u'_i u'_l u'_l} + \frac{1}{\rho} \overline{p' u'_l} \right] \approx \frac{\partial}{\partial x_l} \left[\frac{\nu_t}{\sigma_k} \frac{\partial k}{\partial x_l} \right]. \quad (2.2.13)$$

This closure is based on the assumption that the third velocity moment represents random convection of turbulent kinetic energy which can be modeled by diffusion [29]. It is also assumed that the pressure diffusion term is very small comparatively to other terms. The parameter σ_k in equation 2.2.13 is a modeling constant. It should be pointed out here that the relation 2.2.13 is an empirical one. The assumption that the pressure diffusion term is small and can be grouped with the turbulent transport term is based on the DNS data for simple channel flows [128, 29]. For complex flows, such as those considered here, this hypothesis as well as the general form of equation 2.2.13 may not hold.

With the above modeling procedure equation 2.2.11 can be rewritten as

$$\frac{\partial k}{\partial t} + \overline{U}_l \frac{\partial k}{\partial x_l} = \frac{\partial}{\partial x_l} \left[\left(\nu + \frac{\nu_t}{\sigma_k} \right) \frac{\partial k}{\partial x_l} \right] + \mathcal{P} - \varepsilon. \quad (2.2.14)$$

Only one unclosed term in the k equation remains; the rate of the turbulent kinetic energy dissipation

$$\varepsilon = \nu \frac{\partial u'_i}{\partial x_l} \frac{\partial u'_i}{\partial x_l}. \quad (2.2.15)$$

For this quantity, an exact transport equation can be obtained by applying the following oper-

ator to the Navier-Stokes equation 2.1.2 [128]:

$$2\nu \overline{\frac{\partial u'_i}{\partial x_l} \frac{\partial}{\partial x_l}} \quad (2.2.16)$$

The resulting equation has the form [128, 81]:

$$\begin{aligned} \frac{\partial \varepsilon}{\partial t} + \bar{U}_j \frac{\partial \varepsilon}{\partial x_j} = & \underbrace{-\nu \left(\frac{\partial u'_i}{\partial x_l} \frac{\partial u'_j}{\partial x_l} \right) \left(\frac{\partial \bar{U}_i}{\partial x_j} + \frac{\partial \bar{U}_j}{\partial x_i} \right)}_{\text{mixed production}} \underbrace{-\nu \left(\frac{\partial u'_i}{\partial x_l} \frac{\partial u'_i}{\partial x_j} \right) \left(\frac{\partial \bar{U}_j}{\partial x_l} + \frac{\partial \bar{U}_l}{\partial x_j} \right)}_{\text{production by mean velocity gradient}} \\ & \underbrace{-2\nu u'_j \frac{\partial u'_i}{\partial x_l} \frac{\partial^2 \bar{U}_i}{\partial x_j \partial x_l}}_{\text{gradient production}} \underbrace{-2\nu \frac{\partial u'_i}{\partial x_j} \frac{\partial u'_i}{\partial x_l} \frac{\partial u'_j}{\partial x_l}}_{\text{turbulent production}} \underbrace{-2\nu^2 \frac{\partial^2 u'_i}{\partial x_j \partial x_l} \frac{\partial^2 u'_i}{\partial x_j \partial x_l}}_{\text{dissipation}} \\ & \underbrace{-2 \frac{\nu}{\rho} \frac{\partial}{\partial x_j} \left(\frac{\partial p'}{\partial x_l} \frac{\partial u'_j}{\partial x_l} \right)}_{\text{pressure diffusion}} \underbrace{-\nu \frac{\partial}{\partial x_j} \left(\frac{\partial u'_i}{\partial x_l} \frac{\partial u'_i}{\partial x_l} \right)}_{\text{turbulent diffusion}} \underbrace{+ \nu \frac{\partial^2 \varepsilon}{\partial x_j^2}}_{\text{molecular diffusion}}. \end{aligned} \quad (2.2.17)$$

This equation is much more complex than the exact transport equation for k (equation 2.2.11). It involves several new unknown double and triple correlations of fluctuating velocity, pressure, and velocity gradients. These correlations are essentially impossible to measure. Only a few DNS-based studies on the exact terms of the ε -equation exist [81, 65, 66], and, due to their cost, such studies are typically restricted to the channel and boundary layer flows at moderate Reynolds numbers.

Instead of the exact equation for ε , in engineering practice the following semi-empirical equation is normally used [101]

$$\frac{\partial \varepsilon}{\partial t} + \bar{U}_j \frac{\partial \varepsilon}{\partial x_j} = \underbrace{\mathcal{D}_\varepsilon}_{\text{diffusion}} + \underbrace{C_{\varepsilon 1} \mathcal{P}_\varepsilon \frac{\varepsilon}{k}}_{\text{production}} - \underbrace{C_{\varepsilon 2} \varepsilon \frac{\varepsilon}{k}}_{\text{dissipation}}. \quad (2.2.18)$$

Historically this equation was obtained not as an attempt to model the exact terms of equation 2.2.17 but rather as a result of dimensional analysis, analogy to equation 2.2.14, and rational considerations of the physics of turbulence [128]. If the diffusion term in the equation 2.2.18 is closed similarly to the diffusion term of the k -equation,

$$\mathcal{D}_\varepsilon = \frac{\partial}{\partial x_j} \left[\frac{\nu_t}{\sigma_\varepsilon} \frac{\partial \varepsilon}{\partial x_j} \right], \quad (2.2.19)$$

then the final form of the ε -equation is

$$\frac{\partial \varepsilon}{\partial t} + \bar{U}_j \frac{\partial \varepsilon}{\partial x_j} = \frac{\partial}{\partial x_j} \left[\left(\nu + \frac{\nu_t}{\sigma_\varepsilon} \right) \frac{\partial \varepsilon}{\partial x_j} \right] + C_{\varepsilon 1} \mathcal{P}_\varepsilon \frac{\varepsilon}{k} - C_{\varepsilon 2} \varepsilon \frac{\varepsilon}{k}. \quad (2.2.20)$$

This equation together with equation 2.2.14 builds the basis of the most widespread RANS

turbulence closure - k - ε turbulence model of Jones and Launder (1972) [61] (often referred as standard k - ε model). In this model k and ε are used to build the length scale of the mixing-length hypothesis (equation 2.3.4) as

$$\mathcal{L} \sim \frac{k^{3/2}}{\varepsilon}. \quad (2.2.21)$$

Using the relation 2.2.10 for the length scale the final formula for ν_t is obtained as

$$\nu_t = \mathcal{L} \mathcal{U} = C_\mu \frac{k^2}{\varepsilon}, \quad (2.2.22)$$

where C_μ is the modeling constant. Equations 2.2.14, 2.2.20, and 2.2.22 contain five free parameters - modeling constants: C_μ , $C_{\varepsilon 1}$, $C_{\varepsilon 2}$, σ_k , σ_ε . The standard values of these constants are [101, 128, 29]:

$$C_\mu = 0.09, \quad C_{\varepsilon 1} = 1.44, \quad C_{\varepsilon 2} = 1.92, \quad \sigma_k = 1.0, \quad \sigma_\varepsilon = 1.3. \quad (2.2.23)$$

The established method for deriving model constants for the k - ε and other two-equation turbulence models is by analysis of analytical solutions and experimental measurements from relatively simple flows. In these flows some equation terms can be neglected, thereby isolating other terms such that a unique constant value allows for a meaningful solution. The widely studied canonical flows used for this purpose are: decaying homogeneous isotropic turbulence, homogeneous shear layer, and the logarithmic region of a boundary layer. The derivation of the analytical solutions of k - ε model equations for these test cases can be found in ref. [29]. Here only the main results are listed to illustrate the methodology.

The relation for the dissipation of dissipation constant $C_{\varepsilon 2}$ can be obtained by considering the case of decaying homogeneous isotropic turbulence and simplification of the modeling equations for this type of flow. As a result $C_{\varepsilon 2}$ can be represented by

$$C_{\varepsilon 2} = \frac{n+1}{n}, \quad (2.2.24)$$

where n is the decay exponent which can be found by fitting the decay curve, $k \sim t^{-n}$, obtained through measurements of grid turbulence in a wind tunnel. The experimental values of this parameter are in the range $n = 1.3 \pm 0.2$ [29]. The value of $n = 1.3$ would give $C_{\varepsilon 2} = 1.77$; the standard value in equation 2.2.23 corresponds to a rather low decay exponent $n = 1.09$ [29].

Another formula prescribing the relation between $C_{\varepsilon 2}$ and $C_{\varepsilon 1}$ can be obtained by analytic solution of the modeling equations in the case of homogeneous shear flow.

$$\frac{C_{\varepsilon 2} - 1}{C_{\varepsilon 1} - 1} = \frac{\mathcal{P}}{\varepsilon}. \quad (2.2.25)$$

The experimental values of \mathcal{P}/ε in a homogeneous shear flow are approximately 1.6 ± 0.2 [29]. Taking $\mathcal{P}/\varepsilon = 1.6$ and the standard value of $C_{\varepsilon 2} = 1.92$, $C_{\varepsilon 1} = 1.58$ is found. The standard value $C_{\varepsilon 1} = 1.44$ was chosen historically since it produces more accurate predictions of the

spreading rates in mixing layers. As pointed out in ref. [29] since equation 2.2.25 can be rewritten as

$$\frac{\mathcal{P}}{\varepsilon} - 1 = \frac{C_{\varepsilon 2} - C_{\varepsilon 1}}{C_{\varepsilon 1} - 1}, \quad (2.2.26)$$

the value of $C_{\varepsilon 2} - C_{\varepsilon 1}$ has decisive influence on the predicted spreading rates of shear flows. This implies that the constant $C_{\varepsilon 1}$ actually does not have a unique value that can be determined from a single calibration experiment, and the established value of $C_{\varepsilon 1} = 1.44$ is rather a historical compromise.

A very important class of flows for the calibration of model constants are boundary layer flows. The logarithmic layer is defined as the portion of the boundary layer sufficiently distant from the surface that molecular viscosity is negligible relative to eddy viscosity, yet close enough for convective effects to be negligible [128]. In this layer, the following relation holds for the dimensionless near-wall velocity in the main flow direction [128, 29, 101]:

$$u^+ = \frac{1}{\kappa} \ln y^+ + C_w, \quad (2.2.27)$$

where $u^+ = \bar{U}_x/u_\tau$ and u_τ is the wall friction velocity defined as $u_\tau = \sqrt{\tau_w/\rho}$ with the surface shear stress τ_w . The dimensionless distance from the wall is defined as $y^+ = u_\tau y/\nu$ (y is the absolute distance in the wall-normal direction) and the most widespread values of coefficients are $\kappa \sim 0.41 \pm 0.2$ (von Karman constant) and $C_w \sim 5.5 \pm 0.3$ [30, 128, 29].

In the logarithmic layer Reynolds shear stress $\overline{u'_x u'_y}$ is constant and equal to the u_τ^2 . The log-law can be also stated as

$$\frac{\partial \bar{U}_x}{\partial y} = \frac{u_\tau}{\kappa y}. \quad (2.2.28)$$

Moreover, in the logarithmic layer production and dissipation are locally in balance [29]

$$\mathcal{P} = \varepsilon \quad (2.2.29)$$

and it becomes that

$$\mathcal{P} = -\overline{u'_x u'_y} \frac{\partial \bar{U}_x}{\partial y} = \frac{u_\tau^3}{\kappa y} = \varepsilon \quad (2.2.30)$$

has to be the relation for ε [29]. Using the eddy viscosity definition for this particular case $\nu_t = -\overline{u'_x u'_y} / \frac{\partial \bar{U}_x}{\partial y} = \kappa u_\tau y$ and the k - ε eddy viscosity equation $\nu_t = C_\mu (k^2/\varepsilon)$, following relation for k can be obtained

$$k = \frac{u_\tau^2}{\sqrt{C_\mu}} \quad (2.2.31)$$

or $C_\mu = (\overline{u'_x u'_y}/k)^2$. The experimental value of $|\overline{u'_x u'_y}/k|$ is about 0.3 in the logarithmic layer (Bradshaw constant). This results in $C_\mu = 0.09$. Additionally to the estimation of the turbulent viscosity modeling constant C_μ , the log-law solution can be used to obtain the σ_ε constant (see ref. [29] for details).

Thus with the constants derived as described above the standard k - ε model is closed and can

be used for the practical modeling of the turbulent flows. It is evident that the model equations and their closure coefficients are based on several assumptions and simplifications which do not necessarily hold in complex flows. Despite of this, the standard k - ε model shows a remarkable universality and is the basis for the large family of the engineering turbulence models created later. The next sections will be devoted to the description of the most widespread model refinements, variations, and improvements that may be potentially useful in the context of the complex internal jet flows typical for the GT combustion applications.

2.2.1.2 Round jet correction for the standard k - ε model

The round jet forms the basis for all of the flow patterns considered in this dissertation. In this context, it is of interest to consider the round jet specific corrections to the standard k - ε model [100, 19].

It is a well-known observation that the spreading rates* of free round jets are typically over predicted (by about 20%) by the standard k - ε model, even if the spreading rates of plane jets can be reproduced well by this model. This fact is called round-jet/plane-jet anomaly in the literature [100]. Pope [100] has proposed a modification to the ε -equation of the standard k - ε model (equation 2.2.20) which aims to resolve the round-jet/plane-jet anomaly. In Pope modification, the dissipation of dissipation term in the ε -equation is replaced by

$$C_{\varepsilon 2} \frac{\varepsilon^2}{k} \rightarrow [C_{\varepsilon 2} - C_{\varepsilon 3} \chi_p] \frac{\varepsilon^2}{k} \quad (2.2.32)$$

where χ_p is a non-dimensional measure of vortex stretching defined as

$$\chi_p = \frac{\overline{\Omega}_{ij} \overline{\Omega}_{jk} \overline{S}_{ki}}{(\varepsilon/k)^3}. \quad (2.2.33)$$

The tensors $\overline{\Omega}_{ij}$ and \overline{S}_{ij} are the mean rotation and mean strain-rate tensors defined as

$$\overline{\Omega}_{ij} = \frac{1}{2} \left(\frac{\partial \overline{U}_i}{\partial x_j} - \frac{\partial \overline{U}_j}{\partial x_i} \right) \quad \text{and} \quad \overline{S}_{ij} = \frac{1}{2} \left(\frac{\partial \overline{U}_i}{\partial x_j} + \frac{\partial \overline{U}_j}{\partial x_i} \right). \quad (2.2.34)$$

The reasoning of Pope is that the primary mechanism for the energy transfer from large to small scales is vortex stretching. Any mechanism that enhances vortex stretching will increase the rate of transfer and, consequently, the dissipation. Since the vortex rings are stretched radially, in 2D flows such as a plane jet the parameter χ_p is zero. By contrast, the vortex stretching parameter is nonzero for an axisymmetric mean flow such as a round jet. Using $C_{\varepsilon 3} = 0.79$ reduces the standard spreading rate of the round jet predicted by the k - ε model from $\delta'_{0.5} = 0.120$ to $\delta'_{0.5} = 0.086$ which is consistent with experimental values of this parameter [100] (the experimental spreading rate values reported by different authors for the free round jet are $\delta'_{0.5} = 0.086 - 0.096$ [128, 6, 95]).

*The spreading rate is defined as $\delta'_{0.5} = dr_{0.5}(x)/dx$ where $r_{0.5}$ is the radius at which the mean speed is half its centerline value [101].

Davidenko [19] proposed a limiter to the Pope correction that aims to increase its numerical stability. Pope correction with the Davidenko limiter is formulated as follows:

$$C_{\varepsilon 2} \frac{\varepsilon^2}{k} \rightarrow [C_{\varepsilon 2} - C_{\varepsilon 3} \min(|\chi_p|, \chi_{lim}) \operatorname{sign}(\chi_p)] \frac{\varepsilon^2}{k}, \quad (2.2.35)$$

where χ_{lim} is the constant which can be adjusted depending on the target spreading rate. In the present work the value $\chi_{lim} = 0.143$ is adopted, which results in a compromise spreading rate $\delta'_{0.5} = 0.094$ as reported by Davidenko [19].

In order to illustrate the effect of the described round jet correction on the simulation results, a free round jet simulation was performed at the experimental conditions of ref. [16]. The schematic of the test case is shown in figure 2.2.1. In the experiment slightly heated air was injected from a round pipe into a quiescent air ambient. The jet exit velocity was 11m/s , the jet exit temperature difference to the ambient temperature was 25K (very small temperature and density variations). The diameter of the jet nozzle was $d = 25.5\text{mm}$, and the Reynolds number based on this diameter is $Re_d = 17700$.

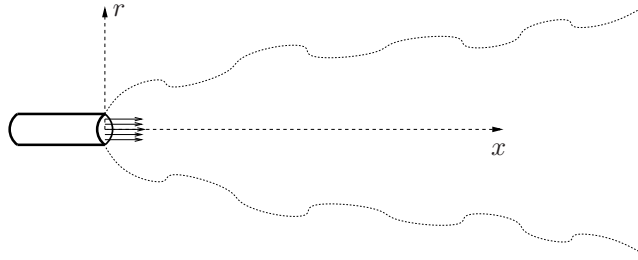


Figure 2.2.1: Free round jet test case [16].

The simulations were carried out with the DLR THETA code described in section 2.4. Structured quasi-2D grid (1 cell in the azimuthal direction, periodic boundary conditions) comprising 78000 points was used for the simulation. Further numerical details can be found in section 2.4. The profiles presented below are extracted in the self-similar region at $x/d = 35$. Using the self-similarity of the solution the reference experimental data from ref. [16] and from the well-known experiment of Panchapakesan and Lumley [95] could be used for a very detailed validation. Furthermore, the data of a well-resolved LES simulation of Bogey and Bailly [8] is used for the comparison with the RANS results in order to develop a better understanding about the possible qualitative differences between RANS and LES accuracy discussed in the introduction to this dissertation and earlier in the current chapter.

First, the profiles of the mean streamwise velocity, turbulent kinetic energy, and the components of the Reynolds stress tensor are shown in figure 2.2.2. All profiles are non-dimensionalized using the centerline velocity values \bar{U}_0 and the absolute axial coordinate $x_a = x - x_0$, where x_0 is the virtual origin of the jet (see for example refs. [128, 6] for the definition). The difference between the results achieved by the standard $k-\varepsilon$ model and its round jet correction [100, 19] is clearly seen on all profiles. The round jet correction matches the experimental velocity profile presentend in figure 2.2.2(a) quite well, whereas the standard $k-\varepsilon$ model over

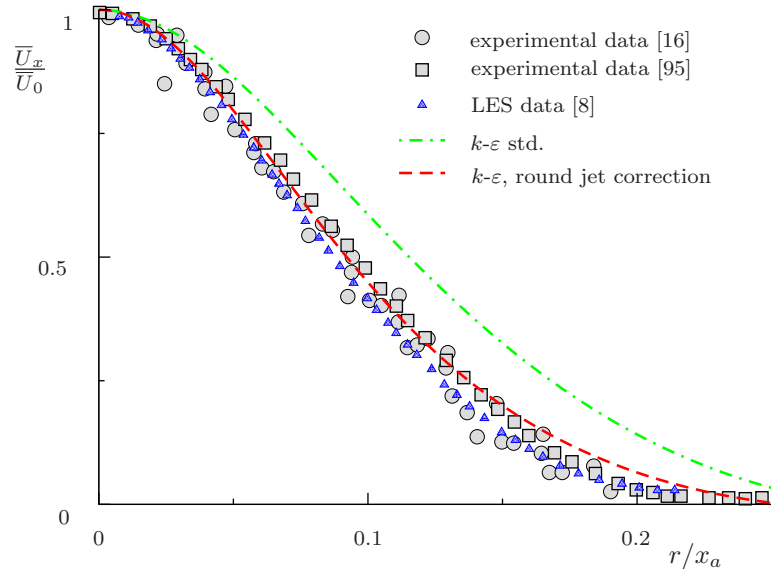
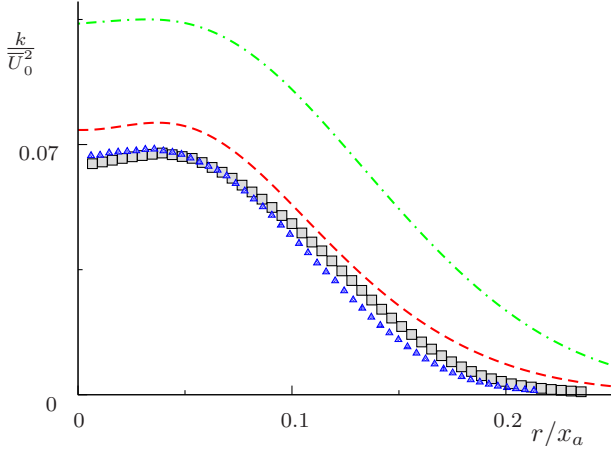
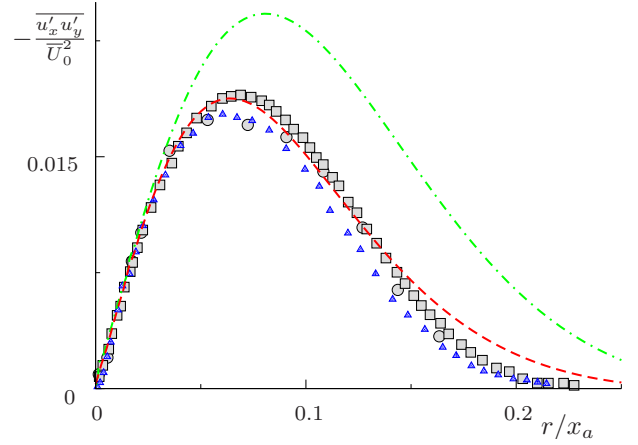
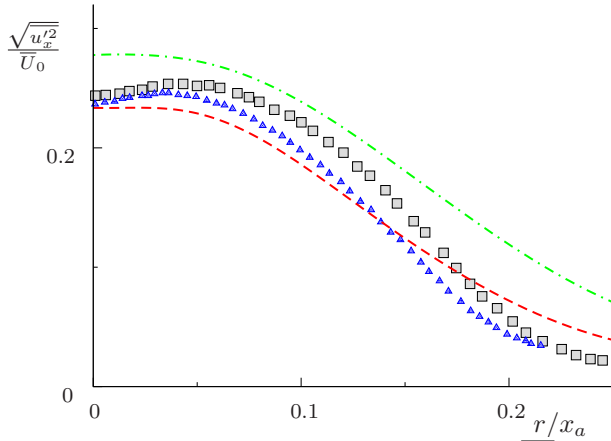
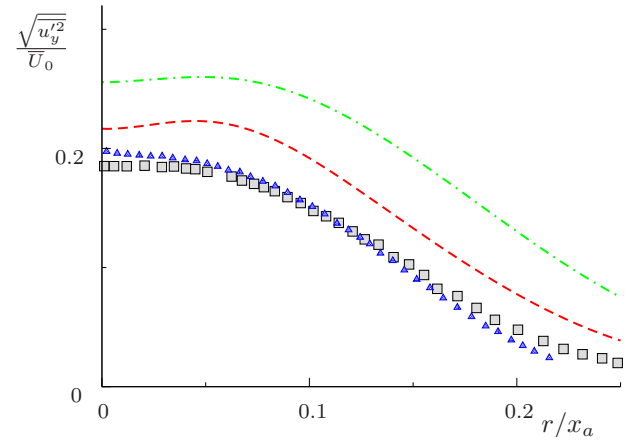

 (a) Dimensionless mean streamwise velocity $\overline{U}_x/\overline{U}_0$.

 (b) Turbulent kinetic energy k/\overline{U}_0^2 .

 (c) Reynolds shear stress $-\overline{u'_x u'_y}/\overline{U}_0^2$.

 (d) RMS of the axial velocity fluctuations $\sqrt{\overline{u'^2_x}}/\overline{U}_0$.

 (e) RMS of the radial velocity fluctuations $\sqrt{\overline{u'^2_y}}/\overline{U}_0$.

 Figure 2.2.2: Free round jet flow. Standard k - ε model and k - ε model with Pope correction and Davidenko limiter [100, 19]. Comparison of the simulation results and the data of refs. [16, 95, 8].

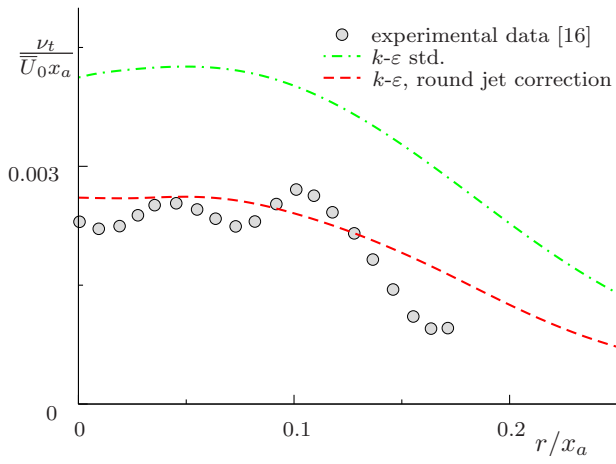
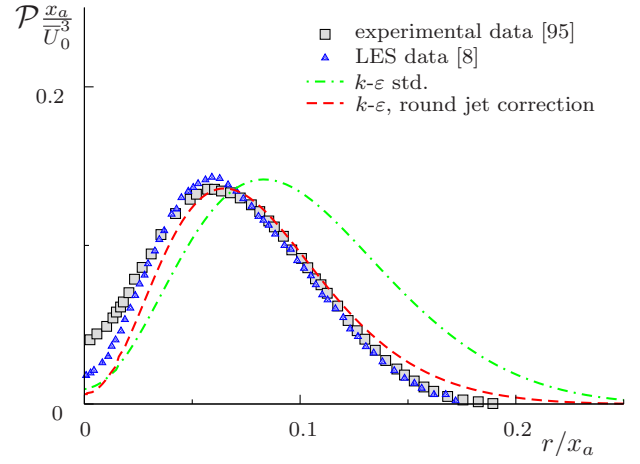
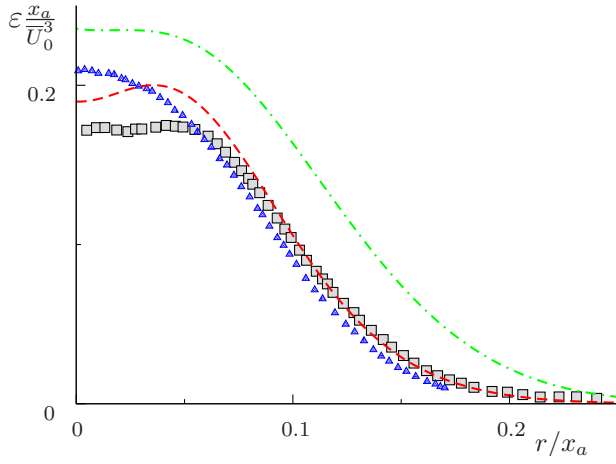
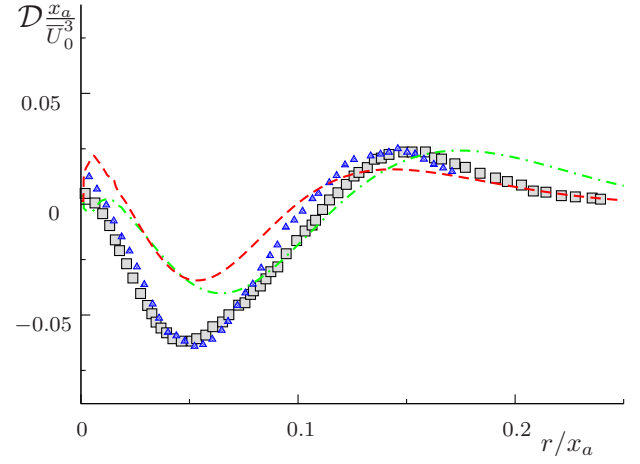
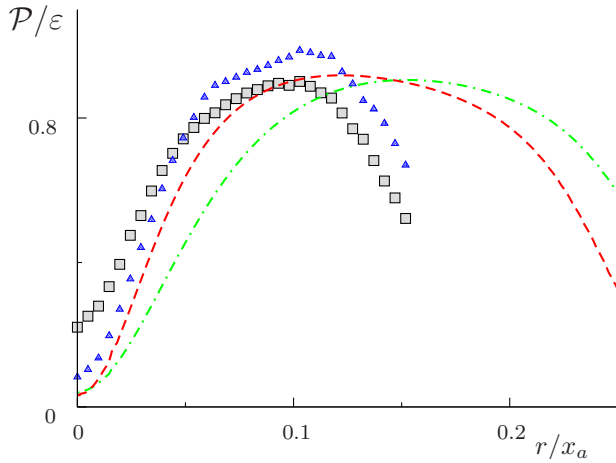
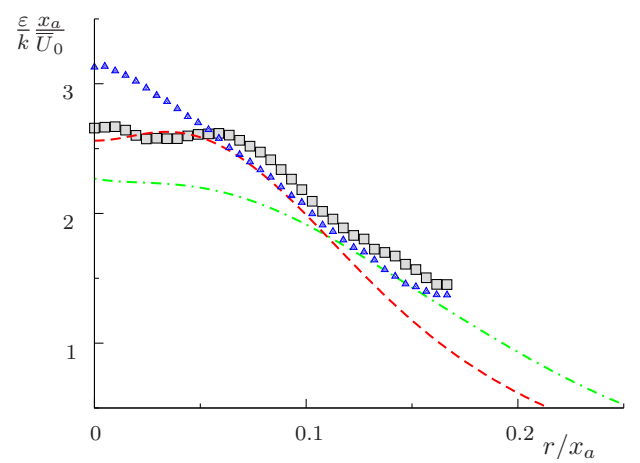

 (a) Turbulent viscosity $\nu_t/\overline{U}_0 x$

 (b) Production of the turbulent kinetic energy $\mathcal{P} \frac{x_a}{\overline{U}_0^3}$

 (c) Dissipation of the turbulent kinetic energy $\varepsilon \frac{x_a}{\overline{U}_0^3}$

 (d) Diffusion of the turbulent kinetic energy $\mathcal{D} \frac{x_a}{\overline{U}_0^3}$

 (e) Production to dissipation ratio \mathcal{P}/ε

 (f) Dimensionless dissipation per unit turbulent kinetic energy $\frac{\varepsilon}{k} \frac{x_a}{\overline{U}_0}$

Figure 2.2.3: Free round jet flow. Standard k - ε model and k - ε model with Pope correction and Davidenko limiter [100, 19]. Turbulent viscosity and budget terms of the turbulent kinetic energy transport equation. Comparison of the simulation results and the data of refs. [16, 95, 8].

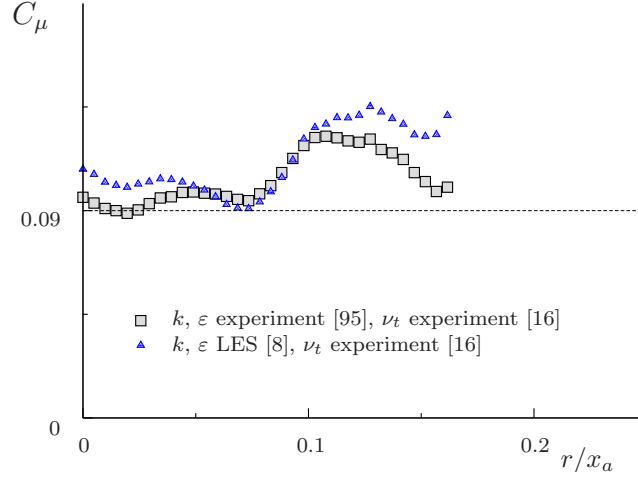


Figure 2.2.4: Turbulent viscosity modeling coefficient C_μ evaluated as $C_\mu = \nu_t \cdot \varepsilon / k^2$ using the data of refs. [16, 95, 8].

predicts the spreading rate as reported in refs. [128, 6, 100]. The level of the turbulent kinetic energy (figure 2.2.2(b)) and the Reynolds shear stress (figure 2.2.2(c)) is overestimated on the peak by about 1.5 times in the standard k - ε model simulations. The round jet correction helps to achieve results close to the experimental values. The largest differences between the experimental and the round jet correction RANS profiles can be observed in figures 2.2.2(d) and 2.2.2(e) presenting the RMS values of the axial and the radial fluctuating velocities. Whereas the $\sqrt{u_x'^2}/\bar{U}_0$ profile is slightly underestimated by the k - ε model with the round jet correction, the $\sqrt{u_y'^2}/\bar{U}_0$ values are over predicted. This is due to the Boussinesq approximation (equation 2.2.3) which results in the similar levels of both x - and y -fluctuations when in reality these levels are different. The standard k - ε model overpredicts both fluctuating components due to the general overprediction of the turbulent kinetic energy. It can be, furthermore, generally stated that regarding the mean velocity, the turbulent kinetic energy, and the Reynolds shear stress predictions the k - ε model with the round jet correction shows the same quality as the LES data of Bogey and Bailly [8]. The main difference is only the $\overline{u_x'^2}$ and $\overline{u_y'^2}$ predictions where LES, which resolves the largest part of the turbulent fluctuations, is able to represent the RMS of each fluctuating velocity component correctly.

Figure 2.2.3 presents additionally the turbulent viscosity and the budget terms of the turbulent kinetic energy balance equation resulting from both considered k - ε model variants and obtained through the evaluation of the experimental and LES data of refs. [16, 95, 8]. The dimensionless turbulent viscosity was evaluated in ref. [16] as

$$\nu_t = -\frac{\overline{u_x' u_y'}}{\frac{\partial \bar{U}_x}{\partial y} + \frac{\partial \bar{U}_y}{\partial x}}. \quad (2.2.36)$$

Such evaluation was possible since the flow is quasi-two-dimensional, and $\overline{u_x' u_y'}$ can be assumed to be the most important Reynolds stress. The turbulent viscosity evaluation procedure for

the essentially 3D flows will be considered in chapter 3. In figure 2.2.3, as in the previous figure 2.2.2, the superiority of the model including the round jet correction is obvious. The level of the turbulent viscosity (figure 2.2.3(a)) as well as of the production (figure 2.2.3(b)) and the dissipation (figure 2.2.3(c)) of k is largely overpredicted by the standard k - ε model and is represented much better by its round jet correction. The turbulent diffusion is not quite well represented by both model variants (figure 2.2.3(d)). This can be a result of the simplified diffusion formulation (equation 2.2.13) used in modeling as discussed earlier in section 2.2.1.1. In contrast to RANS, LES is able to match the experimental diffusion term profile (figure 2.2.3(d)). The pressure diffusion term, normally neglected in the RANS modeling (see equation 2.2.13), was not evaluated in experiments [95]. The LES-based study (ref. [8]) showed that this term, although small, is not negligible for the free round jet flow. The role of this term in complex jet flows will be studied in chapter 3.

Regarding the production to dissipation ratio which peak value is about $\mathcal{P}/\varepsilon = 0.8$, figure 2.2.3(e) shows that here again the profiles recovered by the model with the round jet correction are closer to the experimental and LES data than the profiles given by the standard model. This is especially true for the near-centerline region. Further away from the jet centerline both models overestimate the production to dissipation ratio which drops rapidly in the experiment and the LES. It should be, however, mentioned that the absolute values of both \mathcal{P} and ε at these locations are relatively small, so the impact of this discrepancy is probably not severe.

Since the aim of the Pope correction is to increase the dissipation ratio, underpredicted in the standard k - ε model simulations, the higher \mathcal{P}/ε obtained with the round jet correction near to the jet centerline may seem not logical even if they match the experimental values better. Figure 2.2.3(f), however, reveals that the dissipation per unit turbulent kinetic energy is higher with the round jet correction, as expected, and it is also in a closer agreement with the experimental and the LES data.

Finally here a small remark can be made on the value of the turbulent viscosity modeling parameter C_μ in equation 2.2.22. Characteristic values of this modeling coefficient can be obtained using the turbulent viscosity profile from ref. [16] and the k and ε profiles from refs. [95, 8]. The resulting C_μ calculated as $C_\mu = \nu_t \cdot \varepsilon / k^2$ (see equation 2.2.22) are presented in figure 2.2.4. Although these experimental/LES profiles are close to the traditional values $C_\mu = 0.09$ used in the tested RANS models, the assumption of a constant C_μ does not hold. Furthermore, away from the jet centerline a clear trend of the increasing of C_μ can be detected. Here probably a better choice would be the dynamic adjustment of this coefficient based on certain criteria or the local flow characteristics. An example of such an adjustment of the turbulent viscosity modeling coefficient is the near-wall damping functions used in low-Re k - ε modeling considered in the next section.

2.2.1.3 Near-wall modeling and low-Re modifications of the standard k - ε model

Near-wall modeling is often an essential element of accurate internal flow simulation. However, in the context of k - ε type models accurate representation of the near-wall turbulence is often

a non-trivial challenge. The main problem is that in the near-wall region (inside the viscous sublayer and in the transitional region between the viscous sublayer and the logarithmic layer) the formula of equation 2.2.22 gives an erroneous profile of the turbulent viscosity if the exact values of k and ε are used [29]. Several techniques exist to overcome this restriction near to solid boundaries, and an overview of such techniques is provided in this subsection.

A common approach often used in conjunction with the standard k - ε model are so-called wall functions. The idea is to avoid modeling the near-wall region where the k - ε model equations are unable to give the correct solution by setting the first near-wall computational point and the related boundary conditions for k and ε in the region of the logarithmic layer where, as shown above, the standard k - ε model equations are valid.

As pointed out above in the logarithmic layer the local equilibrium hypothesis defined by equation 2.2.30 holds. Thus ε can be expressed using the ν_t formulation for the k - ε model and the log-law in the form of equation 2.2.28 as

$$\varepsilon = \mathcal{P} = -\overline{u'_x u'_y} \frac{\partial \overline{U_x}}{\partial y} = \nu_t \frac{\partial \overline{U_x}}{\partial y} \frac{\partial \overline{U_x}}{\partial y} = C_\mu \frac{k^2}{\varepsilon} \frac{u_\tau^2}{\kappa^2 y^2}. \quad (2.2.37)$$

The resulting solution for ε is

$$\varepsilon = \frac{u_\tau}{\kappa y} k C_\mu^{1/2}. \quad (2.2.38)$$

Comparing this formula with the previously obtained relation for ε (equation 2.2.30) we can see that the skin-friction velocity u_τ can be written as

$$u_\tau = C_\mu^{1/4} k^{1/2}, \quad (2.2.39)$$

and thus ε in the first grid point (in the logarithmic layer) can be expressed as

$$\varepsilon = \frac{C_\mu^{3/4} k^{3/2}}{\kappa y}. \quad (2.2.40)$$

For the determination of k in this case, the wall boundary condition

$$\frac{\partial k}{\partial y} = 0 \quad (2.2.41)$$

is used where y is the wall-normal direction. The skin friction can also be found from the log-law applied at this point [29]. The above boundary conditions are true only in the case when the first grid point lies in the logarithmic region ($y^+ = u_\tau y / \nu \geq 40$). This is an exceptionally strong condition that does not allow the resolution of the near-wall region. It can introduce a disadvantage when the resolution of the near-wall turbulence is needed, for example in heat transfer problems. Additionally, the log-law does not hold in many realistic flows such as flows with the strong adverse pressure gradients; therefore, in such flows the above relations are incorrect and can lead to large errors.

A way to overcome the demand for a wall function is to find an approach which modifies the equations of the standard k - ε model in such a manner that the behavior of ν_t , k , and ε in the near-wall region more closely resembles the physical reality. In practice, this can be achieved by the application of so-called damping (low Reynolds number or low-Re) functions. With a damping function the eddy viscosity is expressed as

$$\nu_t = C_\mu f_\mu \frac{k^2}{\varepsilon} \quad (2.2.42)$$

with the damping function f_μ . Moreover, the production and dissipation terms of the ε -equation are normally damped as well since the damping of ν_t alone is not sufficient to obtain the correct solution in the near-wall region. The ε -equation takes the form

$$\frac{\partial \varepsilon}{\partial t} + \bar{U}_j \frac{\partial \varepsilon}{\partial x_j} = \frac{\partial}{\partial x_j} \left[\left(\nu + \frac{\nu_t}{\sigma_\varepsilon} \right) \frac{\partial \varepsilon}{\partial x_j} \right] + C_{\varepsilon 1} f_{\varepsilon 1} \mathcal{P} \frac{\varepsilon}{k} - C_{\varepsilon 2} f_{\varepsilon 2} \varepsilon \frac{\varepsilon}{k} \quad (2.2.43)$$

where $f_{\varepsilon 1}$ and $f_{\varepsilon 2}$ are near-wall damping functions. A large number of such near-wall (low-Re) k - ε models were developed by different researchers. Literature overviews on this approach can be found in refs. [97, 128]. In the present work two different low-Re k - ε models are used. The first one is the Lam-Bremhorst (LB) model [71] with:

$$\begin{aligned} f_\mu &= (1 - e^{-0.0165 R_y})^2 (1 + 20.5/Re_T) \\ f_{\varepsilon 1} &= 1 + (0.05/f_\mu)^3 \\ f_{\varepsilon 2} &= 1 - e^{-Re_T^2}. \end{aligned} \quad (2.2.44)$$

The modeling constants are the same as in the standard k - ε model (equation 2.2.23). The dimensionless parameters, Re_T and R_y , are defined as

$$Re_T = \frac{k^2}{\varepsilon \nu} \quad \text{and} \quad R_y = \frac{k^{1/2} y}{\nu}. \quad (2.2.45)$$

The second model is the model of Abe, Kondoh, and Nagano (AKN) [1]. The damping functions are defined in the following manner:

$$\begin{aligned} f_\mu &= (1 - e^{-y^*/14})^2 \left[1 + \frac{5}{Re_T^{3/4}} e^{-(Re_T/200)^2} \right], \\ f_{\varepsilon 1} &= 1, \\ f_{\varepsilon 2} &= (1 - e^{-y^*/3.1})^2 \left[1 - 0.3 e^{-(Re_T/6.5)^2} \right], \end{aligned} \quad (2.2.46)$$

where $y^* = u_\eta y / \nu$ is the dimensionless distance from the wall based on the Kolmogorov velocity scale $u_\eta = (\nu \varepsilon)^{1/4}$. The constants of this model differ slightly from the modeling constants of

the standard k - ε model:

$$C_\mu = 0.09, \quad C_{\varepsilon 1} = 1.5, \quad C_{\varepsilon 2} = 1.9, \quad \sigma_k = 1.4, \quad \sigma_\varepsilon = 1.4. \quad (2.2.47)$$

In the context of low-Re near-wall modeling, several combinations of the wall boundary conditions on k and ε can be used. The natural boundary condition for k on a non-slip solid wall is

$$k|_{wall} = 0. \quad (2.2.48)$$

This equation combined with another natural condition for k defined by equation 2.2.41 would be sufficient to solve the coupled k - ε equation system; however, in practice it is easier to use the condition $k = 0$ for k and a condition on ε . As the wall is approached, $\mathcal{P} \rightarrow 0$ and $\nu_t \rightarrow 0$ so that the equation 2.2.14 for k has the limiting behavior

$$\varepsilon = \nu \frac{\partial^2 k}{\partial y^2}. \quad (2.2.49)$$

Integration of this equation gives

$$k \rightarrow A + By + \frac{\varepsilon y^2}{2\nu}. \quad (2.2.50)$$

Taking into account equation 2.2.48, the integration constants are $A = B = 0$ and the wall value of dissipation is [128]

$$\varepsilon = \lim_{y \rightarrow 0} \frac{2\nu k}{y^2}. \quad (2.2.51)$$

Lam and Bremhorst proposed also a condition

$$\frac{\partial \varepsilon}{\partial y} = 0 \quad (2.2.52)$$

as an easier to implement alternative to equation 2.2.49 [128].

In order to illustrate the role of the low-Re corrections to the standard k - ε model, a simulation of a 2D channel flow was conducted in the present work. The reference data for the model validation was taken from the DNS publication of Kawamura et al. [66]. A structured grid comprising about 200 points over the half of the channel height was used for the simulation. The first grid point lies at $y^+ \approx 0.5$. More details on the numerical realization can be found in section 2.4.

Figure 2.2.5 shows the mean and the fluctuating velocity profiles obtained by the LB and the AKN low-Re k - ε models in comparison with the standard k - ε model results. All RANS predictions are validated against DNS data of Kawamura et al. [66]. The positive effect of the low-Re damping is clearly seen. Results produced by both the AKN and the LB models are much closer to the reference DNS data than the profiles given by standard k - ε model. The mean streamwise velocity, the turbulent kinetic energy, and the Reynolds shear stress (figures

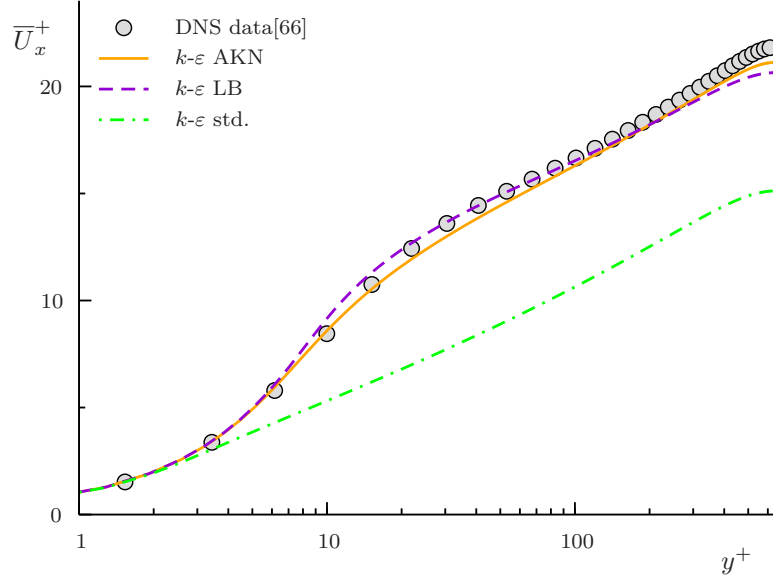
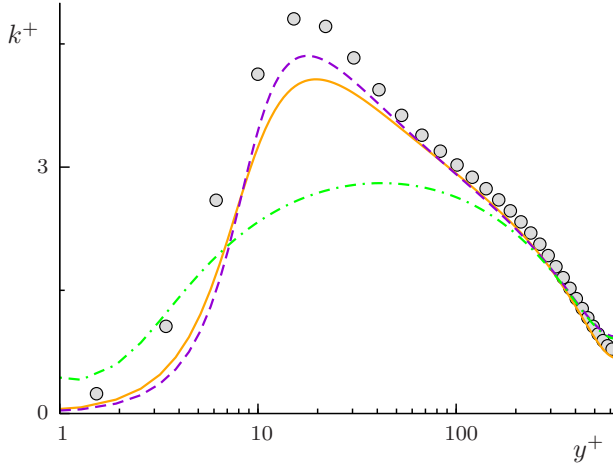
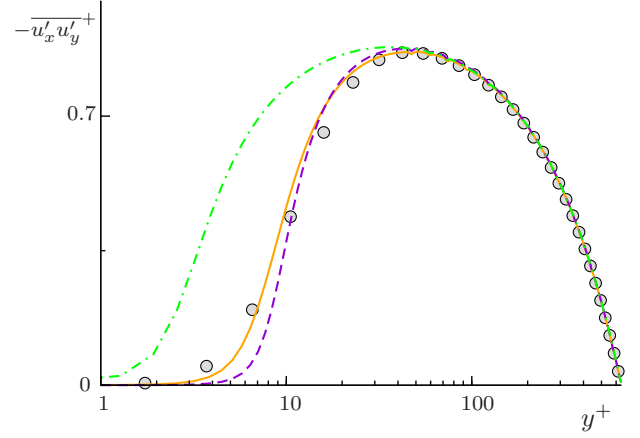
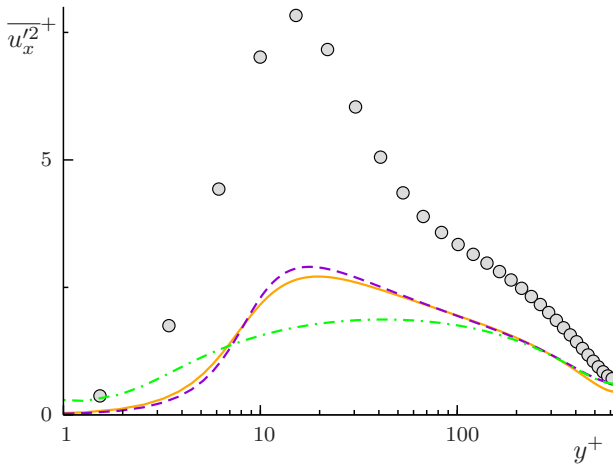
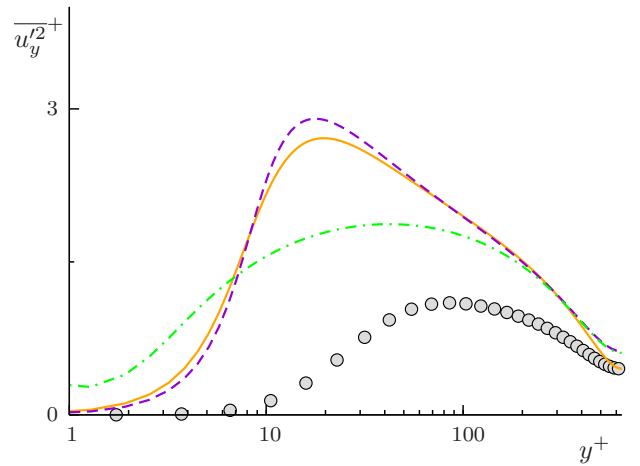

 (a) Mean streamwise velocity \overline{U}_x^+

 (b) Turbulent kinetic energy k^+

 (c) Reynolds shear stress $-\overline{u_x' u_y'^+}$

 (d) Streamwise velocity variance $\overline{u_x'^2}^+$

 (e) Wall-normal velocity variance $\overline{u_y'^2}^+$

Figure 2.2.5: 2D channel flow. Mean and fluctuating velocity field predictions. Standard k - ε model and two low-Re k - ε models in comparison with DNS data of Kawamura et al. [66]. All variables are non-dimensionalized using the skin-friction velocity u_τ and the molecular viscosity ν .

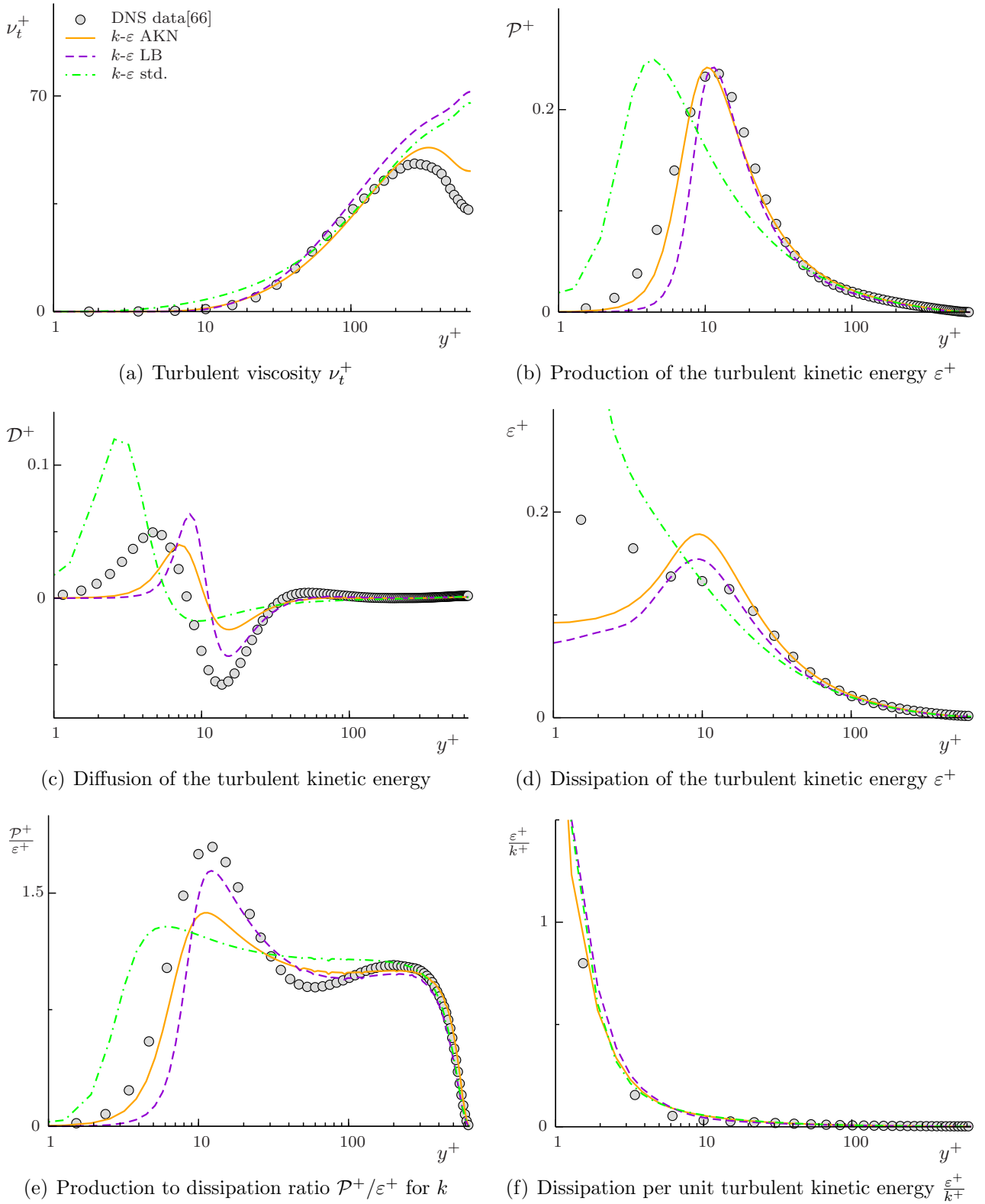


Figure 2.2.6: 2D channel flow. Turbulent viscosity and budget terms of the turbulent kinetic energy transport equation. Standard k - ε model and two low-Re k - ε models in comparison with DNS data of Kawamura et al. [66]. All variables are non-dimensionalized using the skin-friction velocity u_τ and the molecular viscosity ν .

2.2.5(a), 2.2.5(b), and 2.2.5(c) respectively) are predicted well by both low-Re models. The only drawback which can be observed in figures 2.2.5(d) and 2.2.5(e) is that, due to the turbulent viscosity isotropy assumption common for most turbulent viscosity models, both $\overline{u_x'^2}^+$ and $\overline{u_y'^2}^+$ calculated via equation 2.2.3 do not reproduce the DNS profiles even if k is predicted well.

A deeper modeling analysis can be made by the validation of further statistical turbulence quantities, such as modeled turbulent viscosity and the budget terms of the modeled turbulent kinetic energy balance equation, against DNS data. Figure 2.2.6 presents such a validation. First, in figure 2.2.6(a), the modeled turbulent viscosity is compared with ν_t evaluated from the DNS data of Kawamura et al. [66] using equation 2.2.36. It can be seen that ν_t predicted by the AKN model gives the closest agreement with the experimental data. The ν_t resulting from the LB model is similar to the ν_t of AKN in the region $y^+ < 30$. With increasing wall distance the LB ν_t profile becomes more similar to the ν_t given by the standard $k-\varepsilon$ model. This can be explained by the weak influence of the damping functions of LB model away from the wall illustrated in figure 2.2.7 and by the equality of the closure constants of the standard $k-\varepsilon$ and the LB $k-\varepsilon$ modeling equations. Figure 2.2.6(a) also makes evident the decisive importance of the $y^+ < 30$ region for the accuracy of the turbulence prediction further away from the wall. Even if ν_t given by the standard $k-\varepsilon$ and the LB $k-\varepsilon$ models at $y^+ > 30$ are quite similar, the resulting mean and fluctuating velocity profiles are drastically different (figure 2.2.5). Thus a conclusion can be made that this difference is caused by the difference in ν_t modeling at $y^+ < 30$.

The modeling differences between the standard $k-\varepsilon$ and the low-Re $k-\varepsilon$ models become much more evident after the comparison of the profiles of turbulent kinetic energy production, diffusion, and dissipation corresponding to the respective terms of the exact k -equation (equation 2.2.11) evaluated from the DNS data [66] and the respective terms of the modeled k -equation (equation 2.2.14). Such a comparison is given in figures 2.2.6(b), 2.2.6(c), and 2.2.6(d). It can be observed here that the peaks of the turbulent production, diffusion and dissipation predicted by the standard $k-\varepsilon$ model occur at much lower wall distances than in the DNS data

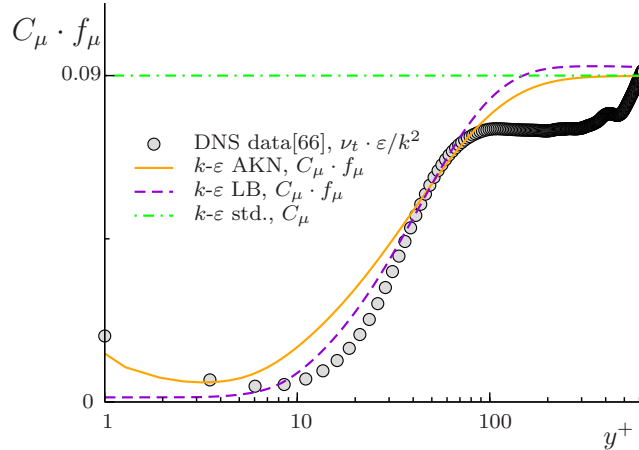


Figure 2.2.7: Turbulent viscosity modeling coefficient $C_\mu \cdot f_\mu$ evaluated from DNS data of ref. [66] as $\nu_t \cdot \varepsilon / k^2$ and used for the modeling.

or predicted by the low-Re models. The profiles resulting from the application of both low-Re models also do not perfectly correspond with the DNS data but are much closer. Regarding the production to dissipation ratio (figure 2.2.6(e)), only the LB model is able to represent its peak of about 1.8 at $y^+ \approx 10$ which also causes the closest agreement of k produced by this model with the DNS data (see figure 2.2.5(b)). Considering the dissipation per unit turbulent kinetic energy ε/k shown in figure 2.2.9(f), it is rather difficult to make a definitive statement about the comparative quality of different models.

The influence of the damping function f_μ on the value of the turbulent viscosity modeling coefficient $C_\mu \cdot f_\mu$ is illustrated in figure 2.2.7. It can be observed that here, as in the free round jet case considered in the previous section, the ν_t modeling coefficient is not constant and takes the values close to 0.09 only far away from the wall. Both low-Re damping functions studied here help to recover this behavior.

It should be mentioned here that, despite of the good results shown in figure 2.2.5, practical application of the low-Re k - ε turbulence models can cause numerical instabilities in the solution [128, 29]. Furthermore, the damping functions such as those shown above are empirically derived based on the individual experience of the model developer and the initial test cases chosen for the parameter setting. This approach thus lacks universality; consequently, an exceptionally large number of various low-Re k - ε models exists which makes the selection for the practical applications difficult. However, the problem of accurate near-wall turbulence resolution is extremely important in a variety of technical applications including those considered in the present work. In the context of engineering RANS modeling, a popular alternative to low-Re k - ε models is the application of k - ω -type models, which due to special features of the ω -equation naturally provide the desired turbulent viscosity damping in the near-wall regions. These models, their advantages and weaknesses are discussed in the next sections.

2.2.1.4 Wilcox 1988 k - ω model

The ε -equation is a natural but not the only possibility to provide the second scale (additionally to the velocity scale defined by k) in the mixing length hypothesis for turbulent viscosity (equation 2.3.4) and provide a closure of the dissipation term in the turbulent kinetic energy equation (equation 2.2.14). The most popular alternative to the ε -equation approach is the construction of a transport equation for the specific dissipation rate per unit turbulence kinetic energy, ω [128]. With this variable, the dissipation rate ε in equation 2.2.14 can be expressed as

$$\varepsilon = \beta_k k \omega \quad (2.2.53)$$

with the modeling constant β_k . The turbulent viscosity can be written as

$$\nu_t = \frac{C_\mu}{\beta_k} \frac{k}{\omega}, \quad (2.2.54)$$

or if $\beta_k = C_\mu$

$$\nu_t = \frac{k}{\omega}. \quad (2.2.55)$$

The ω -variable as dissipation per unit turbulent kinetic energy was introduced first by Kolmogorov in 1942 [70]. In the turbulence model created by Kolmogorov a differential equation similar to the transport equation for k was also proposed for ω . Further essential contribution to the development of the k - ω -type models was made by Wilcox. His model, proposed in 1988 [125] as well as later modifications reported by the same author [127, 128], proved their reliability and accuracy in a large variety of test cases [128] and this success was decisive for the popularity of k - ω - type models in engineering turbulence simulations. The model equations of the Wilcox 1988 k - ω model [125] are as follows:

$$\frac{\partial k}{\partial t} + \bar{U}_l \frac{\partial k}{\partial x_l} = \frac{\partial}{\partial x_l} \left[\left(\nu + \sigma_k \frac{k}{\omega} \right) \frac{\partial k}{\partial x_l} \right] + \mathcal{P} - \beta_k k \omega, \quad (2.2.56)$$

$$\frac{\partial \omega}{\partial t} + \bar{U}_l \frac{\partial \omega}{\partial x_l} = \frac{\partial}{\partial x_l} \left[\left(\nu + \sigma_\omega \frac{k}{\omega} \right) \frac{\partial \omega}{\partial x_l} \right] + \gamma \frac{\omega}{k} \mathcal{P} - \beta_\omega \omega^2, \quad (2.2.57)$$

where equation 2.2.55 defines the turbulent viscosity, and the modeling constants are

$$\beta_k = 0.09, \quad \sigma_k = 0.5, \quad \sigma_\omega = 0.5, \quad \beta_\omega = \frac{3}{40}, \quad \gamma = \frac{5}{9}. \quad (2.2.58)$$

The calibration methods for the modeling constants are essentially the same as described in section 2.2.1.1 for the standard k - ε model (see ref. [128] for details).

2.2.1.5 Cross-diffusion and the near-wall behavior of the Wilcox 1988 k - ω model, low-Re correction

A very important and remarkable property of the Wilcox 1988 k - ω model is its ability to represent the near-wall velocity profile well without application of additional damping functions on ν_t (discussed in section 2.2.1.3 for k - ε type models). This ability of the Wilcox 1988 k - ω model is illustrated in figure 2.2.8(a) on the example of a 2D channel flow velocity field prediction (the same test case as used in section 2.2.1.3). It can be observed that the velocity profile given by the Wilcox 1988 k - ω model (blue dashed line) corresponds favorably with the DNS data of Kawamura et al. [66] and with the predictions given by the low-Re AKN k - ε model described in section 2.2.1.3, whereas the standard k - ε model (without damping function) is not capable of a proper reproduction of the velocity profile. The reason for this favorable behavior of the Wilcox model can be understood by rewriting the ε equation of the standard k - ε model in the ω form and its comparison with the above given 1988 Wilcox ω model equation (equation 2.2.57). The $\varepsilon \rightarrow \omega$ reformulation can be made by inserting equation 2.2.53 into equation 2.2.20 and differentiating. The result is

$$\begin{aligned} \frac{\partial \omega}{\partial t} + \bar{U}_l \frac{\partial \omega}{\partial x_l} = & \frac{\partial}{\partial x_l} \left[(\nu + \sigma_\omega^* \nu_t) \frac{\partial \omega}{\partial x_l} \right] + \gamma^* \frac{\omega}{k} \mathcal{P} - \beta_\omega^* \omega^2 \\ & + \frac{\omega}{k} \frac{\partial}{\partial x_l} \left[(\sigma_\omega^* - \sigma_k^*) \nu_t \frac{\partial k}{\partial x_l} \right] + 2 \frac{(\nu + \sigma_\omega^* \nu_t)}{k} \frac{\partial k}{\partial x_l} \frac{\partial \omega}{\partial x_l} \end{aligned} \quad (2.2.59)$$

where σ_k^* , σ_ω^* , γ^* , and β_ω^* are simple functions of the k - ε closure coefficients. Assuming $\sigma_k^* = \sigma_\omega^*$ for simplicity causes the first term in the second line of equation 2.2.57 to vanish; furthermore, molecular viscosity in the last term can be neglected in the case of free shear flows. This results in

$$\frac{\partial \omega}{\partial t} + \overline{U}_l \frac{\partial \omega}{\partial x_l} = \frac{\partial}{\partial x_l} \left[(\nu + \sigma_\omega^* \nu_t) \frac{\partial k}{\partial x_l} \right] + \gamma^* \frac{\omega}{k} \mathcal{P} - \beta_\omega^* \omega^2 + \sigma_d \frac{1}{\omega} \frac{\partial k}{\partial x_l} \frac{\partial \omega}{\partial x_l}. \quad (2.2.60)$$

The main difference between the ω -equation 2.2.57 of the Wilcox 1988 k - ω model and the equation 2.2.60 is the term

$$CD = \sigma_d \frac{1}{\omega} \frac{\partial k}{\partial x_l} \frac{\partial \omega}{\partial x_l} \quad (2.2.61)$$

appearing on the right-hand side of equation 2.2.60 which depends on the gradients of both k and ω . This term is called the cross-diffusion term. In the viscous sublayer k decreases with the wall distance while ω increases. Thus the cross-diffusion term is negative in the viscous sublayer which lets it act as a sink of ω . The absence of such a sink, as in the case of equation 2.2.57, causes a strong production of ω in the viscous sublayer ($y^+ < 10$) as visualized in figure 2.2.9(f) using $\varepsilon^+/k^+ = 0.09 \cdot \omega^+$. In this figure also the values evaluated from k^+ and ε^+ resulting from the standard and the low-Re AKN k - ε models are presented. It can be observed that the Wilcox 1988 model gives an erroneous overestimation of ω^* whereas the results produced by both the standard and the low-Re k - ε models correspond well with the DNS data. However, the overprediction of ω causes the favorable viscous sublayer damping of the turbulent viscosity ν_t if the formula 2.2.55 is applied for its calculation and an accurate prediction of the turbulent viscosity in the important region $y^+ < 10$ (figure 2.2.9(a)). As a result the Reynolds shear stress (figure 2.2.8(c)) is also reproduced well by the Wilcox 1988 k - ω model (see equation 2.2.3). The level of the turbulent kinetic energy, however, is strongly underestimated, and its peak at $y^+ \approx 10$ cannot be reproduced. This can be disadvantageous in near-wall heat transfer calculations [29].

Thus, the turbulent viscosity damping in the Wilcox 1988 k - ω model, resulting from the specific behavior of equation 2.2.57, can be a useful feature in the cases when a simple stable approach is needed that can produce a reasonably correct velocity profile in the near-wall region. However, the Wilcox 1988 k - ω model is not suited well in the case when an accurate representation of the near-wall turbulence is of particular interest. For the refinement of k - ω modeling in such cases, low-Re damping functions analogous to the damping functions for k - ε models discussed in section 2.2.1.3 can be developed. An example of such a low-Re k - ω model

*It can be shown analytically that in the wall vicinity ω has the limiting behavior

$$\omega \rightarrow \frac{6\nu}{\beta_\omega y^2} \quad \text{as} \quad y \rightarrow 0. \quad (2.2.62)$$

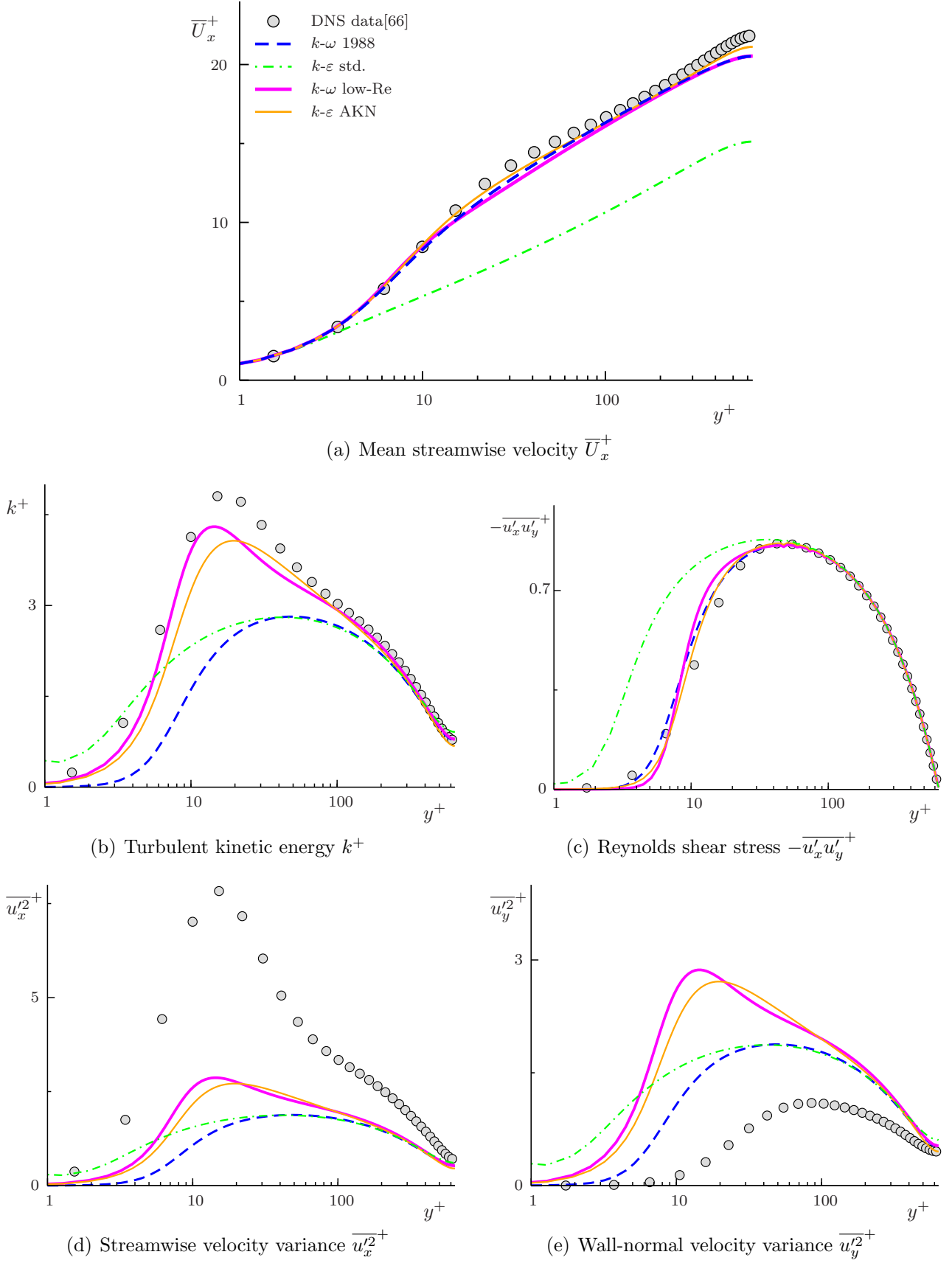


Figure 2.2.8: 2D channel flow. Mean and fluctuating velocity field predictions. Different RANS models in comparison with DNS data of Kawamura et al. [66]. All variables are non-dimensionalized using the skin-friction velocity u_τ and the molecular viscosity ν .

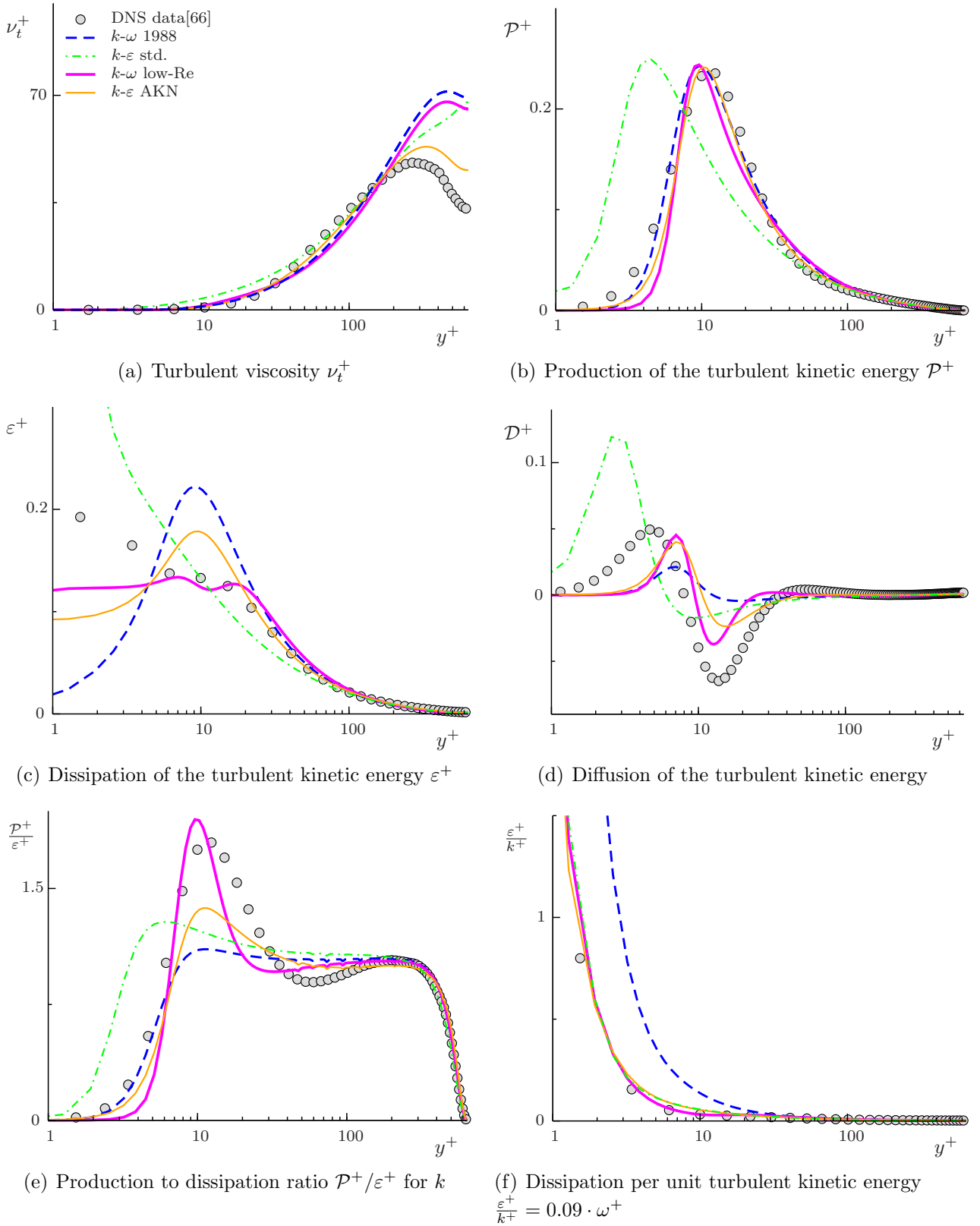


Figure 2.2.9: 2D channel flow. Turbulent viscosity and budget terms of the turbulent kinetic energy transport equation. Different RANS models in comparison with DNS data of Kawamura et al. [66]. All variables are non-dimensionalized using the skin-friction velocity u_τ and the molecular viscosity ν .

can be found in ref. [126]. The modeling equations are as follows:

$$\frac{\partial k}{\partial t} + \bar{U}_l \frac{\partial k}{\partial x_l} = \frac{\partial}{\partial x_l} \left[(\nu + \sigma_k^* \nu_t) \frac{\partial k}{\partial x_l} \right] + \mathcal{P} - \beta_k^* k \omega, \quad (2.2.63)$$

$$\frac{\partial \omega}{\partial t} + \bar{U}_l \frac{\partial \omega}{\partial x_l} = \frac{\partial}{\partial x_l} \left[\left(\nu + \sigma_\omega \frac{k}{\omega} \right) \frac{\partial \omega}{\partial x_l} \right] + \gamma \frac{\omega}{k} \mathcal{P} - \beta_\omega \omega^2, \quad (2.2.64)$$

$$\nu_t = \alpha^* \frac{k}{\omega}. \quad (2.2.65)$$

The constants and the damping functions are

$$\sigma_k = 0.5, \quad \sigma_\omega = 0.5, \quad \beta_\omega = \frac{3}{40}, \quad (2.2.66)$$

$$\alpha^* = \frac{\alpha_0^* + Re_t/R_k}{1 + Re_t/R_k}, \quad R_k = 6.0, \quad \alpha_0^* = \beta_\omega/3, \quad Re_t = \frac{k}{\omega \nu}, \quad (2.2.67)$$

$$\gamma = \frac{5}{9} \frac{\gamma_0 + Re_t/R_\omega}{1 + Re_t/R_\omega} (\alpha^*)^{-1}, \quad R_\omega = 2.7, \quad (2.2.68)$$

$$\beta_k^* = \frac{9}{100} \cdot \frac{5/18 + (Re_t/R_\beta)^4}{1.0 + (Re_t/R_\beta)^4}, \quad R_\beta = 8.0, \quad (2.2.69)$$

$$\sigma_k = 0.5, \quad \sigma_\omega = 0.5. \quad (2.2.70)$$

The results produced by this model for the 2D channel flow are presented in figures 2.2.8 and 2.2.9. The results are quite similar to those produced by the low-Re AKN k - ε model. The profiles of ω , k , \mathcal{P} , ε , and \mathcal{P}/ε correspond well with the DNS data. The peak of the turbulent kinetic energy and \mathcal{P}/ε at $y^+ \approx 10$ is even slightly higher than the DNS data, in contrast to the other tested models (figure 2.2.9(e)).

Despite the improvement given by the low-Re damping functions, this approach in application to the k - ω modeling is not a widely used one. This can be explained by two reasons. On one hand, in the cases when the precise near-wall modeling is important, application of the empiric damping functions for the k - ω modeling can potentially introduce the same numerical instability issues as low-Re k - ε modeling, so the damping functions do not provide much advantage comparatively to the more established low-Re k - ε simulations. On the other hand, in a wide range of engineering applications, the correct reproduction of the turbulent viscosity and of the mean velocity profiles satisfies the desired accuracy requirements and there is no need for a more precise modeling. In such cases the robustness and the simplicity advantages of the original ω -equation are more important than the additional accuracy given by the low-Re damping functions. For the complex flow applications in the present work, both the high- and the low-Re models will be used and the influence of the near-wall modeling on the results will be discussed.

It should be also mentioned here that for the traditional k - ω modeling, even if no low-Re damping functions are applied, the first point of the computational grid should lie in the viscous

sublayer ($y^+ \leq 2$) [86]. In industrial calculations such a grid quality often cannot be assured. From another point of view the application of the standard k - ε model with the wall-function approach implies, as discussed above in section 2.2.1.3, the near-wall grid condition $y^+ \geq 40$ which allows only for much coarser meshes. Consequently, a demand for a so-called universal wall function exists that can ensure the proper reproduction of turbulent quantities if the first grid point lies in the intermediate range of y^+ , and such an approach is described, for example, in ref. [33]. In this case ω is calculated via a blending function which depends on y^+ and combines the behavior of ω in the viscous sublayer and the logarithmic region as

$$\omega_b = \sqrt{\omega_{vis}^2(y^+) + \omega_{log}^2(y^+)}, \quad (2.2.71)$$

with

$$\omega_{vis}(y^+) = \frac{6\nu}{0.075y^2}, \quad \omega_{log}(y^+) = \frac{u_\tau}{0.3\kappa y}, \quad (2.2.72)$$

and for the wall friction velocity

$$u_\tau = \sqrt[4]{u_{\tau(vis)}^4(y^+) + u_{\tau(log)}^4(y^+)}, \quad (2.2.73)$$

$$u_{\tau(vis)}(y^+) = \frac{\overline{U}_{fp}}{y^+}, \quad u_{\tau(log)}(y^+) = \frac{\overline{U}_{fp}}{\frac{1}{\kappa} \ln(y^+) + C_w}. \quad (2.2.74)$$

Here \overline{U}_{fp} is the absolute value of the flow velocity in the first near-wall grid point.

2.2.1.6 Cross-diffusion and SST k - ω model of Menter

The lack of the cross-diffusion term (equation 2.2.61) in the ω -equation (equation 2.2.57) of the Wilcox 1988 k - ω model does not only cause strong production of ω in the viscous sublayer, as discussed in the previous subsection, but also leads to a serious model drawback in free shear flow simulations. The spreading rates of free shear flows can vary significantly depending on the ω freestream boundary conditions, and the model is not reliable in flows with detached shear layers. A detailed discussion on how this problem is related to the absence of the cross-diffusion term in equation 2.2.57 can be found in refs. [83, 84, 128]. To overcome this drawback but still retain the favorable ability of the k - ω model to damp the near-wall turbulent viscosity, Menter [83] proposed a model called the BSL (baseline) k - ω model that is essentially a combination of the Wilcox 1988 k - ω model in the near-wall region and the standard k - ε model (written in k - ω formulation) in the detached regions [83]. Additionally, in the same publication Menter pointed out another (minor) deficiency of the Wilcox 1988 k - ω model with regards to the occasional overestimation of the shear stress. To address this issue a limiter on the turbulent viscosity was proposed in [83], and the model combining both the k - ω - k - ε blending and the turbulent viscosity limiter was created. This model called the SST (shear stress transport) k - ω model is popular in engineering turbulence simulations due to its universality and reasonable accuracy

in a wide range of flows. The SST model equations in their last revision [84] appear as follows:

$$\frac{\partial k}{\partial t} + \bar{U}_l \frac{\partial k}{\partial x_l} = \frac{\partial}{\partial x_l} \left[(\nu + \sigma_k \nu_t) \frac{\partial k}{\partial x_l} \right] + \tilde{\mathcal{P}} - \beta_k k \omega, \quad (2.2.75)$$

$$\frac{\partial \omega}{\partial t} + \bar{U}_l \frac{\partial \omega}{\partial x_l} = \frac{\partial}{\partial x_l} \left[(\nu + \sigma_\omega \nu_t) \frac{\partial k}{\partial x_l} \right] + \gamma \frac{1}{\nu_t} \tilde{\mathcal{P}} - \beta_\omega \omega^2 + 2(1 - F_1) \frac{\sigma_{\omega 2}}{\omega} \frac{\partial k}{\partial x_l} \frac{\partial \omega}{\partial x_l}, \quad (2.2.76)$$

$$\nu_t = \frac{a_1 k}{\max(a_1 \omega, \mathbf{S} F_2)}, \quad (2.2.77)$$

$$\mathbf{S} = \sqrt{2 \bar{S}_{ij} \bar{S}_{ij}}, \quad \tilde{\mathcal{P}} = \min(\mathcal{P}, 10 \cdot \beta_k k \omega). \quad (2.2.78)$$

The modeling coefficients are calculated depending on the near-wall distance as a blend of an inner (1) and an outer (2) constant via

$$\phi = F_1 \phi_1 + (1 - F_1) \phi_2, \quad (2.2.79)$$

with the constants of the inner layer

$$\sigma_{k1} = 0.85, \quad \sigma_{\omega 1} = 0.5, \quad \beta_{\omega 1} = 0.075, \quad \gamma_1 = \frac{\beta_{\omega 1}}{\beta_k} - \frac{\sigma_{\omega 1} \kappa^2}{\sqrt{\beta_k}}, \quad (2.2.80)$$

and the constants of the outer layer

$$\sigma_{k2} = 1, \quad \sigma_{\omega 2} = 0.856, \quad \beta_{\omega 2} = 0.0828, \quad \gamma_2 = \frac{\beta_{\omega 2}}{\beta_k} - \frac{\sigma_{\omega 2} \kappa^2}{\sqrt{\beta_k}}; \quad (2.2.81)$$

furthermore,

$$\beta_k = 0.09, \quad \kappa = 0.41, \quad a_1 = 0.31. \quad (2.2.82)$$

The blending functions F_1 and F_2 are calculated by the following relations:

$$F_1 = \tanh(\arg_1^4), \quad (2.2.83)$$

$$\arg_1 = \min \left[\max \left(\frac{\sqrt{k}}{\beta_k \omega d}, \frac{500\nu}{\omega d^2} \right), \frac{4\rho\sigma_{\omega 2}k}{CD_{k\omega}d^2} \right], \quad (2.2.84)$$

$$CD_{k\omega} = \max \left(2\rho\sigma_{\omega 2} \frac{1}{\omega} \frac{\partial k}{\partial x_l} \frac{\partial \omega}{\partial x_l}, 10^{-10} \right), \quad (2.2.85)$$

$$F_2 = \tanh(\arg_2^2), \quad (2.2.86)$$

$$\arg_2 = \max \left(2 \frac{\sqrt{k}}{\beta_k \omega d}, \frac{500\nu}{\omega d^2} \right). \quad (2.2.87)$$

The publications [83, 84] show that results achieved by the SST model in free shear flow calculations are indeed independent of the ω freestream conditions whereas in the case of 1988 k - ω model of Wilcox this dependence is severe. That behavior is due to the positive influence of

the cross-diffusion term in the ω -equation of the SST model, which is “switched on” in the free shear flows (the walls are absent and all equations and constants are in the “outer layer”-mode). It should be mentioned here, however, that since there is no freestream boundaries in the case of internal flows, the sensitivity of 1988 k - ω model to the ω freestream conditions does not represent a major problem for the applications considered in the present work.

2.2.1.7 Wilcox 1998 and 2006 k - ω models

Considering the apparent interplay between the cross-diffusion term and freestream boundary condition sensitivity, discussed in the previous section 2.2.1.6, as well as the favorable influence of the Pope round jet correction (see section 2.2.1.2) on the round jet k - ε predictions, Wilcox in 1998 [127] and 2006 [128] proposed two improved variants of the 1988 k - ω model. Both variants include the Menter cross-diffusion and the Pope round jet corrections incorporated differently into the modeling equations.

The equations of the 1998 k - ω model of Wilcox [127] are:

$$\frac{\partial k}{\partial t} + \bar{U}_l \frac{\partial k}{\partial x_l} = \frac{\partial}{\partial x_l} \left[\left(\nu + \sigma_k \frac{k}{\omega} \right) \frac{\partial k}{\partial x_l} \right] + \mathcal{P} - \beta_k^* k \omega, \quad (2.2.88)$$

$$\frac{\partial \omega}{\partial t} + \bar{U}_l \frac{\partial \omega}{\partial x_l} = \frac{\partial}{\partial x_l} \left[\left(\nu + \sigma_\omega \frac{k}{\omega} \right) \frac{\partial \omega}{\partial x_l} \right] + \gamma \frac{\omega}{k} \mathcal{P} - \beta_\omega \omega^2, \quad (2.2.89)$$

with the following closure coefficients and auxiliary relations:

$$\gamma = \frac{13}{25}, \quad \beta_k^* = \beta_k f_{\beta k}, \quad \beta_\omega = \beta_0 f_\beta, \quad \sigma_k = \frac{1}{2}, \quad \sigma_\omega = \frac{1}{2}, \quad (2.2.90)$$

$$\beta_0 = \frac{9}{125}, \quad f_\beta = \frac{1 + 70\chi_\omega}{1 + 80\chi_\omega}, \quad \chi_\omega = \left| \frac{\bar{\Omega}_{ij} \bar{\Omega}_{jk} \bar{S}_{ki}}{(\beta_k \omega)^3} \right|, \quad (2.2.91)$$

$$\beta_k = 0.09, \quad f_{\beta k} = \begin{cases} 1, & \chi_k \leq 0 \\ \frac{1+680\chi_k^2}{1+400\chi_k^2}, & \chi_k > 0 \end{cases}, \quad \chi_k = \frac{1}{\omega^3} \frac{\partial k}{\partial x_l} \frac{\partial \omega}{\partial x_l}, \quad (2.2.92)$$

and turbulent viscosity calculated as

$$\nu_t = \frac{k}{\omega}. \quad (2.2.93)$$

The round jet correction is included in the ω -equation via the β_ω -coefficient in the dissipation term and the cross-diffusion correction appears in the dissipation term of the k equation in the β_k^* -coefficient.

A later version proposed in 2006 [128], moreover, contains the strain-rate related limiter for the turbulent viscosity also proposed earlier by Menter for the SST model (see section 2.2.1.6). The Wilcox 2006 k - ω model equations are as follows:

$$\frac{\partial k}{\partial t} + \bar{U}_l \frac{\partial k}{\partial x_l} = \frac{\partial}{\partial x_l} \left[\left(\nu + \sigma_k \frac{k}{\omega} \right) \frac{\partial k}{\partial x_l} \right] + \mathcal{P} - \beta_k k \omega, \quad (2.2.94)$$

$$\frac{\partial \omega}{\partial t} + \bar{U}_l \frac{\partial \omega}{\partial x_l} = \frac{\partial}{\partial x_l} \left[\left(\nu + \sigma_\omega \frac{k}{\omega} \right) \frac{\partial \omega}{\partial x_l} \right] + \gamma \frac{\omega}{k} \mathcal{P} - \beta_\omega \omega^2 + \frac{\sigma_d}{\omega} \frac{\partial k}{\partial x_l} \frac{\partial \omega}{\partial x_l}, \quad (2.2.95)$$

with the modeling coefficients defined as:

$$\beta_k = 0.09, \quad \sigma_k = \frac{3}{5}, \quad \sigma_\omega = \frac{1}{2}, \quad \beta_\omega = \beta_0 f_\beta, \quad \gamma = \frac{13}{25}, \quad \sigma_{d0} = \frac{1}{8}, \quad (2.2.96)$$

$$\sigma_d = \begin{cases} 0, & \frac{\partial k}{\partial x_l} \frac{\partial \omega}{\partial x_l} \leq 0 \\ \sigma_{d0}, & \frac{\partial k}{\partial x_l} \frac{\partial \omega}{\partial x_l} > 0 \end{cases}, \quad (2.2.97)$$

$$\beta_0 = 0.0708, \quad f_\beta = \frac{1 + 85\chi_\omega}{1 + 100\chi_\omega}, \quad \chi_\omega = \left| \frac{\bar{\Omega}_{ij} \bar{\Omega}_{jk} \bar{S}_{ki}}{(\beta_k \omega)^3} \right|. \quad (2.2.98)$$

The turbulent viscosity equation in this model becomes

$$\nu_t = \frac{k}{\omega^*}, \quad \omega^* = \max \left(\omega, C_{lim} \sqrt{\frac{2\bar{S}_{ij}\bar{S}_{ij}}{\beta_k}} \right), \quad C_{lim} = \frac{7}{8}. \quad (2.2.99)$$

Besides of the turbulent viscosity formulation (equation 2.2.99), this model also differs from the 1998 variant by a slightly different form of the included cross-diffusion correction as well as by the values of the modeling constants.

Figures 2.2.10 and 2.2.11 present the validation of the k - ω models described in this section and in sections 2.2.1.4-2.2.1.6 on the free round jet test case from section 2.2.1.2. Mean and fluctuating velocity profiles are shown in figure 2.2.10. The data obtained by the k - ε model employing round jet correction described in section 2.2.1.2 are presented for comparison as well. Since the SST model is running in this case essentially in the “outer layer” mode, its predictions are very similar to those given by the standard k - ε model (see figures 2.2.2 and 2.2.3 for comparison). It shows a clear trend of the over prediction of the jet spreading rate, of the turbulent kinetic energy, and of further fluctuating quantities. The 1988 model of Wilcox overestimates the spreading rate even more than the SST model (see figure 2.2.10(a)); consequently, the model is the least suited of all evaluated approaches for this test case. The fluctuating velocity profiles resulting from the 1988 k - ω model of Wilcox simulations are not shown in figures 2.2.10 and 2.2.11 since they were for the most part out of scale of the graphs (too high values).

The best k - ω model predictions are clearly achieved by two approaches employing the round jet correction (1998 k - ω and 2006 k - ω). The 1998 Wilcox model is the most accurate one among the k - ω type models and gives the profiles close to those obtained with the round jet correction k - ε model discussed in section 2.2.1.2. The 2006 Wilcox model shows a slight overprediction of turbulence in the outer jet region. This is especially clearly seen in the turbulent viscosity profile shown in figure 2.2.11(a). However, even with this overprediction of turbulence the model still performs better than the SST approach and much better than the 1988 k - ω model. Thus, it can be stated that for this particular test case the 1998 and 2006 improvements to the original k - ω 1988 model of Wilcox achieve a highly favorable effect.

The question of the freestream boundary condition dependence of the studied k - ω models will not be discussed here since for the further considerations of this dissertation it is not of significant importance. Menter [84] points out that, in contrast to the SST model, the freestream ω dependence is still quite noticeable even in the latest (2006) Wilcox model. This was also observed in the preliminary calculations of this dissertation, but in the calculations presented in figures 2.2.10 and 2.2.11 the freestream ω values were chosen to be small enough to achieve the target spreading rates allowed by the model equations.

2.2.1.8 Streamline curvature modification of the SST model

In addition to the near-wall and round jet related modeling improvements described previously, streamline curvature related model corrections can also be of relevance for the applications considered in this work. System rotation and streamline curvature can act as an additional source/sink of the turbulent kinetic energy [46]. However, neither the standard k - ε nor the k - ω type models described above are capable of reproducing this behavior. A variety of modifications exists which aim to encode the effects of rotation and streamline curvature into eddy viscosity turbulence models. One example - the modification of the SST model developed by Hellsten [46] is presented here. This modification replaces the original dissipation of ω term $\beta_\omega \omega^2$ in the ω transport equation 2.2.76 by a term sensitive to the Richardson number $F_4(Ri) \beta_\omega \omega^2$ which acts as a measure of system rotation and/or streamline curvature:

$$Ri = \frac{\Omega}{S} \left(\frac{\Omega}{S} - 1 \right), \quad (2.2.100)$$

with

$$S = \sqrt{2\bar{S}_{ij}\bar{S}_{ij}}, \quad \Omega = \sqrt{2\bar{\Omega}_{ij}\bar{\Omega}_{ij}}, \quad (2.2.101)$$

$$F_4(Ri) = \frac{1}{1 + C_{rc} Ri}. \quad (2.2.102)$$

The modeling constant is $C_{rc} = 3.6$. The results produced by the application of this correction for the SST model to the flows relevant for GT combustion applications will be discussed in chapter 3 of the present work.

2.2.1.9 Concluding remarks

It is clear that the equations and models listed above in the sections 2.2.1.1-2.2.1.8 are only a small part of the work on RANS turbulence modeling which can be found in the literature. Reynolds stress modeling, non-linear eddy viscosity models, algebraic models, and one-equation models are not considered here because the aim of the current work is directed towards engineering applications, and the models discussed here are the most widespread ones for the technical simulations of turbulent flows. Their popularity has been established over years and is justified by the remarkable combination of their simplicity and robustness on the one hand and their ability to give reasonable predictions for a large variety of flows [128, 29] on the other hand. This does not imply, however, that the established models can not be modified and

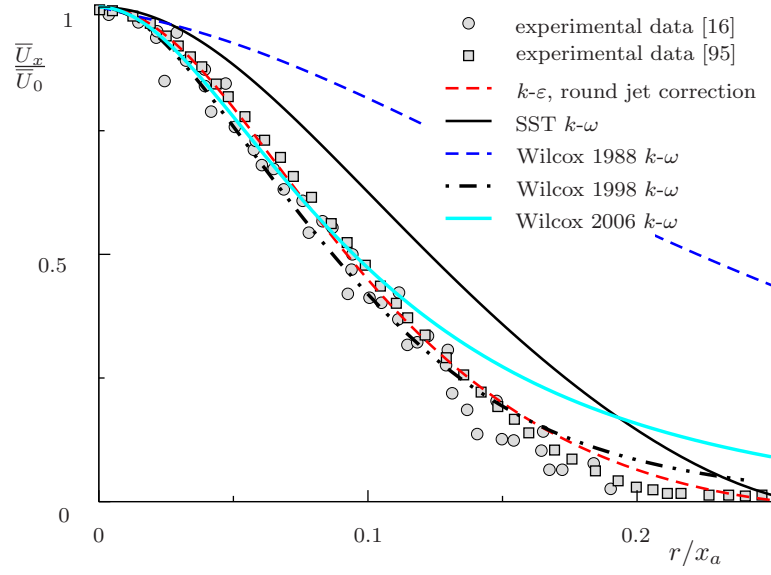
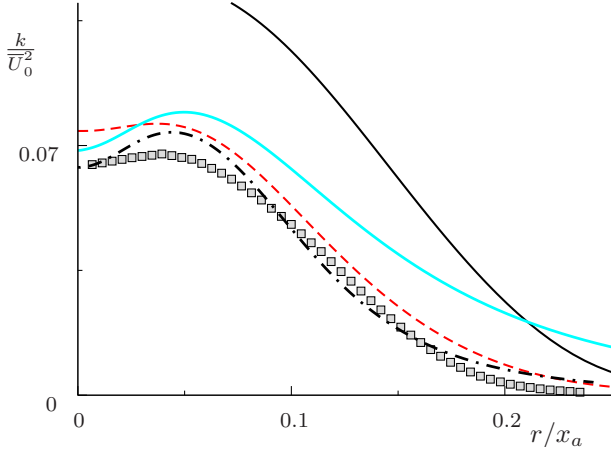
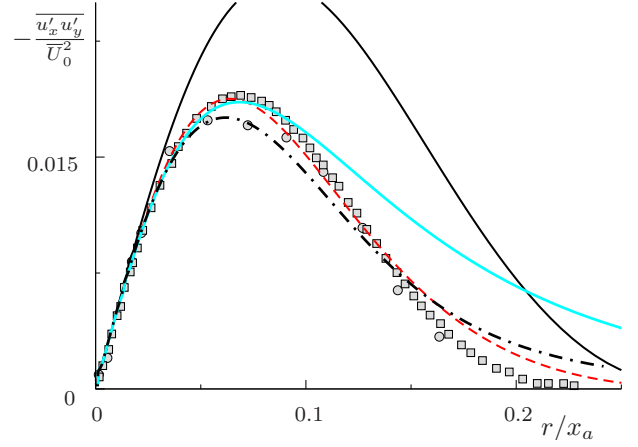
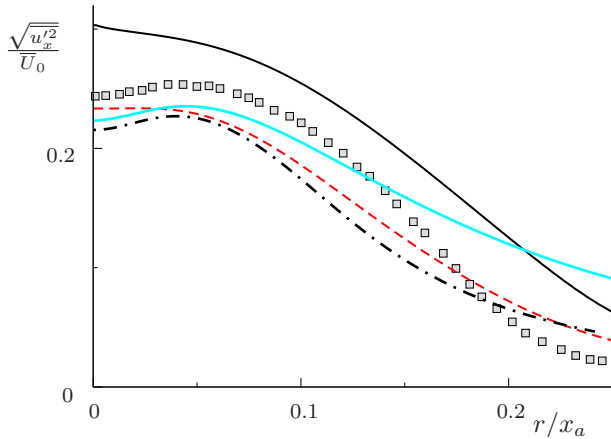
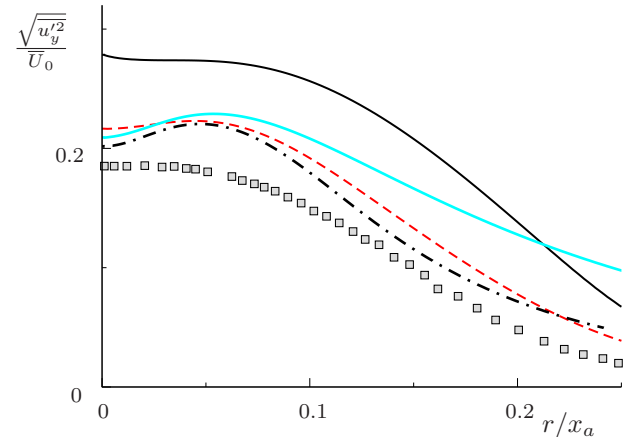

 (a) Dimensionless mean streamwise velocity $\overline{U}_x/\overline{U}_0$.

 (b) Turbulent kinetic energy k/\overline{U}_0^2 .

 (c) Reynolds shear stress $-\overline{u'_x u'_y}/\overline{U}_0^2$.

 (d) RMS of the axial velocity fluctuations $\sqrt{\overline{u'^2_x}}/\overline{U}_0$.

 (e) RMS of the radial velocity fluctuations $\sqrt{\overline{u'^2_y}}/\overline{U}_0$.

 Figure 2.2.10: Free round jet flow. Different $k-\omega$ models and $k-\varepsilon$ model with Pope correction and Davidson limiter. Comparison of the simulation results and the data of refs. [16, 95].

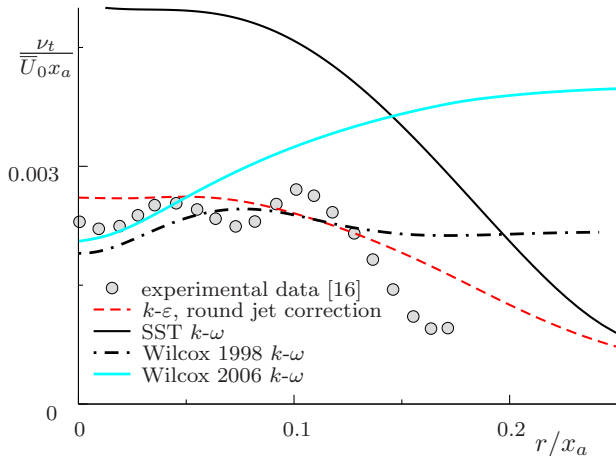
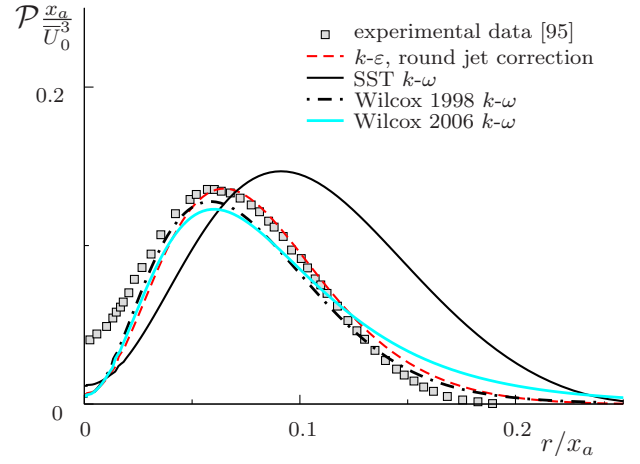
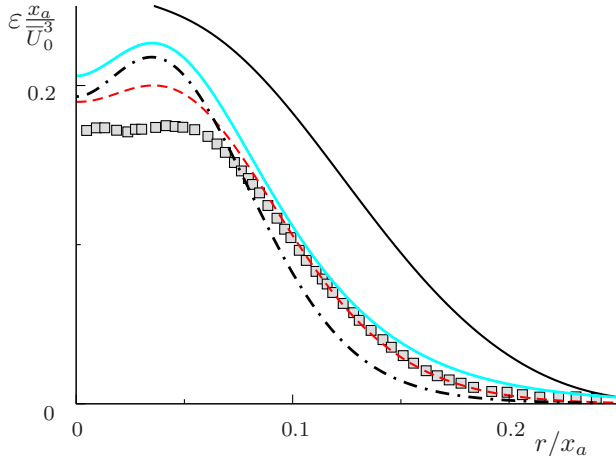
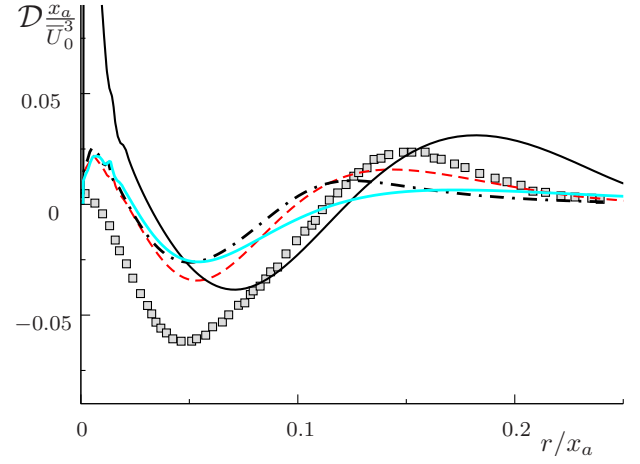
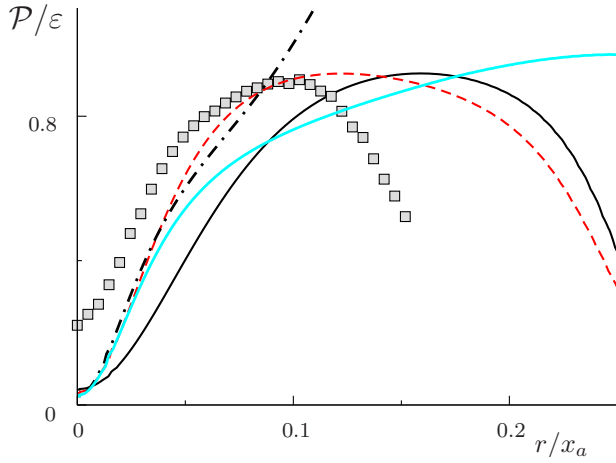
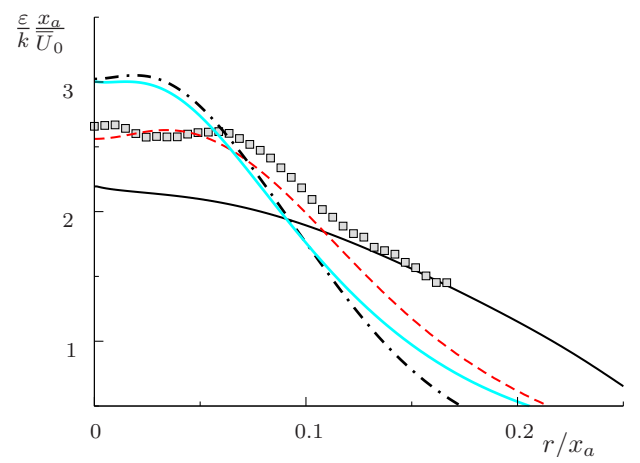

 (a) Turbulent viscosity $\nu_t / \bar{U}_0 x$

 (b) Production of the turbulent kinetic energy $\mathcal{P} \frac{x_a}{\bar{U}_0^3}$

 (c) Dissipation of the turbulent kinetic energy $\varepsilon \frac{x_a}{\bar{U}_0^3}$

 (d) Diffusion of the turbulent kinetic energy $\mathcal{D} \frac{x_a}{\bar{U}_0^3}$

 (e) Production to dissipation ratio $\mathcal{P} / \varepsilon$

 (f) Dimensionless dissipation per unit turbulent kinetic energy $\frac{\varepsilon}{k} \frac{x_a}{\bar{U}_0}$

Figure 2.2.11: Free round jet flow. Different $k-\omega$ models and $k-\varepsilon$ model with Pope correction and Davidenko limiter. Turbulent viscosity and budget terms of the turbulent kinetic energy transport equation. Comparison of the simulation results and the data of refs. [16, 95].

improved.

The modifications directed towards applications to special flow types such as given in section 2.2.1.2 for the round jet flows or in section 2.2.1.8 for the streamline curvature affected flows indeed can help to achieve more accurate predictions in the cases for which they are designed. This was shown, for example, in sections 2.2.1.2 and 2.2.1.7 for the free round jet flow. To understand the general applicability of such corrections, it is important to assess them in more complex configurations where the flow evolution is influenced by multiple factors. Such studies will be presented in chapter 3.

For a further improvement of the considered models, a deep understanding of the mechanisms governing the turbulence dynamics is needed. Detailed validation of the model equation terms and of the statistical turbulence quantities produced by the models would be useful. Also studies on the validity of some basic assumptions employed for the model equation closure and obtaining of the modeling constants can be enlightening. For example, a question on the variability of C_μ in equation 2.2.22 is important. The origin of the near-wall corrections discussed in section 2.2.1.3 was the observation that inside the viscous sublayer and in the transitional region between the viscous sublayer and the logarithmic layer C_μ does not have a constant value of 0.09. The low-Re damping functions for ν_t are a practical technique to vary C_μ in the near-wall region. In the present work, for the considered internal jet flows, the values of C_μ in equation 2.2.22 will be evaluated based on the statistical data for k and dissipation rate obtained from LES in the same fashion as it was done above using the literature data for the free round jet (figure 2.2.4) and for the 2D channel flow (figure 2.2.7). This will help to improve the understanding regarding the variability of C_μ (or its equivalent β_k in k - ω models, see equation 2.2.53) in complex flows. Such a study can be used in order to make a decision if the constant C_μ assumption is sufficient for the considered flows or whether the eddy viscosity approaches employing a variable modeling coefficient are more appropriate. A further important parameter is the production to dissipation ratio. Section 2.2.1 shows that the value of this parameter in different classes of flows is used for deriving of C_μ ($\mathcal{P}/\varepsilon = 1.0$ in the logarithmic layer) and $C_{\varepsilon 1}$ ($\mathcal{P}/\varepsilon = 1.6 \pm 0.2$ in a homogeneous shear layer) in the standard k - ε model. The same relations are used for obtaining of the k - ω model constants. As discussed in section 2.2.1, the value of $C_{\varepsilon 2} - C_{\varepsilon 1}$ has substantial influence on the predicted spreading rates of shear flows. Thus in the shear flows where the relation $\mathcal{P}/\varepsilon = 1.6 \pm 0.2$ does not hold, the spreading rate (and the whole level of turbulence) may be incorrectly predicted. This can be observed for the free round jet, where the peak value of \mathcal{P}/ε is 0.8. Consequently, the spreading rate is over predicted in this flow by the standard k - ε model as well as other models using similar assumptions for the model constants, and the round jet correction is needed to compensate for this behavior. Employing the statistical data obtained in the LES calculations, the value of \mathcal{P}/ε will be evaluated in this work for all considered flows and its relation to the observed model behavior discussed. This and further LES-based studies on the validity of widely used RANS modeling assumptions for complex confined jet flows are presented in chapter 3.

2.2.2 Turbulent scalar diffusivity modeling

2.2.2.1 Turbulent mixing modeling problem, turbulent Prandtl or Schmidt number concept

It was pointed out at the beginning of section 2.2 that if the gradient diffusion hypothesis (equation 2.2.6) is used for the turbulent scalar flux closure a model for the determination of turbulent scalar diffusivity α_t is needed. The most widespread and simple approach for the modeling of α_t is the assumption of a linear dependence on the turbulent viscosity ν_t

$$\alpha_t = \frac{\nu_t}{\sigma_t} \quad (2.2.103)$$

where the constant σ_t is called the turbulent Prandtl or Schmidt number in analogy to the formula $\sigma = \nu/\alpha$ for the Prandtl or Schmidt number, σ , in molecular heat or mass transport. This approach is reasoned by the experience that in simple shear flows the turbulent scalar diffusivity α_t is always of about the same magnitude as the turbulent viscosity ν_t [72]. However, the application of a constant turbulent Prandtl or Schmidt number hypothesis for the engineering turbulent scalar mixing simulations introduces several difficulties.

Figure 2.2.12 presents the profiles of the dimensionless temperature for a 2D channel flow and a free round jet flow (the same test cases are used in the previous sections for the turbulent viscosity modeling validations). Turbulent viscosity is modeled by means of the AKN k - ε model for the 2D channel flow and by means of the k - ε model with the round jet correction described in section 2.2.1.2 for the free round jet flow. These models were chosen since they give the best mean and fluctuating velocity field predictions in the respective cases (see sections 2.2.1.3 and 2.2.1.7). Whereas in the case of the 2D channel flow $\sigma_t = 1.0$ gives the closest agreement with the DNS data, for the free round jet lower values lying between $\sigma_t = 1.0$ and $\sigma_t = 0.7$ are a better choice. Furthermore experimental and DNS studies show that, in reality, even for these and other relatively simple shear flows the turbulent Prandtl or Schmidt number can vary significantly in different flow regions. DNS simulations of heat transfer in the plane channel flows [66, 65] indicate that, depending on the wall temperature conditions, the turbulent Prandtl number can remain close to unity over the full channel height or drop from 1.0 near to the walls to 0.5 in the core region. A review on the values of the turbulent Prandtl or Schmidt number in several free shear flows made by Reynolds [103] gives the following variations (from core to outer region): round jet (such as considered here) 0.73 – 1.7; round wake 0.8 – 0.3, plane jet 0.5 – 1.3; plane wake 0.5 – 0.7.

For complicated flows, particularly in the cases where no information is available about the turbulent Prandtl or Schmidt number variations, the choice of a unique value of this parameter is a non-trivial task and incorrect mixing predictions are often the case in simulations of complex internal flows such as considered in this work. Several possibilities exist to improve simulation accuracy within the turbulent scalar diffusivity framework. First, more information should be gained about the actual values of the turbulent Prandtl or Schmidt number in non-academic

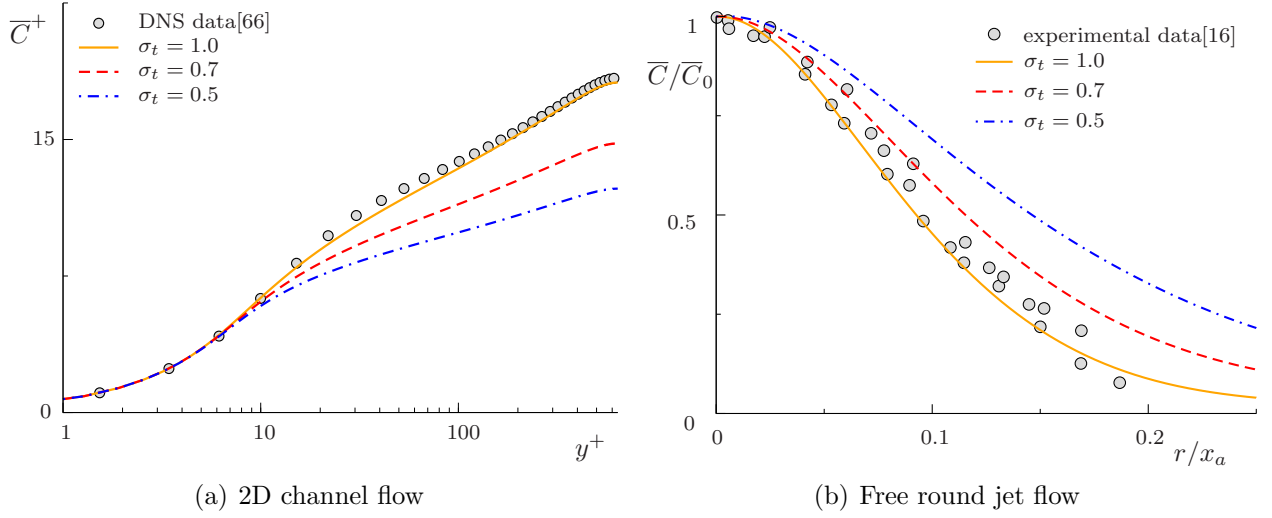


Figure 2.2.12: Dimensionless transported scalar in 2D channel and free round jet flow. Different turbulent Prandtl or Schmidt numbers.

flows, which are often not available due to measurement difficulties. This would help the community to better understand if in such flows a definition of a “compromise” constant value is possible and what is the dependence of the turbulent Prandtl or Schmidt numbers on the flow type and region. This question is addressed in chapter 3. A second potential source of improvement is the application of the turbulent scalar diffusivity models that do not involve the turbulent Prandtl or Schmidt number ansatz. Such models are considered in the next section.

2.2.2.2 Two-equation turbulent scalar diffusivity models

The idea of two-equation turbulent scalar diffusivity modeling is essentially the same as the one of two-equation turbulent viscosity modeling described previously in sections 2.2.1.1-2.2.1.8. Turbulent scalar diffusivity is assumed to be a linear combination of the turbulent velocity scale and the length scale of the turbulent scalar mixing

$$\alpha_t = \mathcal{L}_c \mathcal{U}. \quad (2.2.104)$$

As in the turbulent viscosity modeling, the velocity scale is assumed to be proportional to the square-root of the turbulent kinetic energy. Hence,

$$\alpha_t \sim \mathcal{L}_c \sqrt{k}. \quad (2.2.105)$$

The length scale can be constructed using the velocity scale and the time scale $\mathcal{L}_c \sim \sqrt{k} \tau_\lambda$, and in this case

$$\alpha_t = C_\lambda k \tau_\lambda \quad (2.2.106)$$

with the modeling constant C_λ and the time scale of scalar mixing τ_λ . The first model of this type was proposed by Nagano and Kim in 1988 [89]. The time scale, τ_λ , can be constructed using different arguments. If the turbulent velocity time scale $\tau_d = k/\varepsilon$ is used, then equation 2.2.106

becomes essentially the same as equation 2.2.22 and the ratio C_μ/C_λ is the turbulent Prandtl or Schmidt number. Nagano and Kim [89] proposed to use for the modeling of τ_λ not only the turbulent velocity time scale τ_d but also a time scale which characterizes turbulent scalar fluctuations

$$\tau_c = \frac{\overline{c'^2}}{2\varepsilon_c}, \quad (2.2.107)$$

where $\overline{c'^2}$ is the turbulent scalar variance and ε_c its dissipation rate. This time scale can be used directly to form τ_λ in equation 2.2.106 or, as in the work of Nagano and Kim, in a combination with the turbulent velocity time scale

$$\tau_\lambda = \sqrt{\frac{\overline{c'^2}}{\varepsilon_c} \frac{k}{\varepsilon}} = \sqrt{2} \tau_c \tau_d = \sqrt{2} \tau_d \mathcal{R}^{1/2}, \quad (2.2.108)$$

with the time scale ratio

$$\mathcal{R} = \frac{\tau_c}{\tau_d}. \quad (2.2.109)$$

Formula 2.2.108 or its generalization

$$\tau_\lambda = C_m \tau_c^l \tau_d^k = C_m \tau_d \mathcal{R}^l, \text{ where } l + k = 1, \quad (2.2.110)$$

was successfully adopted in turbulent scalar diffusivity calculations conducted by different research groups for a variety of configurations [89, 14, 68, 11, 67, 10, 12, 129, 112]. There are also examples of application of other forms of the mixed time scale τ_λ . Abe et al. [2] adopted, following the work of Zeman and Lumley [131], the formula

$$\tau_\lambda = C_{m1} \left(\frac{C_{m2}}{\tau_c} + \frac{1}{\tau_d} \right)^{-1} = \tau_d \left(\frac{C_{m1} \mathcal{R}}{C_{m2} + \mathcal{R}} \right), \quad (2.2.111)$$

with the modeling constants C_{m1} and C_{m2} . The question about the optimal choice of the mixing time scale in 2.2.106 is not fully clarified and remains a subject of continuing investigations.

In order to build τ_c , the construction and solution of additional transport equations for the turbulent scalar variance and its dissipation rate are required. The exact equation for $\overline{c'^2}$ can be obtained by multiplying the transport equation for the instantaneous value of the scalar $(\overline{C} + c')$ by c' and application of the ensemble averaging operator [72]

$$\frac{\partial \overline{c'^2}}{\partial t} + \overline{U}_l \frac{\partial \overline{c'^2}}{\partial x_l} = \underbrace{-2\overline{c' u'_l} \frac{\partial \overline{C}}{\partial x_l}}_{\text{production}} - \underbrace{2\alpha \frac{\partial \overline{c'}}{\partial x_l} \frac{\partial \overline{c'}}{\partial x_l}}_{\text{dissipation}} - \underbrace{\frac{\partial \overline{c'^2 u'_l}}{\partial x_l}}_{\text{turbulent diffusion}} + \underbrace{\alpha \frac{\partial^2 \overline{c'^2}}{\partial x_l^2}}_{\text{molecular diffusion}}. \quad (2.2.112)$$

The turbulent diffusion term can be closed using the gradient diffusion hypothesis [89],

$$-\overline{c'^2 u'_l} = \frac{\alpha_t}{\sigma_h} \frac{\partial \overline{c'^2}}{\partial x_l}. \quad (2.2.113)$$

This is the most prevalent way of modeling of the turbulent diffusion term, and this approach was adopted in refs. [89, 2, 129, 112]. It is a direct analogy to the closure of the turbulent diffusion term in the turbulent kinetic energy equation 2.2.13, however, other variants such as $-\overline{c'^2 u'_l} \sim \frac{k}{\varepsilon} \overline{u'_l u'_j} \frac{\partial \overline{c'^2}}{\partial x_j}$ also exist [72]. The production term can be easily closed using equation 2.2.6 for $\overline{c' u'_l}$; thereby, the last term requiring a model is the dissipation of the turbulent scalar variance $2\varepsilon_c$ with

$$\varepsilon_c = \alpha \overline{\frac{\partial c'}{\partial x_l} \frac{\partial c'}{\partial x_l}}. \quad (2.2.114)$$

In order to model ε_c different approaches exist in literature [43, 72]. If the constant turbulent Prandtl or Schmidt number hypothesis is applied (no special modeling of α_t via equation 2.2.106), but the turbulent scalar variance transport is of interest (for example in the combustion simulations), a relatively simple algebraic relation [43] can be used

$$\varepsilon_c = C_t \overline{c'^2} \omega_u, \quad (2.2.115)$$

where $\omega_u = 1/\tau_d$. The widely used value of the model constant C_t is $C_t = 1$, which is equivalent to the assumption that the turbulent scalar to velocity time scale ratio is constant and is equal to $R = 0.5$ [43]. The transport equation for $\overline{c'^2}$ has in this case the form

$$\frac{\partial \overline{c'^2}}{\partial t} + \overline{U_l} \frac{\partial \overline{c'^2}}{\partial x_l} = \frac{\partial}{\partial x_l} \left[\left(\alpha + \frac{\alpha_t}{\sigma_h} \right) \frac{\partial \overline{c'^2}}{\partial x_l} \right] + 2\mathcal{P}_c - 2C_t \overline{c'^2} \omega_u. \quad (2.2.116)$$

This approach, however, is not applicable if equation 2.2.106 is used for the α_t modeling since it does not allow the introduction of the scalar mixing time scale independently from the turbulent velocity time scale. Moreover, the assumption of the constant turbulent scalar to velocity time scale ratio is a considerable simplification [119, 7]. For this reason an additional transport equation for ε_c could be theoretically a more accurate way to model this quantity.

The exact transport equation for ε_c can be obtained by taking the derivative of the equation for $(\overline{C} + c')$, multiplying by $2\alpha \partial c' / \partial x_l$, and ensemble averaging [72]

$$\begin{aligned} \frac{\partial \varepsilon_c}{\partial t} + \overline{U_l} \frac{\partial \varepsilon_c}{\partial x_l} = & \underbrace{-2\alpha \frac{\partial u'_l}{\partial x_k} \frac{\partial c'}{\partial x_k} \frac{\partial \overline{C}}{\partial x_l} - 2\alpha u'_l \frac{\partial c'}{\partial x_k} \frac{\partial^2 \overline{C}}{\partial x_l \partial x_k} - 2\alpha \frac{\partial c'}{\partial x_l} \frac{\partial c'}{\partial x_k} \frac{\partial \overline{U_l}}{\partial x_k}}_{\text{mean-field production}} \\ & \underbrace{-2\alpha \frac{\partial u'_l}{\partial x_k} \frac{\partial c'}{\partial x_k} \frac{\partial c'}{\partial x_l}}_{\text{fine-scale (turbulent) production}} \underbrace{-2 \left(\alpha \frac{\partial^2 c'}{\partial x_l \partial x_k} \right)^2}_{\text{dissipation}} \underbrace{- \frac{\partial u'_l \varepsilon'_c}{\partial x_l}}_{\text{turbulent diffusion}} \underbrace{+ \alpha \frac{\partial^2 \varepsilon_c}{\partial x_l^2}}_{\text{molecular diffusion}}. \end{aligned} \quad (2.2.117)$$

The terms of equation 2.2.117 are discussed in ref. [72]. It is stated that the dominant terms are those of the fine-scale production and the dissipation whereas the mean-field generation plays rather a minor role. The problem of closing equation 2.2.117 is quite similar to the problem of modeling the terms of the ε equation as discussed in section 2.2.1.1. In the same way this model derivation is essentially based on dimensional analysis and on general physical considerations.

The task of the closure of the ε_c equation is actually even more challenging since the terms of this equation depend on both velocity and scalar fields, so the possible number of parameters is twice as large as in the case of the ε equation [72].

The turbulent diffusion term is usually [89, 2, 112, 21] closed in the same manner as the turbulent diffusion term of the scalar variance transport equation,

$$-\overline{u_l \varepsilon'_c} = \frac{\alpha_t}{\sigma_\phi} \frac{\partial \varepsilon_c}{\partial x_l}, \quad (2.2.118)$$

where σ_ϕ is the model constant. Launder [72] notes, however, that the question about the diffusion term closure is of less importance than the modeling of the creation and dissipation terms of ε_c equation. Regarding the dissipation term, the common view [72, 89, 2, 112, 21, 32, 60, 91] is that the rate of dissipation is dependent on both velocity and scalar time scales. The most obvious approximation is

$$-2 \overline{\left(\alpha \frac{\partial^2 c'}{\partial x_l \partial x_k} \right)^2} = -C_{d1} \frac{\varepsilon_c^2}{c'^2} - C_{d2} \frac{\varepsilon \varepsilon_c}{k}, \quad (2.2.119)$$

with modeling constants C_{d1} and C_{d2} .

Several approximations exist for the production terms in the ε_c equation [89, 21, 32, 60, 91, 72]. As mentioned above, the mean-field generation terms of equation 2.2.117 are normally neglected [72] and only the turbulent production term is modeled. The rate of production is in most models assumed to be sensitive to changes in both the turbulent velocity and scalar fields. Typically the mechanical and the scalar production rates,

$$\mathcal{P} = -\overline{u'_i u'_i} \frac{\partial \overline{U}_i}{\partial x_i} \quad \text{and} \quad \mathcal{P}_c = -\overline{u'_i c'} \frac{\partial \overline{C}}{\partial x_i} \quad (2.2.120)$$

respectively, are used for the modeling of ε_c generation. It is not immediately clear in which form P and P_c as well as the scalar and mechanical time scales should appear in the approximation of the ε_c production. The most popular approach is to use both P and P_c in the form

$$-2\alpha \overline{\frac{\partial u'_i}{\partial x_k} \frac{\partial c'}{\partial x_k} \frac{\partial c'}{\partial x_i}} = C_{p1} \frac{\varepsilon_c}{c'^2} \mathcal{P}_c + C_{p2} \frac{\varepsilon_c}{k} \mathcal{P} \quad (2.2.121)$$

with the modeling constants C_{p1} and C_{p2} [89, 2, 112]. Some authors employ only the scalar production rate in combination with the scalar ε_c/c'^2 [91, 32] or mixed $\sqrt{(\varepsilon \varepsilon_c)/(k c'^2)}$ [21] time scale that results in

$$-2\alpha \overline{\frac{\partial u'_i}{\partial x_k} \frac{\partial c'}{\partial x_k} \frac{\partial c'}{\partial x_i}} = C_p \frac{\varepsilon_c}{c'^2} \mathcal{P}_c \quad \text{or} \quad -2\alpha \overline{\frac{\partial u'_i}{\partial x_k} \frac{\partial c'}{\partial x_k} \frac{\partial c'}{\partial x_i}} = C_p \sqrt{\frac{\varepsilon \varepsilon_c}{k c'^2}} \mathcal{P}_c. \quad (2.2.122)$$

Furthermore, Jones and Musonge propose [60] the following formulation for the production

term:

$$-2\alpha \frac{\partial u'_l}{\partial x_k} \frac{\partial c'}{\partial x_k} \frac{\partial c'}{\partial x_l} = C_{p1} \frac{\varepsilon}{k} \mathcal{P}_c + C_{p2} \frac{\varepsilon_c}{k} \mathcal{P}. \quad (2.2.123)$$

Thus for the production terms no consensus solution exists and further investigations are needed. For the calculations of the current work, three models were chosen which employ different formulations of the time scale τ_λ in equation 2.2.106 and different formulations of the production term. In order to compare their effectiveness, the model of Nagano and Kim [89] (NK), the model of Abe et al. [2] (AKN) (variant “a” from ref. [2]), and the model of Deng et al. [21] (DWX) are selected as representative scalar transport models. The general form of the governing equations for all models can be expressed as

$$\frac{\partial \overline{c'^2}}{\partial t} + \overline{U}_l \frac{\partial \overline{c'^2}}{\partial x_l} = \frac{\partial}{\partial x_l} \left[\left(\alpha + \frac{\alpha_t}{\sigma_h} \right) \frac{\partial \overline{c'^2}}{\partial x_l} \right] + 2\mathcal{P}_c - 2\varepsilon_c, \quad (2.2.124)$$

$$\frac{\partial \varepsilon_c}{\partial t} + \overline{U}_l \frac{\partial \varepsilon_c}{\partial x_l} = \frac{\partial}{\partial x_l} \left[\left(\alpha + \frac{\alpha_t}{\sigma_\phi} \right) \frac{\partial \varepsilon_c}{\partial x_l} \right] + C_{p1} \mathcal{P}_1 + C_{p2} \mathcal{P}_2 - C_{d1} \frac{\varepsilon_c^2}{c'^2} - C_{d2} \frac{\varepsilon \varepsilon_c}{k}, \quad (2.2.125)$$

and equation 2.2.106 is used for the calculation of the turbulent scalar diffusivity. Tables 2.1 and 2.2 summarize the modeling constants, the ε_θ production terms \mathcal{P}_1 , \mathcal{P}_2 , and τ_λ formulations of all models.

Model constants presented in table 2.2 are derived using the methods similar to those which are applied for the derivation of the constants of two-equation eddy viscosity models discussed in section 2.2.1.1. However, as stated previously, selecting the optimal model constants is a more difficult task here due to additional equation terms and a larger variety of options available for the mixed time scale as well as production and dissipation terms of the modeling equations.

For example in the work of Nagano and Kim [89] (NK model), the value of C_λ in equation 2.2.106 is specified using the definitions of both turbulent viscosity and turbulent scalar diffusivity and the values of the turbulent Prandtl numbers as well as thermal to mechanical time scale ratio in the logarithmic region of the thermal flat-plate boundary layer [89]. Using the

Table 2.1: Model time scales and ε_θ production terms.

Model	τ_λ	\mathcal{P}_1	\mathcal{P}_2
NK	$(2\tau_c \tau_d)^{0.5}$	$\frac{\varepsilon_c}{c'^2} \mathcal{P}_c$	$\frac{\varepsilon_c}{k} \mathcal{P}$
AKN	$\tau_d \left(\frac{2\mathcal{R}}{0.5 + \mathcal{R}} \right)$	$\frac{\varepsilon_c}{c'^2} \mathcal{P}_c$	$\frac{\varepsilon_c}{k} \mathcal{P}$
DWX	$(2\tau_c \tau_d)^{0.5}$	$\sqrt{\frac{\varepsilon \varepsilon_c}{k c'^2}} \mathcal{P}_c$	0

Table 2.2: Model constants.

Model	C_λ	C_{p1}	C_{p2}	C_{d1}	C_{d2}	σ_h	σ_ϕ
NK	0.11	1.8	0.72	2.2	0.8	1.0	1.0
AKN	0.1	1.9	0.6	2.0	0.9	1.6	1.6
DWX	0.1	2.34	0	2.0	0.9	1.0	1.0

definition of the turbulent Prandtl number $\sigma_t = \nu_t/\alpha_t$, the standard k - ε model ν_t definition, and α_t of NK model the following formulas can be obtained

$$\sigma_t = \frac{\nu_t}{\alpha_t} = \frac{C_\mu k \tau_d}{C_\lambda k \sqrt{2\tau_c \tau_d}} = \frac{C_\mu}{C_\lambda \sqrt{2\mathcal{R}}} \quad (2.2.126)$$

and

$$C_\lambda = \frac{C_\mu}{\sigma_t \sqrt{2\mathcal{R}}}. \quad (2.2.127)$$

Taking into account that in logarithmic layer $\sigma_t \approx 0.9$ and $\mathcal{R} = 0.4 - 0.5$ (according to the measurements of Beguer et al. [7]), Nagano and Kim choose $C_\lambda = 0.11$ [89]. This or very similar values of C_λ are normally also used in other two-equation turbulent scalar diffusivity models especially for near-wall heat transfer calculations. In some calculations of free shear flows higher values of C_λ can be found (0.14 - 0.17) [117, 14, 68, 11, 67, 10, 12].

The constants C_{d1} and C_{d2} of the ε_c equation can be obtained from the measurement results for decaying homogeneous scalar turbulence. The simplified equations for turbulence (k and ε) and turbulent mixing ($\overline{c'^2}$ and ε_c) for this case can be found in refs. [89, 32, 91]. After some algebraic operations, Nagano and Kim [89] come to the formulas

$$C_{d1} = 2\mathcal{R}(C_{\varepsilon 2} - 1) \quad \text{and} \quad C_{d2} = \frac{1}{\mathcal{R}} \quad (2.2.128)$$

where $C_{\varepsilon 2}$ is the dissipation of dissipation constant of the k - ε model. The experimental values of \mathcal{R} in homogeneous decaying scalar turbulence [119] can vary from 0.6 to 2.4 which implies an uncertainty in the selection of both dissipation constants. Nagano and Kim assumed $1.13 < \mathcal{R} < 1.25$ and, following the work of Elgobashi and Launder [32], adopted the constants $C_{d1} = 2.02$ and $C_{d2} = 0.8$ obtained as a result of a computer optimization for the case of homogeneous scalar turbulence. The constant C_{p1} in the NK model also originates from the work of Elgobashi and Launder whereas C_{p2} was obtained by Nagano and Kim using their own computational optimization.

The constants of two other $\overline{c'^2}$ - ε_c models considered in the present work were derived using similar assumptions (see refs. [2] and [21] for details). Further possibilities to obtain the modeling coefficients are also investigated in another publication of Nagano and coworkers [90]. Depending on the assumptions made by different authors for their simplified equations

employed for the development of the constants, the resulting model coefficients can be slightly different in each closure (see table 2.2).

The results achieved by three $\overline{c'^2}$ - ε_c models summarized in tables 2.1 and 2.2 for the free round jet mixing test case (earlier described and used for the turbulence model testing in section 2.2.1.2) are presented in figure 2.2.13. The profiles given by the constant turbulent Prandtl number approach ($\sigma_t = 1.0$ and $\sigma_t = 0.7$) are presented as well. The velocity field was modeled by means of the k - ε model with the round jet correction discussed in section 2.2.1.2. The results are non-dimensionalized using the scalar and the velocity values on the jet centerline \overline{C}_0 and \overline{U}_0 respectively (here the transported scalar is $C = T - T_\infty$ with the actual temperature value T and the freestream temperature value T_∞).

The mean transported scalar profiles are shown in figure 2.2.13(a). The AKN scalar mixing model gives the worst results, underpredicting the mixing. The NK model returns a profile similar to the results given by $\sigma_t = 0.7$, only slightly more narrow in the outer edge region. The DWX model results in a profile similar to the one generated by $\sigma_t = 1.0$. The form of the profiles achieved by the NK and the DWX models is closer to the experimental trends than the form of the profiles given by the constant turbulent Prandtl number approach.

The turbulent scalar variance (figure 2.2.13(b)) is better represented by the NK and the DWX models than by using equation 2.2.116 and the constant turbulent Schmidt number approach. The source of these results is probably connected to not only the variability of the turbulent Schmidt number in the NK and in the DWX calculations but also to a more accurate approximation of the dissipation term in the turbulent scalar variance transport equation. The AKN model results are here unsatisfactory as previously observed for the mean scalar profiles.

The turbulent scalar flux (figure 2.2.13(c)) seems to be slightly overestimated by the NK model and slightly underestimated by the DWX model. The turbulent scalar diffusivity (figure 2.2.13(d)) is reproduced by the DWX model very well, and so is the turbulent Prandtl number (figure 2.2.13(e)). It follows that the NK model by over predicting α_t (figure 2.2.13(d)) will underestimate σ_t (figure 2.2.13(e)); however, the form of all profiles given by the NK model is still closer to the experimental one than the profile form obtained using the constant turbulent Prandtl number approach. The turbulent Prandtl number is clearly variable and all tested $\overline{c'^2}$ - ε_c models can represent the trend of increasing σ_t at the jet outer edge. The mixing underprediction displayed by the ANK model can result from the mixing time scale formulation that differs from the one used in the NK and in the DWX models (see table 2.1). A slight mixing overprediction shown by the NK model can originate from a higher value of the C_λ modeling constant (0.11 vs. 0.1 in DWX); however, these hypotheses need additional investigations.

2.2.2.3 Near-wall modeling in $\overline{c'^2}$ - ε_c models

Since most $\overline{c'^2}$ - ε_c models were initially developed as near-wall heat transfer models, near-wall modeling is treated with exceptional care in the corresponding publications. Analogously to the k - ε modeling of turbulence, in order to correctly represent the near-wall behavior of α_t and ε_c near-wall damping functions have to be developed. Thus each of the three models considered

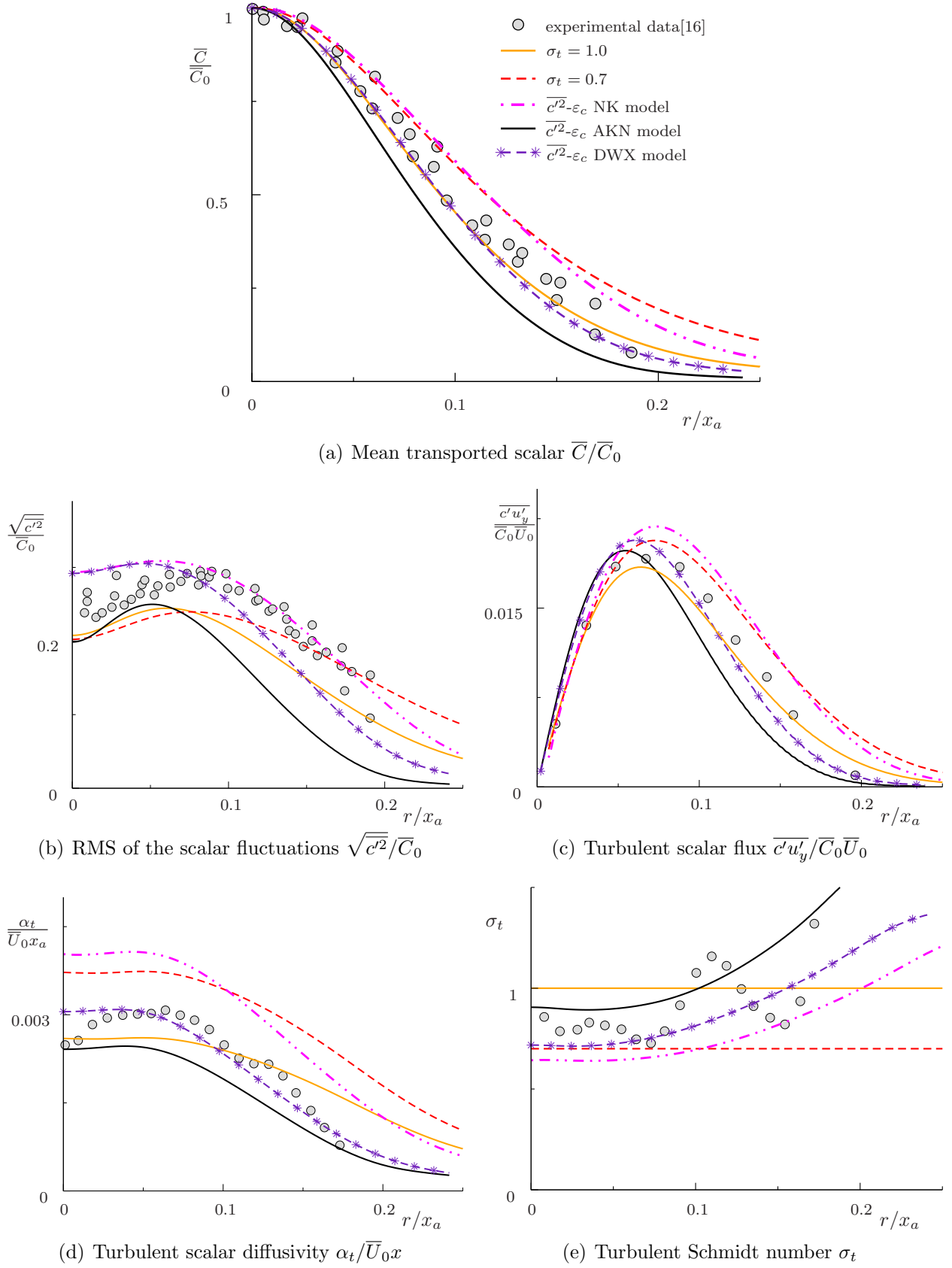


Figure 2.2.13: Free round jet mixing. Mean and fluctuating scalar field predictions, turbulent scalar diffusivity, and turbulent Schmidt numbers. Different RANS turbulent scalar diffusivity models in comparison with experimental data of Chua and Antonia [16]. Turbulent viscosity is modeled by means of the k - ε model with Pope correction and Davidenko limiter.

in the previous section (NK, AKN and DWX) has a low-Reynolds number formulation. Two of them, AKN [2] (variant “a” from ref. [2]) and of DWX [21], are studied in the present work. The turbulent scalar diffusivity of the ANK model in its low-Re formulation is given as follows:

$$\alpha_t = \left[\frac{k^2}{\varepsilon} \left(\frac{2\mathcal{R}}{0.5 + \mathcal{R}} \right) + 3\sqrt{k} \left(\frac{\nu^3}{\varepsilon} \right)^{1/4} \frac{\sqrt{2\mathcal{R}}}{\sigma} f_d \right] [1 - e^{-y^*/14}] [1 - e^{-\sqrt{\sigma}y^*/14}] \quad (2.2.129)$$

with

$$f_d = e^{-(Re_T/200)^2}, \quad (2.2.130)$$

where y^* and Re_T are defined in equation 2.2.1.3. The ε_c equation of the AKN model is

$$\frac{\partial \varepsilon_c}{\partial t} + \bar{U}_l \frac{\partial \varepsilon_c}{\partial x_l} = \frac{\partial}{\partial x_l} \left[\left(\alpha + \frac{\alpha_t}{\sigma_\phi} \right) \frac{\partial \varepsilon_c}{\partial x_l} \right] + C_{p1} f_{p1} \mathcal{P}_1 + C_{p2} f_{p2} \mathcal{P}_2 - C_{d1} f_{d1} \frac{\varepsilon_c^2}{\mathcal{C}^2} - C_{d2} f_{d2} \frac{\varepsilon \varepsilon_c}{k} \quad (2.2.131)$$

with damping functions

$$\begin{aligned} f_{p1} &= f_{d1} = (1 - e^{-y^*})^2 \\ f_{p2} &= 1 \\ f_{d2} &= \frac{1}{C_{d2}} (C_{\varepsilon 2} f_2 - 1) [1 - e^{-y^*/5.7}]^2 \\ f_2 &= 1 - 0.3e^{-(Re_T/6.5)^2}, \end{aligned} \quad (2.2.132)$$

where $C_{\varepsilon 2}$ is the modeling constant of the corresponding k - ε model. In the DWX model, the damping functions of ε_c equation are [21]

$$\begin{aligned} f_{p1} &= f_{p2} = 1 \\ f_{d1} &= (1 - e^{-y^*/1.7})^2 \\ f_{d2} &= \frac{1}{C_{d2}} (C_{\varepsilon 2} f_2 - 1) [1 - e^{-y^*/5.8}]^2 \\ f_2 &= 1 - 0.3e^{-(Re_T/6.5)^2}, \end{aligned} \quad (2.2.133)$$

and α_t is given by

$$\alpha_t = [1 - e^{-y^*/16}]^2 \left[1 + \frac{3}{Re_T^{3/4}} \right] C_\lambda \frac{k^2}{\varepsilon} \sqrt{2\mathcal{R}}. \quad (2.2.134)$$

Regarding the wall boundary conditions for $\overline{c'^2}$ and ε_c , different variants can be found in the literature. The most popular condition for $\overline{c'^2}$ is

$$\overline{c'^2} = 0 \quad (2.2.135)$$

applied in [89, 2, 64]. However, as discussed, in ref. [113] this is true only in the case of wall heat transfer problems under the assumption of the constant wall temperature. In the cases of constant wall heat or mass flux a more natural condition is

$$\frac{\partial \overline{c'^2}}{\partial y} = 0 \quad (2.2.136)$$

applied for example in [90, 21, 113, 129] for the walls with constant heat fluxes or adiabatic walls. Regarding ε_c , the strict condition at the wall is

$$\varepsilon_c = \alpha \frac{\partial^2 \overline{c'^2} / 2}{\partial y^2}, \quad (2.2.137)$$

and it holds irrespective of the wall conditions. This equation can be replaced by a more simple one [129]

$$\varepsilon_c = \alpha \left(\frac{\partial \sqrt{\overline{c'^2}}}{\partial y} \right)^2. \quad (2.2.138)$$

The results of the application of all considered models for the heat transfer modeling in a 2D channel are presented in figure 2.2.14. The results are non-dimensionalized using u_τ , ν , and the wall friction temperature $\theta_w = q_w / \rho c_p u_\tau$, where q_w is the wall heat flux. Turbulent viscosity is modeled by means of the AKN k - ε model. The results given by the constant turbulent Prandtl number $\sigma_t = 1.0$ are presented as well. The plots show that the results produced by both $\overline{c'^2}$ - ε_c models using the near-wall damping functions (AKN and DWX) are much more accurate than the NK model predictions produced without damping functions. This is a direct analogy to the near-wall k - ε turbulence modeling discussed in section 2.2.1.3. It should be, however, stated that the improvement over the constant turbulent Prandtl number approach is not a drastic one since $\sigma_t = 1.0$ predictions are already quite accurate. Only the α_t^+ (figure 2.2.14(d)) and the σ_t (figure 2.2.14(e)) plots reveal the difference between the constant turbulent Prandtl number and the AKN or DWX predictions. The α_t^+ profile is indeed reproduced better by both low-Re $\overline{c'^2}$ - ε_c models. Furthermore, in the $y^+ > 30$ region where the turbulent mixing effects become especially important, the turbulent Prandtl number trend given by the AKN and the DWX models is more realistic than the assumption of a constant σ_t (see figure 2.2.14(e)).

2.2.2.4 $\overline{c'^2}$ - ω_c model

Alternatively to the ε_c transport equation, a transport equation for the scalar dissipation rate per unit turbulent scalar variance ω_c (dimension equal to $1/t$) can be derived to obtain the time scale characterizing turbulent scalar fluctuations, which is needed for the turbulent scalar diffusivity formulation (equation 2.2.106) and for the closure of the scalar variance transport equation 2.2.124. This variable ω_c is analogous to the ω -variable in the k - ω turbulent viscosity models.

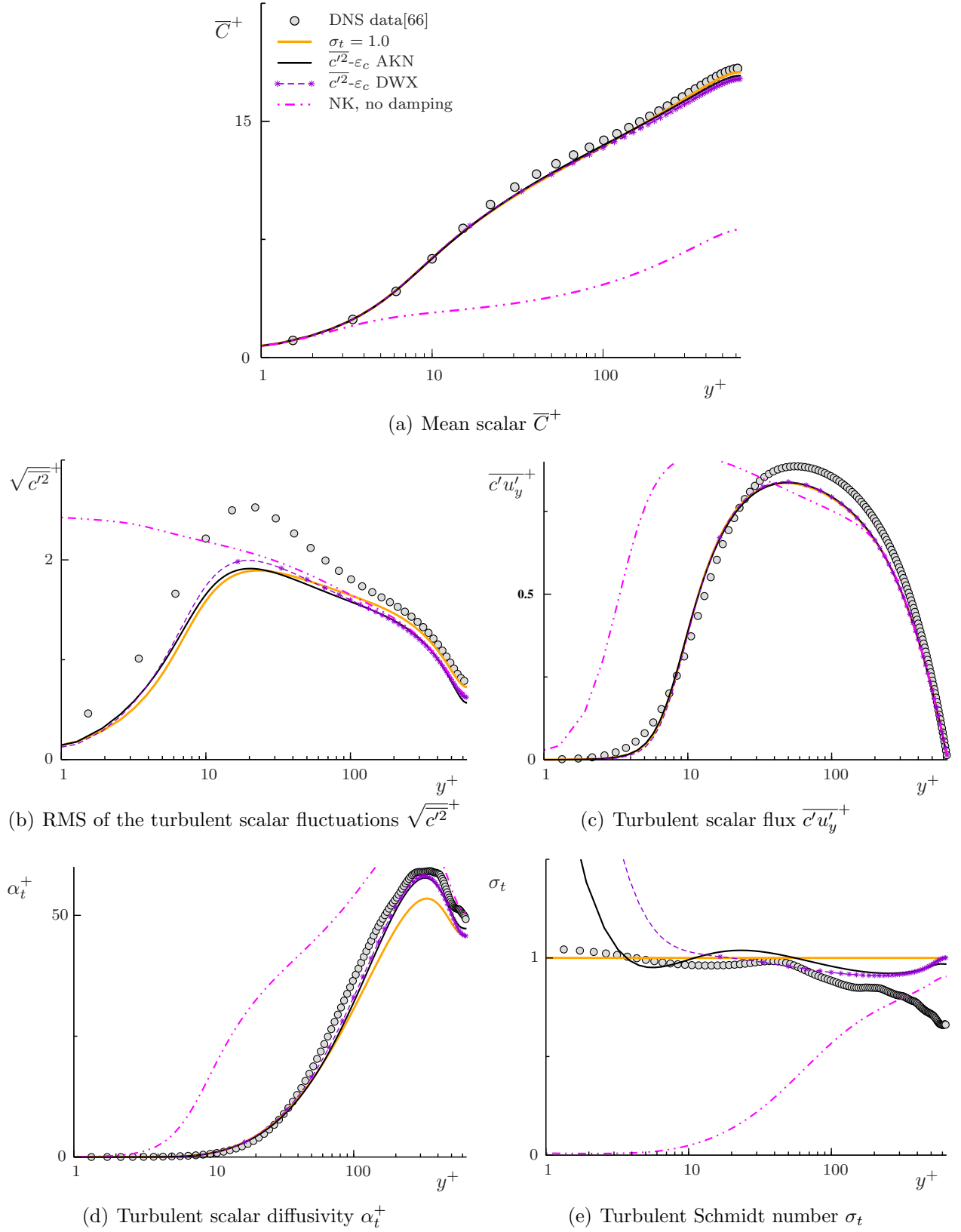


Figure 2.2.14: 2D channel flow. Mean and fluctuating scalar field predictions, turbulent scalar diffusivity, and turbulent Schmidt numbers. Different RANS scalar mixing models in comparison with DNS data of Kawamura et al. [66]. Turbulent viscosity is modeled by means of the low-Re k - ε AKN approach.

A $\overline{c'^2}$ - ω_c model proposed by Huang and Bradshaw in ref. [48] can be written as [18]

$$\alpha_t = C_\lambda k \left(\tau_d \frac{1}{\omega_c} \right)^{1/2}, \quad (2.2.139)$$

$$\frac{\partial \overline{c'^2}}{\partial t} + \overline{U}_l \frac{\partial \overline{c'^2}}{\partial x_l} = \frac{\partial}{\partial x_l} \left[\left(\alpha + \frac{\alpha_t}{\sigma_h} \right) \frac{\partial \overline{c'^2}}{\partial x_l} \right] + 2\mathcal{P}_c - 2\overline{c'^2}\omega_c, \quad (2.2.140)$$

$$\frac{\partial \omega_c}{\partial t} + \overline{U}_l \frac{\partial \omega_c}{\partial x_l} = \frac{\partial}{\partial x_l} \left[\left(\alpha + \frac{\alpha_t}{\sigma_\phi} \right) \frac{\partial \varepsilon_c}{\partial x_l} \right] + C_{p1} \frac{\omega_c}{\overline{c'^2}} \mathcal{P}_c + C_{p2} \frac{\omega_c}{k} \mathcal{P} - C_{d1} \omega_c^2 - C_{d2} \frac{1}{\tau_d} \omega_c \quad (2.2.141)$$

with following modeling constants

$$C_\lambda = 0.11; \quad C_{p1} = -0.2; \quad C_{p2} = 0.94; \quad C_{b1} = 0.2; \quad C_{d2} = 0.83; \quad \sigma_h = 1; \quad \sigma_\phi = 2.0. \quad (2.2.142)$$

This model was derived by means of dimensional analysis and comparison with the existing $\overline{c'^2}$ - ε_c models. The model coefficients are obtained employing the same procedures as for the $\overline{c'^2}$ - ε_c model equations and additionally refined using computer optimization [48]. The wall-limiting behavior of ω_c described in [48] is as follows:

$$\omega_c \rightarrow \left(1 - \frac{C_{d1}\sigma}{\beta_\omega} \right) \frac{6\nu}{\sigma C_{d1}y^2}, \quad \text{as } y \rightarrow 0. \quad (2.2.143)$$

where β_ω is the modeling coefficient of the corresponding turbulent viscosity k - ω model.

Figure 2.2.15 shows the results generated by the $\overline{c'^2}$ - ω_c model of Huang and Bradshaw applied to the 2D channel flow heat transfer problem. The 1988 k - ω model of Wilcox was used for the turbulent viscosity modeling. The results produced by $\sigma_t = 1.0$ are presented as well; furthermore, the k - ε AKN, $\overline{c'^2}$ - ε_c AKN profiles are shown for comparison. The results given by the $\overline{c'^2}$ - ω_c model, although quite accurate, do not improve the $\sigma_t = 1.0$ predictions and are less accurate than those produced by the $\overline{c'^2}$ - ε_c AKN model. This is especially clearly seen in the turbulent scalar variance predictions (figure 2.2.15(b)). The trend of underprediction of the peak $\overline{c'^2}$ values is quite similar to the trend of underprediction of k by the 1988 k - ω model without low-Re corrections discussed in section 2.2.1.5.

It should be also added that in this particular test case the $\overline{c'^2}$ - ω_c model is only capable of producing accurate results in conjunction with the 1988 k - ω model of Wilcox (or other k - ω models not employing the low-Re corrections). Figure 2.2.16(a) illustrates this result. In that figure the temperature profiles given by the $\overline{c'^2}$ - ω_c model in conjunction with different turbulence models are presented. Despite the fact that the low-Re k - ε and the low-Re k - ω models produce more accurate turbulence and velocity profiles in the considered test case than the 1988 Wilcox model, the HB $\overline{c'^2}$ - ω_c temperature predictions given in conjunction with low-Re k - ε models are worse than with the 1988 k - ω model. This trend of the turbulent viscosity model dependence is much weaker for the $\overline{c'^2}$ - ε_c AKN model discussed in the previous section (figure 2.2.16(b)). This

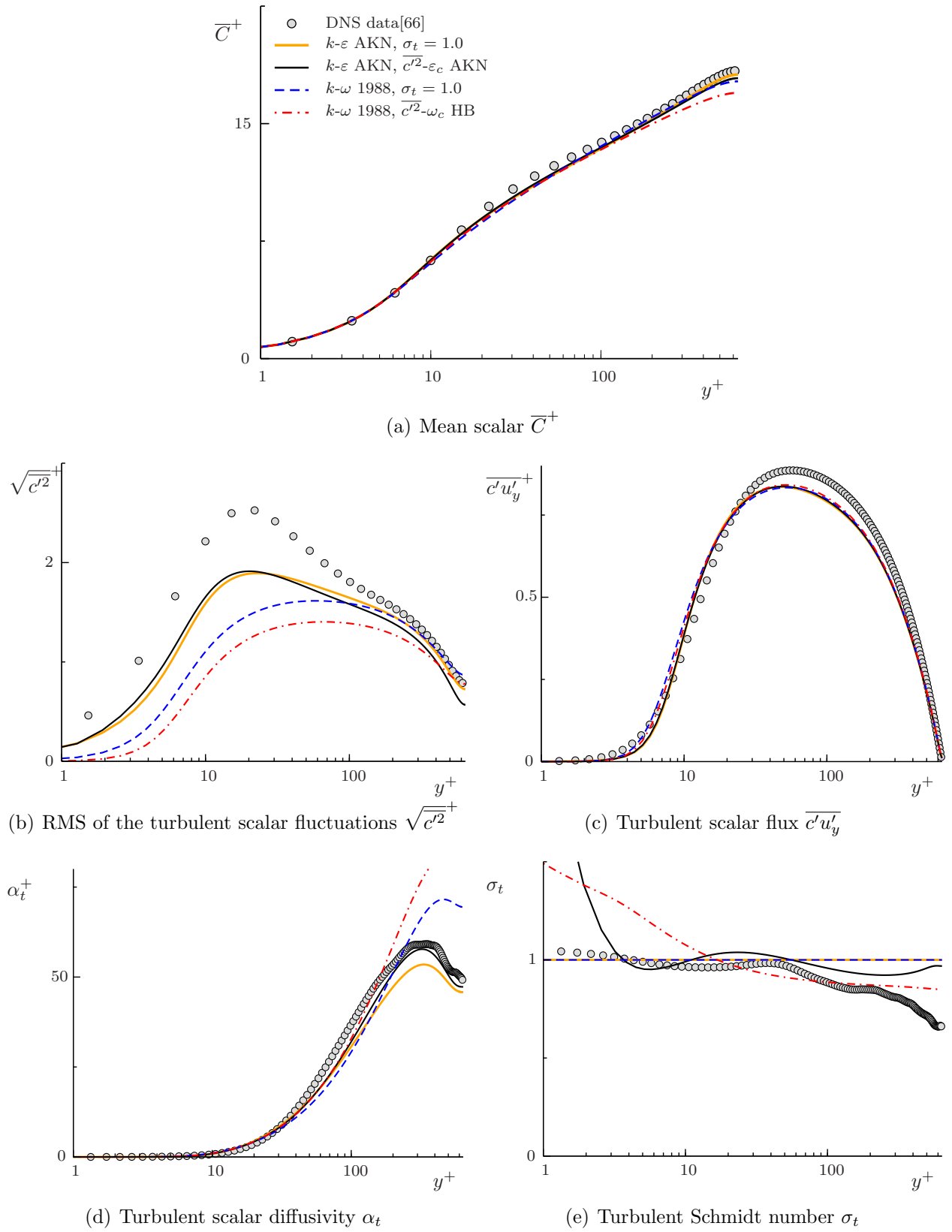


Figure 2.2.15: 2D channel flow. Mean and fluctuating scalar field predictions, turbulent scalar diffusivity, and turbulent Schmidt numbers. Different RANS scalar mixing models in comparison with DNS data of Kawamura et al. [66].

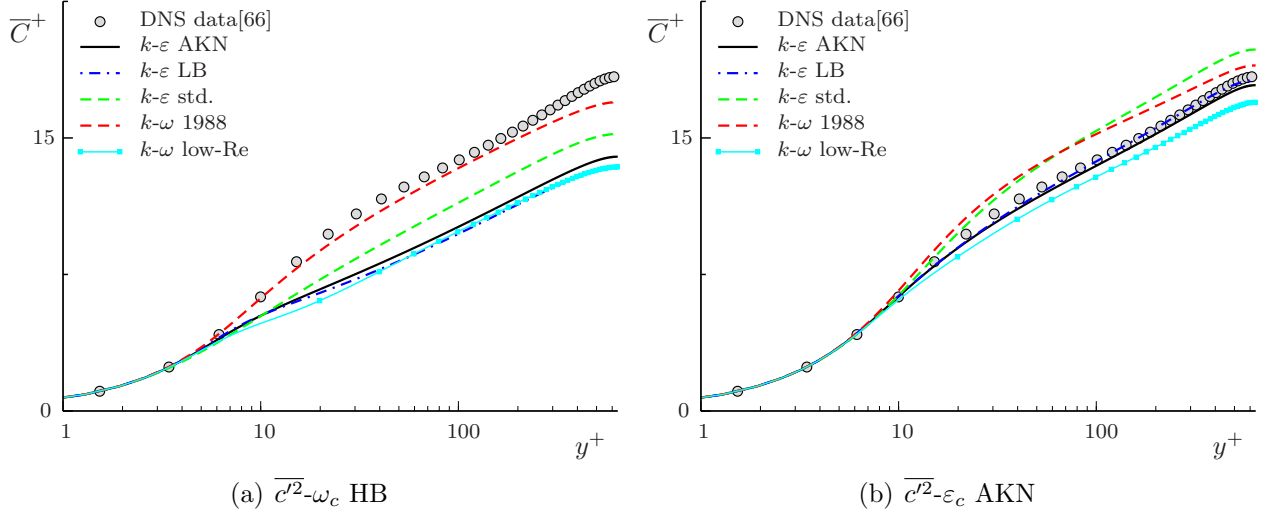


Figure 2.2.16: Mean transported scalar profiles in 2D channel flow given by the $\overline{c'^2-\epsilon_c}$ AKN model and the $\overline{c'^2-\omega_c}$ HB model. Dependence on the turbulence modeling approach.

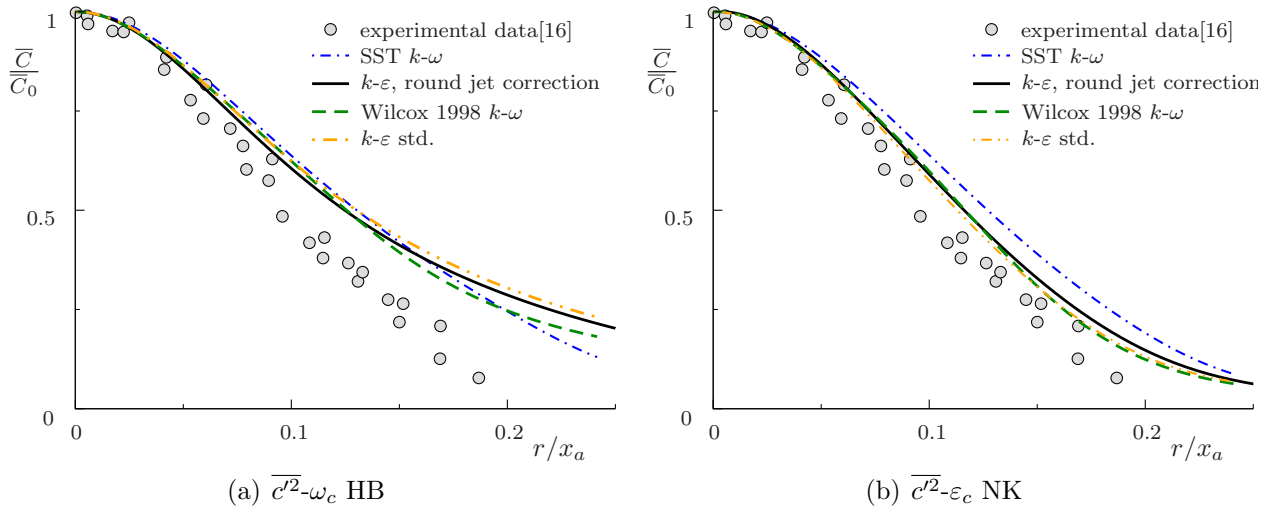


Figure 2.2.17: Mean transported scalar profiles in free round jet flow given by the $\overline{c'^2-\epsilon_c}$ NK model and the $\overline{c'^2-\omega_c}$ HB model. Dependence on the turbulence modeling approach.

study indicates that some additional attention to the choice of the turbulent viscosity model has to be paid in the two-equation scalar mixing simulations. Not only does the accuracy of the turbulent viscosity model play an important role, but also its compatibility with the turbulent scalar diffusivity approach. This does not necessarily imply that the studied scalar mixing models always have to be used in conjunction with one particular specially selected turbulent viscosity approach. In some cases, the turbulent viscosity model dependence is mild. This is illustrated in figure 2.2.17 that shows the turbulence model dependence for both the $\overline{c'^2-\omega_c}$ HB (figure 2.2.17(a)) and the $\overline{c'^2-\epsilon_c}$ NK (figure 2.2.17(b)) models for the free round jet flow. The dimensionless scalar profiles obtained using quite different turbulence modeling approaches lie close to each other.

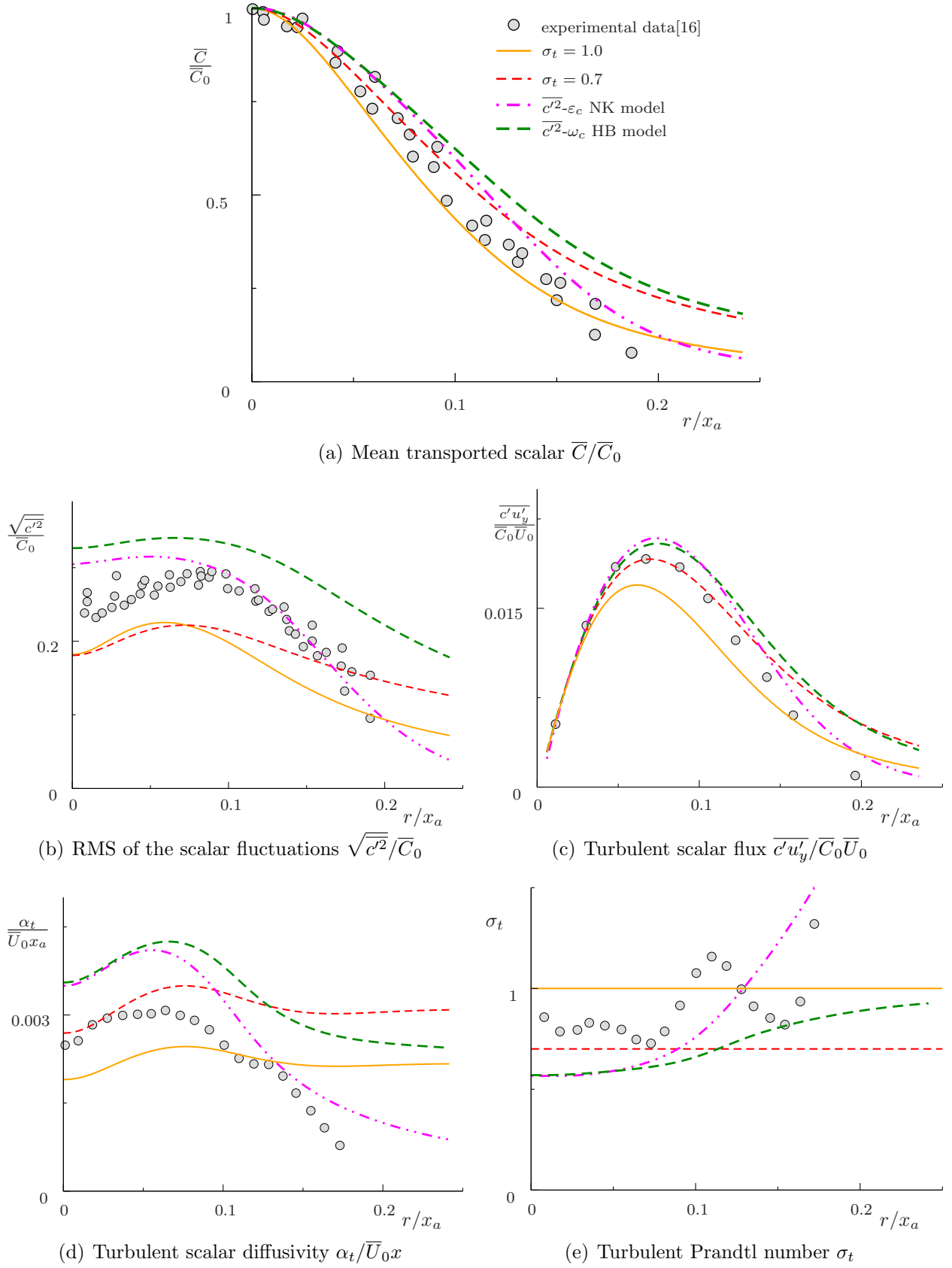


Figure 2.2.18: Free round jet flow. Mean and fluctuating scalar field predictions, turbulent scalar diffusivity, and turbulent Schmidt numbers. Different RANS turbulent scalar diffusivity models in comparison with experimental data of Chua and Antonia [16]. Turbulent viscosity is modeled by means of the Wilcox 1998 k - ω model.

For the round jet test case the $\overline{c'^2}-\omega_c$ HB model performs with approximately the same quality as for the 2D channel flow test case. It represents the experimental trends in the turbulent Prandtl number profile, cannot, however, reach the accuracy of the $\overline{c'^2}-\varepsilon_c$ NK model (figure 2.2.18). As the NK model, the $\overline{c'^2}-\omega_c$ HB approach tends to the overestimation of mixing in the round jet case. This can originate from the fact that all modeling constants and equations for the HB model were developed based on the $\overline{c'^2}-\varepsilon_c$ NK model constants and equations.

Generally it can be stated that the $\overline{c'^2}-\omega_c$ HB approach, although showing positive trends, needs some improvement to capture the experimental and the DNS profiles in the test cases considered here with the same degree of accuracy as the $\overline{c'^2}-\varepsilon_c$ models. Its performance for the more complex test cases will be considered later in the present work.

2.2.2.5 Concluding remarks

Despite the fact that a number of the turbulent scalar diffusivity approaches exist in literature, it can be stated that the constant turbulent Prandtl or Schmidt number hypothesis is still the most popular model. Unfortunately notably few measurements on the value of this parameter in many complex flows exist. Knowledge about the actual values and the variation range of the turbulent Prandtl or Schmidt number is essential to make practical conclusions about the values which should be chosen for the modeling as well as about general applicability of this hypothesis. This question will be addressed in the present work in chapter 3.

The two-equation turbulent scalar diffusivity models discussed in this dissertation were included because of their analogy with common two-equation turbulent viscosity models and the promising results these models displayed in the academic mixing problems considered in this section. Additionally, the scalar variance equation often provides an input for assumed-PDF combustion modeling. In such combustion models, a transport equation for ε_c is not typically solved rather scalar variance dissipation is determined by the simple relation of equation 2.2.115. It is of interest to know if the transport equation for ε_c helps to achieve more accurate predictions of $\overline{c'^2}$ than does the application of equation 2.2.115. This question will be studied for practically relevant flow configurations in the present work in chapter 3. The dissipation as well as the other terms of the exact $\overline{c'^2}$ equation will be evaluated from the resolved LES data for complex jet flows and will be compared with the respective terms of different modeling approaches. Furthermore, two important parameters concerning the equation closure problems in the two-equation turbulent scalar diffusivity approach will be evaluated: the turbulent scalar diffusivity constant C_λ (to study the variability of its actual values), and the turbulent scalar to velocity time scale ratio \mathcal{R} . The last parameter is not only used in equation 2.2.115 for the ε_c modeling, but it is a central physical criterion for deriving of almost all modeling constants of the two-equation turbulent scalar diffusivity closures (see section 2.2.2.2).

2.3 LES and hybrid RANS/LES modeling

In this section an overview will be given on the LES and hybrid RANS/LES models used in the present dissertation. Since the development of the novel modeling approaches in this area does not form the focus of the present work, this overview is brief and concentrated only on significant modeling details. Deeper theoretical considerations and wider reviews can be found for example in refs. [39, 107] for LES and in refs. [108, 41] for hybrid methods.

2.3.1 Velocity field modeling

2.3.1.1 Subgrid scale (SGS) models for LES

There are various approaches for modeling the subgrid scale terms in the filtered equations 2.1.23 and 2.1.24. (see refs. [39, 107]). The most traditional method are models based on the same principles as RANS models. In theory, as for RANS, many different modeling approaches and philosophies are possible including direct subgrid stress modeling, algebraic, one-equation subgrid viscosity and scalar diffusivity models etc. However, within the LES subgrid turbulent viscosity concept there is no need to model the turbulent (subgrid) length scale as it is already given by the grid or more strictly speaking by filter width. The application of two-equation turbulent viscosity or scalar diffusivity models can be regarded as unnecessary since the second equation in such models exists to provide the length scale. Besides this, as discussed previously, LES modeling should in theory be simpler than RANS modeling since only the fine scales which are characterized by a more universal and isotropic character than the large ones have to be reproduced by a model. Also the high computational cost of LES encourages simple and inexpensive closures.

The subgrid Reynolds stresses $\overline{U_i U_j} - \overline{U_i} \overline{U_j}$ in the filtered momentum equations can be modeled using the Boussinesq approximation similar to how it is commonly done in RANS approximations.

$$-(\overline{U_i U_j} - \overline{U_i} \overline{U_j}) = -\frac{2}{3} k^{SGS} \delta_{ij} + \nu_t^{SGS} \left(\frac{\partial \overline{U_i}}{\partial x_j} + \frac{\partial \overline{U_j}}{\partial x_i} \right) = -\frac{2}{3} k^{SGS} \delta_{ij} + 2\nu_t^{SGS} \overline{S}_{ij} = -\frac{1}{3} \tau_{ii} \delta_{ij} - \tau_{ij}^a, \quad (2.3.1)$$

where the deviatoric part

$$\tau_{ij}^a = -2\nu_t^{SGS} \overline{S}_{ij}^a \quad (2.3.2)$$

is the component explicitly modeled and directly appears in the solved momentum equation, and the isotropic part,

$$\frac{1}{3} \tau_{ii} = \frac{2}{3} k^{SGS} \delta_{ij}, \quad (2.3.3)$$

is combined with the pressure term to form a pseudo-pressure $\mathbf{P} = \overline{P} + \frac{1}{3} \tau_{ii} \rho$ in the same manner as in the RANS equation 2.2.7.

As in the case of RANS turbulent viscosity modeling, ν_t^{SGS} can be expressed via a combination

of the velocity and length scales

$$\nu_t^{SGS} \sim \mathcal{L}_{SGS} \mathcal{U}_{SGS}. \quad (2.3.4)$$

In the LES approach, as mentioned before, the length scale \mathcal{L}_{SGS} is the filter width Δ . In general, the size of a filter does not have to correspond with the grid size (actually for increased accuracy one filter element should comprise several grid elements), but in order to reduce the computational cost the most usual approach is to take the filter size equal to the grid size. There are also different ways of computing the characteristic length of one grid element [39]. Typically it is the cubic root of the grid element volume \mathcal{V} ,

$$\mathcal{L}_{SGS} = \Delta = \Delta_{grid} = \mathcal{V}^{1/3}. \quad (2.3.5)$$

The velocity scale can be built as

$$\mathcal{U}_{SGS} = \Delta \mathbf{S}, \quad (2.3.6)$$

where \mathbf{S} is the norm of the filtered strain-rate tensor,

$$\mathbf{S} = \sqrt{2\overline{S_{ij}}\overline{S_{ij}}}. \quad (2.3.7)$$

Hence, with the modeling constant C_s and the above choice of the length and velocity scales

$$\nu_t^{SGS} = (C_s \Delta)^2 \mathbf{S}, \quad (2.3.8)$$

and

$$\tau_{ij}^a = -2(C_s \Delta)^2 \mathbf{S} \overline{S_{ij}}. \quad (2.3.9)$$

The modeling constant C_s can be derived based on the theory of the homogeneous isotropic turbulence [39]. The most popular value is $C_s = 0.18$, however, other values also can be found in the literature.

This approach (Smagorinsky model) is the most widespread one among the LES models due to its simplicity and implementation convenience. This modeling approach is based on the assumption of the local balance of production and dissipation of the turbulent kinetic energy for the fine scales. Additionally, since ν_t in 2.3.8 is always positive, the Smagorinsky model is a purely dissipative model because [39]

$$\varepsilon = -\tau_{ij}^a \overline{S_{ij}} = \nu_t^{SGS} \mathbf{S}^2 \geq 0. \quad (2.3.10)$$

This contradicts the actual turbulent energetics since, in general, the energy transport from the small to the large scales (backscatter) is possible. Another issue is the behavior of the model in the laminar flows. Generally $\mathbf{S} > 0$ in both laminar and turbulent regimes, so that even if no turbulent fluctuations are present, the eddy viscosity does not vanish. This leads to problems especially in near-wall regions where laminar conditions can be found in the viscous sublayer. Thus in near-wall region the application of the Smagorinsky model necessitates the need for

damping functions for the subgrid viscosity [39].

In order to avoid damping functions in the near-wall region in the present work, the so-called WALE model (Wall-Adapted Local Eddy Viscosity) [92] is used. This model applies an improved eddy viscosity formulation which assures the proper behavior of the turbulent viscosity near to the solid walls [92]

$$\nu_t^{SGS} = (C_w \Delta)^2 \frac{(\mathcal{S}_{ij}^d \mathcal{S}_{ij}^d)^{3/2}}{(\bar{S}_{ij} \bar{S}_{ij})^{5/2} + (\mathcal{S}_{ij}^d \mathcal{S}_{ij}^d)^{5/4}} \quad (2.3.11)$$

where

$$\mathcal{S}_{ij}^d = \frac{1}{2}(\bar{g}_{ij}^2 + \bar{g}_{ji}^2) - \frac{1}{3}\bar{g}_{kk}^2 \delta_{ij} \quad (2.3.12)$$

is the traceless symmetric part of the tensor $\bar{g}_{ij}^2 = \bar{g}_{ik}\bar{g}_{kj}$, and $\bar{g}_{ij} = \partial \bar{U}_i / \partial x_j$. In the current work the value of the eddy viscosity modeling constant $C_w = 0.5$ obtained in [92] on the basis of the proper reproduction of the decay of homogeneous isotropic turbulence is adopted for all presented calculations.

It should be mentioned that despite the improved near-wall behavior of the WALE model there is still a general problem with wall-resolving LES which arises due to the demand of a very fine grid resolution in boundary-layer regions since the length and time scales of the turbulent vortical structures decrease significantly in the wall vicinity. There are several methods to overcome these difficulties. First, wall functions can be used whose idea is similar to the idea of wall functions for the RANS models discussed above. They avoid modeling inside of the boundary layer and just attempt to represent the behavior of the modeled quantities at the outer edge of the layer. However, the wall function construction for LES is a more demanding task than for RANS because in LES the continuous exchange between the modeled and the resolved scales exists, and the wall function not only has to model accurately the averaged shear stress as in RANS but also to correctly represent the amount of the resolved turbulent kinetic energy in this region [39]. Furthermore, as in RANS, the wall function method implies very strict requirements regarding the grid construction - the first near-wall grid point should lie exactly in the region intended by the model. Another possible method to overcome the problems of LES wall modeling are hybrid RANS/LES approaches discussed in the next section.

2.3.1.2 Hybrid RANS/LES

As pointed out in the introduction and in the previous section, in practical engineering computations LES is often not affordable because of its high grid requirements. The application of RANS methods helps in such cases to obtain the time-averaged solutions, but often time-resolved information is needed. In those cases URANS (Unsteady RANS) can be applied as discussed in section 2.1.3. If URANS is not applicable (no well-defined large-scale coherent structures or pulsations are present in the flow) or a better resolution of turbulence in some flow regions is needed, RANS/LES methods can be applied. This class of methods has become in the last few years a fast developing and promising technique for industrial turbulence simu-

lations. The idea is to combine RANS and LES approaches in such a way that RANS modeling is applied in the regions of the flow where the grid resolution demands of LES cannot be realized (for example in the near-wall regions) and LES in the regions where a finer resolution is desirable (i.e. where the RANS models fail). According to Spalart [114], the computational cost of such methods can be about six orders of magnitude less than those of the well-resolved wall-bounded LES. From the theoretical perspective the possibility of RANS/LES combination can raise principal questions since the Reynolds-averaging and filtering approaches are not equivalent, as discussed above in section 2.1.4. However, inspecting the Reynolds-averaged equations 2.1.16 and filtered equations 2.1.23 one can see that they essentially have the same form, and if the Boussinesq approximation is applied to close both the averaged and the filtered stresses, the only difference which remains is just the relation for the eddy viscosity modeling. This observation is the basis for most of the existing RANS/LES models. There is a variety of methods to combine RANS and LES which differ by the target application area, employed models, ways to handle the RANS to LES transition zones, and criteria of the RANS to LES switching. Comprehensive overviews can be found in ref. [41] and in ref. [108].

For the calculations of the present work the Scale-Adaptive Simulation (SAS) approach was chosen whose origin is in the RANS modeling tradition and which can be easily implemented in an existing RANS-oriented code. The idea behind this approach is the introduction of an additional production term $Q_{SST\,SAS}$ in the ω equation of the SST k - ω model (equation 2.2.76)

$$Q_{SST\,SAS} = \max \left[\widehat{\zeta} \kappa \mathbf{S}^2 \frac{L_t}{L_{vK}} - C \cdot \frac{2}{\sigma_\phi} k \cdot \max \left(\frac{1}{\omega^2} \frac{\partial \omega}{\partial x_j} \frac{\partial \omega}{\partial x_j}, \frac{1}{k^2} \frac{\partial k}{\partial x_j} \frac{\partial k}{\partial x_j} \right), 0 \right]. \quad (2.3.13)$$

Here $\widehat{\zeta} = 3.51$, $C = 2$, $\kappa = 0.41$, and $\sigma_\phi = 2/3$ are the model constants. The von Karman length scale L_{vK} is defined as

$$L_{vK} = \max \left(\kappa \frac{\sqrt{2S_{ij}S_{ij}}}{\sqrt{\frac{\partial^2 U_i}{\partial x_k^2} \frac{\partial^2 U_i}{\partial x_j^2}}}, C_s \sqrt{\frac{\kappa \widehat{\zeta}}{\beta_{\omega 2}/\beta_k - \gamma_2}} \Delta \right) \quad (2.3.14)$$

with the modeling constants of the k - ω SST model $\beta_{\omega 2}$, β_k , and γ_2 . C_s is also a constant and has to be calibrated in the code to represent the proper rate of decay of the homogeneous isotropic turbulence to avoid either the accumulation or excessive dissipation of energy at the smallest scales [85, 31]. In the current work the baseline value of C_s is $C_s = 0.145$.

The SAS term comes into effect when the ratio of the turbulent length scale, $L_t = k^{1/2}/\omega$, to the von Karman length scale, L_{vK} , increases [85, 31, 84]. The von Karman length scale is smaller for an unsteady velocity profile than for a steady velocity profile (see [85, 31, 84] for details). When the grid is fine and the flow equations are able to resolve the small-scale movements, the SAS term detects the unsteadiness and increases the production of the dissipation rate ω . The result is that the turbulent viscosity ν_t is reduced; thereby, the dissipating (damping) effect of the turbulent viscosity on the resolved fluctuations is reduced. Eventually the momentum equations can thus work in a “LES-like” mode. Further details concerning the SST SAS model

as well as examples of its application can be found in refs. [31, 84].

2.3.2 Scalar transport modeling

Regarding the scalar transport modeling in LES and closure of the subgrid scalar fluxes in the equation 2.1.24, the most widespread method is, as in RANS, the gradient diffusion hypothesis

$$-(\overline{CU_j} - \overline{C} \overline{U_j}) = \alpha_t^{SGS} \frac{\partial \overline{C}}{\partial x_j}, \quad (2.3.15)$$

and also, similar to RANS, the constant subgrid Prandtl or Schmidt number hypothesis is a widespread approach to model the subgrid scalar diffusivity,

$$\alpha_t^{SGS} = \frac{\nu_t^{SGS}}{\sigma_t^{SGS}}. \quad (2.3.16)$$

Many different values of σ_t^{SGS} can be found in literature (in the range of 0.3 – 1.0) [39]. In this dissertation $\sigma_t^{SGS} = 1.0$ is applied. Additional studies on the SGS turbulent Schmidt number dependence of the solution were accomplished for all considered test cases in preparation of this dissertation and σ_{SGS} dependence was found to be minor (see for example ref. [50])* . This result can be explained by the dominance of the resolved turbulent scalar flux over the modeled (SGS) one in the LES calculations [50]. This is a noteworthy distinction between LES and RANS simulations where in the later the turbulent scalar flux is modeled entirely; consequently, the turbulent scalar flux largely depends on the selected σ_t value.

In the hybrid URANS/LES calculations, the dependence on the turbulent Prandtl or Schmidt number value can be expected to be more pronounced in the RANS than in the LES regions. A study on the turbulent Schmidt number dependence for the SAS scalar mixing predictions in a jet in crossflow test case was performed in preparation of this dissertation in ref. [51]. As in LES, σ_t dependence was found to be minor. In the SAS simulations of ref. [51] the largest part of the turbulent fluctuations was resolved. The situation can, however, be different in a different test case where, for example, the role of the RANS region is larger than in the case considered in ref. [51]. This problem presents a topic for the future investigations directed towards the detailed studies of the hybrid URANS/LES scalar mixing modeling. In the present dissertation, all SAS results shown in chapter 4 were obtained using $\sigma_t = 1.0$.

Regarding further possibilities of the LES scalar transport modeling not employing the constant subgrid Prandtl or Schmidt number hypothesis, several publications based on the dynamic subgrid scalar diffusivity concept can be found (see refs. [105, 115]). Also several models solving the transport equations for the SGS scalar flux or the SGS scalar variance exist [57]; however, since LES scalar mixing modeling is not the main topic of the present study, those models will not be considered here.

*This statement is not meant to imply that the results of LES are independent of the SGS scalar transport model, but a thorough study on this subject is not the focus of the present work.

2.4 Numerical realization

All models investigated in this dissertation were implemented in the DLR combustion CFD research code THETA. The THETA code flow solver works on 3D unstructured grids and is designed for the calculations of low-Mach number flows with strongly varying density and temperature fields.

For the spatial discretization in the RANS and URANS calculations a second order linear upwind differencing scheme [34, 43] was used for all equations. In the LES and hybrid URANS/LES calculations, the spatial discretization of the momentum and scalar transport equations was a second order central differencing scheme [34, 43] selected in order to avoid the strong numerical dissipation of the upwind schemes. For the scalar transport equation a total variation diminishing-type limiter was applied [34] since the preliminary calculations revealed its favorable influence on the scalar field results in the considered cases. For the spatial discretization of the turbulence and scalar variance transport equations, the second order linear upwind differencing scheme was applied in SAS.

In the steady-state calculations the SIMPLE method was used for the pressure-velocity coupling [34, 96], and in the unsteady calculations a projection method [34, 15] was used. A second order backwards differentiation formula [34, 43] was selected for time discretization. In all RANS simulations grid independence of the presented results was verified by additional calculations on a variety of grids with different resolutions.

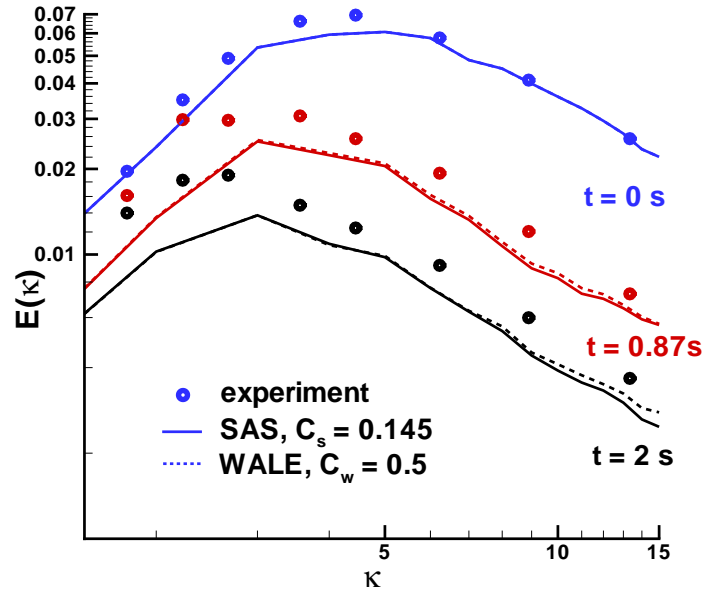


Figure 2.4.1: Decay of homogeneous isotropic turbulence, comparison with the reference experiment of Comte-Bellot and Corrsin [17], SST SAS and WALE LES results.

To validate proper LES and SAS behavior within the THETA code numerical framework, as recommended in [39, 31, 84], a test on the homogeneous isotropic turbulence case of Comte-

Bellot and Corrsin [17] was conducted (see figure 2.4.1). This calculation confirmed that the selected baseline modeling constants ($C_w = 0.5$ for the WALE LES model 2.3.11 and $C_s = 0.145$ for the SST SAS model 2.3.13) ensure a proper representation of the decay of homogeneous isotropic turbulence.

It was assured for the presented LES calculations that more than 80% of the turbulent Reynolds shear stresses or turbulent kinetic energy were resolved. The WALE model is turbulent viscosity based and in order to obtain the SGS turbulent kinetic energy empirical formulas (see ref. [107]) have to be used. This can introduce some uncertainty in the estimation of the SGS turbulent kinetic energy. Thus, additionally, the resolution of the Reynolds shear stresses was considered since the SGS Reynolds shear stresses can be reconstructed from the SGS viscosity directly using the Boussinesq approximation without further empirical constants. The resolution quality of the presented SAS results is discussed in section 4.1.

Moreover, it should be noted that, as discussed in ref. [102], the “80% - resolution” criterion, is necessary but not sufficient for LES quality assurance. For this reason, as proposed in ref. [102], a variety of grids were generated for every test case, and in preliminary calculations it was assured that the solution obtained on the basic LES grid does not change drastically with the further grid refinement.

3 Study on the accuracy of RANS modeling using experimental and LES data

In this chapter the accuracy of the RANS approaches which are discussed in section 2.2 is analyzed for three complex jet flow configurations that are important in the context of gas turbine combustion: jet in crossflow, confined coaxial swirling jets, and confined coaxial jets without swirl. The approach of the presented investigations is the same for all three cases. First, the results of RANS mean and fluctuating velocity field simulations are validated against experimental data and the results of accompanying LES calculations. The results obtained with different RANS models are compared, and the influence of different equation terms and corrections is studied. Then, using the resolved data fields from LES, the profiles of the Reynolds-averaged turbulent viscosities and of the main budget terms of the turbulent kinetic energy transport equation are obtained and compared with the respective output of the RANS models. This study is done to obtain a deeper insight into the flow physics and to additionally highlight the comparative advantages and weaknesses of different RANS approaches. Furthermore, a study on the validity of the simplifications and approximations used for RANS equation closure is performed. Finally, investigations on the scalar mixing modeling are presented. Mean and fluctuating scalar fields given by different RANS models are compared with experimental and LES data. The turbulent scalar diffusivities and the model equation terms of the scalar variance transport equation are evaluated from the resolved LES fields and compared with the RANS modeling results. Practically important question regarding turbulent Schmidt number values in complex jet flows is clarified.

3.1 Jet in crossflow

The first flow configuration considered in this chapter is jet in crossflow. Testing of the turbulence and mixing model performance for jet in crossflow is important since this configuration is often used for the mixing enhancement in the gas turbine combustion applications. The literature study on the previous numerical work for transverse jets can be found in section 1.2.1. The test case used for the studies performed in the present dissertation was chosen to mimic the configurations typical for the premixing and dilution zones of gas turbine combustion chambers and is, therefore, characterized by the relatively high jet to crossflow momentum ratio $J = 36$.

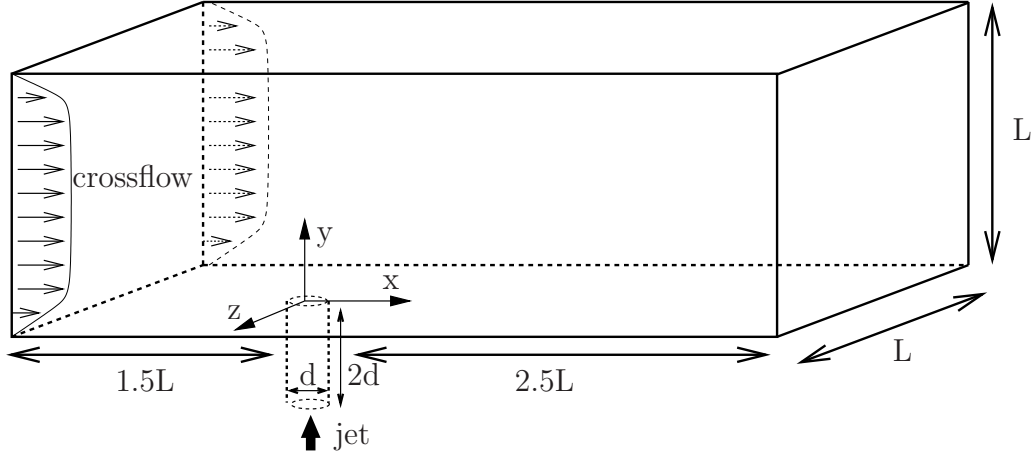


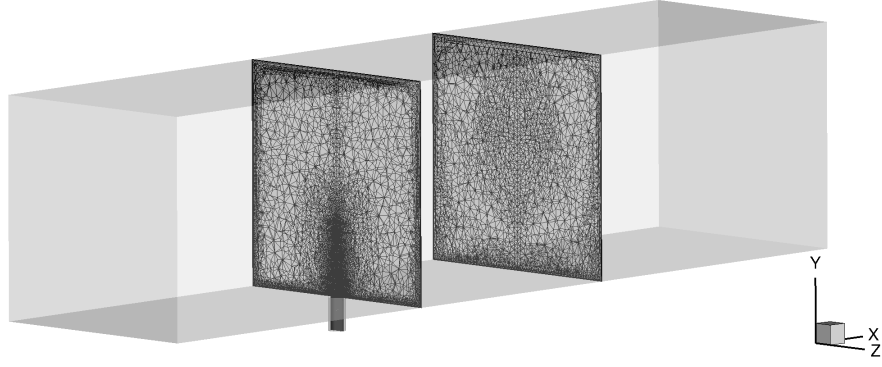
Figure 3.1.1: Jet in crossflow test case [78, 13, 42]. Flow configuration, computational domain and coordinate system.

3.1.1 Description of the basis test case and computational setup

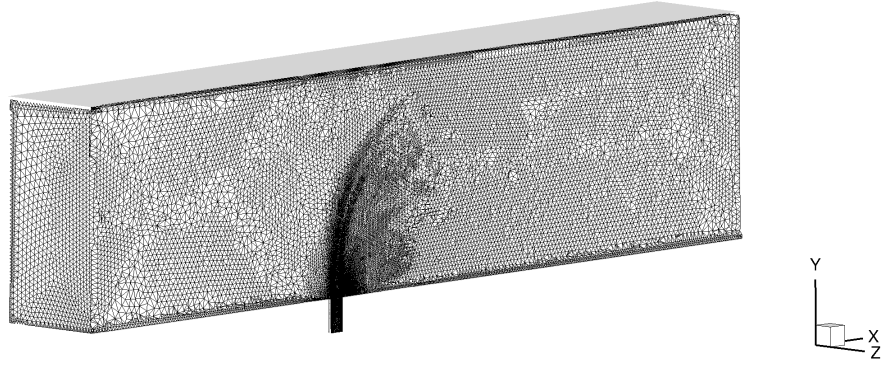
A sketch that illustrates the basic jet in crossflow test case considered in the current study is presented in figure 3.1.1. The respective experimental measurements are described in [78, 13, 42]. In the experiments, turbulent mixing of a round jet that is normally injected into a crossflow channel has been studied by means of a simultaneous 2D PIV/LIF method (working medium is air, tracer substance is NO_2). The density ρ can be assumed constant. The diameter of the jet is $d = 8mm$, and the main channel has a quadratic cross section with a side length $L = 108mm$. The Reynolds number of the jet is $Re_{jet} = 2 \cdot 10^4$ (mean velocity of the jet is $U_{jet} = 37.7m/s$). The jet turbulence intensity is about 5%. In the experimental measurements [78, 13, 42] different jet to crossflow momentum ratios were considered. For the present study, the case with $J = 36$ is selected. The turbulence intensity at the inflow of the main channel is about 1.5%. More details about the experimental conditions and measurement techniques can be found in refs. [78, 13, 42].

The dimensions of the basic computational domain used in the LES calculations are shown in figures 3.1.1 and 3.1.2. For the steady-state RANS computations, a symmetry boundary condition was applied on the jet center plane; thereby, reducing the computational domain width from L to $L/2$ (see figure 3.1.3). All simulations were done on polyhedral unstructured grids refined in the regions of high velocity gradients which were identified on the basis of preliminary RANS calculations. The basic meshes for the LES and for the RANS are shown in figures 3.1.2 and 3.1.3 respectively. The grid dimensions are $3 \cdot 10^5$ points for the RANS computations and $1.2 \cdot 10^6$ points for the LES computations. Preliminary grid studies were conducted in preparation of the current work in order to assure sufficient LES resolution (see section 2.4) and grid independence of the RANS results for the used meshes.

The mean velocity on the main channel inlet was set as a block profile corresponding to the experimental boundary conditions described in refs. [78, 13, 42]. For the jet pipe a preliminary calculation using the SST $k-\omega$ model was conducted in order to obtain the velocity profile of



(a) $x/d = 0$ and $x/d = 15$ planes



(b) $z/d = 0$ plane

Figure 3.1.2: Jet in crossflow test case. Basic computational domain and computational grid for LES calculations.

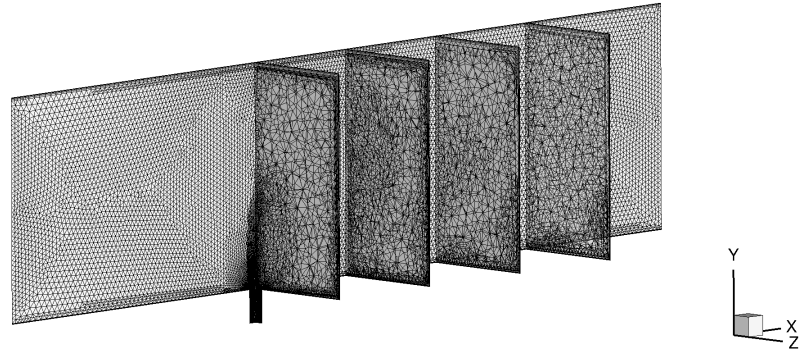


Figure 3.1.3: Jet in crossflow test case. Basic computational domain and computational grid for RANS calculations. Grid is shown in $z/d = 0$, $x/d = 0$, $x/d = 7.5$, $x/d = 15$, and $x/d = 22.5$ planes.

a fully developed pipe flow with the mean velocity $U_{jet} = 37.7m/s$. This profile was imposed on the jet pipe inlet. This was necessary since in the present computational domain the jet pipe length comprises two pipe diameters, whereas in the experiment the pipe is much longer and the flow at the jet exit can be assumed fully developed. In the RANS computations the turbulence data on the jet pipe inlet was also set using the values from the preliminary pipe flow simulation. Regarding the turbulence boundary conditions for LES, both the steady-

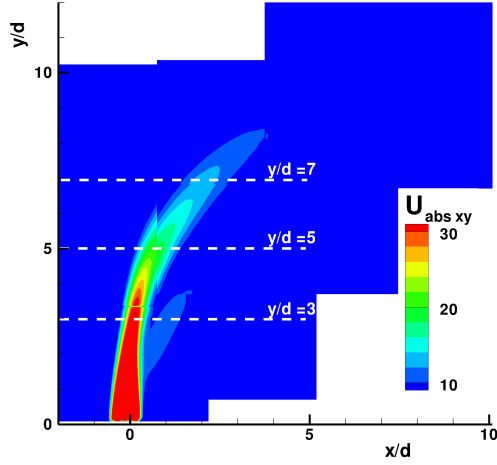
state velocity profiles (without additional fluctuations) and the unsteady fluctuating boundary conditions of Klein et al. [69] were applied in the preliminary studies on both the jet pipe and the main channel inlets with the turbulent intensities prescribed according to the experimentally measured values. Since the last method produced slightly more accurate results, it was chosen for the simulations presented below.

The numerical setup of all calculations is described in section 2.4. For the LES calculations the computational time step was $10^{-6}s$, which ensured maximal CFL numbers of around 1.1. The time-averaging in the LES calculations started after about three characteristic flow-through times (equal to $0.015s$) for the establishing of a well-developed flow field. The time-averaging procedure comprised an integration time of about $0.23s$ which is equal to more than 15 characteristic flow-through times. The time convergence was assured for all mean and fluctuating variables.

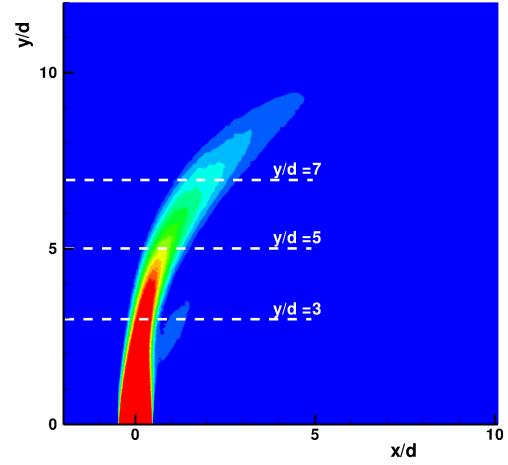
3.1.2 Velocity field modeling

3.1.2.1 Mean and fluctuating velocity field predictions

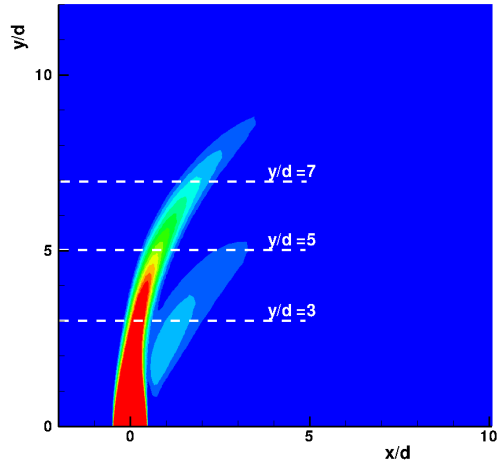
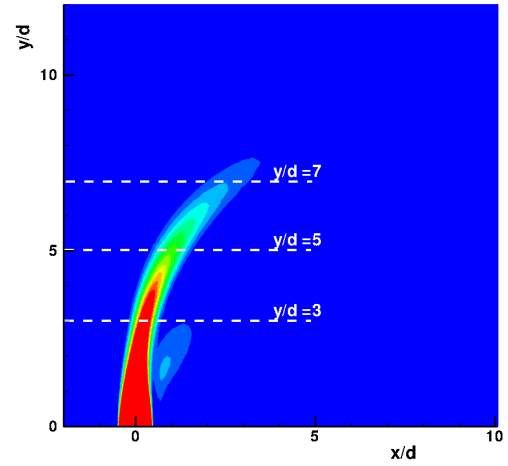
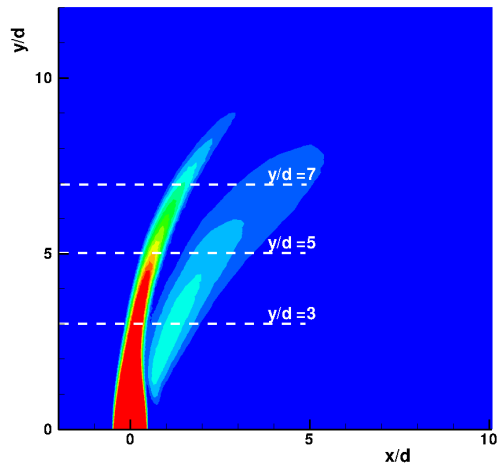
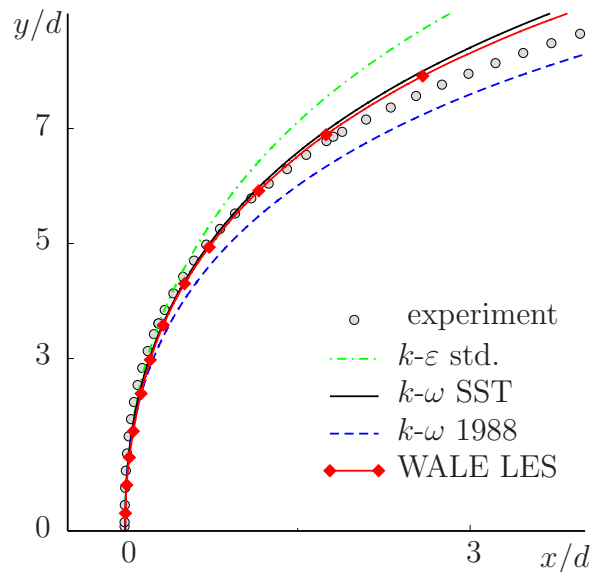
The velocity fields obtained from LES and by different RANS models discussed in section 2.2 are presented and validated against the experimental data of refs. [78, 13, 42]. The aim is a comparison of the accuracy achieved by different turbulence modeling approaches in a jet in crossflow configuration. Figure 3.1.4 presents the contours of the mean xy -velocity $U_{abs\ xy}$ (calculated as $U_{abs\ xy} = \sqrt{\overline{U_x^2} + \overline{U_y^2}}$) on the jet center plane $z/d = 0$. Figure 3.1.4(a) shows the PIV measurement data; the contours obtained by LES are given in figure 3.1.4(b); the results achieved by the SST $k-\omega$ model of Menter (section 2.2.1.6), by the 1988 $k-\omega$ model of Wilcox (section 2.2.1.4), and by the standard $k-\varepsilon$ model (section 2.2.1.1) are presented in figures 3.1.4(c) - 3.1.4(e) respectively. Finally, figure 3.1.4(f) assesses the numerical predictions of the jet mean centerline trajectory against experimental data. Deviations from the measured values can be observed in all simulations, but the degree of this inaccuracy varies strongly depending on the used approach. The standard $k-\varepsilon$ model gives the least accurate results: it under predicts the jet spreading; the jet penetration depth is overestimated; a strong and large recirculation zone can be observed in the jet wake region whereas in the experimental measurements this zone is much less emphasized. The SST model shows better agreement with the experimental data: the jet centerline trajectory is closer to the measured one, the jet penetration depth is less over predicted than by the standard $k-\varepsilon$ model. However, the size and the strength of the recirculation zone in the jet wake are still overestimated by the SST model. The 1988 Wilcox model reproduces this region better, but the jet velocity decay is stronger than in experiment. In contrast to the $k-\varepsilon$ and the SST model, the jet centerline trajectory given by the 1988 Wilcox model (figure 3.1.4(f)) lies lower than the experimental one. Regarding the LES results, it is observed that the jet downstream region and the recirculation zone are predicted well but the mean xy -velocity in the jet core is overestimated. At this point in the analysis a clear statement about the accuracy of LES data in comparison to RANS is rather difficult to formulate, but



(a) Experimental data [78, 13, 42].



(b) WALE LES


 (c) SST $k-\omega$ model

 (d) 1988 Wilcox $k-\omega$ model

 (e) Standard $k-\epsilon$ model


(f) Jet centerline trajectory.

Figure 3.1.4: Mean absolute xy -plane velocity ($U_{abs\,xy} = \sqrt{\overline{U_x^2} + \overline{U_y^2}}$) and positions of the extracted profiles on the jet center plane $z/d = 0$. LES and different RANS models in comparison with experimental data.

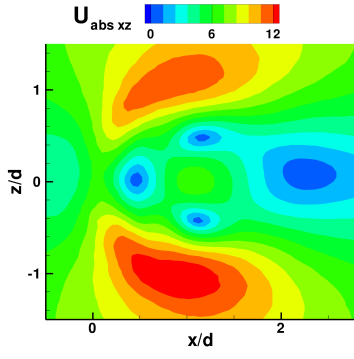
this ambiguity is clarified in the paragraphs that will follow.

Figure 3.1.5 presents the contours of the mean absolute xz -plane velocity calculated as $U_{abs\,xz} = \sqrt{\overline{U}_x^2 + \overline{U}_z^2}$ in three different y/d planes. The locations of these planes are indicated by the white dashed lines in the contour plots of figure 3.1.4. The experimental and the LES data are compared to the 1988 $k-\omega$ and the SST modeling results. The $k-\varepsilon$ model predictions are not included in this comparison since, as already indicated by figure 3.1.4, their quality is poor. LES produces more accurate results than the two presented RANS $k-\omega$ models especially at $y/d = 5$ and $y/d = 7$. Figure 3.1.5 shows that, although at the $y/d = 3$ plane the SST model seems to be more accurate than the 1988 $k-\omega$ model, at the higher y/d locations the quality of the SST predictions decreases, whereas the 1988 $k-\omega$ model shows more realistic results. Thus, for this particular case, the 1988 $k-\omega$ approach results in a more accurate velocity field modeling than the SST $k-\omega$ and the standard $k-\varepsilon$ models.

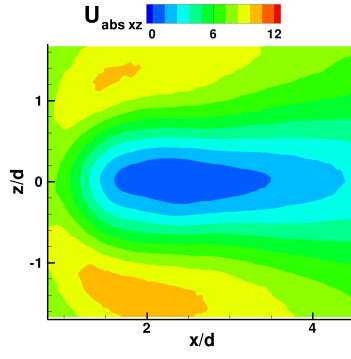
A more detailed evaluation can be made by the comparison of one-dimensional profiles of mean and fluctuating velocities. The profiles were extracted at the jet center plane, $z/d = 0$, along the white dashed lines shown in figure 3.1.4. Figure 3.1.6 first presents the validation of the mean x - and y -velocity components against experimental data. With regards to the RANS models, superiority of the 1988 Wilcox model predictions over the standard $k-\varepsilon$ and the $k-\omega$ SST results can be observed. The standard $k-\varepsilon$ model tends to give the worst agreement with experiment. Seen particularly clearly is the overestimation of the recirculation zone in the \overline{U}_x plots. LES reproduces the x -velocity exceptionally well, and in the y -velocity profiles the overestimation of the local maxima of \overline{U}_y at $y/d = 5$ and $y/d = 7$ can be observed. The general agreement of the LES mean velocity field predictions with experimental data is nevertheless better than in RANS.

The fluctuating velocity field data are compared in figures 3.1.7 and 3.1.8. For LES the resolved fluctuations obtained in the time-averaging process are presented. For RANS the Reynolds stresses are calculated using the Boussinesq approximation (equation 2.2.3). The profiles of the turbulent kinetic energy, k , shown in figure 3.1.7(a) reveal that the level of this characteristic turbulence parameter is extremely low in the standard $k-\varepsilon$ model results. The $k-\omega$ SST model also shows a slight underestimation of k but not as strong as the standard $k-\varepsilon$ model. The predictions made by the 1988 Wilcox model show a better agreement with experimental data. However, it is seen at $y/d = 5$ that the 1988 Wilcox model underestimates k in the downstream locations, even if its level is well predicted in the jet core, and at $y/d = 7$ it shows instead an overestimation of k . LES gives here the best agreement with experimental data. Only at $y/d = 3$, in the region downstream of the jet injection location, k is slightly overestimated by LES. At $y/d = 7$ the peak values of k given by LES may be too high, but in this region no measurement data for k are available in the locations upstream of the jet centerline. For the additional quantification of the LES and RANS data, other fluctuating variables are considered below.

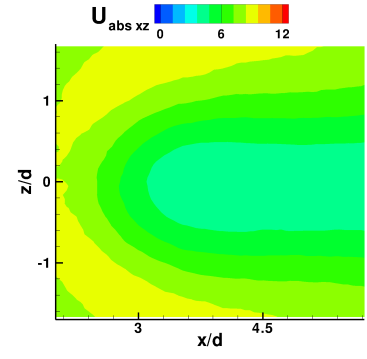
Figures 3.1.7(b) and 3.1.8(a, b) present the xy -, xx -, and yy -components of the Reynolds stress tensor. The differences between the SST model and the Wilcox 1988 $k-\omega$ model can be



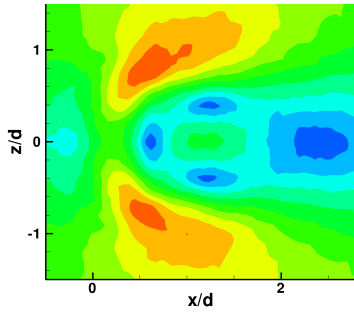
(a) Experimental data, $y/d = 3$.



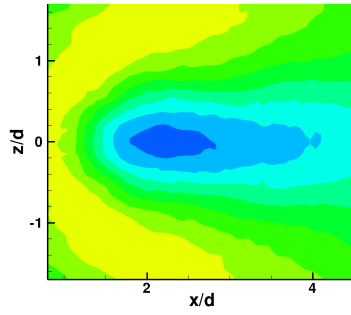
(b) Experimental data, $y/d = 5$.



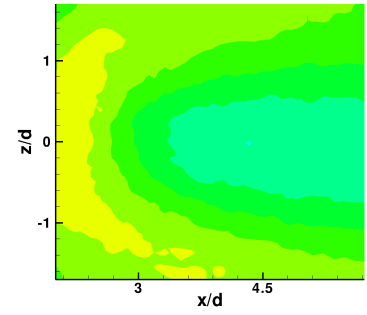
(c) Experimental data, $y/d = 7$.



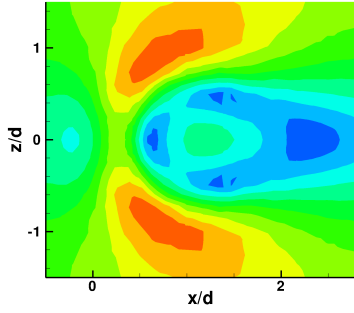
(d) WALE LES, $y/d = 3$.



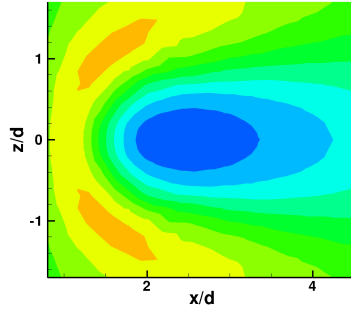
(e) WALE LES, $y/d = 5$.



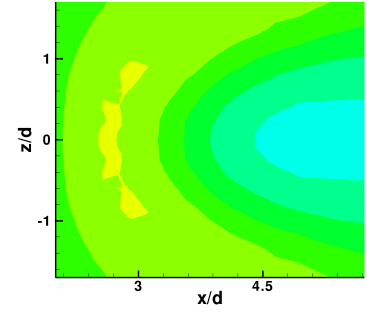
(f) WALE LES, $y/d = 7$.



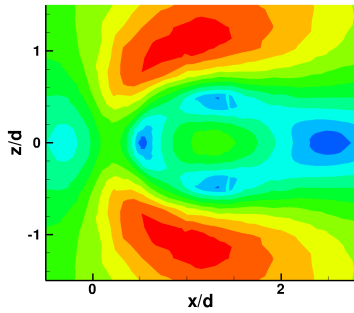
(g) 1988 $k-\omega$, $y/d = 3$.



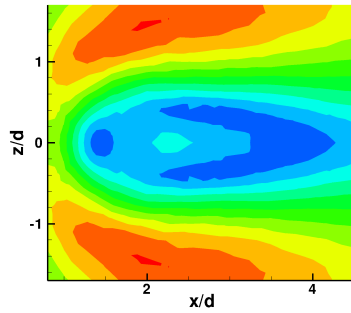
(h) 1988 $k-\omega$, $y/d = 5$.



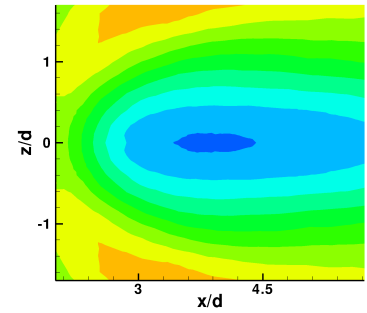
(i) 1988 $k-\omega$, $y/d = 7$.



(j) SST $k-\omega$, $y/d = 3$.



(k) SST $k-\omega$, $y/d = 5$.



(l) SST $k-\omega$, $y/d = 7$.

Figure 3.1.5: Mean absolute xz -plane velocity ($U_{abs\,xz} = \sqrt{\overline{U_x^2} + \overline{U_z^2}}$), different y/d planes. LES and different RANS models in comparison with experimental data.

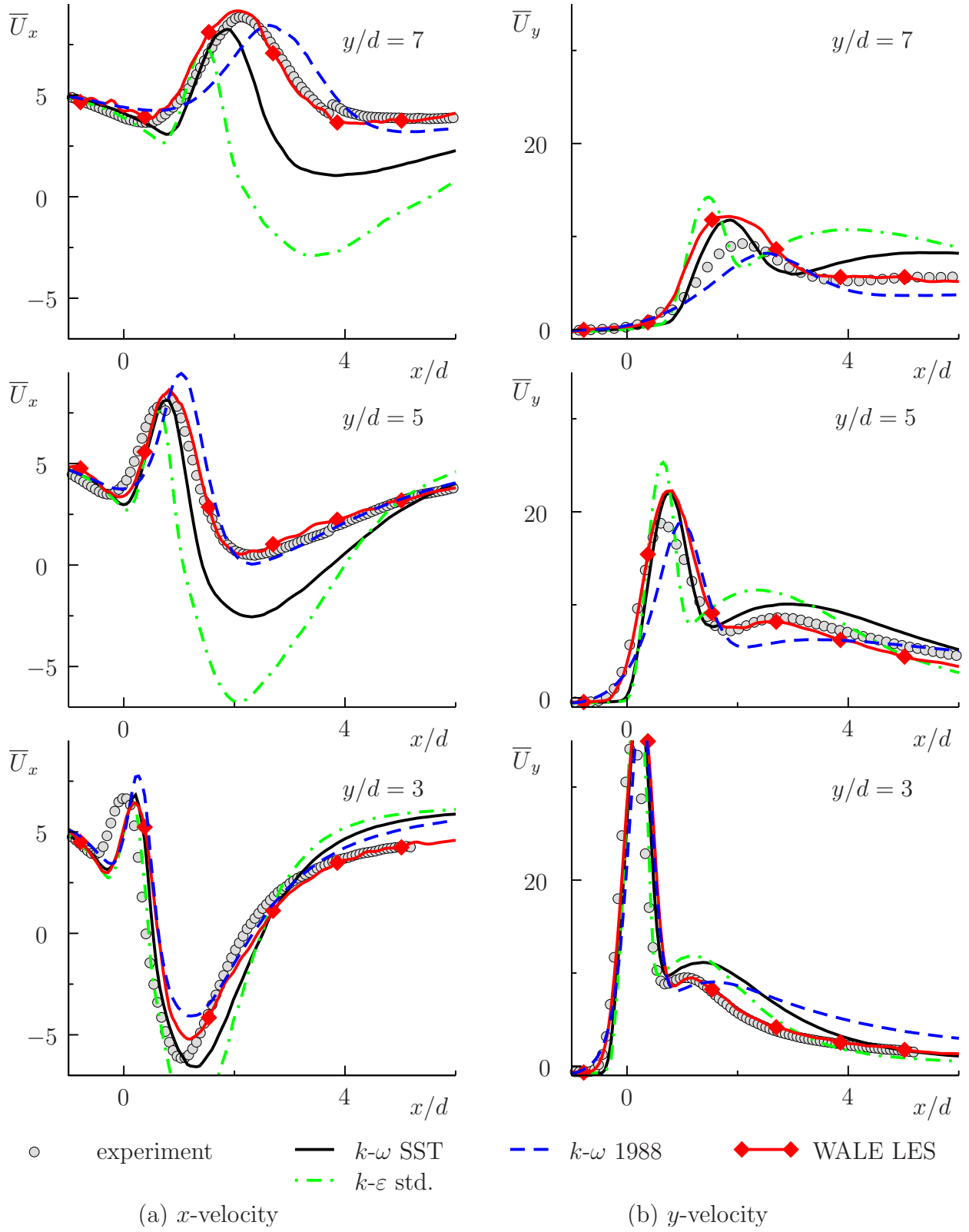


Figure 3.1.6: x - and y -components of the flow velocity vector. $z/d = 0$. LES and different RANS turbulence models in comparison with experimental data.

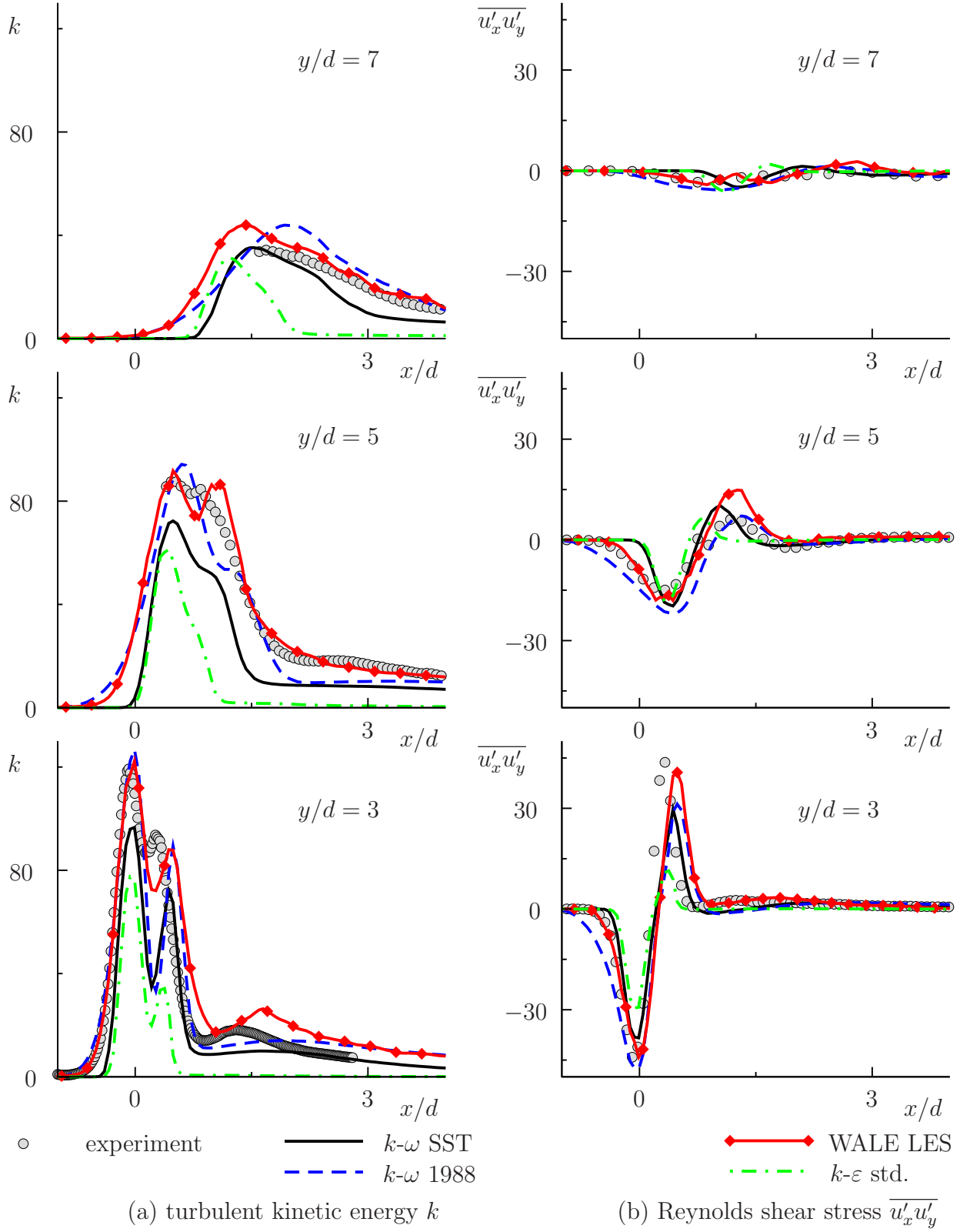


Figure 3.1.7: Turbulent kinetic energy and Reynolds shear stress. $z/d = 0$. LES and different RANS turbulence models in comparison with experimental data. [42, 78, 13].

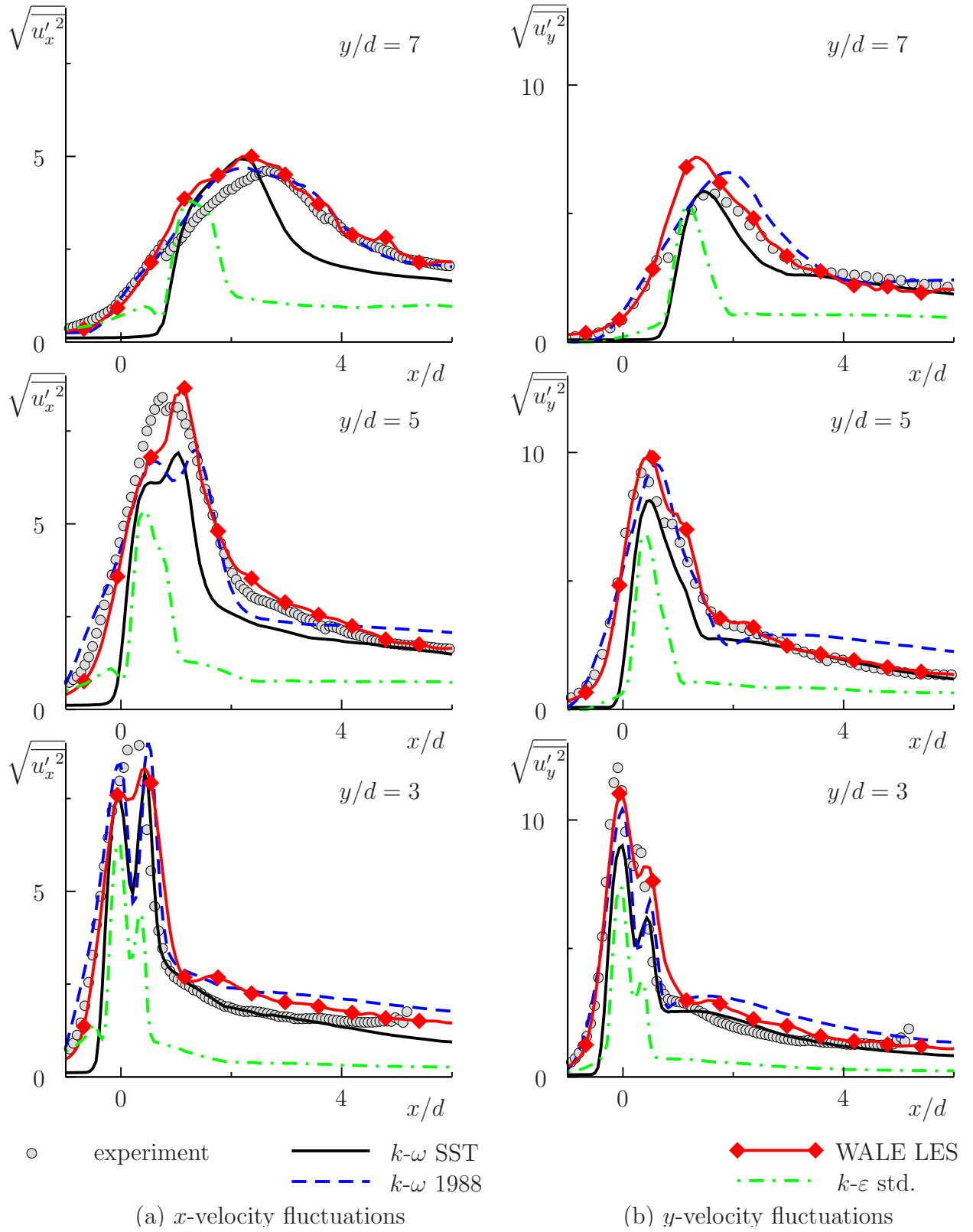


Figure 3.1.8: RMS fluctuations of the x - and y -components of the flow velocity vector. $z/d = 0$. LES and different RANS turbulence models in comparison with experimental data. [42, 78, 13].

clearly seen in figure 3.1.8 in the jet upstream region where the Wilcox 1988 k - ω model gives a good estimation of the velocity fluctuations whereas the SST model under predicts their level. The standard k - ε model shows here again a strong underestimation of all fluctuating velocity components. LES results, apart from the slight overestimation of the peaks of $\overline{u_y'^2}$ at $y/d = 7$ and of $\overline{u_x' u_y'}$ at $y/d = 5$, show good agreement with experimental data.

A positive aspect for the RANS modeling in this flow configuration is the observation that, due to the flow complexity, equation 2.2.3 is not reduced to $-\overline{u_i' u_i'} = -\frac{2}{3}k$ for the $\overline{u_x'^2}$ and $\overline{u_y'^2}$ components of the Reynolds stress tensor, and these quantities can be realistically predicted if k and ν_t are reproduced accurately. This is in contrast to the $\overline{u_x'^2}$ and $\overline{u_y'^2}$ given by RANS in simple quasi 2D flows such as a plane channel discussed in section 2.2 where the variances of all three velocity components have the same levels in contrast to the experimental evidence.

3.1.2.2 Further studies on the accuracy of RANS models for the velocity field predictions

The previous subsection shows that the accuracy of RANS simulations for a jet in crossflow configuration can differ drastically depending on the selected modeling approach. Among the three models tested above only the Wilcox 1988 k - ω was able to reproduce the mean and the fluctuating velocity fields with a satisfactory degree of accuracy. The standard k - ε and the SST model demonstrated an under prediction of turbulence. This trend is especially strong for the standard k - ε model which delivers the worst results. Such an outcome can be slightly surprising considering the results for a free round jet flow discussed in sections 2.2.1.2 and 2.2.1.7. For that academic test case, the level of turbulence was overestimated by all three models considered here - modestly by the standard k - ε and the SST k - ω models and largely by the Wilcox 1988 k - ω model. In order to obtain a more complete understanding of the reasons for such different behavior between the free jet and the jet in crossflow as well as to find a path to improve the RANS simulation quality for jets in crossflow, a study involving several additional turbulence models described earlier in section 2.2.1 is performed in this section.

3.1.2.2.1 Different variants of the Wilcox k - ω model First, the 1988, 1998, and 2006 variants of the Wilcox k - ω model (see sections 2.2.1.4 and 2.2.1.7) are compared. Figure 3.1.9 presents the profiles of the x -component of the flow velocity vector and of the turbulent kinetic energy given by these approaches. Additionally, the profiles produced by the SST k - ω model are presented. Both later versions of the Wilcox k - ω model (1998 and 2006) overestimate the recirculation zone and show an under prediction of turbulence (the level of k too low, the jet spreading rate is less than in the experimental data). The 2006 version produces the worst results. The profiles generated by the 1998 version are of equivalent quality as the profiles given by the SST model. In contrast to the 1998 and 2006 Wilcox models, the earlier 1988 version tends rather to a slight overestimation of the turbulence in the jet core region, particularly visible at $y/d = 7$. The differences between the predictions given by different versions of the Wilcox model are caused by the modifications introduced in the 1998 and 2006 model versions and absent in the original (1988) formulation. The individual effects of each of these

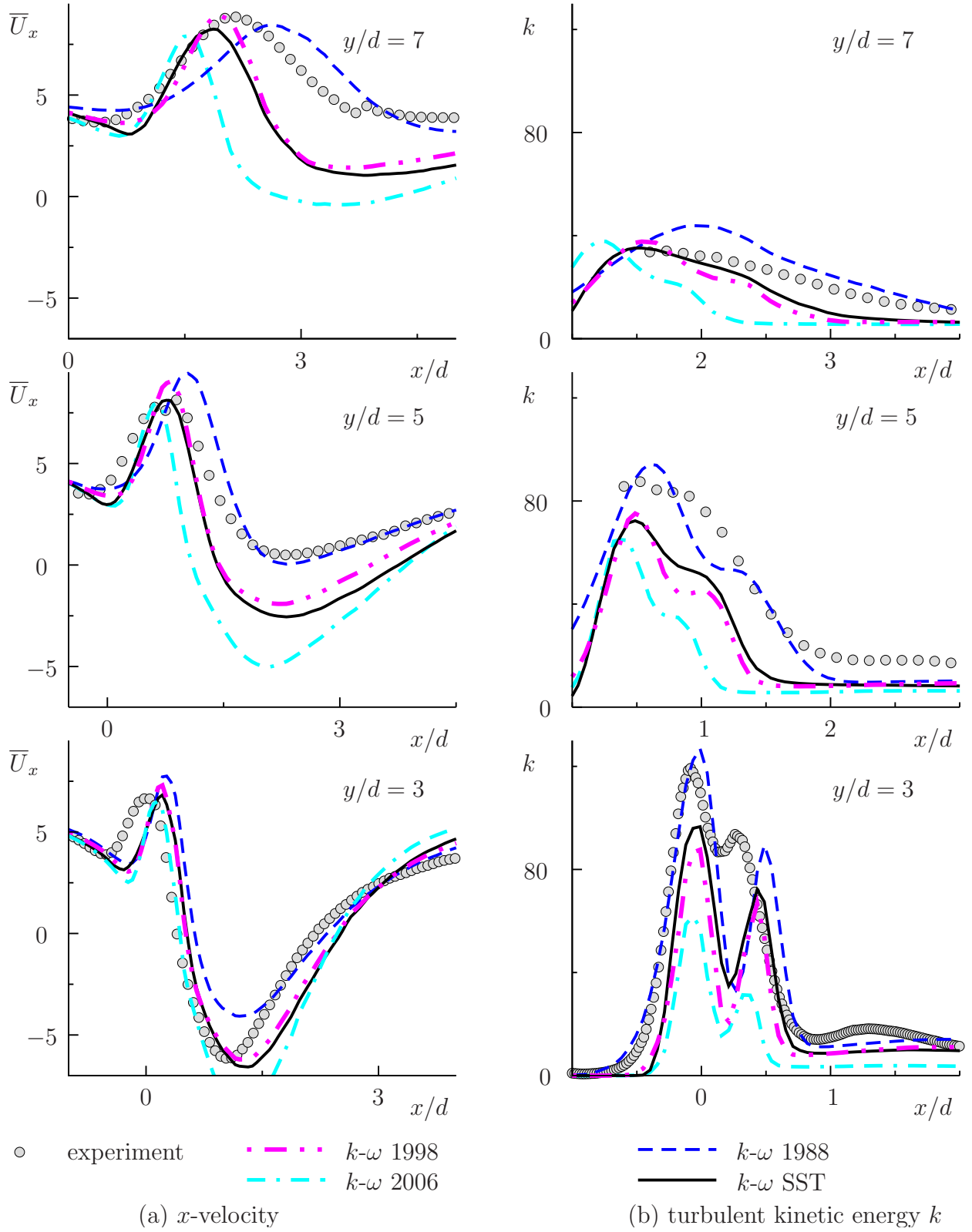


Figure 3.1.9: Different $k-\omega$ models. x -component of the flow velocity vector and turbulent kinetic energy. $z/d = 0$.

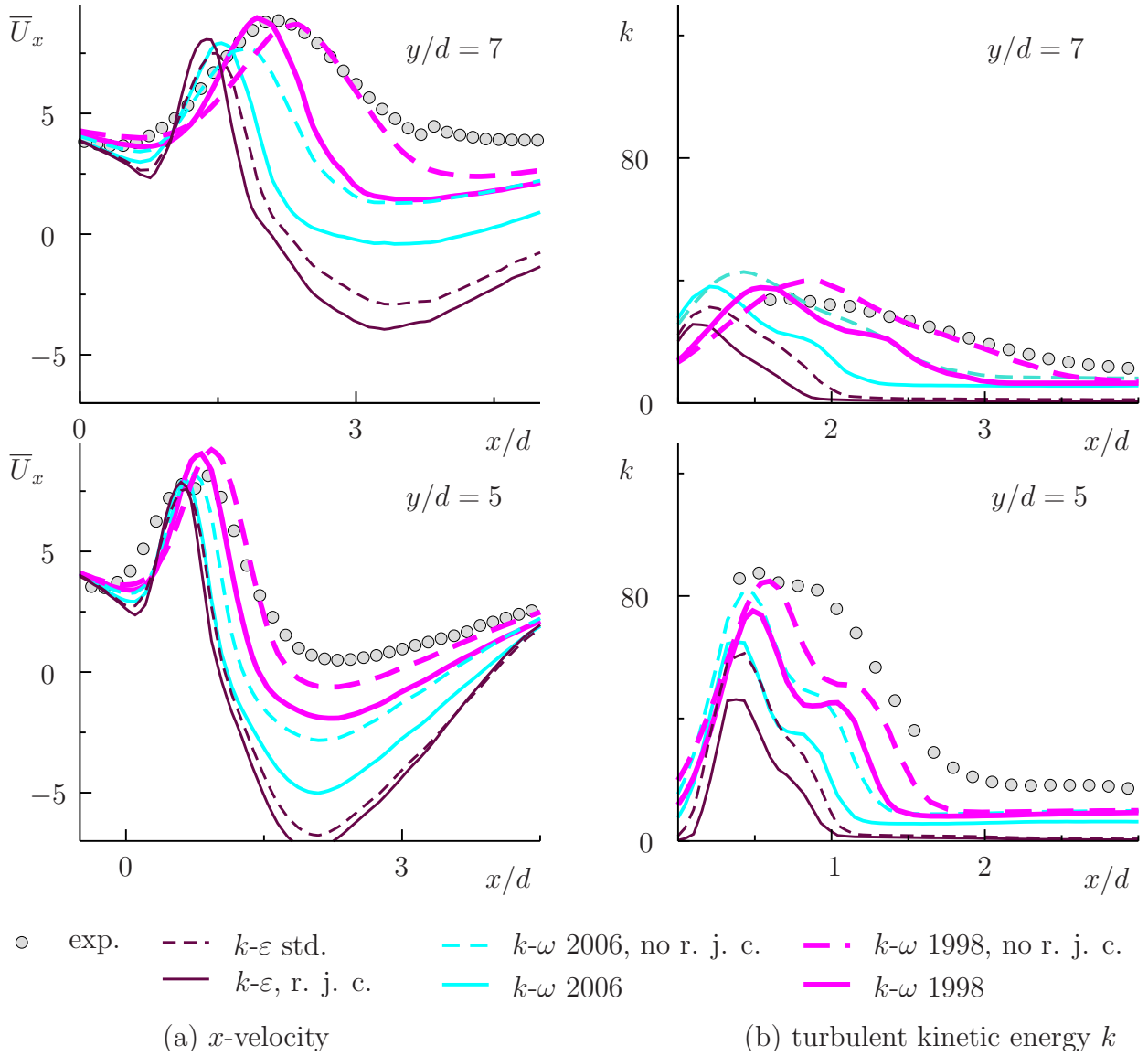


Figure 3.1.10: Influence of the round jet correction in different turbulence models. x -component of the flow velocity vector and turbulent kinetic energy. $z/d = 0$.

modifications on the simulation results are discussed in detail in the next sections.

3.1.2.2.2 Influence of the round jet correction The influence of the round jet correction initially created by Pope for the standard k - ε model (see section 2.2.1.2) and later introduced by Wilcox for both the 1998 and the 2006 variants of his k - ω model (see section 2.2.1.7) is discussed first. Figure 3.1.10 shows in solid lines the profiles of the x -component of the flow velocity vector and of the turbulent kinetic energy given by the 1998 and the 2006 k - ω models of Wilcox as well as by the standard k - ε model with the limited version of the Pope correction described in section 2.2.1.2. Dashed lines present the profiles obtained by the same models but without the round jet correction terms (Pope vortex stretching measure χ_ω or χ_p deliberately set to zero values). The absence of the round jet correction increases the level of k and thus the prediction accuracy for all approaches tested here. The reason is in the mechanism and the aim of this correction. It was initially created in order to prevent the over prediction of

k observed in the free round jet flow simulations. The model equation terms related to the round jet correction always work towards increasing the dissipation of k . This produces rather a negative effect in the jet in crossflow case since here the level of k tends to be underestimated even by the equations not including the χ_ω - or χ_p -related terms (see figure 3.1.10(b)).

The negative influence of the round jet correction revealed here does not imply that its incorporation in the modeling equations is a wrong choice or that in the jet in crossflow case the vortex stretching effects are neglectable. More probable, additional physical effects not yet encoded into the studied models are dominant in the considered flow. These effects should be identified and a suitable model developed in order to improve the simulation quality and turbulence model universality.

3.1.2.2.3 Influence of the streamline curvature correction One of the effects that can play an important role in the considered flow configuration is streamline curvature. As discussed in ref. [46], streamline curvature can enhance both the production and the dissipation of the turbulent kinetic energy in the flow. Its effects are not taken into account by any of the models studied in the previous sections. For this reason a curvature correction to the SST model created by Hellsten [46] is tested here (see section 2.2.1.8 for description).

The results are presented in figure 3.1.11. Although, theoretically, the correction of Hellsten can act as both a source and a sink of turbulence, figure 3.1.11 shows clearly that the source effects are dominant in this case. The correction increases the level of the turbulent kinetic energy that is underestimated by the Menter SST model. This is a desirable effect, however, at the high y/d positions the model tends to “overreact” as shown in the profiles of figure 3.1.11. Whereas at the $y/d = 5$ position the SST model with the curvature correction gives more accurate predictions than the original SST formulation, at $y/d = 7$ the magnitude of k obtained with the model employing the curvature correction becomes too high. This also causes an unphysically flat velocity profile at the higher position.

For a better illustration of the driving mechanism of the curvature correction in this case, figure 3.1.12 shows the values of the function $F_4(Ri)$ modifying the dissipation term of the ω transport equation (see equation 2.2.102). $F_4(Ri) = 1$ implies that the dissipation of ω is equivalent to the values produced by the original SST model without the curvature-related modifications; $F_4(Ri) > 1$ leads to higher dissipation of ω that, consequently, increases the turbulent kinetic energy; $F_4(Ri) < 1$ leads to the increase of ω and higher dissipation of k . The impact of the curvature correction is obviously directed mostly towards increasing ω dissipation and is particularly strong at $y/d > 5$. Hence, these regions are characterized by higher levels of turbulent kinetic energy.

The observed improvement in the turbulent kinetic energy predictions indicates that the application of the curvature correction is a step in the right direction. However, it is evident that further validation and calibration of the parameters governing the behavior of the correction term is needed. For the most part the streamline curvature-related modifications proposed in the literature are validated on cases quite different from the current flow pattern

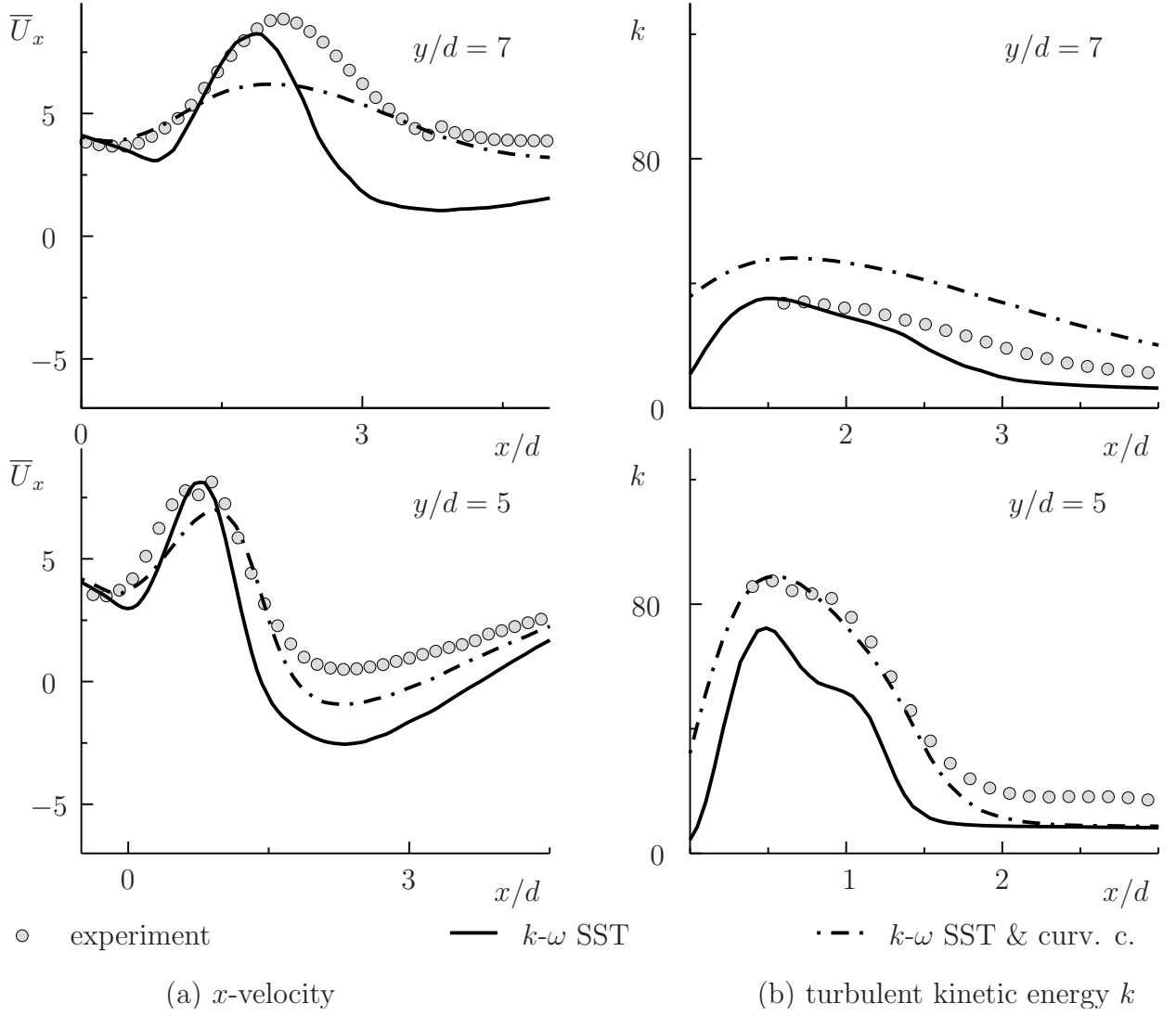


Figure 3.1.11: Influence of the streamline curvature correction on the SST model predictions. x -component of the flow velocity vector and turbulent kinetic energy. $z/d = 0$.

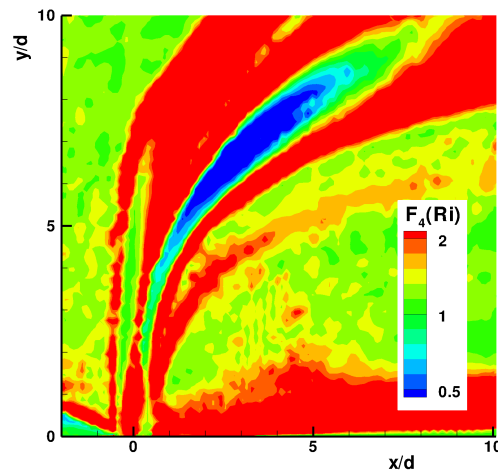


Figure 3.1.12: Curvature correction. Contours of $F_4(Ri)$, see equation 2.2.102. $z/d = 0$.

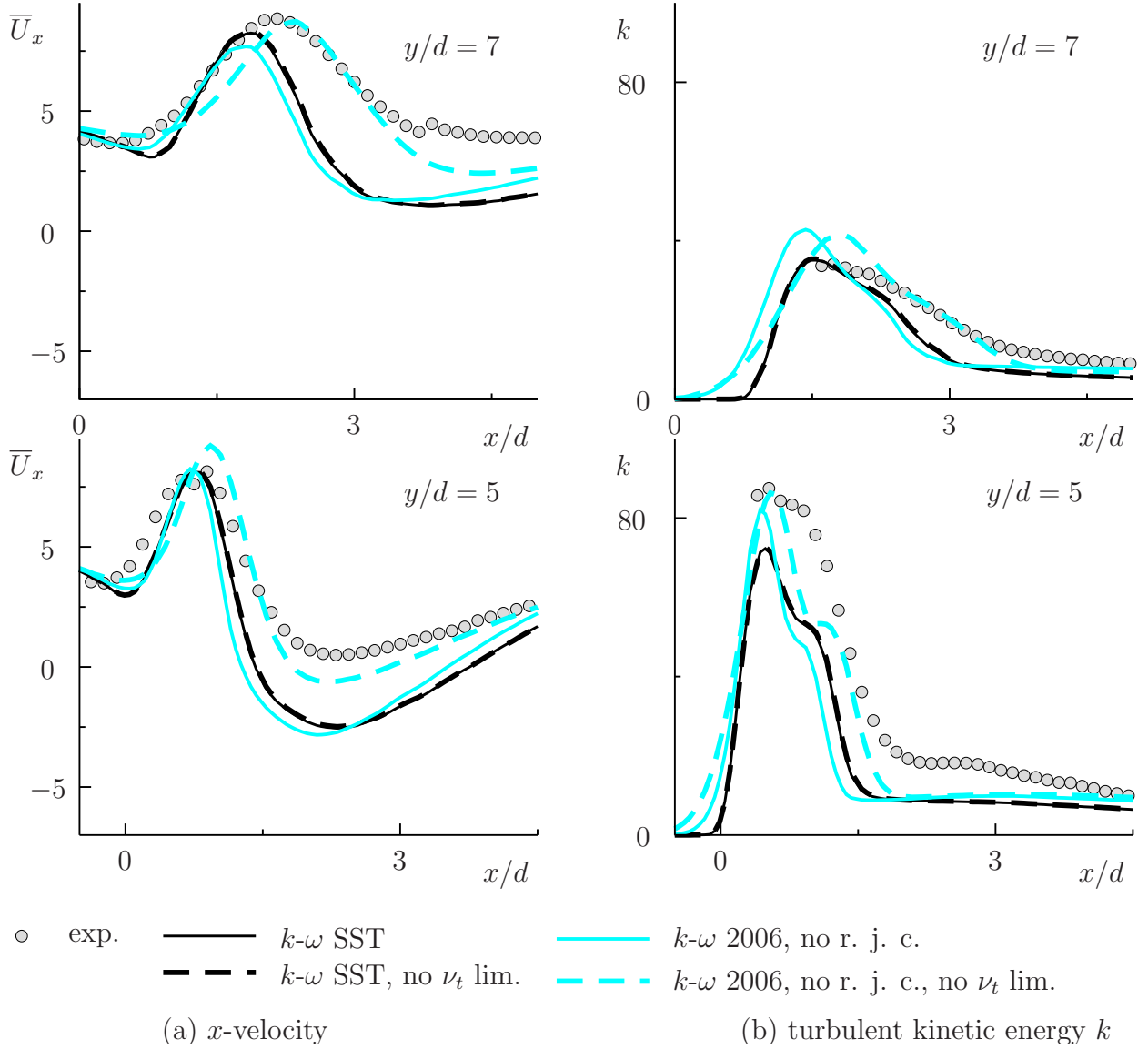


Figure 3.1.13: Influence of the shear stress viscosity limiter in the SST and the Wilcox 2006 $k\text{-}\omega$ models. x -component of the flow velocity vector and turbulent kinetic energy. $z/d = 0$.

(see ref. [46]). Obviously a more intensive testing on jets in crossflow is needed in order to improve the correction behavior for the considered flow type*.

3.1.2.2.4 Influence of the shear stress turbulent viscosity limiter After the discussion on the round jet and the streamline curvature corrections presented in two previous sections, this and the next section will examine more closely the Wilcox 2006 and the Menter SST $k\text{-}\omega$ model equations. The objective is to study the specific terms differentiating these two models from the original 1988 $k\text{-}\omega$ model of Wilcox. It should be clarified why the Menter SST model and the Wilcox 2006 model (even without the round jet correction) tend to under predict the level of turbulence in the considered case whereas the 1988 $k\text{-}\omega$ model shows a slightly opposite trend.

*Additional studies made in preparation of this dissertation have shown that a simple variation of the modeling constant C_{rc} in the equation 2.2.102 does not help to improve the results significantly; therefore, more intensive work on the form of the correction is probably needed.

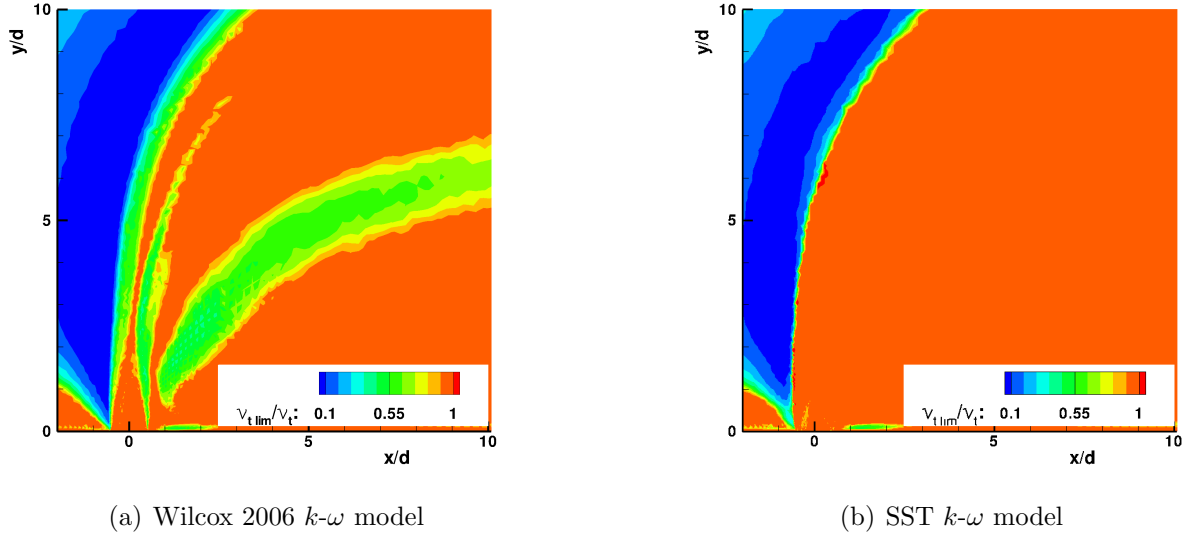


Figure 3.1.14: Turbulent viscosity shear stress limiter correction in the Wilcox 2006 and the Menter SST $k-\omega$ models. ν_{tlim}/ν_t where ν_{tlim} is calculated using equations 2.2.99 and 2.2.77 respectively and $\nu_t = k/\omega$. $z/d = 0$.

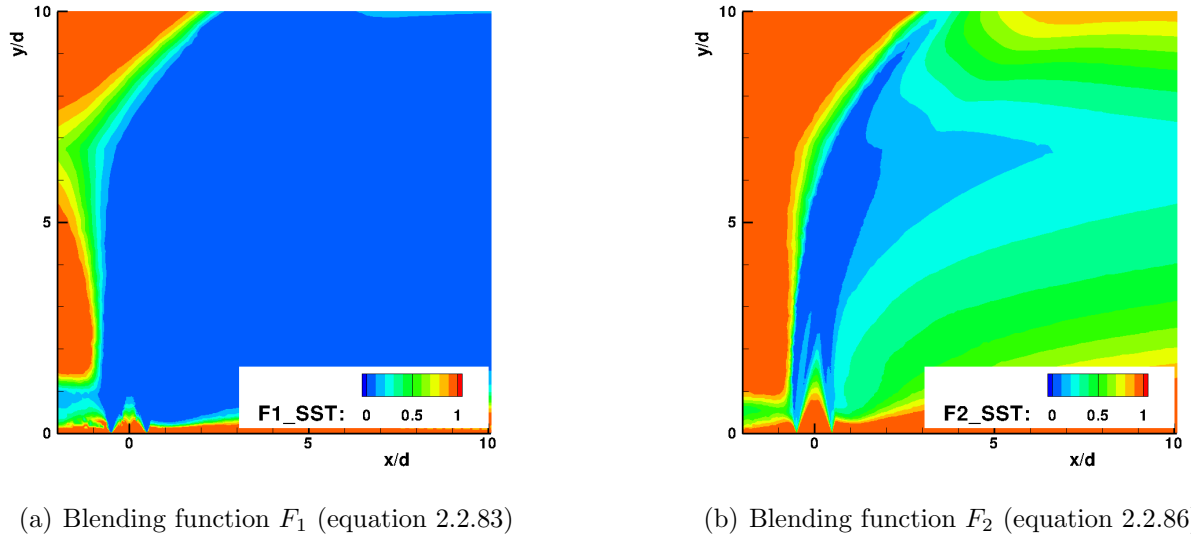


Figure 3.1.15: Blending functions F_1 and F_2 of the Menter SST $k-\omega$ model in the considered jet in crossflow test case. $z/d = 0$.

First, the influence of the shear stress transport related turbulent viscosity limiter is studied. The limiter is described in sections 2.2.1.6 and 2.2.1.7 (equations 2.2.77 and 2.2.99). Figure 3.1.13 compares the profiles of the x -component of the flow velocity vector and of the turbulent kinetic energy given by the SST model and by the Wilcox 2006 $k-\omega$ model without round jet correction (black and light-blue solid lines). The profiles given by both approaches are similar. This is not surprising since, neglecting the round jet correction employed in the Wilcox model, the other equation terms of both approaches are similar. Only the form of their model specification and the values of the modeling constants are slightly different. However, the study presented here and in the next section will reveal that these differences can become important

if the influence of individual equation terms is considered closely.

The dashed lines show the results produced by same models without the turbulent viscosity limiters (turbulent viscosity calculated simply as $\nu_t = k/\omega$). A large difference between the reaction of the SST model and the reaction the Wilcox 2006 model on the absence of the turbulent viscosity limiter can be observed. Whereas the SST model without the shear stress limiter (essentially the BSL model from the Menter's publication [83]) returns almost the same profiles as the original SST model, the predictions given by the Wilcox 2006 model without the round jet correction and without the shear stress limiter are quite different to those produced with the limiter. The level of turbulence is increased without the limiter which has a favorable effect on the modeling accuracy. The profiles returned by the Wilcox 2006 model without the round jet correction and without the viscosity limiter are quite similar to the profiles given by the 1998 k - ω model of Wilcox without the round jet correction shown in figure 3.1.10. This observation is easy to explain since the 1998 and 2006 models of Wilcox are very similar, and the presence of the shear stress viscosity limiter in the 2006 version of the model is the most important difference between them.

Although the influence of the limiter is not seen in the \bar{U}_x and k predictions given by the SST model (figure 3.1.13), the contour plot 3.1.14(b) identifies that in the jet upstream region the limiter nevertheless has influence on the turbulent viscosity produced by the SST model. In figures 3.1.14(b) and 3.1.14(a) the ratio of the limited turbulent viscosity calculated by the SST and the Wilcox 2006 models via equations 2.2.77 and 2.2.99 to the ν_t obtained as $\nu_t = k/\omega$ is presented. Consequently, $\nu_{tlim}/\nu_t < 1$ indicates the regions where the shear stress limiter works. Figure 3.1.14(a) shows, that in contrast to the SST model, the shear stress limiter of the Wilcox 2006 model impacts not only in the jet upstream region but also in the jet shear layers and in the downstream region on the lee side of the jet. This causes the limiter to have a strong influence on the mean and fluctuating velocity fields produced by the Wilcox 2006 model.

The different influence the shear stress turbulent viscosity limiter had on the Wilcox 2006 and the SST model predictions can be explained by how the limiter appears in equations 2.2.99 and 2.2.77 of the respective models. Whereas in the Wilcox 2006 model the limiter coefficient remains the same everywhere (see equation 2.2.99), equation 2.2.77 of the SST model is constructed such that the limiter influence decreases with the decreasing values of the blending function F_2 (equation 2.2.86). Figure 3.1.15(b) shows that this function reaches its maximum values of $F_2 = 1$ in the region upstream of the jet. In the same locations the influence of the limiter is seen in figure 3.1.14(b). Further downstream and especially in the jet core, F_2 decreases to values close to zero, so the limiter does not have any effect. This explains the extreme similarity of the results given by the SST model with and without limiter in figure 3.1.13. Since the turbulent viscosity limiter impacts negatively the predictions of the Wilcox 2006 model by further decreasing the turbulence, incorporating the limiter into a turbulence model via blending functions, as done in the SST model, is more favorable in this case.

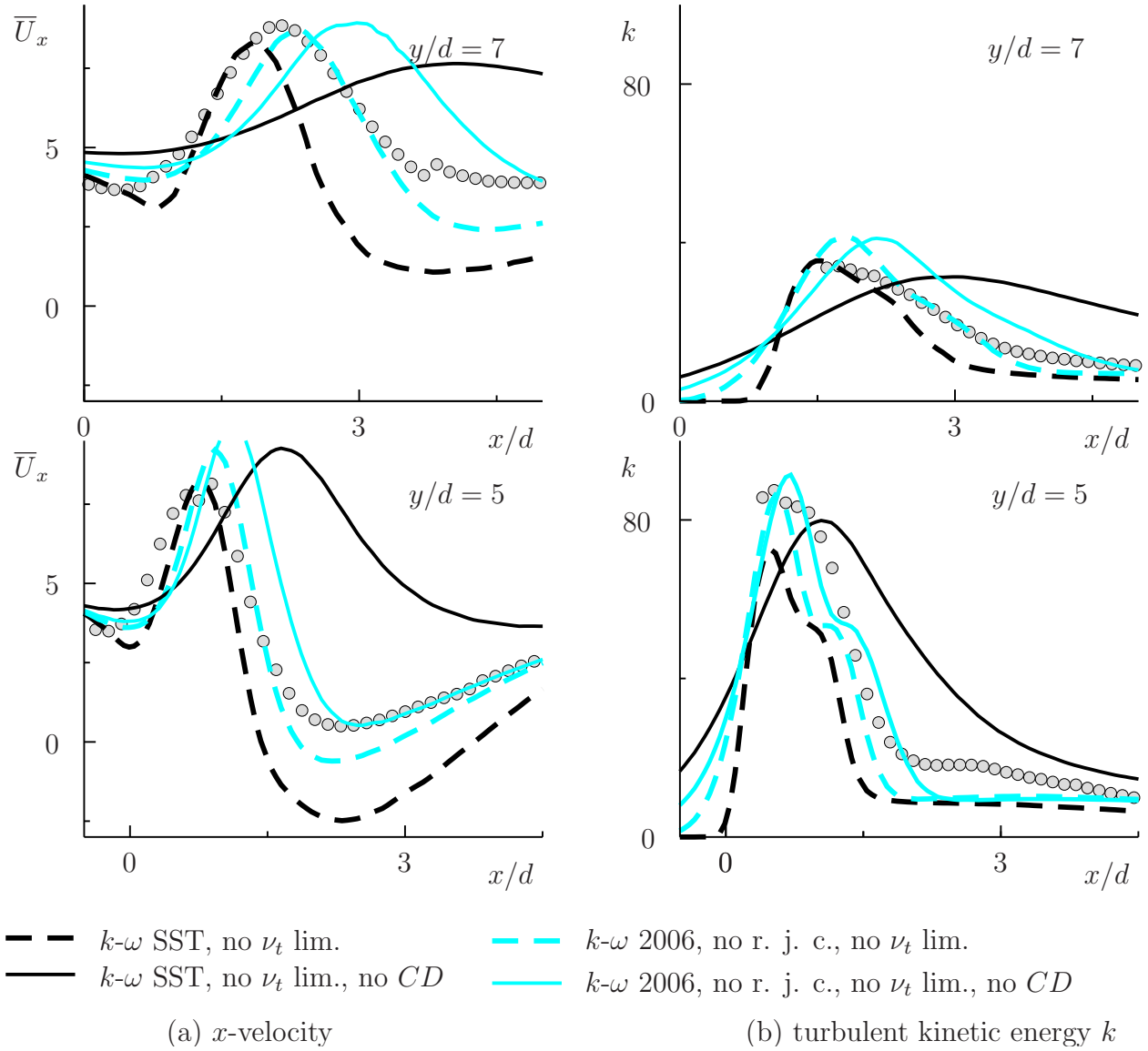


Figure 3.1.16: Influence of the of the cross-diffusion term in the SST and the Wilcox 2006 k - ω models. x -component of the flow velocity vector and turbulent kinetic energy. $z/d = 0$.

3.1.2.2.5 Influence of the cross-diffusion term Figure 3.1.13 discussed in the previous section reveals that, in contrast to the Wilcox 2006 model, the turbulence under prediction shown by the SST approach in the considered case is not even partly a consequence of the turbulent viscosity limiter. In the case of the SST model, the cross diffusion term generates a much stronger turbulence damping effect than the turbulent viscosity limiter. This is clearly seen from the plots presented in figure 3.1.16. The dashed lines represent the x -velocity and the k profiles generated in the studies of the previous section: the SST and the Wilcox 2006 models without the turbulent viscosity limiter (and without the round jet correction for the Wilcox 2006 model). The solid lines represent the profiles generated by the same equations but after the additional elimination of the cross-diffusion terms. The SST model results change drastically. Without the cross-diffusion term the equations largely over predict the level of turbulence

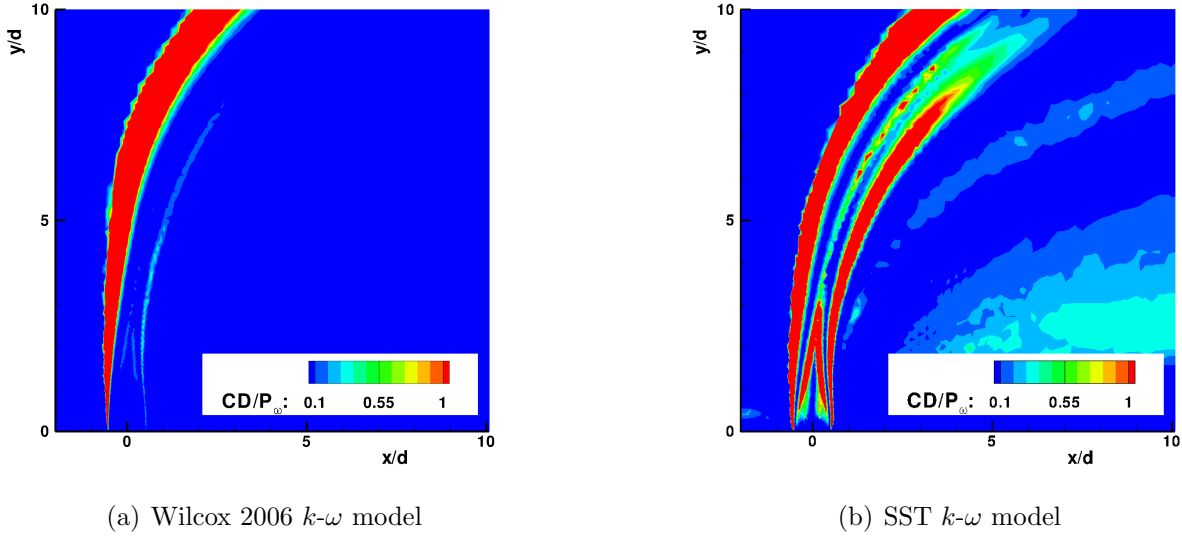


Figure 3.1.17: Cross-diffusion correction in the Wilcox 2006 and the Menter SST k - ω models. Ratio of the cross-diffusion term to the ω production term. $z/d = 0$.

and produce completely inaccurate profiles. The predictions made by the Wilcox 2006 model change as well in the absence of the cross-diffusion term but the model reaction is much weaker. However, here the overestimation of turbulence is also evident. The reason for the observed behavior of both models is in the different magnitude of the cross-diffusion coefficient and in the different modeling constants of the ω equation.

In the Wilcox 2006 approach (see section 2.2.1.7, equation 2.2.95) the coefficient of the cross-diffusion term is more than an order of magnitude lower than in the SST model (0.125 vs. 1.7). In the SST model this coefficient is scaled using the $(1 - F_1)$ blending function (see section 2.2.1.6), but figure 3.1.15(a) shows that in the considered case $F_1 = 0$ in all essential flow regions and so in these regions the cross-diffusion coefficient has its standard high value. Thus it is not surprising that the reaction of the model equations on the absence of this term is much stronger for the SST approach.

The difference between the impact of the cross-diffusion term in the Wilcox 2006 k - ω model and the SST model is additionally illustrated in the contour plots presented in figure 3.1.17. It shows the ratio of the cross-diffusion term to the ω production in equations 2.2.76 and 2.2.95. For the Wilcox 2006 k - ω model the values of the cross-diffusion term are comparable to the ω production values only in the narrow region of the upstream shear-layer. In the case of the SST model the impact of the cross-diffusion term can be observed in the full jet body.

It should be furthermore taken into account that the modeling constants of the ω production and dissipation terms in both studied models are different. As discussed in section 2.2.1.1, the difference between the dissipation and the production constants of the dissipation equation has deceptive influence on the predicted spreading rates of shear flows. The SST model employs in the outer region the constants of the standard k - ε model $C_{\varepsilon 1} = 1.44$ and $C_{\varepsilon 2} = 1.92$, which leads to $\gamma_2 = 0.44$ and $\beta_{\omega 2} = 0.0828$ after rewriting the ε -equation in SST k - ω terms. Similarly, reformulating the ω equation of the Wilcox 2006 model in k - ε fashion will result in a constant

set of $C_{\varepsilon 1} = 1.52$ and $C_{\varepsilon 2} = 1.78$. The difference between the dissipation of dissipation and the production of dissipation constants is much smaller in this case than in the SST model; consequently, the turbulence level predicted by the Wilcox 2006 model equations is generally lower (see discussion in section 2.2.1.1). That is the reason why even with the very small cross-diffusion coefficient or in its total absence the Wilcox 2006 model does not overestimate the turbulence drastically.

The above discussion also elucidates the mechanisms responsible for creating the significant differences observed between the standard $k-\varepsilon$ and the Wilcox 1988 $k-\omega$ profiles shown in section 3.1.2.1. In the standard $k-\varepsilon$ model simulations the damping effect of the cross-diffusion is present in the full flow field since the cross-diffusion is naturally present in the ε equation (see discussion in sections 2.2.1.5, 2.2.1.6). Therefore the turbulence damping effect is even stronger than in the SST model where it is partly weakened by the blending functions. In contrast, the Wilcox 1988 $k-\omega$ model does not contain the cross-diffusion term at all. Thus the level of turbulence generated by this model is much higher. Moreover, its modeling constants, similar to those employed in the Wilcox 2006 model, prevent the 1988 Wilcox model from a strong turbulence over prediction. This results in quite accurate profiles shown by the 1988 Wilcox model in section 3.1.2.1.

The present discussion is not meant to imply that using models without a cross-diffusion term is the best choice for jet in crossflow simulations. Many results available in the literature [83, 84, 128] show the positive effect of the cross-diffusion term for the modeling accuracy in a large variety of cases. The elimination of this term or its simple ad hoc adjustment just based on the present case in order to compensate for the under predicted turbulence levels would reduce the universality of the model and probably cause unsatisfactory results for other applications. A more rigorous approach would be the incorporation of additional corrections reacting to jet in crossflow specific flow physics such as streamline curvature correction tested in section 3.1.2.2.3.

3.1.2.2.6 Influence of the low-Re damping functions The influence of near-wall modeling in the $k-\varepsilon$ case is the final topic investigated in this section. The justification for this study is that the computational grid was made with the aim to resolve the boundary layer, i.e. $y^+ < 5$ was assured in the important regions. Such a grid is well suited for the $k-\omega$ calculations, but for the $k-\varepsilon$ model with the wall functions as employed for generation of the results presented in section 3.1.2.1, it may be an additional source of uncertainty. The models with near-wall viscous damping, theoretically, should be better suited for this grid (see discussion in section 2.2.1.3). However, figure 3.1.18 shows that the absence of the viscous damping functions is not the reason why the standard $k-\varepsilon$ model produces results of a poor accuracy. It is seen that the low-Re AKN $k-\varepsilon$ model, discussed in section 2.2.1.3, does not give more accurate results. The additional viscous damping also does not alter the significantly more accurate results of the Wilcox 1988 $k-\omega$ model as the comparison with the low-Re $k-\omega$ model, described in section 2.2.1.5, reveals. Thus, acknowledging the importance of near wall resolution, the mean field

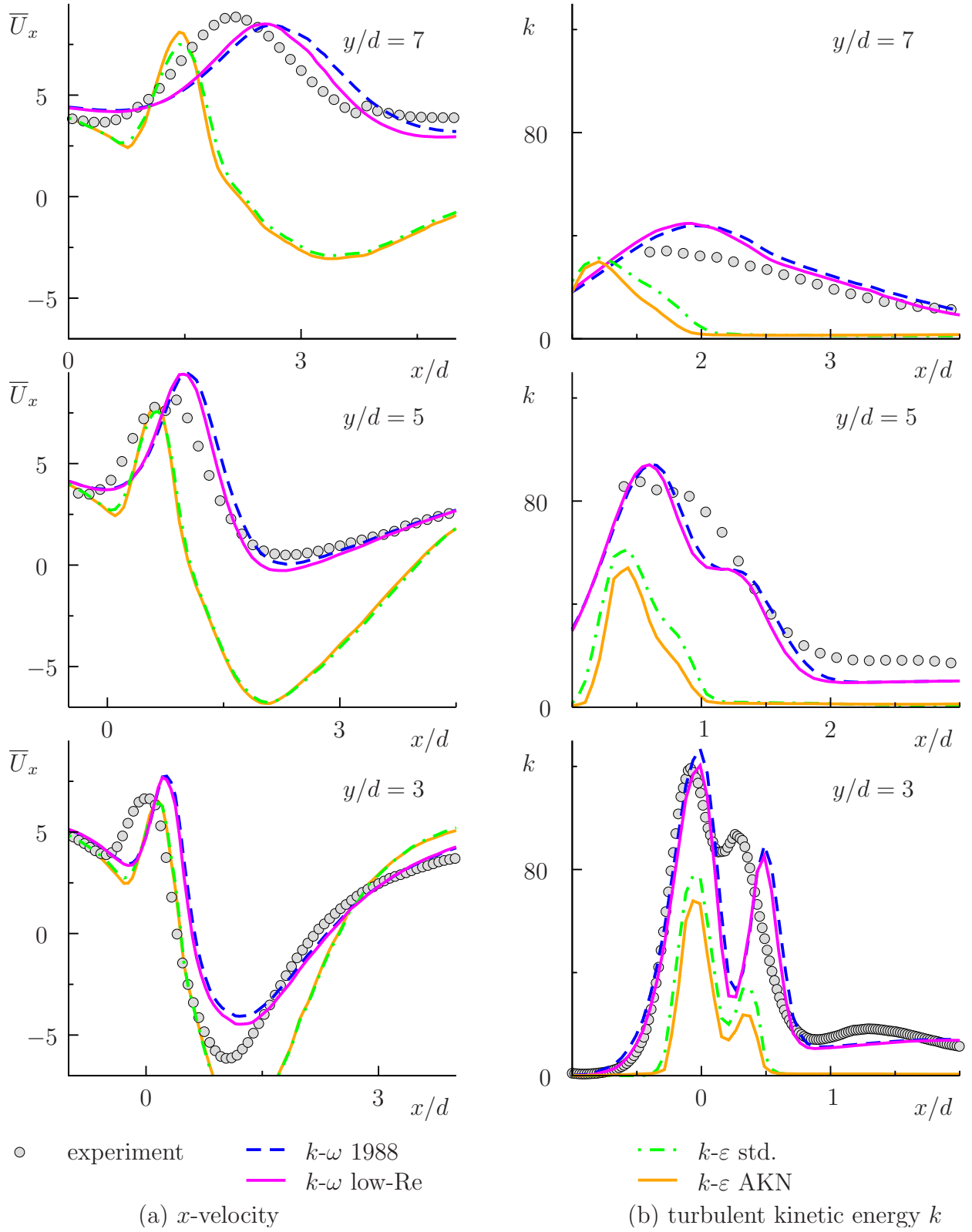


Figure 3.1.18: Study on the wall damping function influence. x -component of the flow velocity vector and turbulent kinetic energy. $z/d = 0$.

turbulence modeling plays in this case, apparently, a more important role.

3.1.2.3 Evaluation of LES data

The aim of this section is to obtain additional knowledge about the actual values of the turbulent viscosity in the considered configuration. As a further matter, the budget terms of the k transport equation should be evaluated and compared with the RANS modeling results. Turbulence closures based on the turbulent viscosity hypothesis rely on several assumptions and simplifications, as discussed in the theory section 2.2. The deviation of these simplifications from the physical reality can cause inaccuracies. A careful validation of single terms in the model equations against their actual values in a variety of test cases can help to define directions for improvement of the modeling. Unfortunately neither the turbulent viscosity nor the budget terms of the modeling equations can be easily evaluated from experimental data because three-dimensional mean and fluctuating velocity fields are needed. In the experiments of refs. [78, 13, 42] only two velocity components (x and y or x and z) were measured in the respective planes; hence, derivatives in the third direction are difficult to determine. Moreover, the evaluation of the first and especially of the second derivatives of the measured variables in the post-processing often lead to strong spurious oscillations in the obtained data fields.

Since a DNS of the considered test case is also not feasible because of the high Reynolds numbers, the LES data shown in the previous sections will be used for the evaluation. Although the agreement of the LES results with the experimental data is not ideal (the main problem is the overestimation of the y -direction velocity), the overall accuracy of the LES is much better than of the Wilcox 1988 k - ω model, which shows the best results of all RANS models used in this work. LES gives a more realistic representation of the trends in the behavior of the turbulent velocity field. Thus, the statistical data gained from the LES post-processing can help to obtain additional information needed to elucidate the weaknesses of the considered RANS modeling approaches.

3.1.2.3.1 Turbulent viscosity

3.1.2.3.1.1 Evaluation from the time-averaged LES data fields First, the turbulent viscosity ν_t field is analyzed based on LES data. The primary objective of the analysis is to provide the ν_t values that can be used to validate RANS models. In the evaluations of the experimental data for quasi 2D flows, for instance, channel flow or the axisymmetric round jet (see for example ref. [16]), the turbulent viscosity is usually obtained by employing the Boussinesq approximation (equation 2.2.3) for the Reynolds stress component assumed to be the most important for momentum modeling accuracy (for example $\overline{u'_x u'_y}$). In a 3D flow, such as the one considered here, determination of the most important Reynolds stress component is a rather difficult task, and this is illustrated in figure 3.1.19 which compares the LES data for three different components of the Reynolds stress tensor for jet in crossflow*. Only near to the jet symmetry plane ($z/d = 0.1$, figure 3.1.19(a)) is the $\overline{u'_x u'_y}$ stress clearly larger than

*The diagonal components of the Reynolds stress tensor are not included for the sake of the plot clarity.

the $\overline{u'_x u'_z}$ and $\overline{u'_y u'_z}$ stresses and can be assumed to be a “safe” choice for the evaluation of the characteristic turbulent viscosities. With the increasing distance from the jet symmetry plane ($z/d = 1.0$, figure 3.1.19(b)), the relative magnitude of the $\overline{u'_x u'_z}$ and especially of the $\overline{u'_y u'_z}$ components grows significantly. In those locations, the ν_t estimate based only on the $\overline{u'_x u'_y}$ stress is not as easily justified.

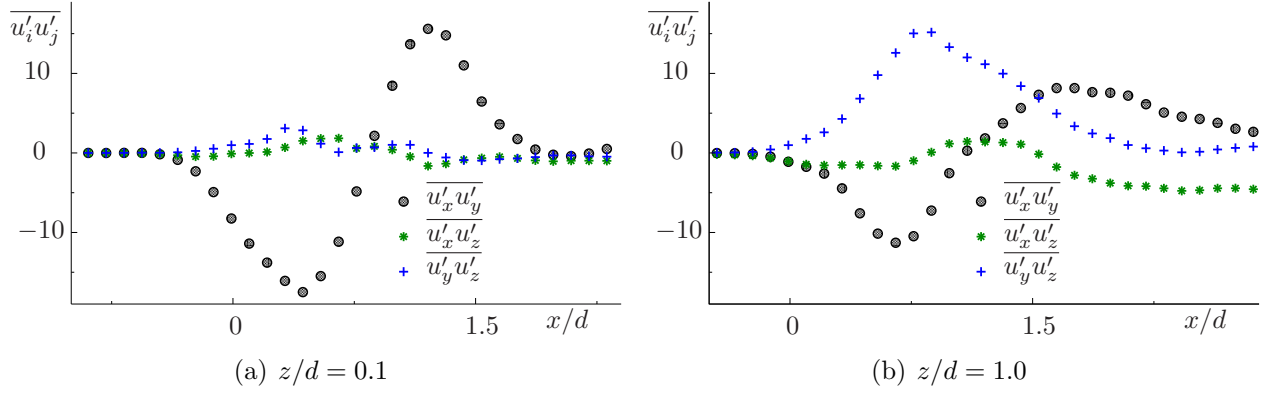


Figure 3.1.19: Different components of the Reynolds stress tensor $\overline{u'_i u'_j}$ in dependence on the z/d distance from the jet symmetry plane. $y/d = 5$.

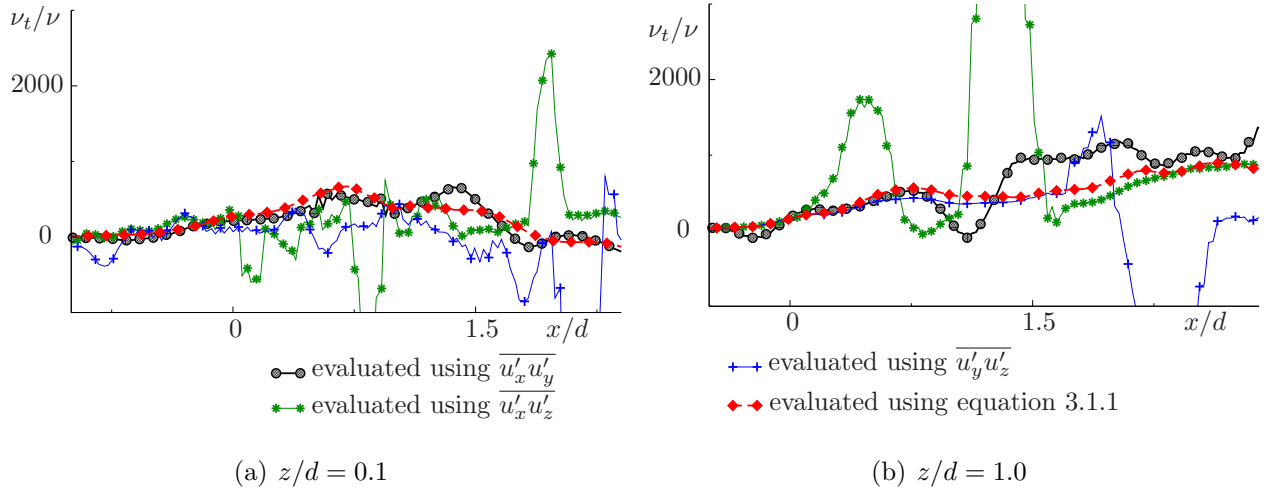


Figure 3.1.20: Dimensionless turbulent viscosity ν_t/ν evaluated from LES data using different Reynolds stresses and via least-square fit (equation 3.1.1). Dependence on the z/d distance from the jet symmetry plane. $y/d = 5$.

Figure 3.1.20 compares the turbulent viscosities obtained using the anisotropic components of the Reynolds stress and the strain-rate tensors using equation 2.2.3. Here several important observations can be made. First, ν_t varies depending on the employed Reynolds stress. Second, the ν_t profiles obtained from the larger components of the Reynolds stress tensor (such as $\overline{u'_x u'_y}$) are naturally much less serrated than the profiles obtained from the smaller components (such as $\overline{u'_x u'_z}$). Third, the ν_t profiles obtained from the larger components of the Reynolds stress tensor are much closer to each other than to the profiles given by the smaller components. This is shown in figure 3.1.20(b) where the ν_t profiles given at $z/d = 1.0$ by the $\overline{u'_x u'_y}$ and

the $\overline{u'_y u'_z}$ stress components are quite similar. As discussed previously, at this location both the $\overline{u'_x u'_y}$ and the $\overline{u'_y u'_z}$ stresses play much more important role than $\overline{u'_x u'_z}$. It can be seen here particularly clearly that the disparities between different ν_t values start to grow at the locations at which the respective Reynolds stresses become smaller. The last observation is a positive indicator for the RANS turbulent viscosity modeling. It implies that using the same ν_t in the modeling of the most important asymmetric components of the Reynolds stress tensor will not introduce large errors into the simulation. However, for the evaluation of the ν_t from LES, DNS, or experimental data it presents the challenge of an a-priori identification of the dominant Reynolds stress at every location. Otherwise, the ν_t obtained in the data post-processing cannot be considered suitable for the RANS model evaluation. For example at $z/d = 1.0$, if the ν_t values obtained from LES using the $\overline{u'_x u'_z}$ stress component would be applied to model the other Reynolds stresses via equation 2.2.3, than this would lead to a clear overprediction of $\overline{u'_x u'_y}$ and $\overline{u'_y u'_z}$. Therefore, the comparison of such ν_t with the turbulent viscosity given by the RANS model would not yield a viable quality metric of the RANS model.

To overcome this problem, it is proposed here to evaluate the turbulent viscosity from the overdetermined system of the Boussinesq approximation equations 2.2.3 using a least-square fit over all resolved Reynolds stresses

$$\nu_t = \frac{\left(-\overline{u'_i u'_j} + \frac{2}{3}k\delta_{ij}\right) \cdot \left(\frac{\partial \overline{U_i}}{\partial x_j} + \frac{\partial \overline{U_j}}{\partial x_i}\right)}{\left(\frac{\partial \overline{U_k}}{\partial x_l} + \frac{\partial \overline{U_l}}{\partial x_k}\right) \cdot \left(\frac{\partial \overline{U_k}}{\partial x_l} + \frac{\partial \overline{U_l}}{\partial x_k}\right)}, \quad (3.1.1)$$

with the summation over the repeating indices i, j, k , and $l = 1-3$, and the operator $\overline{(\)}$ denotes the variables obtained from the resolved LES data fields after the time-averaging. This method aims to minimize the error in the ν_t solution of the overdetermined system of equations 2.2.3. The turbulent viscosity obtained by this method represents an optimal value of the assumed isotropic modeled ν_t thereby providing the best possible closure of the Reynolds stress tensor.

Figure 3.1.20 compares the turbulent viscosity profiles given by equation 3.1.1 with the profiles computed earlier using several individual stress components. The profiles obtained using the least-square approximation are close to the profiles given by the dominant Reynolds stresses in the regions where those can be clearly identified. This makes ν_t given by equation 3.1.1 a “safe” choice for the estimation of the effective turbulent viscosity in a flow, particularly in the cases when the relative importance of different Reynolds stresses varies strongly depending on the location.

In the following sections the profiles of the turbulent viscosity given by equation 3.1.1 on the jet symmetry plane $z/d = 0$ at the locations $y/d = 5$ and $y/d = 7$ will be used for the comparison with the RANS results. These profiles are shown in figure 3.1.21. For the further presentation and studies of the present work, these profiles are slightly smoothed as shown in figure 3.1.21. The smoothing is made by averaging over the short coordinate distances corresponding to about 1/20 of the characteristic integral length. This is done for the sake of figure clarity, and, as it will be seen below in the context of comparison with the RANS modeling

results, does not influence the validity of the conclusions. The same smoothing procedure is also applied to LES-based evaluation of other variables presented below in this dissertation (budget terms of the turbulent kinetic energy transport equation, turbulent scalar diffusivity, etc.).

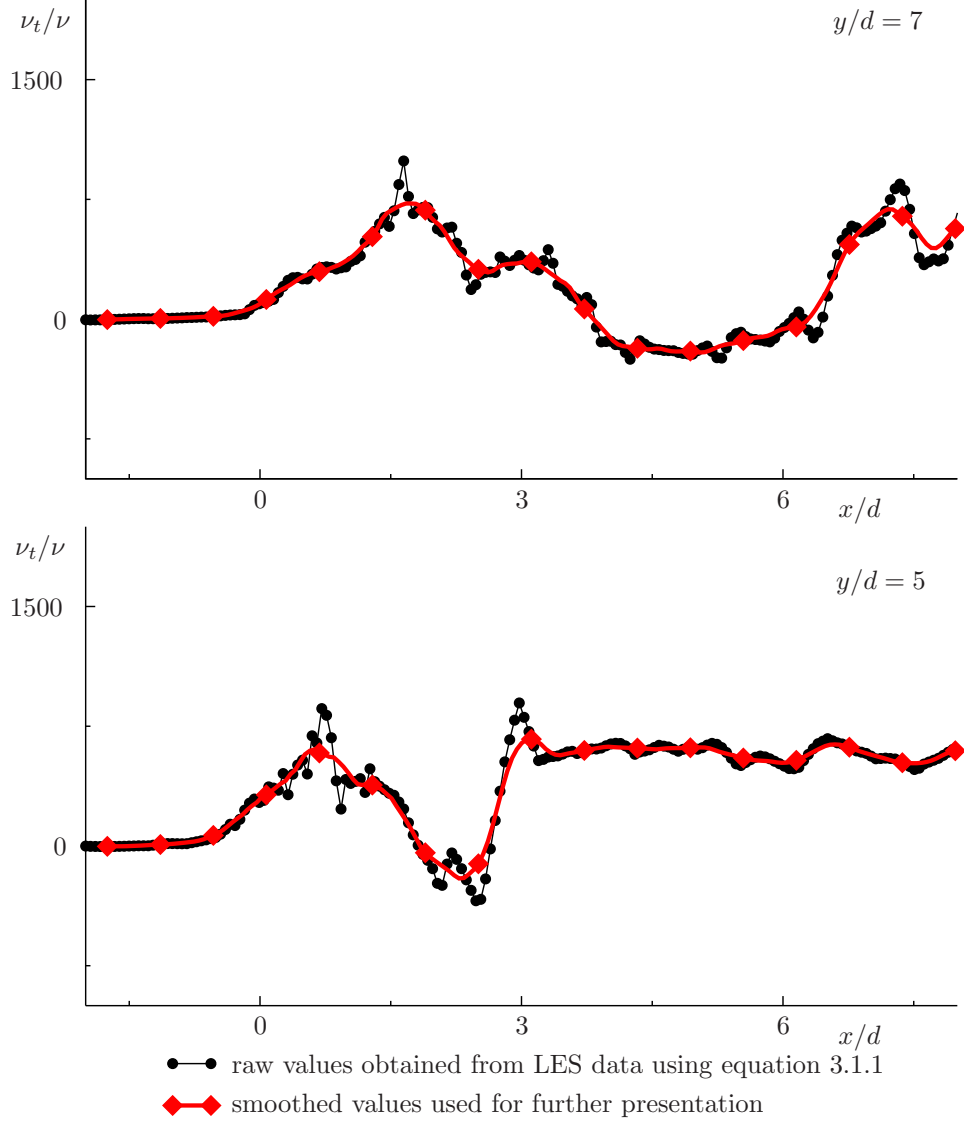


Figure 3.1.21: Dimensionless turbulent viscosity ν_t/ν profiles, raw and smoothed, evaluated from LES data using equation 3.1.1. $z/d = 0$.

3.1.2.3.1.2 Comparison with the RANS modeling results The profiles recovered from LES data are compared in figure 3.1.22 with the results of RANS simulations using the Wilcox 1988 $k-\omega$ model, the SST model of Menter, and the SST model additionally employing the curvature correction of Hellsten. The performance of these models is discussed in section 3.1.2.2. As an immediate observation, around the jet core location the magnitude of the turbulent viscosity given by equation 3.1.1 for LES data is comparable to the turbulent viscosity levels resulting from RANS modeling. The peak of the evaluated jet viscosity lies between the value given by the SST model and the value given by the Wilcox 1988 $k-\omega$ model. The modeled ν_t resulting

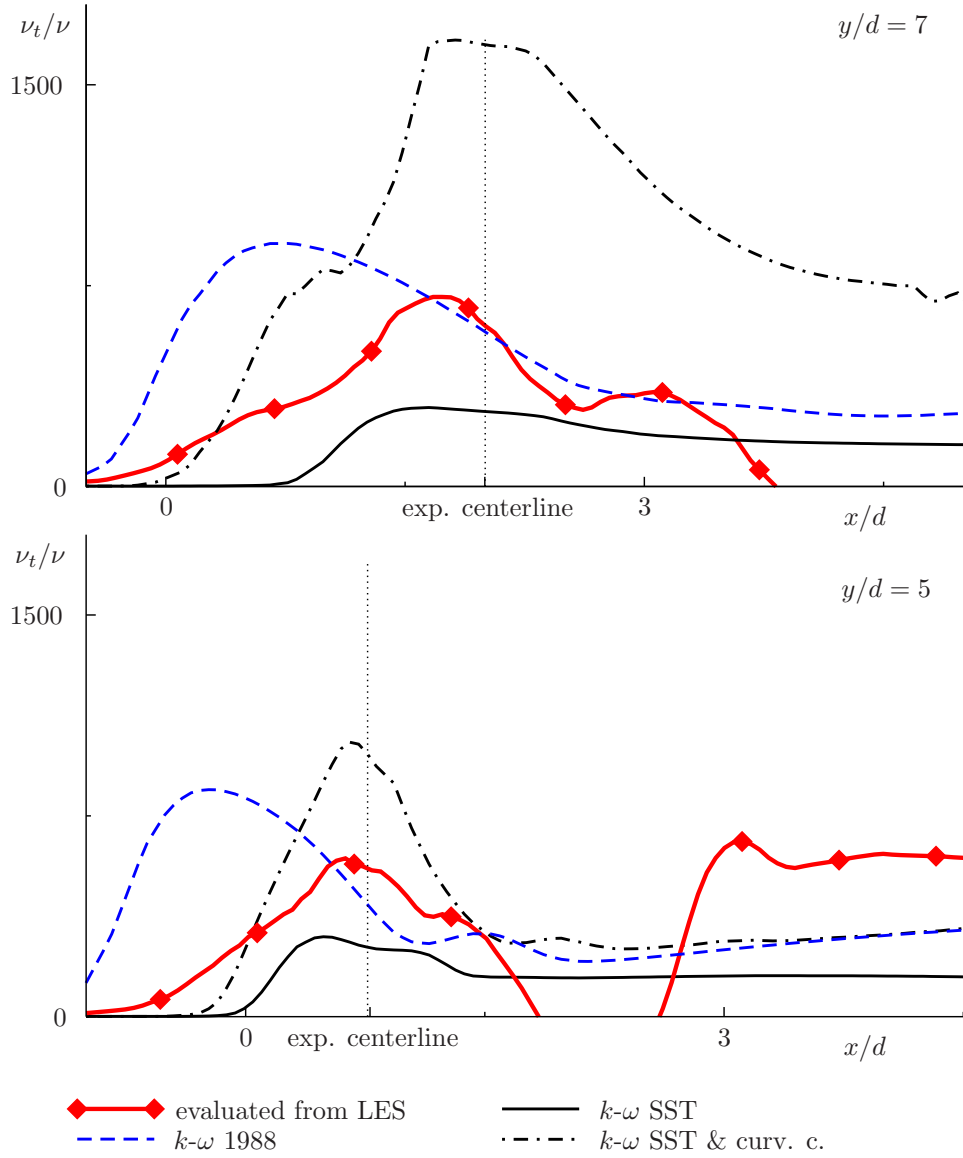


Figure 3.1.22: Dimensionless turbulent viscosity ν_t/ν evaluated from LES data and resulting from RANS modeling. $z/d = 0$.

from the SST model with the curvature correction are much higher. This agrees with the results shown in section 3.1.2.2 where it was demonstrated that the level of turbulence is obviously over predicted by the SST model with the curvature correction, under predicted by the standard SST model, and actually at the higher y/d locations is under the level given by the Wilcox 1988 model.

It should be noted that whereas the maxima of the turbulent viscosity evaluated from the LES data and given by both SST-type models are located on the experimental jet centerline, the Wilcox 1988 $k-\omega$ model produces the maximal values of the the turbulent viscosity in the jet upstream region. This excessive level of the turbulent momentum diffusivity on the upstream side of the jet is responsible for the shift of the jet centerline downstream of its actual location observed in figure 3.1.6. The high turbulent viscosity values given by the Wilcox 1988 $k-\omega$ model in the outer shear-layer regions can be explained by the absence of the cross-diffusion

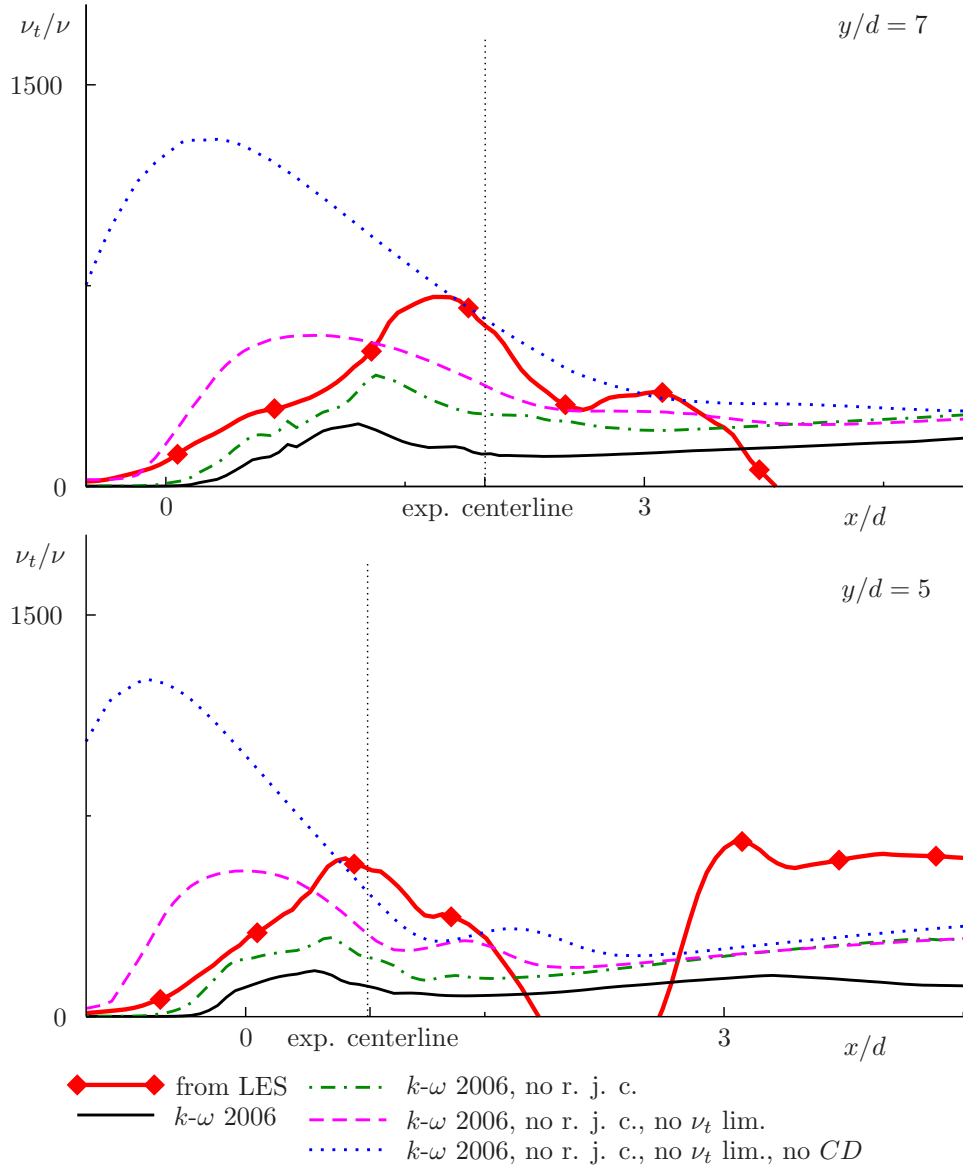


Figure 3.1.23: Dependence of the turbulent viscosity on different terms of the 2006 Wilcox $k-\omega$ model. Comparison with the values ν_t/ν evaluated from LES data. $z/d = 0$.

term and of the turbulent viscosity limiter discussed in sections 3.1.2.2.5 and 3.1.2.2.4. This is illustrated in figure 3.1.23 where the influence of different modeling equation terms and corrections discussed in sections 3.1.2.2.2-3.1.2.2.5 on the produced turbulent viscosity values is shown for the example of the Wilcox 2006 model. In the original model the level of the turbulent viscosity is strongly underestimated but its peak is located near to the position predicted by LES. The absence of the round jet correction just slightly increases the general level of the turbulent viscosity. In contrast, the absence of the shear stress turbulent viscosity limiter and, especially, of the cross-diffusion term leads to excessively large values of ν_t in the upstream shear-layer region. This is not surprising since, as shown in sections 3.1.2.2.5 and 3.1.2.2.4, both corrections have their maximal impact in this region.

Figures 3.1.24 and 3.1.25 additionally present 2D plots of ν_t non-dimensionalized by the molecular viscosity values in the planes $z/d = 0$ and $y/d = 7$. The same conclusions as in the

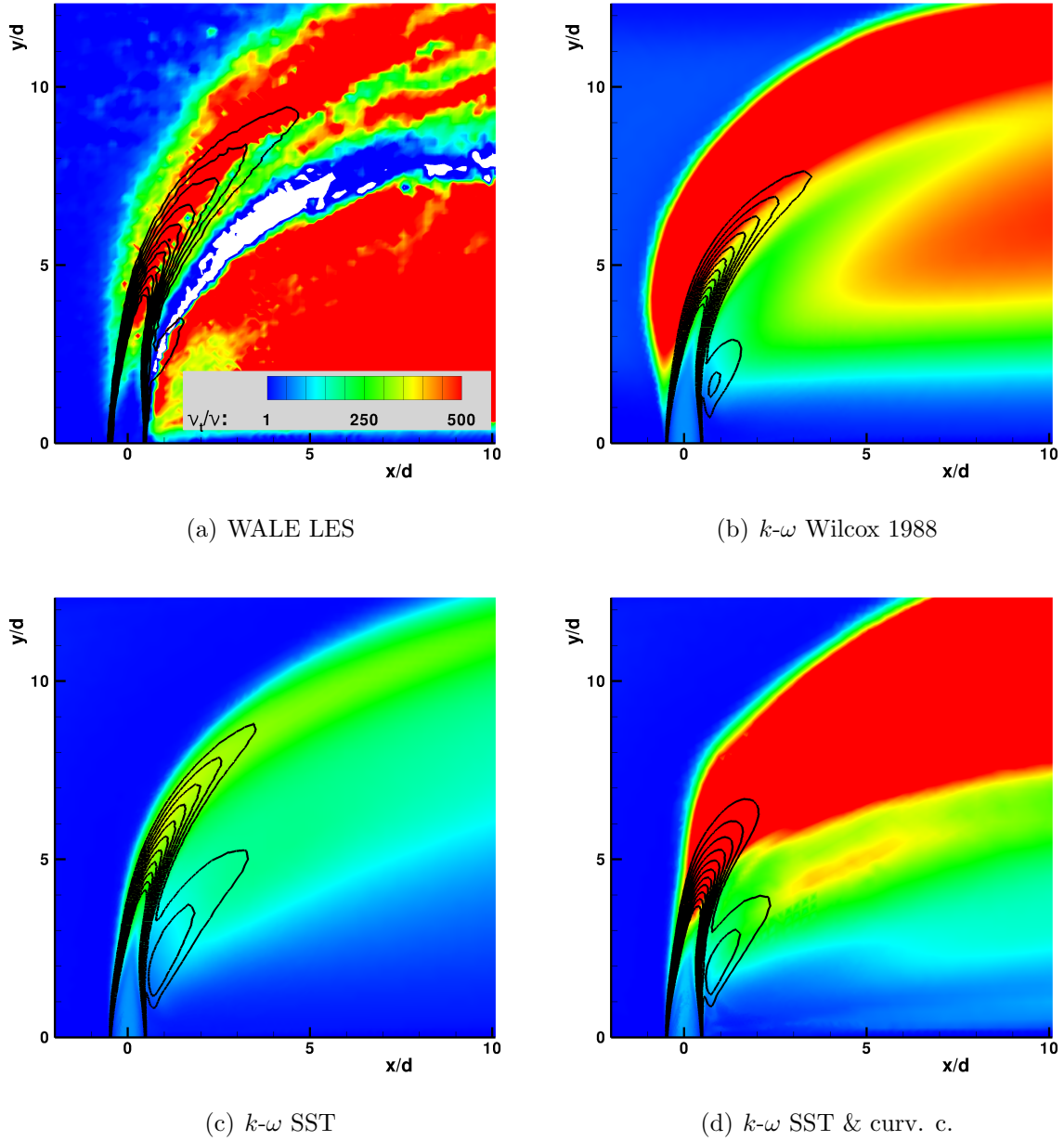


Figure 3.1.24: Dimensionless turbulent viscosity ν_t/ν evaluated from LES data and resulting from RANS modeling in $z/d = 0$ plane. The regions of $\nu_t/\nu < -100$ are blanked.

last paragraphs can be reached from these figures. The level of ν_t is given correctly by the Wilcox 1988 model, but the peaks are incorrectly shifted towards the outer shear layer. LES shows much higher levels of the turbulent viscosity in the downstream locations than all RANS models. Comparisons of the fluctuating velocity field in this region made in section 3.1.2.1 indicate that the higher values given by LES are appropriate whereas the RANS models gave too low of turbulence levels.

A significant difference between the profiles given by the RANS models and evaluated from LES is that the turbulent viscosities found from LES post-processing take negative values on the downstream side of the jet (see figures 3.1.22, 3.1.24(a), and 3.1.25(a)); however, in RANS the turbulent viscosity is always positive by definition. The appearance of regions of

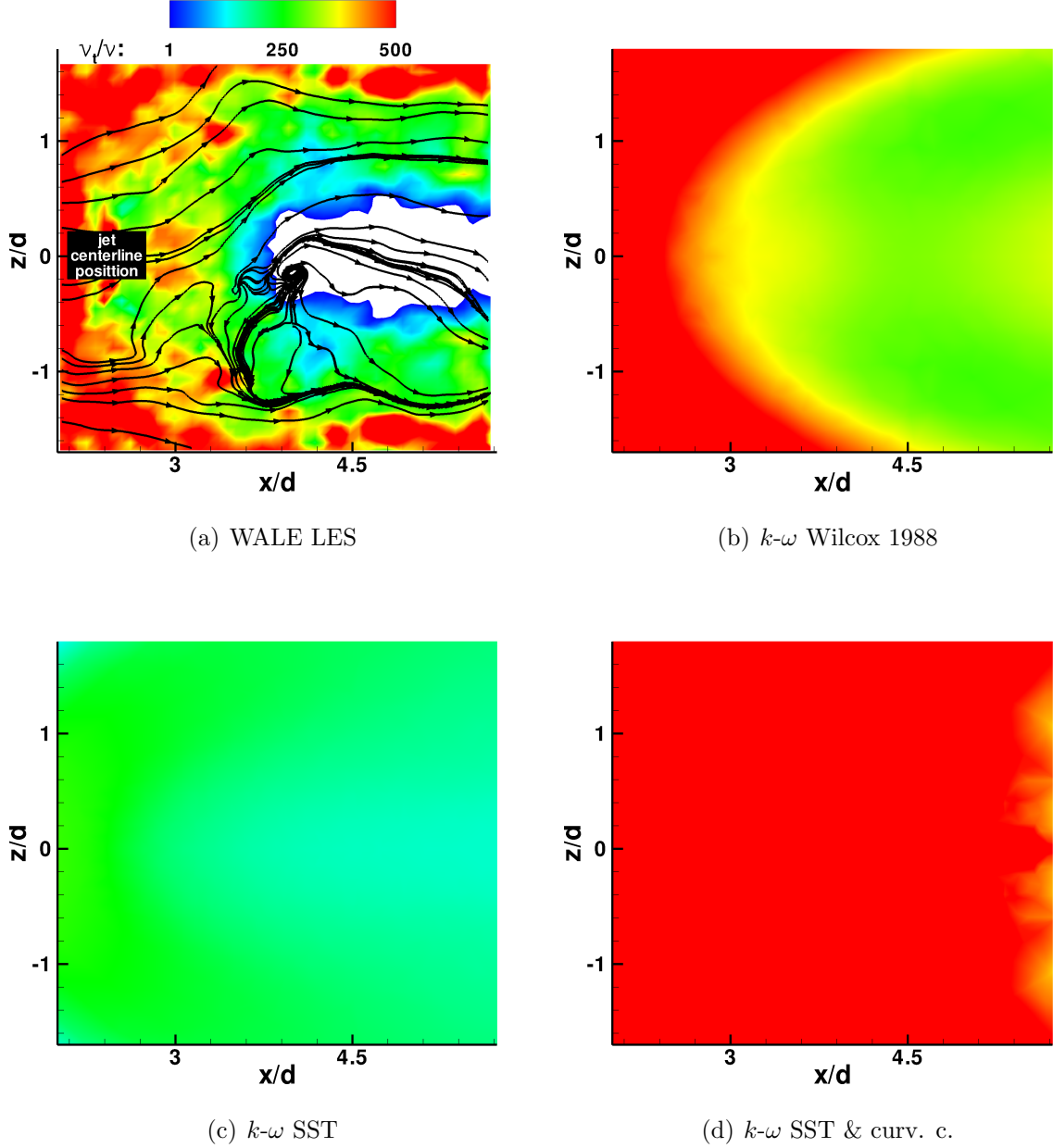


Figure 3.1.25: Dimensionless turbulent viscosity ν_t/ν and xz - streamlines evaluated from LES data and resulting from RANS modeling in $y/d = 7$ plane. The regions of the negative ν_t/ν are blanked.

negative turbulent viscosity can be caused by the complex structure of the velocity and the pressure fields in this flow pattern. First, the negative turbulent viscosity appears in the region where the xy -streamline curvature becomes especially strong. It is a well-known observation that the streamline curvature can lead to the negative turbulent viscosities evaluated from $\overline{u'_x u'_y}$ Reynolds stress (see ref. [29] for the explanation of the reasons). Second, the region of the negative turbulent viscosity corresponds most likely with the vortex roll-up region of the counter-rotating vortex pair (see figure 1.2.1). This is indicated in figure 3.1.25(a), where the black lines visualize the instantaneous xz -streamlines and the blanked zones indicate the area of the negative turbulent viscosity. It is seen that the location of this area correlates with

the appearance of a strong vortex that is probably a part of the counter-rotating vortex pair temporally evolving on the downstream side of the jet. The relative impact of both the xy -streamline curvature and the vortex roll-up of the counter-rotating vortex pair on the sign of the turbulent viscosity needs to be clarified in future investigations.

3.1.2.3.2 Turbulent kinetic energy budget

3.1.2.3.2.1 Evaluation from the time-averaged LES data As a supplement to the discussion on turbulent viscosity, the budget terms of the turbulent kinetic energy transport equation obtained from LES are presented in figure 3.1.26. In this plot all results are non-dimensionalized using the jet diameter d and the jet mean velocity U_{jet} . The time evolution term of equation 2.2.11 is not relevant here since the statistical steadiness of the flow is assumed. The convection term being transferred to the right-hand side of equation 2.2.11 becomes $-\overline{U}_i \frac{\partial k}{\partial x_i}$. This term appears in the RANS models in the same form as in the exact k -equation and presents rather a minor interest for the RANS model evaluation.

The production term shown in figure 3.1.26 is defined by equation 2.2.12 and can be easily computed in the post-processing of the resolved velocity field from LES. The production profile evaluated from LES data is characterized by two peaks - a larger one on the upstream side of the jet and a smaller one on the lee side. These peaks are corresponding to the shear layer regions. At the location $y/d = 7$ the peak on the lee side has almost vanished.

The turbulent diffusion \mathcal{D}_t presented in figure 3.1.26 is evaluated from LES using the exact three-point correlation term $-\frac{1}{2} \frac{\partial \overline{u'_i u'_i u'_l}}{\partial x_l}$ of equation 2.2.11. Figure 3.1.26 reveals that although the magnitude of the turbulent diffusion term in the considered case is generally lower than the magnitude of the turbulent production, the impact of the diffusion process in the creation and destruction of energy can become significant particularly at higher y/d locations. Consequently, questions regarding the accuracy of the turbulent diffusion modeling in RANS cannot be neglected.

Figure 3.1.26 similarly presents the pressure diffusion term $\mathcal{D}_p = -\frac{1}{\rho} \frac{\partial \overline{p' u'_l}}{\partial x_l}$ of equation 2.2.11. A typical assumption widely used in the RANS modeling is that the pressure-diffusion term is small and can be grouped with the turbulent transport term \mathcal{D}_t (see equation 2.2.13). This assumption is essentially based on the DNS data for simple channel flows [128, 29]. The current evaluation reveals that the impact of the pressure diffusion term, although smaller than the impact of other components of the turbulent kinetic energy balance equation (equation 2.2.11), is certainly not neglectable.

The last term presented in figure 3.1.26 is the dissipation of the turbulent kinetic energy $-\varepsilon$. It should be noted here that this term is not directly obtained from LES using the formula 2.2.15, but determined indirectly from the imbalance of other terms of the exact k -equation. This method allows to omit the separate evaluation of the viscous and the subgrid scale dissipation, which is needed for the estimation of $-\varepsilon$ from the LES data [20]. In the same manner the dissipation term is also often evaluated in experiments [95]. The profile of the turbulent dissipation, similar to the production profile, shows two peaks corresponding to the upstream

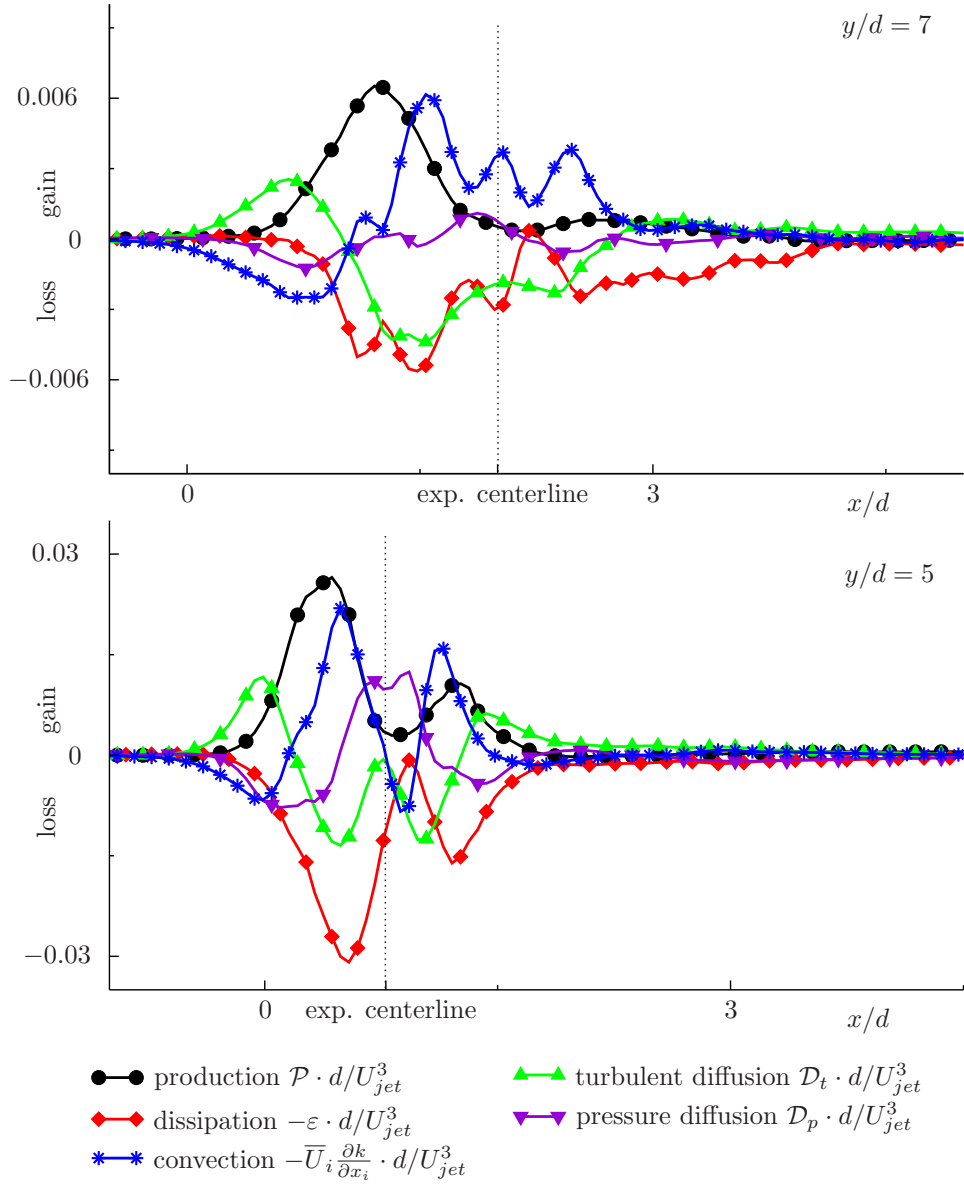


Figure 3.1.26: Main budget terms of the turbulent kinetic energy balance equation evaluated from LES. All terms are non-dimensionalized using the jet diameter d and the mean velocity at the jet inlet U_{jet} . $z/d = 0$.

and the lee side shear layers. The peak on the lee side is more than twice lower than the peak on the upstream side and becomes flat at the higher location $y/d = 7$.

It can be generally observed that the absolute magnitude of all budget terms drops rapidly with the increasing y/d position. The level of the local maxima of the budget terms at $y/d = 7$ is about five times lower than at $y/d = 5$.

3.1.2.3.2.2 Comparison with the RANS modeling results The budget terms obtained in the LES data evaluation are compared in the present section with the respective terms of the k transport equation returned by the Wilcox 1988 $k-\omega$ model, the SST model of Menter, and the SST model with the curvature correction of Hellsten for the studied test case. All presented results are, for the sake of clarity, non-dimensionalized using the jet diameter d and \bar{U}_{ymax} -

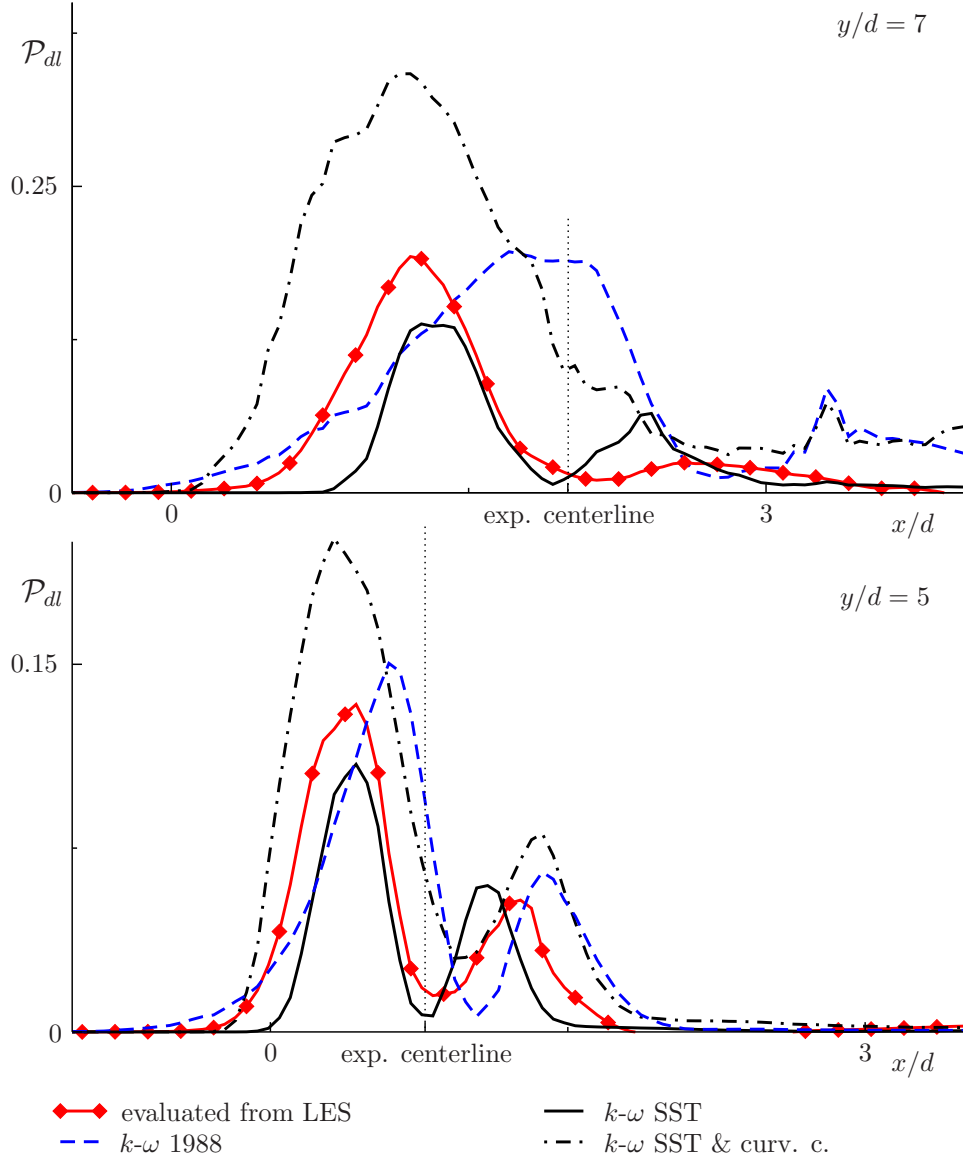


Figure 3.1.27: Dimensionless production of the turbulent kinetic energy \mathcal{P}_{dl} evaluated from LES data and resulting from RANS modeling. All values are non-dimensionalized using the jet diameter d and $\overline{U}_{y\max}$ - the respective maximal vertical velocity at the extraction plane, $\mathcal{P}_{dl} = \mathcal{P} \cdot d / \overline{U}_{y\max}^3$. $z/d = 0$.

the respective maximal vertical velocities at the extraction plane in each simulation.

First the production terms are compared in figure 3.1.27. The trends shown by the SST model and by its curvature correction are not surprising when considering the results presented in sections 3.1.2.2.3 and 3.1.2.3.1.2. Whereas the original SST model underestimates the level of the turbulent production, the SST model employing the curvature correction largely overpredicts this term. The location of the production peaks on the upstream jet side is the same as in LES. The peaks on the lee side given by the SST model are slightly shifted towards the upstream direction in comparison to the LES peaks. The opposite situation can be observed considering the downstream side production peaks of the SST model employing the curvature correction. This behavior can be explained by the under prediction of the jet spreading in the

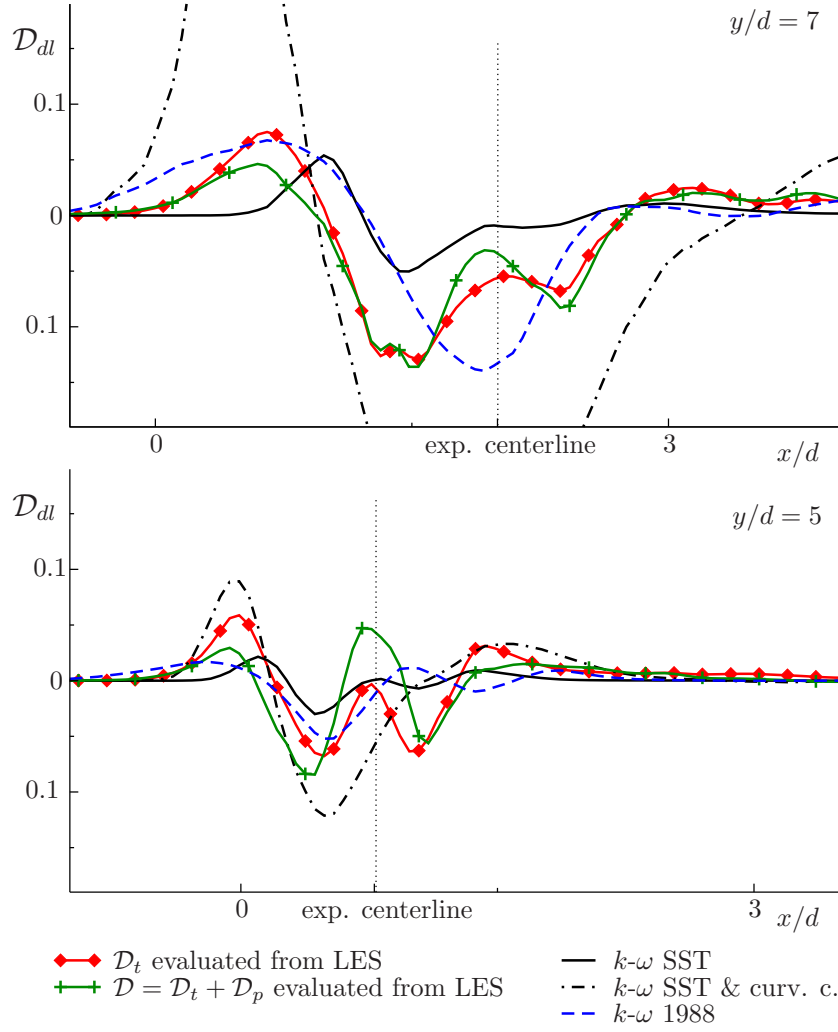


Figure 3.1.28: Dimensionless diffusion of the turbulent kinetic energy evaluated from LES data and resulting from RANS modeling. All values are non-dimensionalized using the same variables as in figure 3.1.27. $z/d = 0$.

SST simulations and its overestimation in the SST curvature correction calculations.

In the results shown by the Wilcox 1988 $k-\omega$ model, the magnitude of the production maxima correlates well with the results given by LES. However, their x/d locations are strongly shifted further downstream in comparison with the LES data. This corresponds to the observations made in section 3.1.2.3.1.2 and figure 3.1.4(f) that the jet centerline in the Wilcox 1988 $k-\omega$ model calculations is shifted in the downstream direction as a consequence of too high turbulent viscosity in the upstream shear layer.

The profiles of the turbulent kinetic energy diffusion are compared in figure 3.1.28. Regarding the LES data, two profiles are shown. The first one is the turbulent diffusion $\mathcal{D}_t = -\frac{1}{2} \frac{\partial u'_i u'_i u'_l}{\partial x_l}$, and the second one is the sum of the turbulent and the pressure diffusion $\mathcal{D} = \mathcal{D}_t + \mathcal{D}_p$ (see equation 2.2.13). The second profile is given since, as shown in the previous section, the impact of the pressure diffusion is not neglectable in the considered case. As in the case of production, the diffusion levels are overestimated by the SST model employing the curvature correction of Hellsten. This over prediction becomes especially drastic at $y/d = 7$. Since the level of the

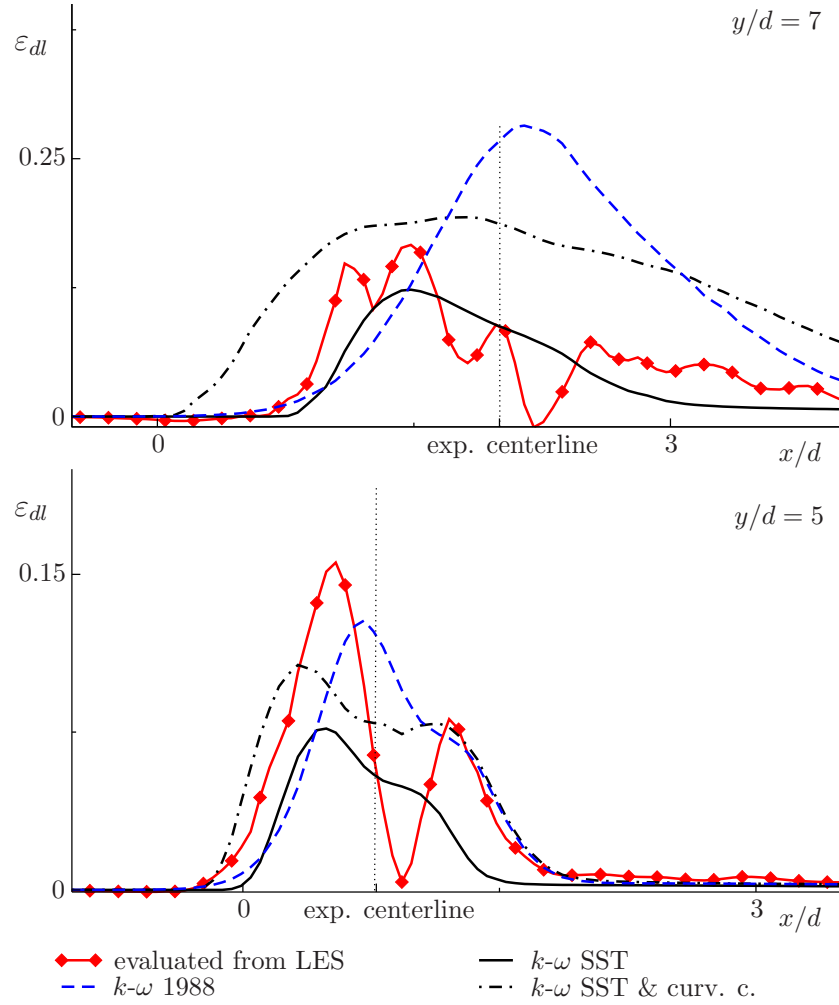


Figure 3.1.29: Dimensionless dissipation of the the turbulent kinetic energy evaluated from LES data and resulting from RANS modeling. All values are non-dimensionalized using the same variables as in figure 3.1.27. $z/d = 0$.

modeled diffusion of k directly depends on the calculated turbulent viscosity shown in figure 3.1.22, the high diffusion levels obtained here are expected. The underestimation of the turbulent diffusion by the SST model is expected as well because, as figure 3.1.22 shows, the turbulent viscosity given by the SST model is too low. The Wilcox 1988 k - ω model underestimates the level of the turbulent diffusion at $y/d = 5$, especially considering the pressure diffusion impact predicted by LES. At the position $y/d = 7$ the level of the turbulent diffusion is reproduced by the Wilcox model better, but the location of the peak values is again strongly shifted in the downstream direction.

The dimensionless dissipation profiles are presented in figure 3.1.29. For the RANS k - ω models used in this study, ε is evaluated using equation 2.2.53. This parameter together with the turbulent viscosity is extremely important for the assessment of RANS modeling quality. Whereas accurate modeling of the production and diffusion of k is a consequence of the turbulent viscosity equation, accurate representation of the dissipation term measures the quality of the ε or ω evolution equation. Figure 3.1.29 demonstrates that none of the tested models is able

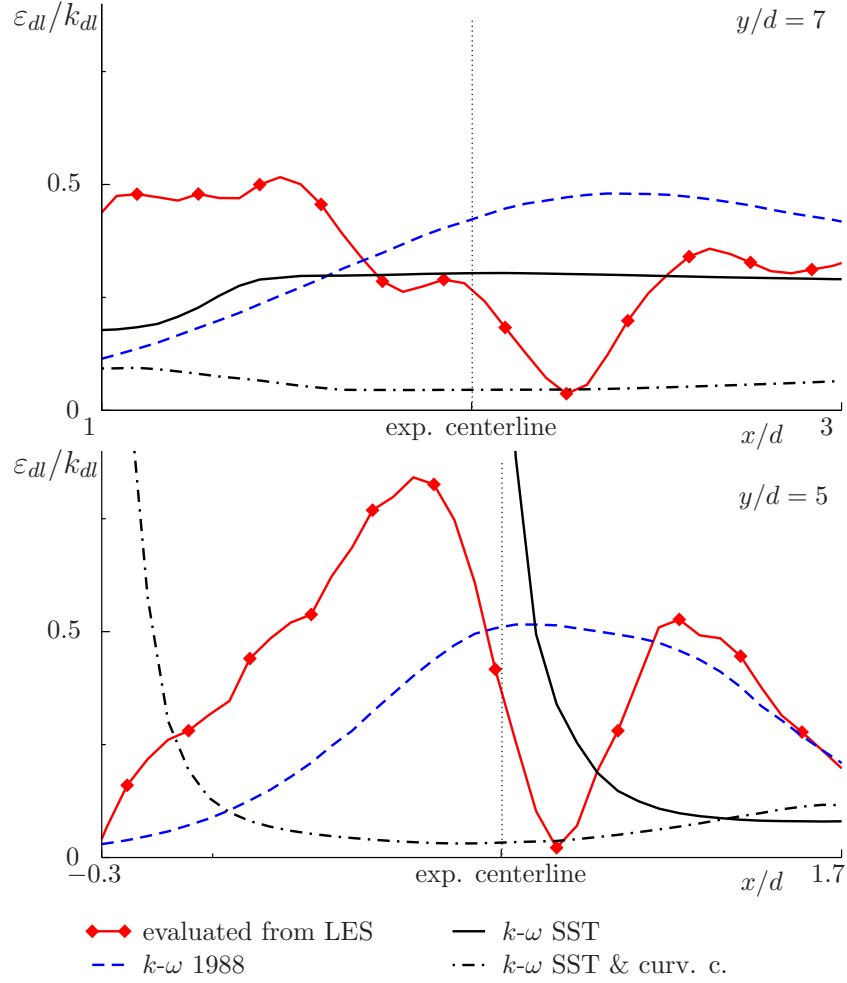


Figure 3.1.30: Dimensionless dissipation per unit turbulent kinetic energy ε_d/k_d evaluated from LES data and resulting from RANS modeling. All values are non-dimensionalized using the same variables as in figure 3.1.27. $z/d = 0$.

to represent the dissipation of k correctly. At the $y/d = 5$ location all considered RANS approaches under predict the dissipation level, and at the higher location $y/d = 7$ the SST model shows a quite accurate estimate whereas the SST model with the curvature correction of Hellsten and the Wilcox 1988 model over predict the dissipation level.

For a better understanding of the influence of the dissipation and production values shown above on the turbulence prediction in the studied flow, a consideration of the dissipation ratio per unit turbulent kinetic energy ε/k and of the production to dissipation ratio \mathcal{P}/ε can be useful. These profiles are presented in figures 3.1.30 and 3.1.31. First, figure 3.1.30 demonstrates clearly that the dissipation per unit turbulent kinetic energy is strongly underestimated by the SST model employing the curvature correction. This additionally suggests that the curvature correction, as discussed in section 3.1.2.2.3, “overreacts” here and decreases the level of dissipation too strongly. The Wilcox 1988 model gives adequate ε/k ratios. The SST model overestimates ε/k at $y/d = 5$ at the upstream side of the jet. This is an indicator of excessively strong turbulence damping. At the $y/d = 7$ location the SST model gives a good agreement with the ε/k levels given in the LES data evaluation.

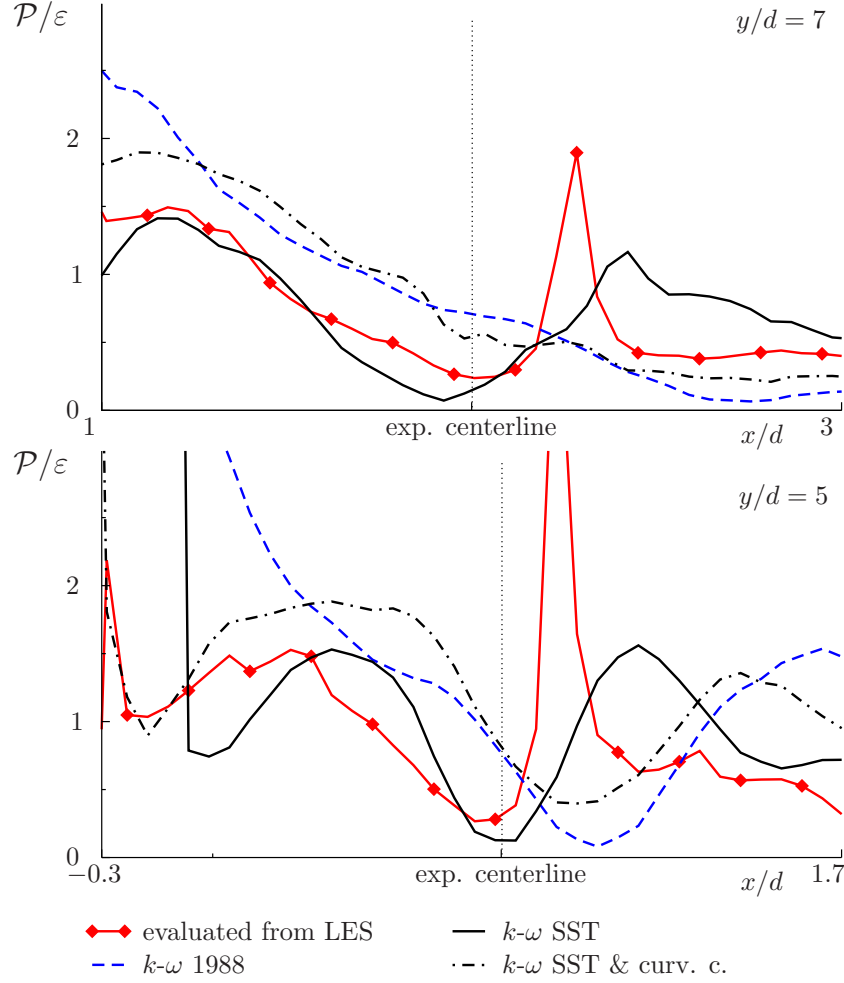


Figure 3.1.31: Production to dissipation ratio evaluated from LES data and resulting from RANS modeling. $z/d = 0$.

The production to dissipation ratios given by LES data alternate around $\mathcal{P}/\varepsilon = 1.0$ at $y/d = 5$ and decrease to lower values at $y/d = 7$. This indicates the dominance of dissipation at the higher locations. The \mathcal{P}/ε ratios are overestimated by the Wilcox 1988 model and by the SST model with curvature correction especially at the upstream locations. These results are in agreement with the observations revealing the turbulence over prediction by these two models made before in sections 3.1.2.1, 3.1.2.2.3, and 3.1.2.3.1.2.

Finalizing the studies devoted to the evaluation of the turbulent viscosity and of the turbulent kinetic energy budget terms from LES data, the turbulent viscosity modeling coefficient C_μ is obtained as $C_\mu = \nu_t \cdot \varepsilon / k^2$. This coefficient C_μ (or β_k in the $k-\omega$ type models, see equations 2.2.53 and 2.2.55) is assumed to be $C_\mu = 0.09$ in all models studied in the present dissertation. Figure 3.1.32 reveals that in the present test case the value of this coefficient, although fluctuating around $C_\mu = 0.09$, is highly variable. Its magnitude reaches $C_\mu > 0.18$ in the upstream jet region and drops to the values of an order of magnitude lower downstream of the jet centerline. Furthermore, resulting from the negative ν_t on the downstream side of the jet demonstrated in figure 3.1.21, in the regions not included in the plot 3.1.32, C_μ also can be negative. Failure to account for these observations in the modeling can negatively influence the quality of the RANS

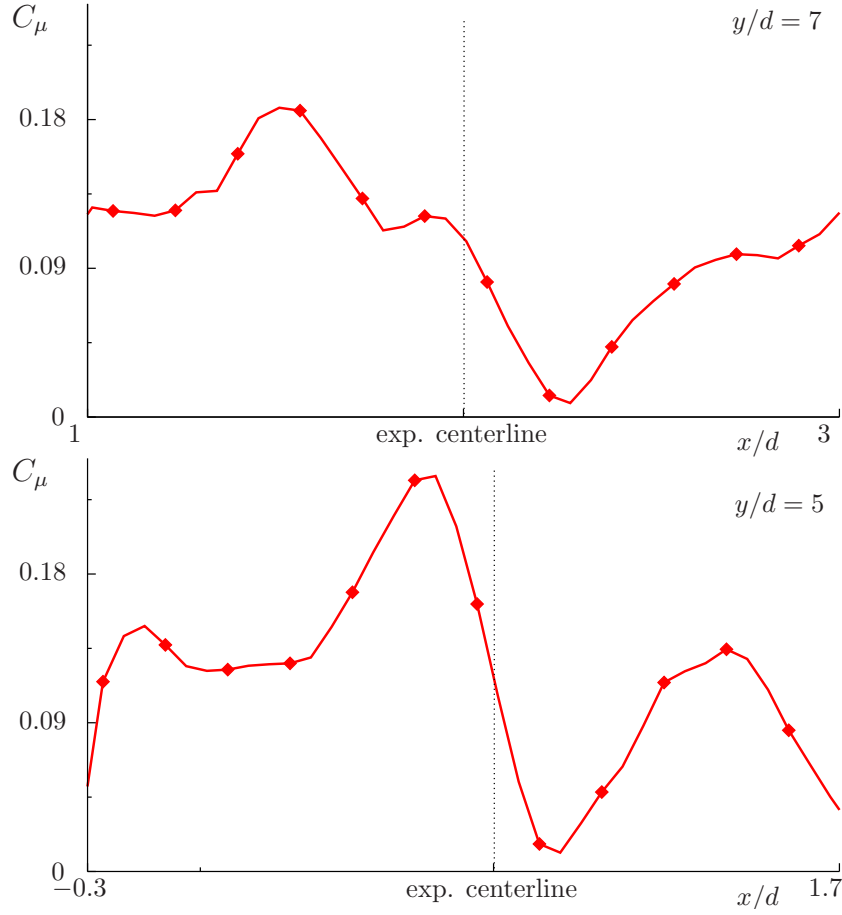


Figure 3.1.32: Turbulent viscosity modeling coefficient C_μ evaluated as $C_\mu = \nu_t \cdot \varepsilon / k^2$ using the LES data. $z/d = 0$.

predictions. One of the possible solutions may be the employment of the turbulent viscosity models using a variable or a dynamically adjusted C_μ .

It can be additionally observed, that the curvature correction of Hellsten, considered in this work (see section 3.1.2.2.3 and figure 3.1.12), is actually responding correctly to the underlying flow physics since it increases the turbulence level exactly in the same regions in which C_μ evaluated from LES becomes larger (upstream side of the jet) and decreases it at the same locations where C_μ becomes smaller (lee side of the jet). Instead of incorporation of the streamline curvature related terms in the ω -equation as proposed by Hellsten, adjustment of the C_μ coefficient based on the same streamline curvature detector may be favorable for the turbulence model improvement.

3.1.3 Scalar mixing modeling

3.1.3.1 Mean and fluctuating scalar field predictions

In this section the scalar mixing predictions for the jet in crossflow test case obtained from RANS simulations will be presented and compared with appropriate LES results. Dependence of the results on the RANS turbulence model used and on the selected turbulent Schmidt number value will be discussed. Furthermore, the mean and the fluctuating scalar profiles

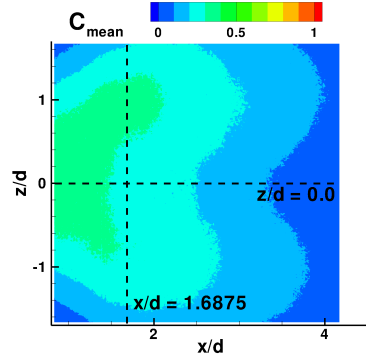
obtained by the two-equation turbulent scalar diffusivity models not employing the constant turbulent Schmidt number approach will be analyzed.

3.1.3.1.1 Dependence on the turbulent viscosity model The experimental scalar measurements of [78, 13, 42] were made only in xz -planes; hence, only contour plots obtained in these planes are shown. The y/d locations of these planes are $y/d = 5$ and $y/d = 7$. Figure 3.1.33 presents the mean dimensionless scalar contours obtained by means of LES, the 1988 $k-\omega$ model of Wilcox, and the SST model. These contours are compared with experimental data. In the RANS simulations, the constant value of the turbulent Schmidt number $\sigma_t = 1.0$ was used. The same value of the analogous SGS modeling parameter was chosen for LES. Despite of some differences between LES and experimental data, figure 3.1.33 clearly demonstrates the superiority of this method over the RANS approaches employed here. The 1988 model of Wilcox gives better predictions than SST but the agreement is still unsatisfactory.

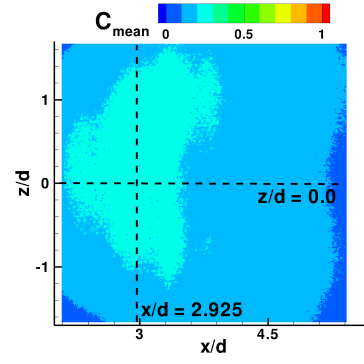
A more detailed comparison can be performed based on the profiles of the mean dimensionless scalar presented in figure 3.1.34 (the profile locations are indicated by the black dashed lines in figure 3.1.33). It should be noted that for the profiles along the z -axis both the positive and the negative directions are presented together since the experimental results are slightly asymmetric. The profiles produced by the Wilcox 1988 $k-\omega$ model are indicated by blue dashed lines, and the profiles given by the SST model are shown in black solid lines. Additionally, the results given by the standard $k-\varepsilon$ model (green dash-dot-dot lines) and by the SST $k-\omega$ model with the curvature correction of Hellsten (black dash-dot lines) are presented. Here different trends can be observed depending on the chosen RANS model. The standard $k-\varepsilon$ and the SST models underestimate the mixing. The Wilcox 1988 $k-\omega$ model shows the same trend of mixing under prediction at $y/d = 5$, but at $y/d = 7$ the scalar profiles are represented quite well. The SST model employing the curvature correction also under predicts the mixing at $y/d = 5$ but largely over predicts it at $y/d = 7$.

The LES returns very accurate scalar profiles along the z -axis (agreement with the experimental data is better than for all RANS models), but the LES data displays well defined peaks of the scalar concentration at $y/d = 5, z/d = 0$ and $y/d = 7, z/d = 0$ which are absent in the experimental profiles. Considering the velocity modeling results discussed above and the accurate mixing predictions along the z -axis, it is concluded that these peaks in LES scalar profiles are probably not caused by a deficiency of the scalar SGS model used in LES, but by the failure to properly capture the y -velocity (see figure 3.1.6) at these positions. Even taking into account this issue of the presented LES calculations, their overall mixing predictions are more accurate than given here by RANS, as figures 3.1.33 and 3.1.34 reveal.

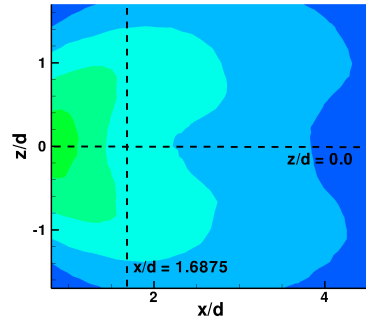
With regards to RANS, a clear connection between the scalar mixing results and the accuracy of the turbulence modeling, discussed in sections 3.1.2.1 and 3.1.2.2.3, can be observed. The standard $k-\varepsilon$ and the SST $k-\omega$ models gave the most obvious underestimation of the turbulent velocity fluctuations (see section 3.1.2.1) and also produced the least accurate mean scalar profiles. The Wilcox 1988 $k-\omega$ model displayed the best results of all RANS models in section



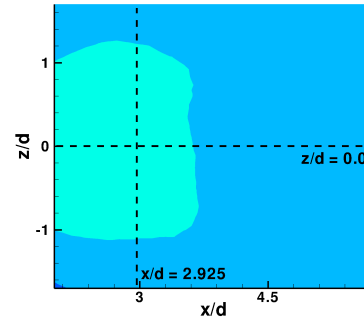
(a) Experimental data, $y/d = 5$.



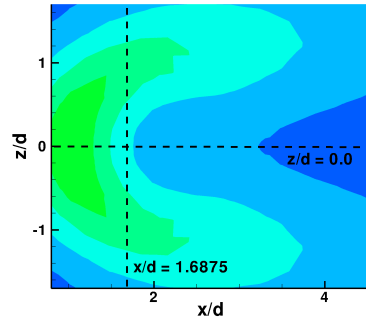
(b) Experimental data, $y/d = 7$.



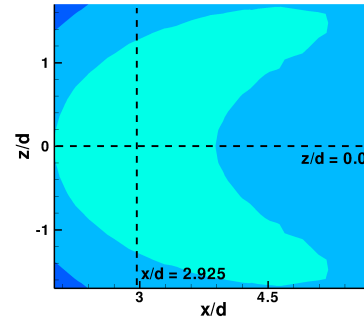
(c) WALE LES, $y/d = 5$.



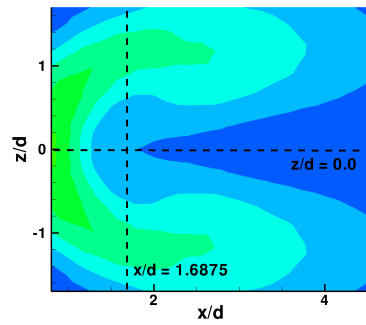
(d) WALE LES, $y/d = 7$.



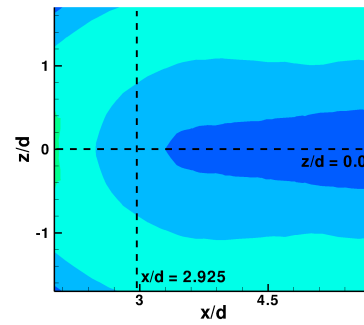
(e) 1988 $k-\omega$, $y/d = 5$.



(f) 1988 $k-\omega$, $y/d = 7$.



(g) SST $k-\omega$, $y/d = 5$.



(h) SST $k-\omega$, $y/d = 7$.

Figure 3.1.33: Mean transported passive scalar and positions of the extracted profiles at different y/d planes. LES and different RANS turbulence models in comparison with experimental data.

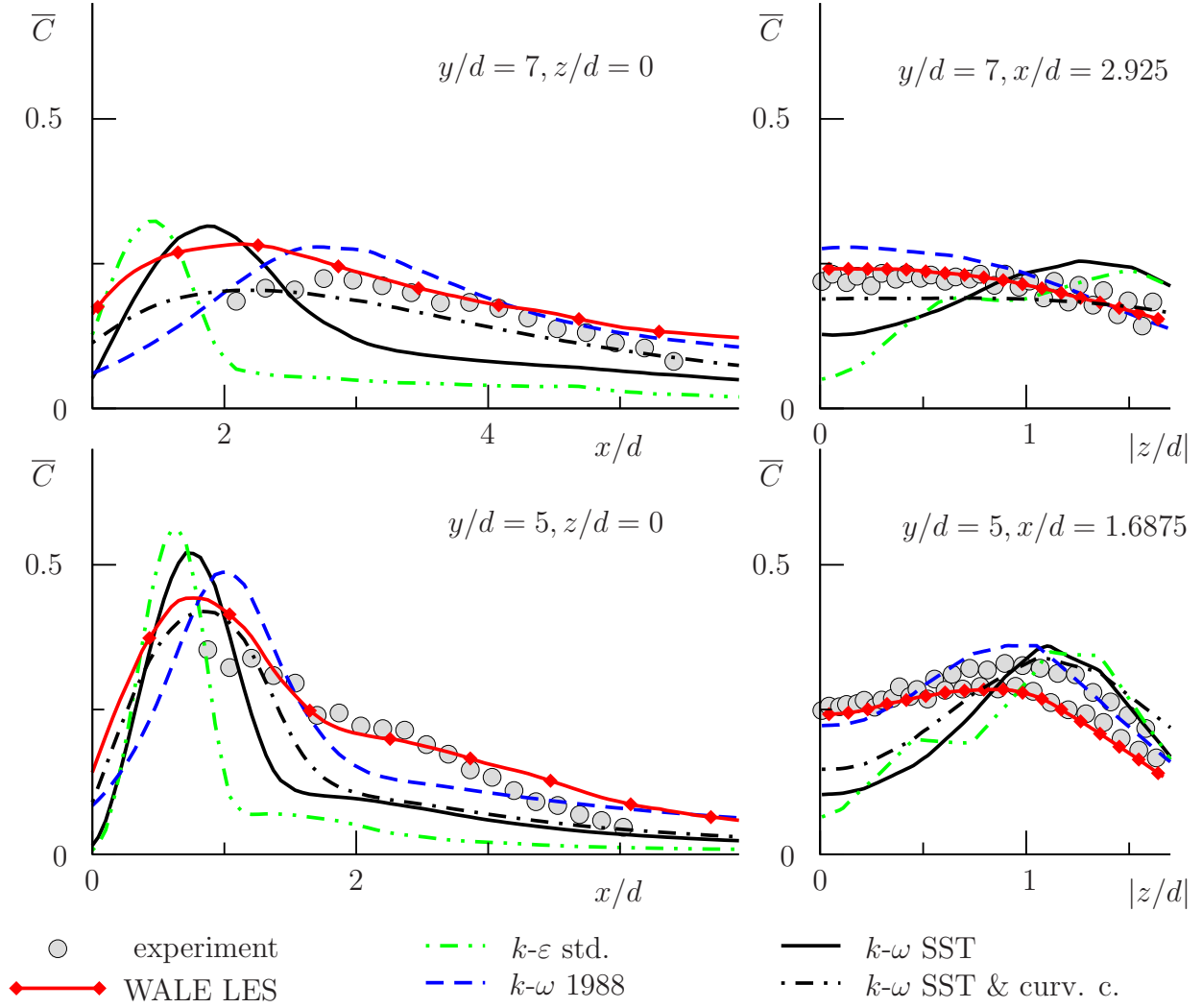


Figure 3.1.34: Mean values of the transported passive scalar. LES and different RANS turbulence models in comparison with experimental data.

3.1.2.1, and here it also shows more satisfactory agreement with the experimental mixing data. Finally, the SST $k-\omega$ model with the curvature correction largely overestimated the level of the turbulent kinetic energy at $y/d = 7$ (see section 3.1.2.2.3), so it is not surprising it over predicts the mixing at the same location. That said, it cannot be assumed that only the quality of the turbulence model defines the mixing prediction accuracy. The influence of the scalar mixing modeling approach in RANS is considered in the next two sections.

3.1.3.1.2 Dependence on the turbulent Schmidt number values The constant turbulent Schmidt number approach and its accuracy in the present calculations are discussed first. For this discussion, two turbulence models (the Menter SST model and its variation employing the curvature correction of Hellsten) are selected to perform turbulent Schmidt number dependence studies. The results from this study are shown in figure 3.1.35. The mean scalar profiles produced by both models at three different turbulent Schmidt numbers ($\sigma_t = 1.0$, $\sigma_t = 0.5$, and $\sigma_t = 0.25$) are presented. Figure 3.1.35(a) reveals that $\sigma_t = 0.25$ is an optimal value for modeling mixing in this jet in crossflow configuration when used in conjunction with the SST

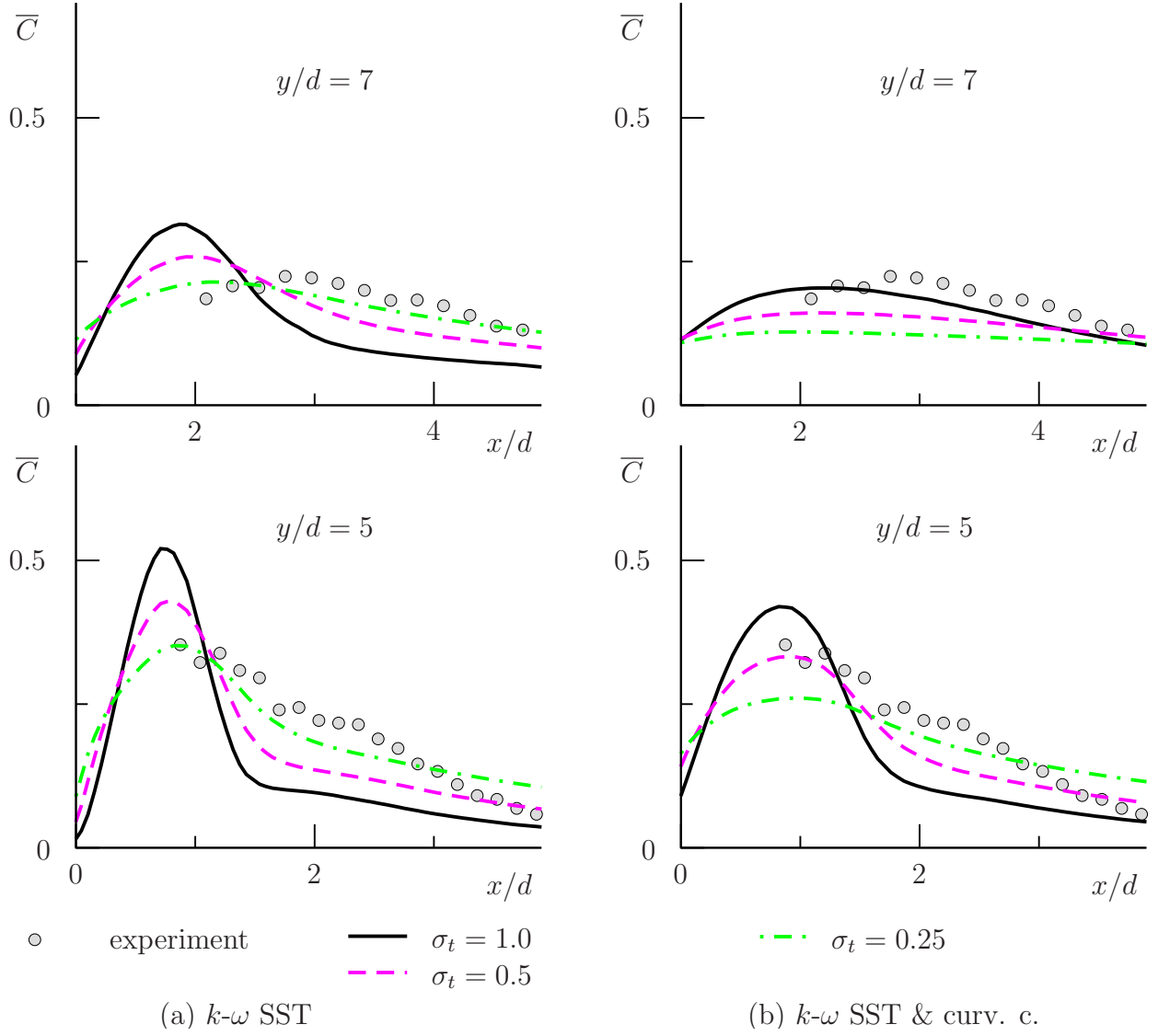


Figure 3.1.35: Mean values of the transported passive scalar. Dependence of the RANS results on the turbulent Schmidt numbers σ_t values. $z/d = 0$.

closure. A different situation with regards to the turbulent Schmidt number can be observed in figure 3.1.35(b) for the mixing modeling in conjunction with the SST model with curvature correction. Here the optimal value at $y/d = 5$ is $\sigma_t = 0.5$ whereas at $y/d = 7$ it is rather $\sigma_t = 1.0$. Smaller values of σ_t largely over predict the mixing.

As discussed previously (section 3.1.2.1), the SST model generally underestimates the level of turbulence. The low value of the turbulent Schmidt number $\sigma_t = 0.25$ produces α_t necessary to compensate for the deficits of the turbulence model and thus leads to satisfactory mixing predictions in this case. The SST model with curvature correction reproduces the level of the turbulent kinetic energy more accurately than the SST model at $y/d = 5$ (see section 3.1.2.2.3) and largely over predicts the level of the turbulent fluctuations at $y/d = 7$. Consequently, at $y/d = 5$ the SST model with curvature correction does not need large adjustment of α_t to compensate for an underestimated level of turbulence, so $\sigma_t = 0.5$ gives accurate mixing predictions. To correct for the excessive turbulence level at $y/d = 7$, higher values of σ_t have

to be used in conjunction with the SST model with curvature correction.

Thus, the values of the turbulent Schmidt numbers giving the optimal mixing predictions in conjunction with different RANS turbulence models do not necessarily resemble the physical reality but are more often an artificial correction for poor turbulence modeling. That is certainly the case with regards to the values of $\sigma_t = 0.2 - 0.3$ found to be optimal for jet in crossflow calculations in refs. [45, 53, 54, 51, 80, 42]. In the studies of these publications either the standard $k-\varepsilon$ or the SST $k-\omega$ model were used. As shown in section 3.1.2.1, the standard $k-\varepsilon$ model returns even lower levels of turbulence in the considered test case than the SST model. From the results presented here, it can be concluded that the actual turbulent Schmidt numbers in the considered configuration are higher than $\sigma_t = 0.25$. Section 3.1.3.2.1.1 presents a more thorough investigation on the actual turbulent Schmidt number values in the considered test case by evaluating σ_t from the time-averaged LES data fields.

3.1.3.1.3 Two-equation turbulent scalar diffusivity models Generally speaking, the employment of the constant turbulent Prandtl or Schmidt number hypothesis can always be a source of inaccuracy in the mixing calculations. This is argued by the experimental and DNS observations that the turbulent Prandtl or Schmidt numbers are not constant even in such simple configurations as the plane channel and the round jet flows considered in the theoretical background section (section 2.2.2). For this reason, the two-equation turbulent scalar diffusivity models described in section 2.2.2.2 and not employing the constant turbulent Schmidt number concept are also evaluated for modeling jet in crossflow mixing in this work.

Figure 3.1.36 presents the mean scalar profiles obtained by the $\overline{c'^2}-\varepsilon_c$ model of Nagano and Kim[89] (NK), the $\overline{c'^2}-\varepsilon_c$ model of Abe et al.[2] (AKN), the $\overline{c'^2}-\varepsilon_c$ model of Deng et al.[21] (DWX), and the $\overline{c'^2}-\omega_c$ model of Huang and Bradshaw [48] (HB). The turbulent viscosity was modeled by means of the Wilcox 1988 $k-\omega$ model since this model in the present case returned the most accurate mean and fluctuating velocity fields among all tested RANS approaches (see section 3.1.2.1). The mixing results obtained employing a constant turbulent Schmidt number of $\sigma_t = 1.0$ are presented in figure 3.1.36 as well.

It is seen that the two-equation turbulent scalar diffusivity models do not bring significant improvement in the scalar field predictions comparatively to the constant turbulent Schmidt number approach. The NK, the HB, and the DWX models produce quite similar results which are almost identical to the predictions given by $\sigma_t = 1.0$. The AKN model yields levels of mixing significantly less than the values observed in experiments. This model displayed similar behavior in the free round jet mixing calculations (see figure 2.2.13). This leads to the conclusion that the AKN model being developed primarily for near-wall heat transfer simulations is at the same time not well suited for modeling jet mixing. The fact that the three other models tested did not improve the jet in crossflow mixing results can potentially be explained by two different reasons. The first reason could be the slightly incorrect computation of the turbulent velocity time scale τ_d by the Wilcox 1988 $k-\omega$ model. This deficiency can be seen in figure 3.1.30 presenting the reciprocal dimensionless profiles of τ_d obtained by different RANS models and

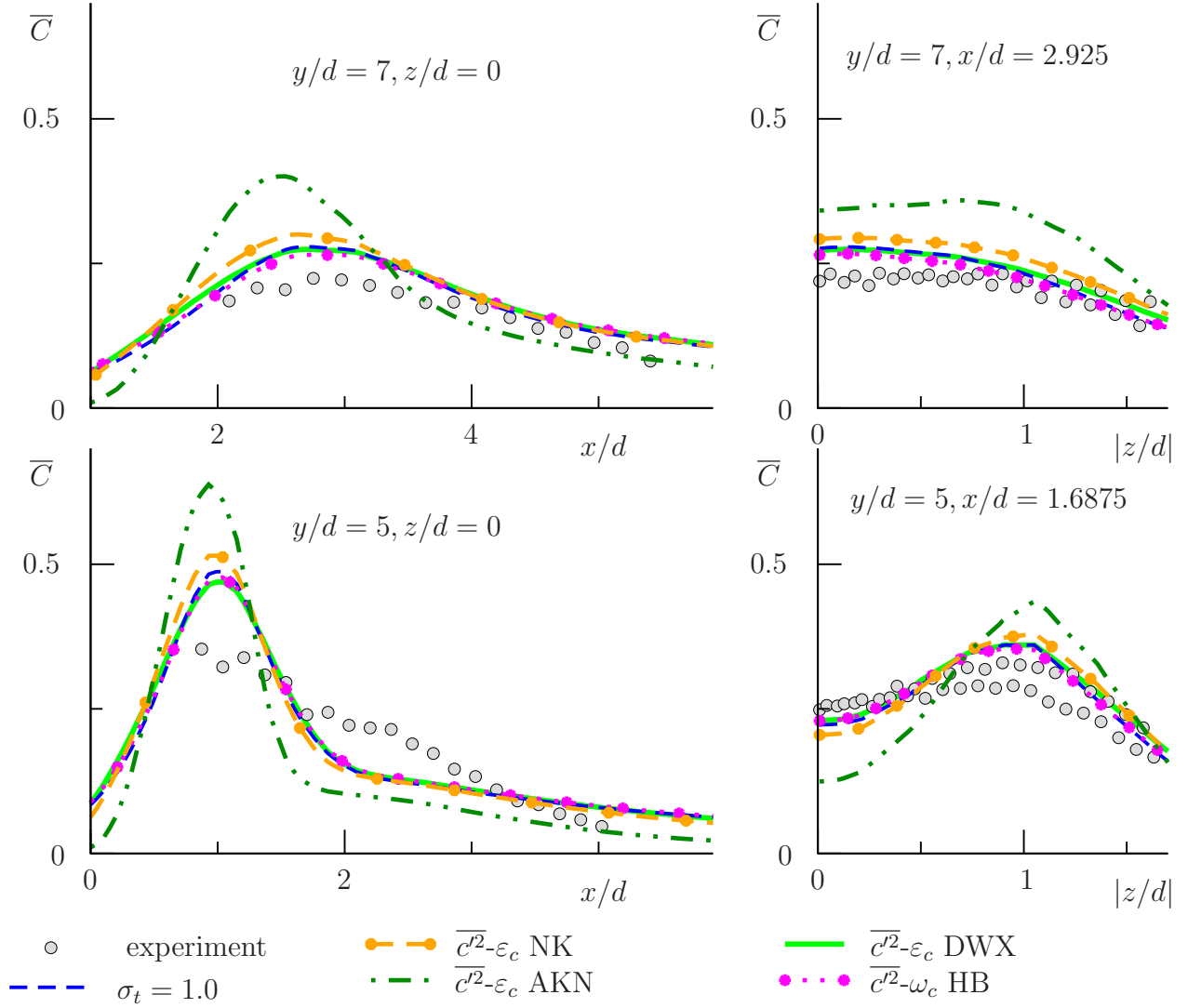


Figure 3.1.36: Mean values of the transported passive scalar. $k-\omega$ 1988 turbulence model, different turbulent scalar diffusivity models in comparison with experimental data and $\sigma_t = 1.0$. $z/d = 0$.

resulting from LES data evaluation. Since the turbulent velocity time scale is actively used in the turbulent scalar diffusivity formulation and in the ϵ_c or ω_c equations (see section 2.2.2.2), its incorrect computation can lead to the deficiencies observed in the scalar mixing predictions. The second reason for the mediocre performance of the studied two-equation mixing models could be the fundamental structure of the modeling equations and their constants. Being primarily formulated for near-wall heat transfer computations (see section 2.2.2), these models may not be optimal for the application considered here. Additional studies on this subject are presented in section 3.1.3.2.

3.1.3.1.4 Turbulent scalar variance and turbulent scalar flux For a more thorough analysis of mixing prediction accuracy, the fluctuating variables - turbulent scalar variance and turbulent scalar fluxes - have to be validated against experimental data. Such validation for RANS and LES is presented in figures 3.1.37 and 3.1.38. Figure 3.1.37 shows the profiles generated by

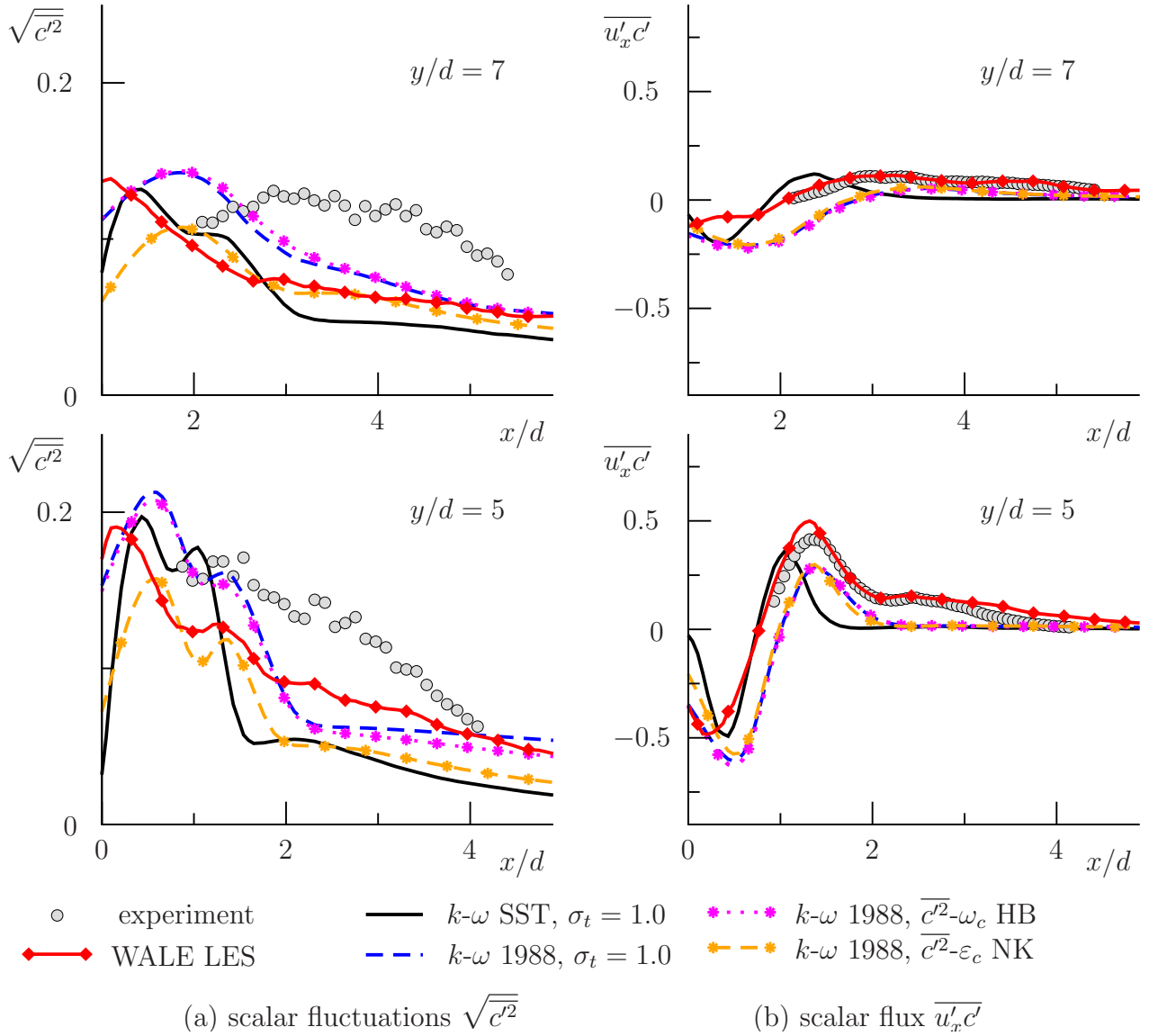


Figure 3.1.37: RMS fluctuations of the transported passive scalar and the turbulent scalar flux in x -direction. RANS and LES in comparison with experimental data. $z/d = 0$.

two different RANS turbulence models (Wilcox 1988 and SST $k-\omega$) in conjunction with the constant turbulent Schmidt number $\sigma_t = 1.0$. In this case the scalar variance is calculated using equation 2.2.116. Furthermore, the results obtained using the $\overline{c'^2}-\omega_c$ HB and the $\overline{c'^2}-\epsilon_c$ NK models are shown, and here the Wilcox 1988 $k-\omega$ model is used for the turbulent viscosity calculation. None of the tested approaches shows a satisfactory degree of accuracy. The results generated by the SST model and $\sigma_t = 1.0$ show the worst agreement with experimental data. As figure 3.1.38 additionally demonstrates, this situation can be marginally improved if a lower turbulent Schmidt number value of $\sigma_t = 0.25$ is used in the SST model calculations. The results generated by the HB model are almost identical to the profiles given by the Wilcox 1988 $k-\omega$ model with $\sigma_t = 1.0$. The turbulent scalar variance is recovered the worse by the NK model than by all other approaches.

The LES achieves much more accurate scalar flux profiles than RANS, as shown in figures

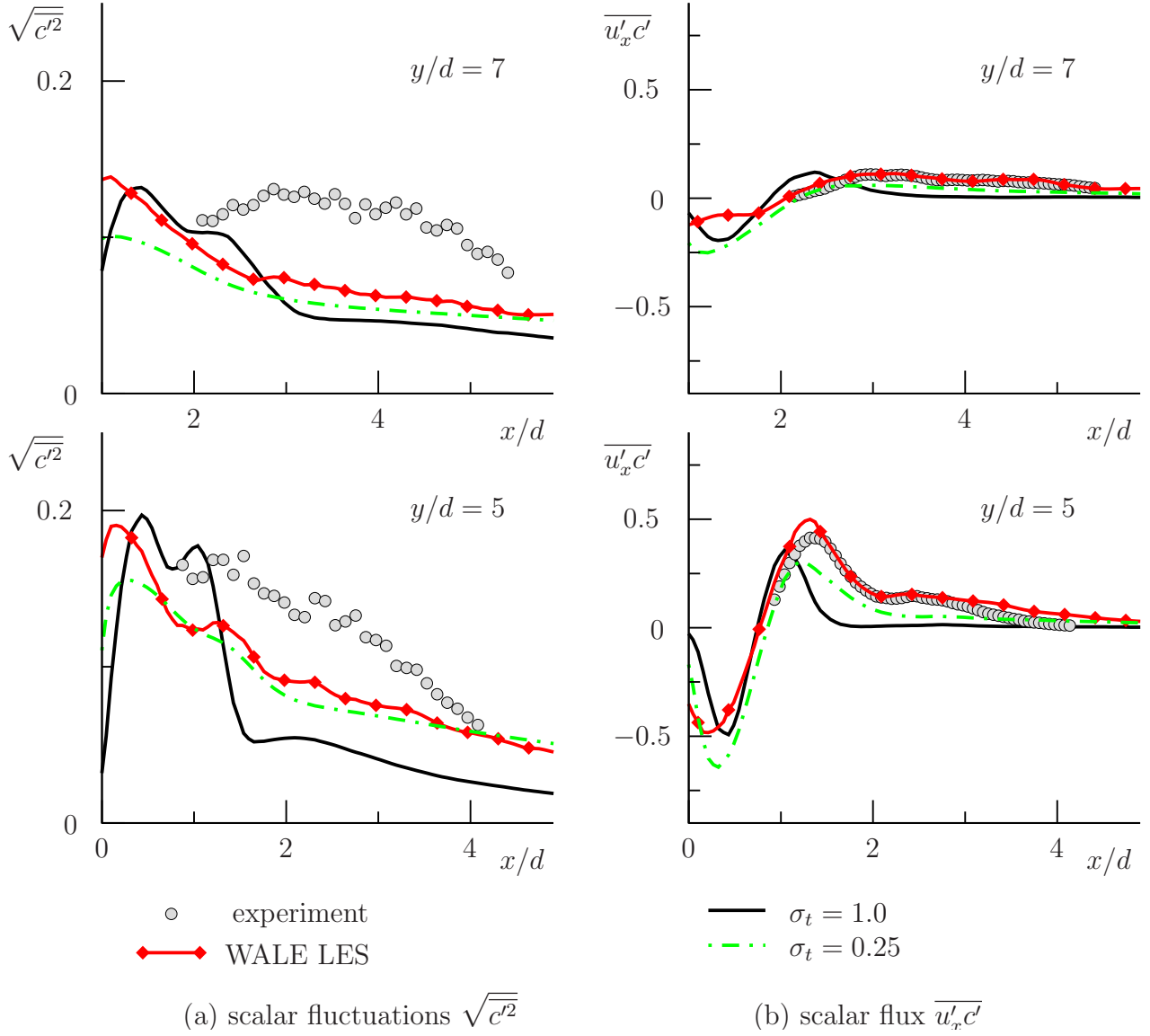


Figure 3.1.38: RMS fluctuations of the transported passive scalar and the turbulent scalar flux in x -direction. k - ω SST with different turbulent Schmidt numbers and LES. $z/d = 0$.

3.1.37(b) and 3.1.38(b). Regarding the scalar variance no clear statement can be made about the quality of the LES data. The LES results differ from the RANS predictions and the LES scalar variance profiles are more similar to the experimental ones. However, the magnitude of the scalar variance is lower than given in the experimental measurements. In the experimental works [78, 13, 42], no error bars are shown, so the uncertainties in the scalar variance measurements are difficult to quantify. In summary, besides of the scalar variance all mean and fluctuating variables obtained in the present LES calculations show satisfactory agreement with experimental data. Moreover, LES of two additional test cases studied in this work (see section 3.2.3.1) show good agreement with the experimental scalar variance data. Thus here a decision was made to use the present LES scalar variance data for the further evaluations since at least the trends shown by this data can be assumed to be more realistic than given by RANS.

3.1.3.2 Evaluation of LES scalar mixing data

As shown in the previous section, the mean and fluctuating scalar fields obtained in LES simulations do not perfectly recover the experimental data. However, they are generally closer to the measured fields than the RANS results. The accuracy of scalar mixing within the RANS framework depends heavily on both the choice of the turbulence model and on the approach for the turbulent scalar flux closure. The aim of the following sections is to gain a more complete understanding of the actual trends of the turbulent scalar diffusivity, turbulent Schmidt numbers, and budget terms of the turbulent scalar variance transport equation in the considered flow. This study is accomplished by post-processing the resolved LES data. The comparison of the obtained results with the results and assumptions of the RANS scalar mixing modeling should help to define future directions for model improvement.

3.1.3.2.1 Turbulent scalar diffusivity

3.1.3.2.1.1 Evaluation from the time-averaged LES data fields First, the Reynolds-averaged turbulent scalar diffusivity, α_t , will be recovered from the LES data and compared with the values given by the RANS models. As in the case of the turbulent viscosity evaluation (see section 3.1.2.3), a problem arises in this complex flow because of the anisotropy of α_t and of the difficulty in selecting the dominant scalar flux. This problem is addressed here in detail and supported by figures 3.1.39 - 3.1.41.

Figure 3.1.39 compares the turbulent scalar fluxes in different directions (LES data) in dependence on the distance from the jet symmetry plane. In the location near to the symmetry plane ($z/d = 0.1$, figure 3.1.39(a)), $\overline{u'_x c'}$ and $\overline{u'_y c'}$ clearly dominate the scalar transport, whereas the $\overline{u'_z c'}$ component is negligibly small. The scalar flux in the z -direction has greater relative influence on the scalar field with increasing distance from the jet symmetry plane ($z/d = 1.0$, figure 3.1.39(b)), and the magnitude of the other two fluxes, particularly $\overline{u'_y c'}$, drops.

It should be noted that the relative gradient of the mean transported scalar in the y -direction is small comparatively to the gradient in the x -direction even at $z/d = 0.1$ and becomes especially small at $z/d = 1.0$ (see figure 3.1.40). In combination with the large scalar fluxes in the y -direction, this scalar gradient distribution leads to high absolute values of the turbulent scalar diffusivities obtained as $-\overline{u'_y c'}/\frac{\partial \overline{C}}{\partial y}$, drastically so at $z/d = 1.0$ as seen in figure 3.1.41. The absolute values of α_t evaluated as $-\overline{u'_x c'}/\frac{\partial \overline{C}}{\partial x}$ and $-\overline{u'_z c'}/\frac{\partial \overline{C}}{\partial z}$ are smaller and lie closer to each other. The problem of the anisotropy of α_t appears here to be even more severe than the problem of the anisotropy of ν_t discussed in section 3.1.2.3.1.1. For the turbulent viscosity, the strong anisotropy was observed when evaluating the Reynolds stresses characterized by a relatively low magnitude. In the current evaluation, the flux $\overline{u'_y c'}$ is quite large particularly at $z/d = 0.1$; however, the employment of $\alpha_{ty} = -\overline{u'_y c'}/\frac{\partial \overline{C}}{\partial y}$ for the closure of equation 2.2.6 in x - and z -directions would clearly overestimate $\overline{u'_x c'}$ and $\overline{u'_z c'}$ and the overall scalar transport. Thus, for the comparison with the RANS models which use a unique, scalar, α_t for all three fluxes the data obtained from LES or experiment in only one direction could be misleading. For that reason, analogously to the calculation of the turbulent viscosity (see section 3.1.2.3),

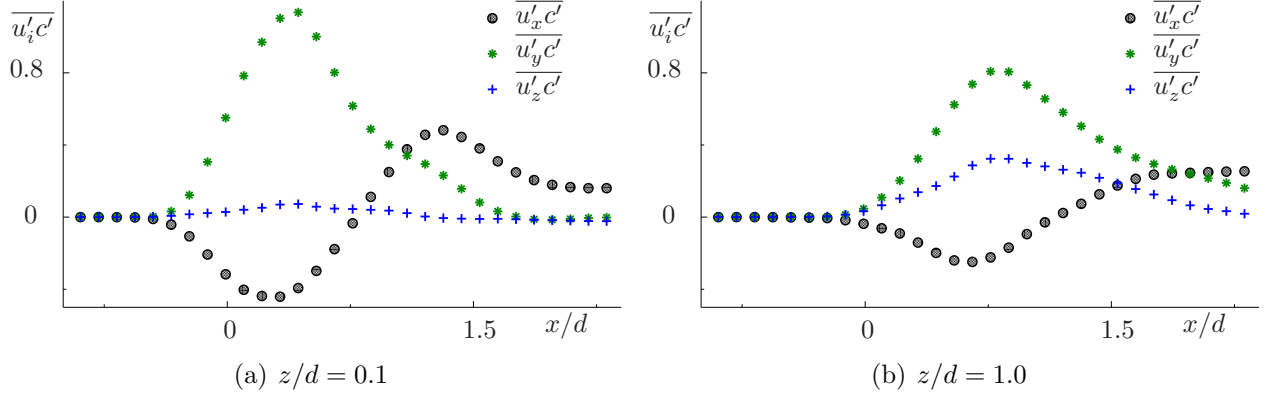


Figure 3.1.39: Different components of the turbulent scalar flux vector $\overline{u'_i c'}$. Dependence on the z/d distance from the jet symmetry plane. $y/d = 5$.

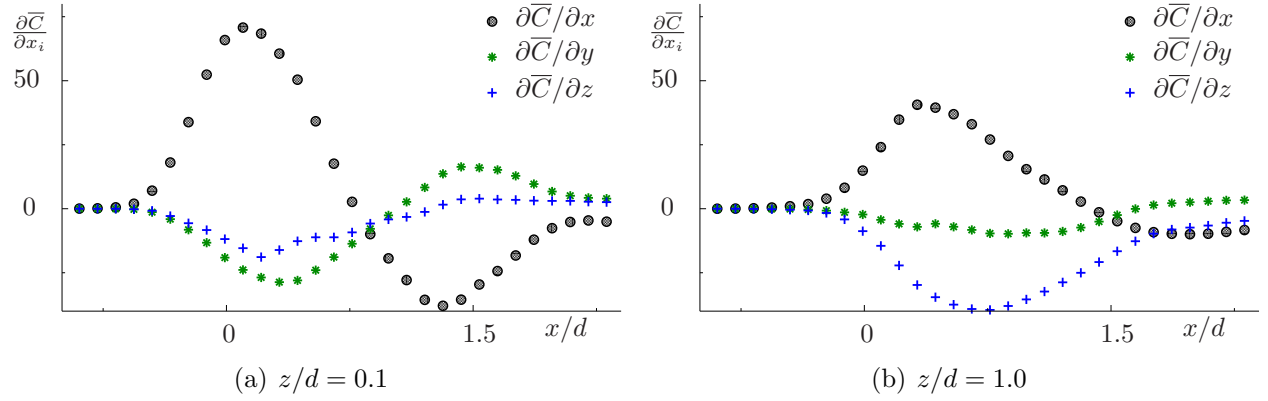


Figure 3.1.40: Different components of the mean scalar gradient vector $\partial \overline{C} / \partial x_i$. Dependence on the z/d distance from the jet symmetry plane. $y/d = 5$.

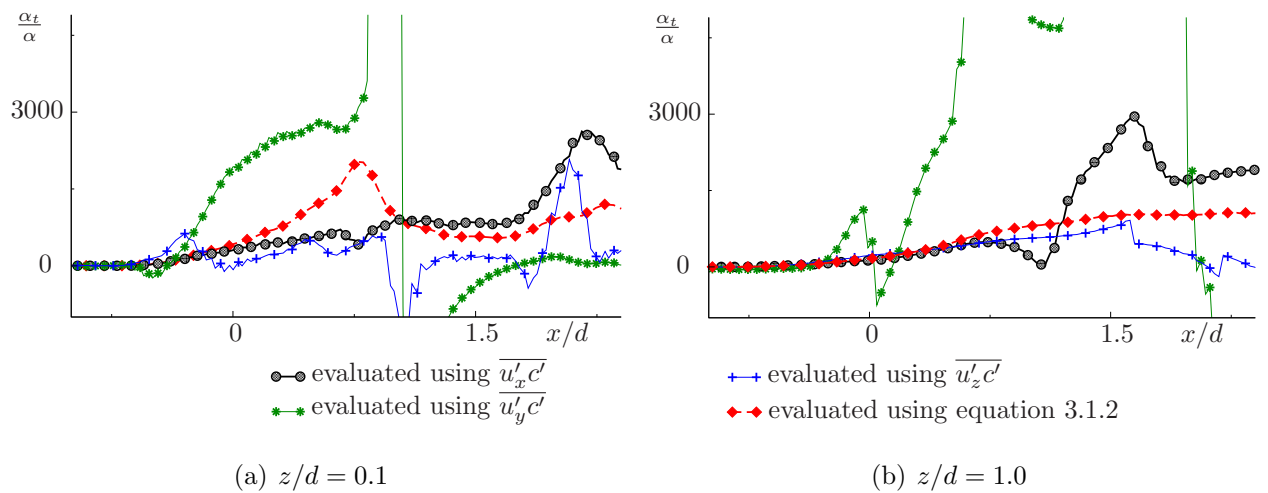


Figure 3.1.41: Dimensionless turbulent scalar diffusivity α_t / α evaluated from LES data using different turbulent scalar fluxes and equation 3.1.2. Dependence on the z/d distance from the jet symmetry plane. $y/d = 5$.

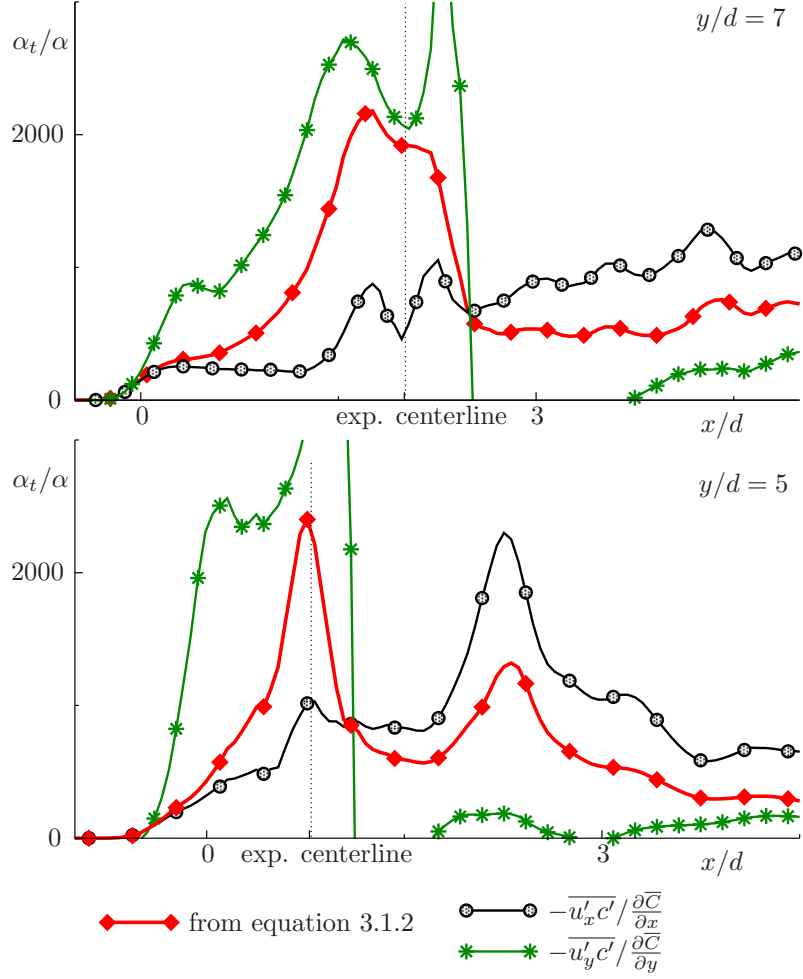


Figure 3.1.42: Dimensionless turbulent scalar diffusivity α_t/α . Comparison of different evaluation methods. $z/d = 0$.

α_t is evaluated in this work using the least-squares fit over all turbulent scalar fluxes,

$$\alpha_t = \frac{-\overline{c' u'_j} \cdot \frac{\partial \overline{C}}{\partial x_j}}{\left(\frac{\partial \overline{C}}{\partial x_l} \right) \left(\frac{\partial \overline{C}}{\partial x_l} \right)}, \quad (3.1.2)$$

with the summation over repeating indices $j = 1 - 3$ and $l = 1 - 3$. This formulation yields a direction-independent α_t that minimizes the error in the solution of the overdetermined system of equations 2.2.6. Practically, such an α_t represents a compromise value needed in RANS models to provide the best possible approximation of the turbulent scalar transport in equation 2.1.17, if anisotropic closures are not under consideration*.

The turbulent scalar diffusivities obtained using equation 3.1.2 at different locations are shown in figures 3.1.41 and 3.1.42. Figure 3.1.42 presents α_t on the jet symmetry plane which will be used in the next sections for the comparison with the RANS results. Here, as in the previous figure 3.1.41, a comparison is also made with $\alpha_{tx} = -\overline{u'_x c'} / \frac{\partial \overline{C}}{\partial x}$ and $\alpha_{ty} = -\overline{u'_y c'} / \frac{\partial \overline{C}}{\partial y}$.

*It should be, however, noted that taking into account the results demonstrated in figures 3.1.39 - 3.1.41, an anisotropic model for α_t would be extremely useful.

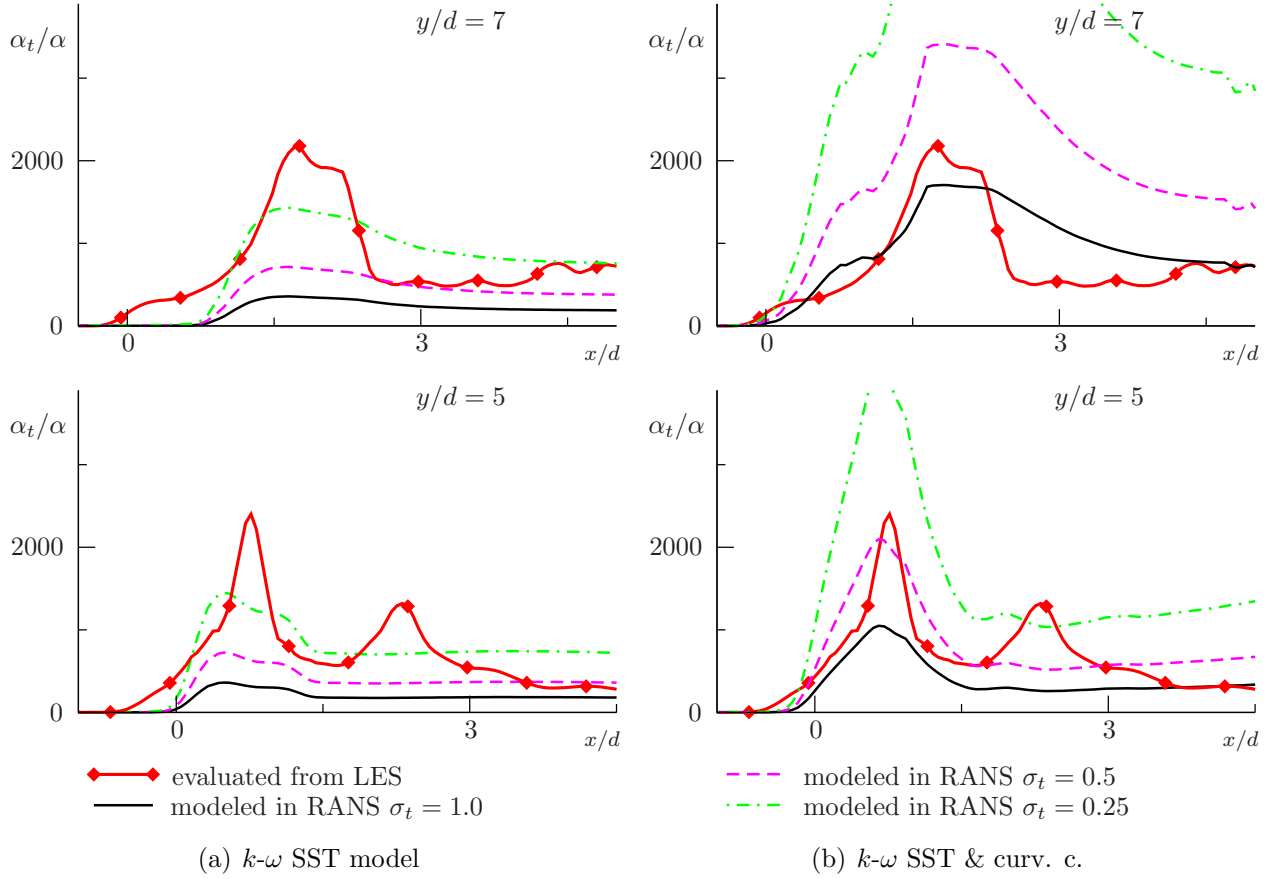


Figure 3.1.43: Dimensionless turbulent scalar diffusivity α_t/α evaluated from LES data and resulting from RANS modeling at different σ_t . $z/d = 0$.

It can be seen in both figures 3.1.41 and 3.1.42 that α_{ty} evaluated from $\overline{u_y'c'}$ tend to take negative values on the lee side of the jet. The same behavior was observed for this parameter in the evaluation of the experimental and LES jet in crossflow data which was made by Salewski et al. [109]. This phenomenon probably has the same origin as the negative values of ν_t in this region discussed in section 3.1.2.3.1.2, but in contrast to the averaged ν_t , α_t evaluated according to equation 3.1.2 does not become negative here.

3.1.3.2.1.2 Comparison with the RANS modeling results The profiles of α_t found from equation 3.1.2 are compared with the modeled α_t of RANS in figures 3.1.43 and 3.1.44. The profiles are non-dimensionalized using the molecular scalar diffusivity α . First figure 3.1.43 validates the turbulent scalar diffusivities resulting from the SST model and the SST model with the curvature correction of Hellsten at three different turbulent Schmidt numbers. The corresponding mean scalar profiles are discussed in section 3.1.3.1.2. As it can be expected from the scalar profiles presented in figure 3.1.35, the value of α_t given by the SST model and $\sigma_t = 1.0$ is much lower than needed for a correct mixing prediction. Only the extremely small $\sigma_t = 0.25$ value recovers the α_t levels similar to those obtained from LES (figure 3.1.43(a)). A different situation can be observed in the α_t given by the SST curvature modification at different σ_t (figure 3.1.43(b)). Here the optimal α_t , as it was already proposed in section 3.1.3.1.2, can be

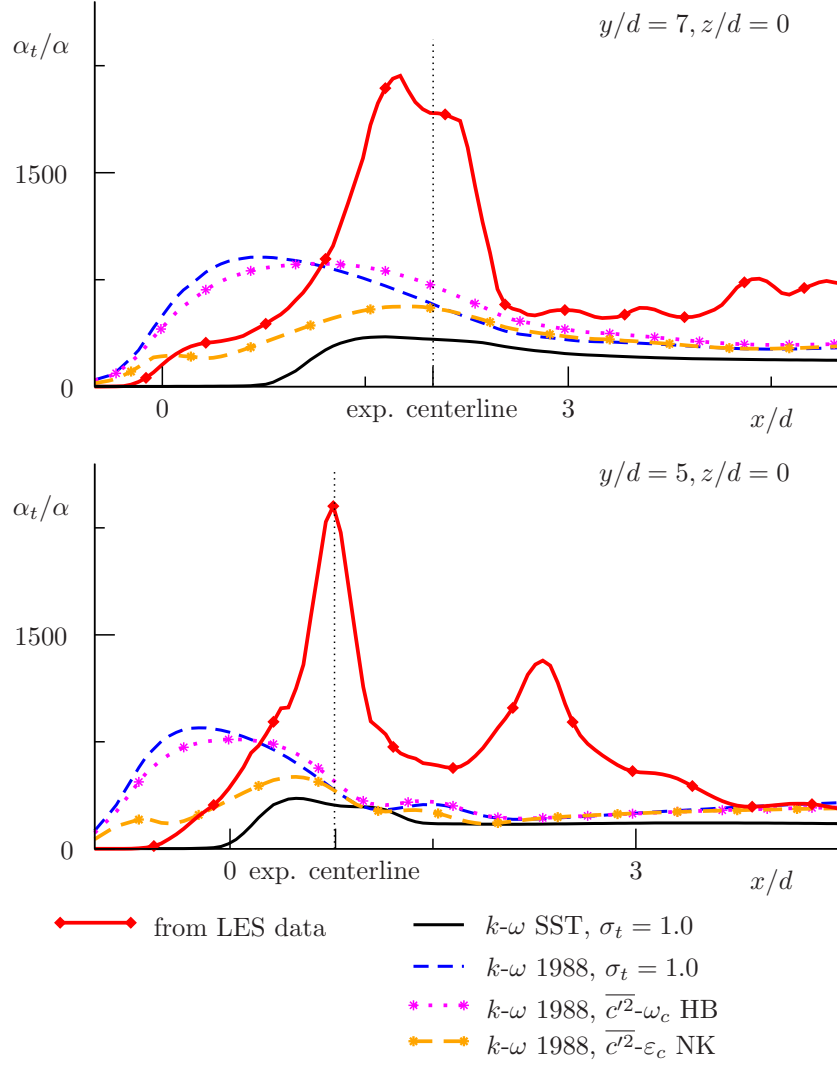


Figure 3.1.44: Dimensionless turbulent scalar diffusivity α_t/α evaluated from LES data and resulting from RANS modeling.

obtained with $\sigma_t = 0.5$ in the $y/d = 5$ location and $\sigma_t = 1.0$ in the $y/d = 7$ location. Since only at $y/d = 5$ does the SST model with curvature modification represent the turbulent velocity field with the satisfactory degree of accuracy, only the optimal value of σ_t in this location can be considered close to the actual one.

Validation of the α_t obtained in the RANS simulations employing other approaches discussed in section 3.1.3.1 against LES data is presented in figure 3.1.44. The most noticeable feature of the profiles given by the Wilcox 1988 $k\text{-}\omega$ model in conjunction with the constant turbulent Schmidt number and with the $\overline{c'^2}\text{-}\omega_c$ HB model is the location of the local maxima of α_t . Whereas the peaks of α_t predicted by LES and by the SST model (with and without the curvature correction) coincide with the experimental jet centerline location, the local maxima given by the Wilcox 1988 $k\text{-}\omega$ model with $\sigma_t = 1.0$ or $\overline{c'^2}\text{-}\omega_c$ HB model are located further upstream. The $\overline{c'^2}\text{-}\epsilon_c$ NK approach even in conjunction with the Wilcox 1988 $k\text{-}\omega$ model shows the local turbulent scalar diffusivity maximum on the jet centerline.

For the constant σ_t approach used with the Wilcox 1988 $k\text{-}\omega$ model, the upstream location of

the turbulent scalar diffusivity maximum can be easily explained since the form of α_t profiles just replicates the form of the turbulent viscosity profile shown in figure 3.1.22. As discussed in section 3.1.2.3, this ν_t shape given by the Wilcox 1988 k - ω model is rather unrealistic, so it may be one of the sources of inaccuracy in the turbulent mixing modeling. The differences between the predictions given by the HB and the NK models originate from the different formulation of the model equations. As in the case of the turbulent viscosity modeling, the ε_c equation of the NK model being rewritten in the ω_c formulation will not be identical to the ω_c equation of Huang and Bradshaw model. The terms analogous to the cross-diffusion term of the k - ω turbulence models discussed in section 3.1.2.2.5 will appear. These terms are not included in the ω_c equation of the Huang and Bradshaw model. The influence of these terms has to be further studied, but most likely, analogous to the cross-diffusion terms of the turbulent viscosity models (see section 3.1.2.2.5), they produce here additional turbulent scalar variance damping in the upstream locations resulting in the lower level of α_t given by the NK model but the correct location of the local maxima of α_t .

In summary, none of the assessed RANS approaches recovers in this jet in crossflow configuration either the functional form or the magnitude of the turbulent scalar diffusivity profiles given by LES. Although the shape of the profile given by the SST model in conjunction with the constant turbulent Schmidt number hypothesis agrees well with the profile evaluated from LES (see figure 3.1.43), reproducing the magnitude of α_t correctly requires the variation of σ_t values. In this context a question regarding the actual values of the turbulent Schmidt number in the considered flow and on their differences compared to the values used in the modeling arises. This question is clarified in the next section.

3.1.3.2.2 Turbulent Schmidt numbers The actual values of the turbulent Schmidt number in the considered flows can be obtained from LES data by division of the least-square mean turbulent viscosities evaluated in section 3.1.2.3.1.1 by the least-square mean turbulent scalar diffusivities shown above in figure 3.1.42. These turbulent Schmidt numbers evaluated from LES data are presented in figure 3.1.45. Besides σ_t profiles which, as anticipated, vary in space, the averaged values of σ_t in every respective location are also shown in this figure. The averaged values fall in the 0.53 - 0.55 range. Not surprisingly considering the discussion in section 3.1.3.1.2, these values are higher than $\sigma_t = 0.25$ needed by the SST model to attain accurate mixing predictions. The values around 0.2 - 0.3 can be observed only in the jet centerline region and certainly do not represent the averaged σ_t in this flow.

It can be furthermore observed in figure 3.1.45 that the turbulent Schmidt numbers evaluated from LES data become negative on the lee side of the jet. This is a direct consequence of the negative values of ν_t present in this region which are discussed in section 3.1.2.3. Such behavior cannot be represented by the most widespread RANS approaches for turbulent scalar diffusivity modeling; consequently, studies on alternative models are needed.

Figure 3.1.46 compares the turbulent Schmidt numbers evaluated from LES with the results given by the Wilcox 1988 k - ω model in conjunction with the \overline{c}^2 - ε_c NK and the \overline{c}^2 - ω_c HB

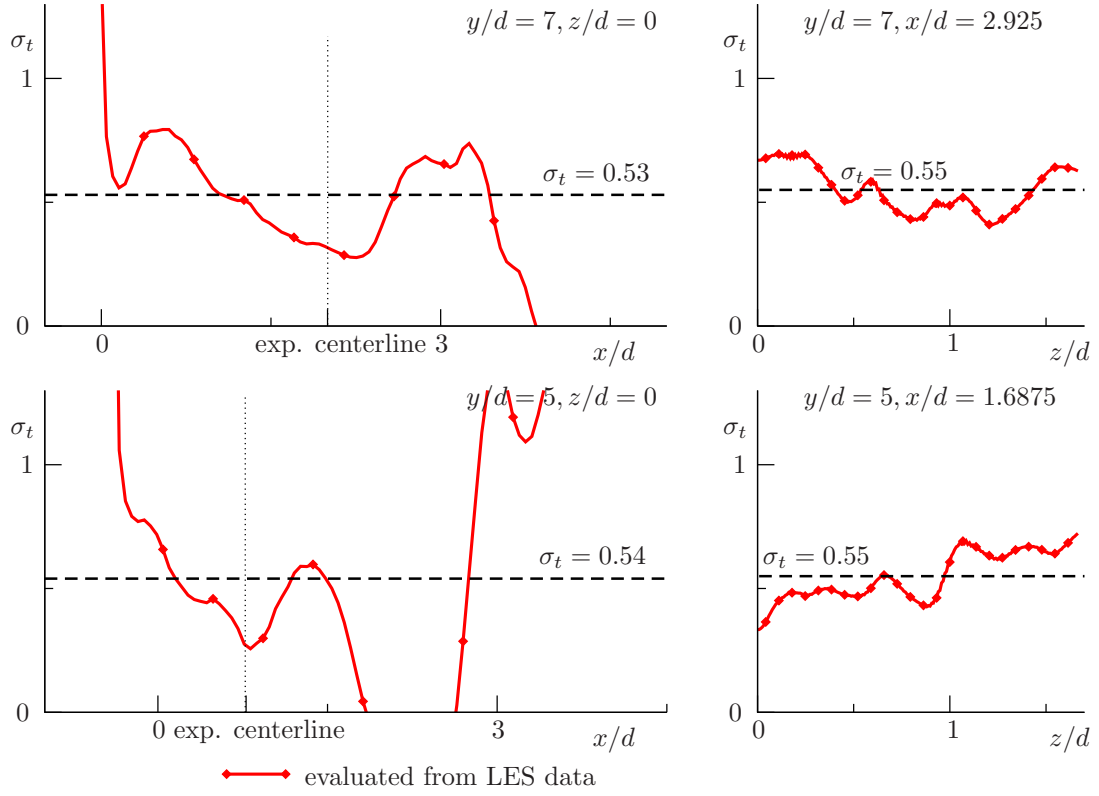


Figure 3.1.45: Turbulent Schmidt number σ_t evaluated from LES data.

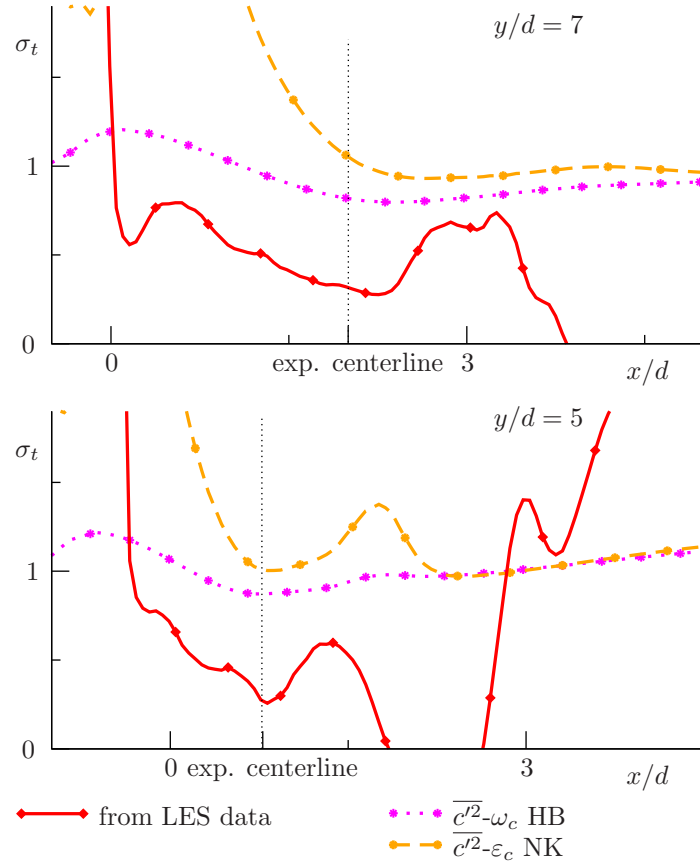


Figure 3.1.46: Turbulent Schmidt number σ_t evaluated from LES data and resulting from RANS modeling. $z/d = 0$.

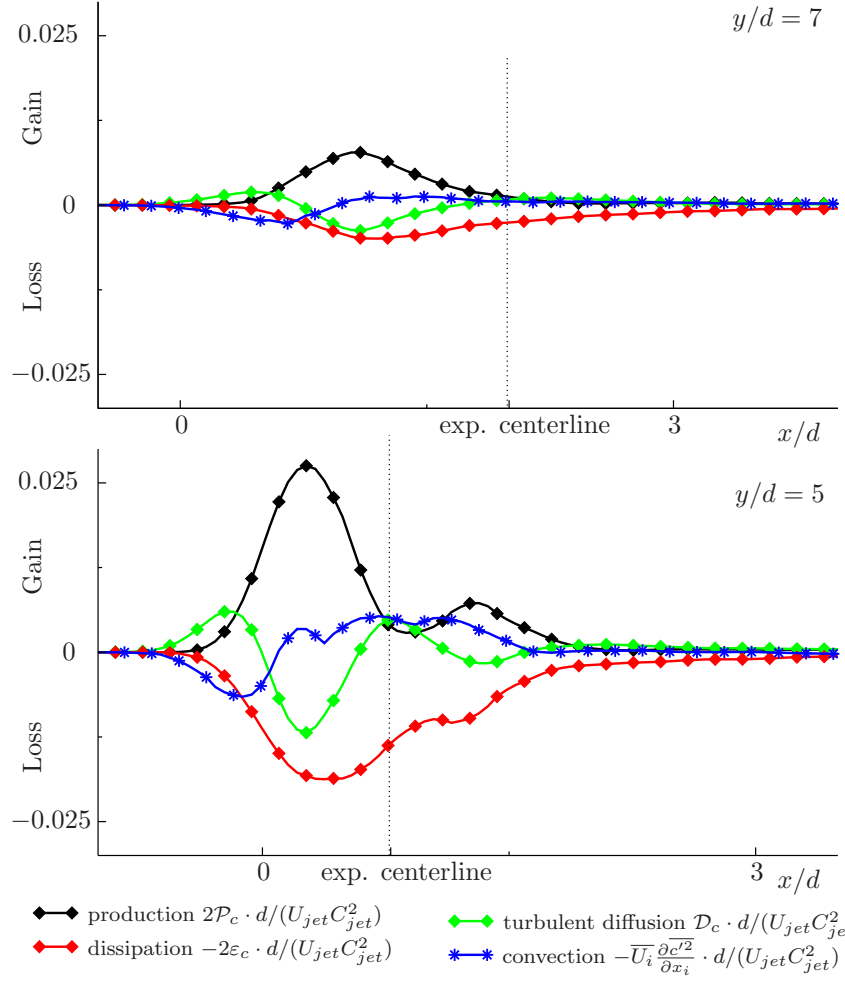


Figure 3.1.47: Main budget terms of the scalar variance transport equation evaluated from LES data. All terms are non-dimensionalized using the jet diameter d , the mean jet exit velocity U_{jet} , and the mean scalar concentration on the jet exit (here $C_{jet} = 1.0$). $z/d = 0$.

approaches. The values of σ_t obtained in the RANS modeling are greater than the values given by LES and fluctuate around $\sigma_t = 1.0$ for the HB model and are even higher for the NK model. This result explains the similarity of the scalar profiles obtained by both studied two-equation scalar mixing models and the constant turbulent Schmidt number approach at $\sigma_t = 1$.

3.1.3.2.3 Budget terms of the turbulent scalar variance transport equation

3.1.3.2.3.1 Evaluation from the time-averaged LES data In the final part of the present LES data evaluation, the budget terms of the turbulent scalar variance transport equation 2.2.112 obtained from the resolved scalar field of LES are visualized, discussed, and compared with the RANS modeling results. First, figure 3.1.47 presents the main budget terms of equation 2.2.112 obtained from LES solutions. As for the evaluation of the budget terms of the turbulent kinetic energy balance equation (see section 3.1.2.3.2), all terms besides of the dissipation are computed directly from the time-averaged LES scalar and velocity fields. The dissipation is computed indirectly from the imbalance of other terms. All terms are non-dimensionalized using the jet diameter d , the mean jet exit velocity U_{jet} , and the mean scalar concentration on

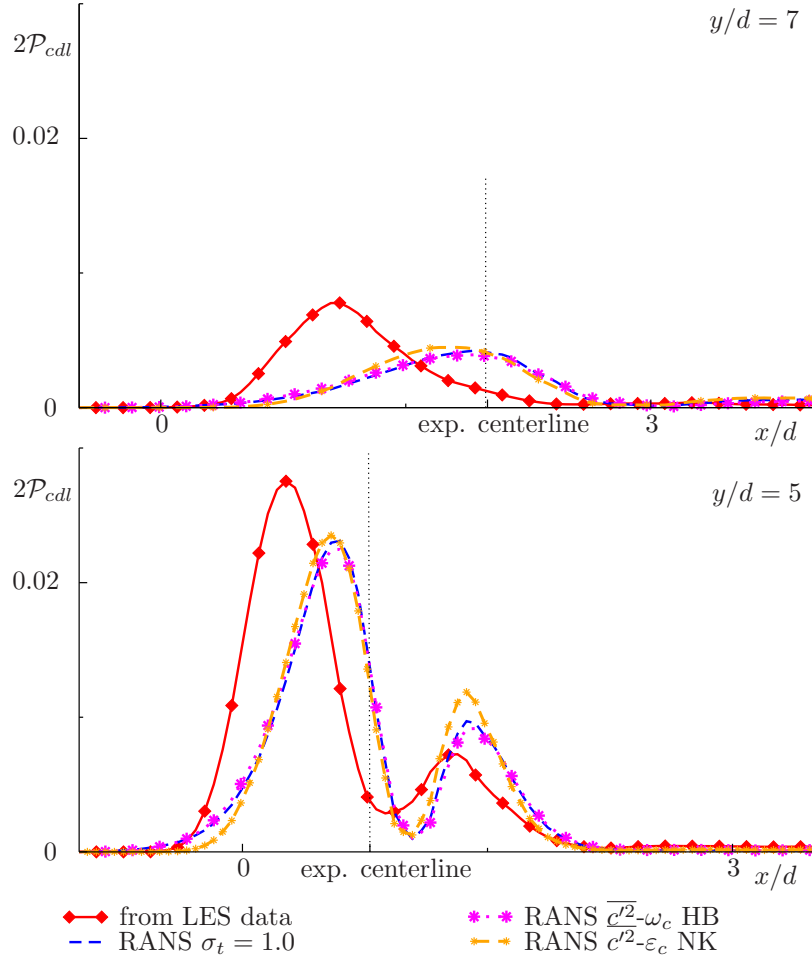


Figure 3.1.48: Dimensionless production of the turbulent scalar variance $2\mathcal{P}_{cdl} = 2\mathcal{P}_c \cdot d/(U_{jet}C_{jet}^2)$ evaluated from LES data and resulting from RANS modeling. Equation 2.2.116 is used in conjunction with the constant σ_t . For turbulence modeling in RANS $k-\omega$ 1988 approach is employed. $z/d = 0$.

the jet exit (here $C_{jet} = 1.0$).

The profile shape of the production, dissipation, and the turbulent diffusion terms are similar to the profile shape of the respective terms of the turbulent kinetic energy balance equation discussed in section 3.1.2.3.2. All profiles are characterized by two peaks - the larger one lying on the upstream side and the smaller one lying on the lee side of the jet. At the higher location $y/d = 7$ the peaks on the lee side are almost vanished. The absolute magnitude of all budget terms drops with the increasing y/d position.

3.1.3.2.3.2 Comparison with the RANS modeling results Figures 3.1.48, 3.1.49, and 3.1.50 show the individual comparison of the production, the turbulent diffusion, and the dissipation terms evaluated from LES data with the respective terms of the scalar variance transport equations of different RANS scalar mixing models. For the turbulence modeling here the Wilcox 1988 $k-\omega$ approach is employed and the scalar mixing models under study are: the constant turbulent Schmidt number of $\sigma_t = 1.0$ with equation 2.2.116 employed for the modeling of the turbulent scalar variance, the $\overline{c'^2}-\epsilon_c$ NK model, and the $\overline{c'^2}-\omega_c$ HB model.

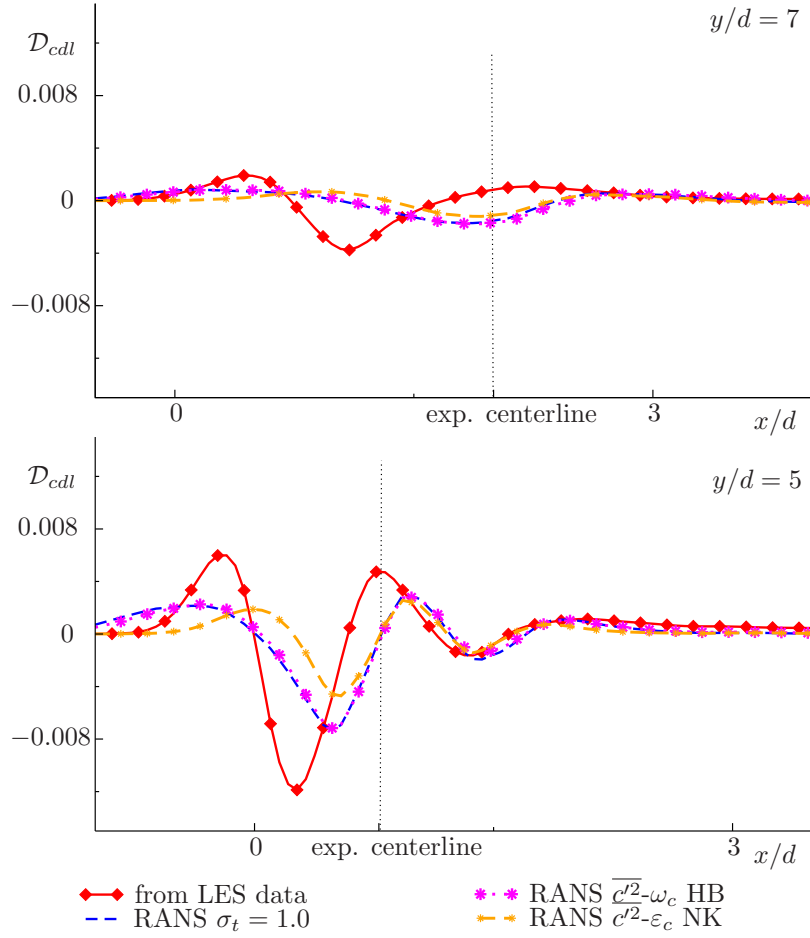


Figure 3.1.49: Dimensionless diffusion of the turbulent scalar variance $\mathcal{D}_{cdl} = \mathcal{D}_c \cdot d / (U_{jet} C_{jet}^2)$ evaluated from LES data and resulting from RANS modeling. Equation 2.2.116 is used in conjunction with the constant σ_t . For turbulence modeling in RANS $k-\omega$ 1988 approach is employed. $z/d = 0$.

The main disagreement between the data evaluated from LES and the results of RANS modeling is the location of the peaks of all budget terms. Whereas in LES both the positive and the negative peaks are located on the upstream side of the experimental jet centerline, in RANS they lie further downstream on the x -axis. This difference, however, can be easily explained by the discrepancy in the jet trajectory given by LES and the RANS 1988 Wilcox model simulations (see figures 3.1.4 and 3.1.6). Since in the Wilcox model simulation, the jet shear layer lies further downstream on the x -axis, the peaks of the budget terms also tend to be shifted in this direction. The magnitudes of the modeled production and the modeled turbulent diffusion terms are lower than those evaluated from LES. This corresponds with the trend of underestimated turbulent mixing shown by the studied RANS approaches in section 3.1.3.1. The profiles generated by all considered RANS modeling approaches are similar.

As discussed in section 2.2.2.2, in the scalar variance transport equation 2.2.116 used in conjunction with the constant turbulent Schmidt number approach, the dissipation term is typically closed using the scalar turbulent time scale obtained as $\tau_c = \mathcal{R}\tau_d$. Here τ_d is the turbulent velocity time scale and \mathcal{R} is the constant turbulent scalar to velocity time scale ratio

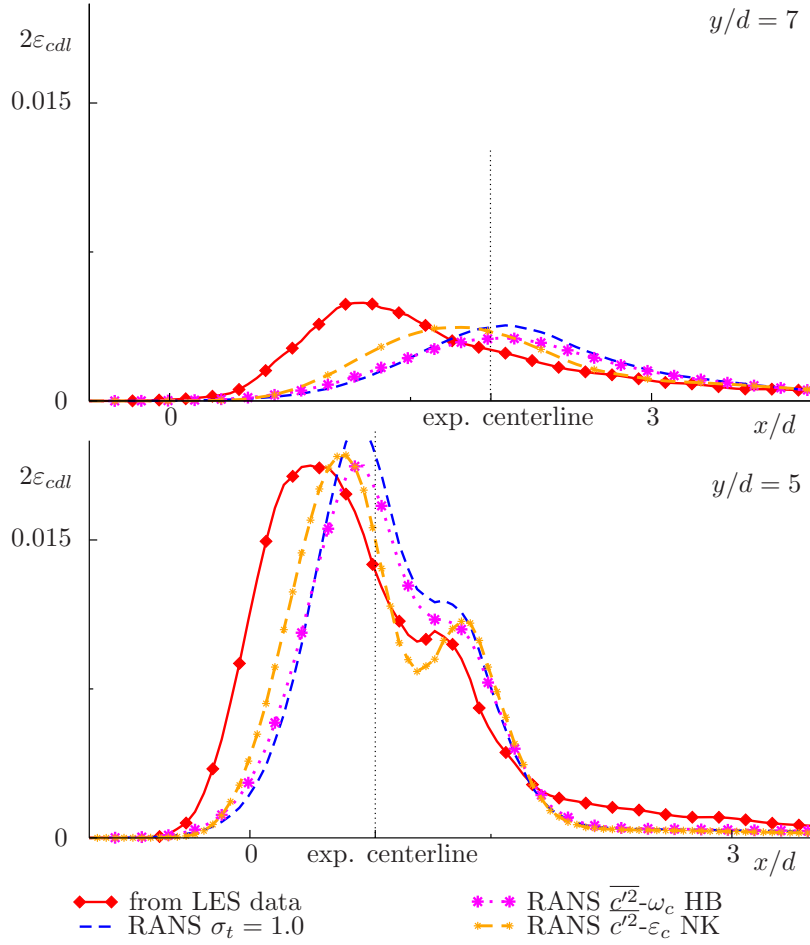


Figure 3.1.50: Dimensionless dissipation of the turbulent scalar variance $2\varepsilon_{cdl} = 2\varepsilon_c \cdot d/(U_{jet}C_{jet}^2)$ evaluated from LES data and resulting from RANS modeling. Equation 2.2.116 is used in conjunction with the constant σ_t . For turbulence modeling in RANS $k-\omega$ 1988 approach is employed. $z/d = 0$.

commonly assumed to be equal $\mathcal{R} = 0.5$. By contrast, in the two-equation turbulent scalar diffusivity models, the dissipation term is modeled using the ε_c or the ω_c equation, so τ_c is obtained as $\tau_c = \overline{c'^2}/2\varepsilon_c$. Figure 3.1.51 compares the scalar time scales τ_c evaluated from LES, the values given by both two-equation turbulent scalar diffusivity models, and τ_c obtained as $\tau_c = \mathcal{R}\tau_d$ with τ_d returned by the Wilcox 1988 $k-\omega$ model. Surprisingly, though the NK model gives slightly worse scalar mixing predictions than those produced by the HB model and the constant turbulent Schmidt number approach (see figures 3.1.36, 3.1.37), it closely reproduces the turbulent scalar time scale evaluated from LES (figure 3.1.51(a)). The model of Huang and Bradshaw gives the values close to those obtained using $\mathcal{R} = 0.5$ (employed in equation 2.2.116 for the constant turbulent Schmidt number calculations). Figure (figure 3.1.51(b)) shows that $\mathcal{R} = 0.5$ is a relatively good approximation of the turbulent scalar to velocity time scale ratio in the current case. The contours of \mathcal{R} given by the HB model show a good representation of the LES data on this parameter. The NK model underestimates the \mathcal{R} value.

The final study regarding the two-equation turbulent scalar diffusivity models accomplished in this section is the evaluation of the turbulent scalar diffusivity coefficient C_λ from equation 2.2.106.

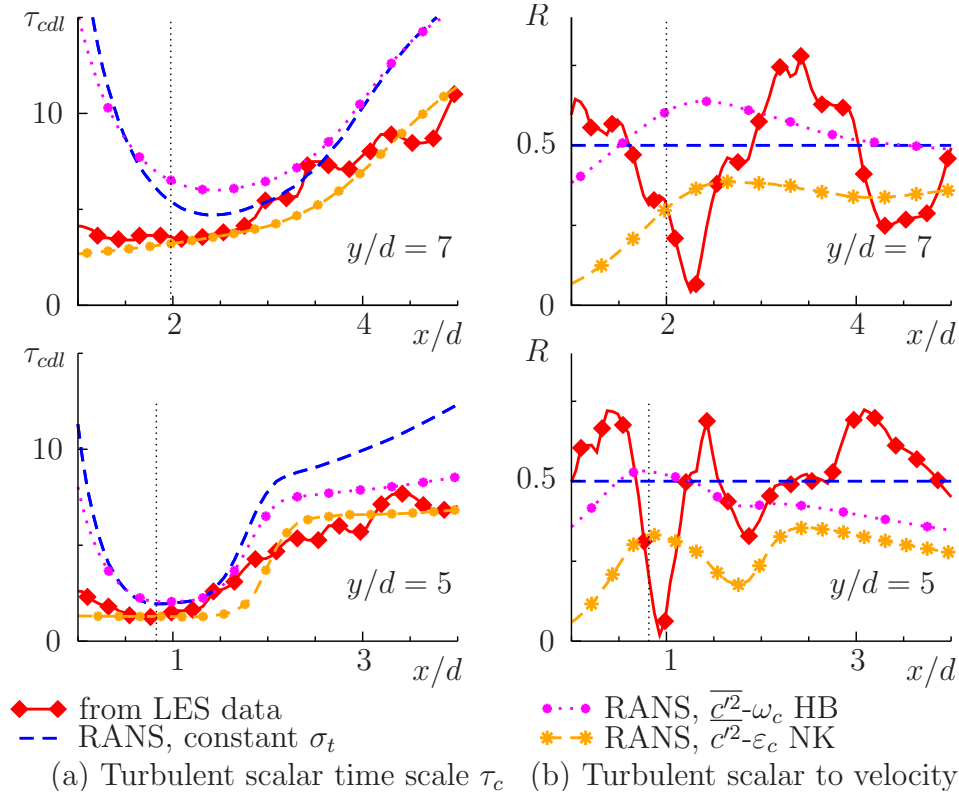


Figure 3.1.51: Dimensionless turbulent scalar time scale $\tau_{cdl} = \tau_c \cdot U_{jet}/d$ and turbulent scalar to velocity time scale ratio R evaluated from LES data and resulting from RANS modeling. The jet centerline locations are indicated by the vertical dotted lines. Equation 2.2.116 is used in conjunction with the constant σ_t . For turbulence modeling in RANS $k-\omega$ 1988 approach is employed. $z/d = 0$.

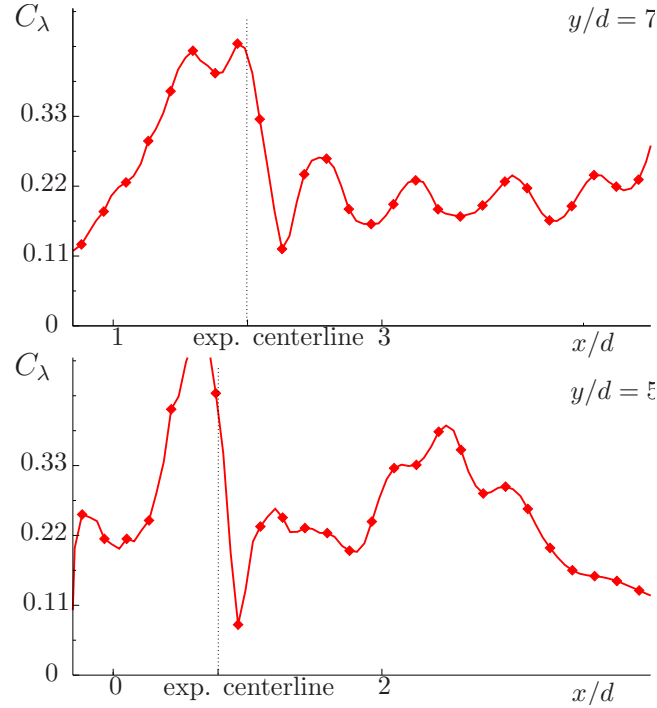


Figure 3.1.52: Turbulent scalar diffusivity modeling coefficient C_λ evaluated as $C_\lambda = \alpha_t/(k\tau_\lambda)$ using the LES data.

This coefficient is a direct analog to the turbulent viscosity coefficient C_μ of the turbulent viscosity models. Both the NK and the HB models employ the value $C_\lambda = 0.11$. From the present LES data C_λ can be computed as $C_\lambda = \alpha_t/(k\tau_\lambda)$ where τ_λ is the mixed time scale. As discussed in section 2.2.2.2, different variants for the construction of τ_λ exist. In the present evaluation this time scale is computed using the formulation from the NK and the HB models, $\tau_\lambda = \sqrt{(\overline{c'^2}/\varepsilon_c)(k/\varepsilon)}$. The profile of the resulting C_λ is presented in figure 3.1.52. The C_λ obtained from LES fluctuates around the values slightly higher than $C_\lambda = 0.11$ and drastically increases in the region upstream of the jet centerline. The trends observed here correspond with the observations of refs. [117, 14, 68] in which the values higher than $C_\lambda = 0.11$ (0.14 - 0.17) were needed in order to obtain correct mixing predictions in free shear flows. Taking into account the variability of the C_λ coefficient observed here, a conclusion can be made that either the models not employing the constant C_λ value would be a superior choice or an improved formulation of the τ_λ time scale is needed.

3.2 Confined coaxial jets

Complementing the studies regarding turbulence and mixing modeling for jet in crossflow, presented in the first part of this chapter, the second part is devoted to the analogous investigations for the swirling and non-swirling confined jets. These configurations are widely implemented for the primary fuel-oxidizer mixing in gas turbine combustors. Consequently, the accuracy of the mixing predictions for such flows is of extreme importance for the reliability of the gas turbine combustion simulations. A literature study on the previous numerical work for swirling and non-swirling confined coaxial jets can be found in section 1.2.2. In the same section also a more detailed motivation discussion is presented.

3.2.1 Description of the test cases and computational setup

The experimental data concerning confined jets used in this work comes from the studies of Roback and Johnson [104] and of Johnson and Bennett [58, 59]. In ref. [104] comprehensive measurements of the mean and fluctuating velocity and scalar field in confined coaxial swirling jets were reported. In the studies presented in refs. [58, 59] analogous measurements for non-swirling coaxial jets were performed. The test rig geometry and the boundary conditions in both test cases under investigation are similar. The geometry was chosen to mimic the confined coaxial jet combustor configuration (figure 3.2.1). The fuel is injected from the main central inlet and is mixed with the coflow in the mixing section after a sudden expansion. In the case of the swirling flow, the swirl is generated in the coflow channel. The swirl number which can be defined as

$$S = \frac{\int_0^{R_0} r^2 \overline{U} \overline{V}_\theta dr}{R_0 \int_0^{R_0} r \overline{U}^2 dr} \quad (3.2.1)$$

is $\mathcal{S} = 0.41$. Here R_0 is the radius of the swirler nozzle and \bar{U} and \bar{V}_θ are the components of mean velocity in the axial and tangential directions respectively. The expansion ratio of the mixing section defined as $(R/(R-h))$ is 2.1. Here R is the radius of the mixing section and h is the expansion step height. The radius of the mixing section is $R = 0.061m$; the length of the main annulus is $L = 0.775m$; the outer radius of the main inlet is $r_i = 0.0153m$. The Reynolds numbers of the main inlet based on its diameter $d_i = 2r_i$ is $Re = 15900$. The Reynolds number of the coflow based on the height of the coflow channel is $Re = 23700$. The bulk coflow velocity is about 3 times higher than the bulk inner jet velocity. The mass flow of the main jet is $0.391kg/s$, and the mass flow of the coflow is $3.331kg/s$. In the experiments [104, 58] water was used as the working fluid and dye was injected to visualize the mixing of the main jet; consequently, the density in the considered test cases is constant and the mixed scalar is passive and conservative.

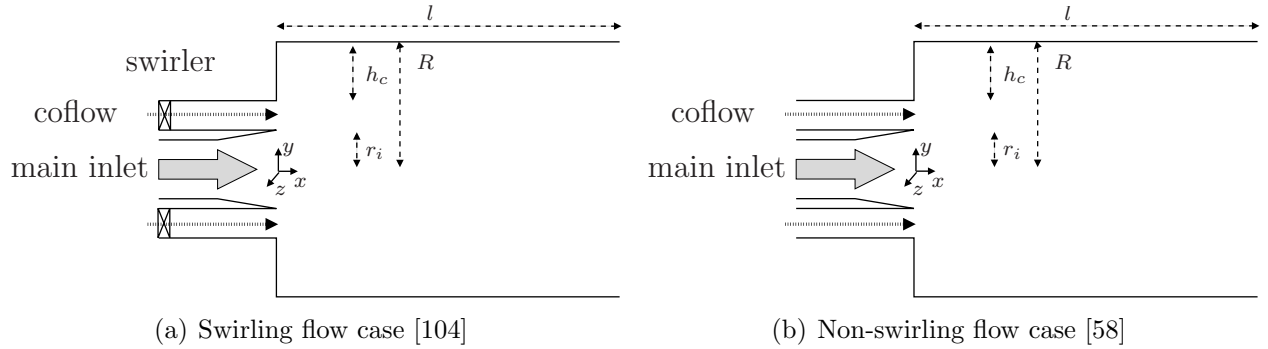


Figure 3.2.1: Schematic of the considered flow configurations.

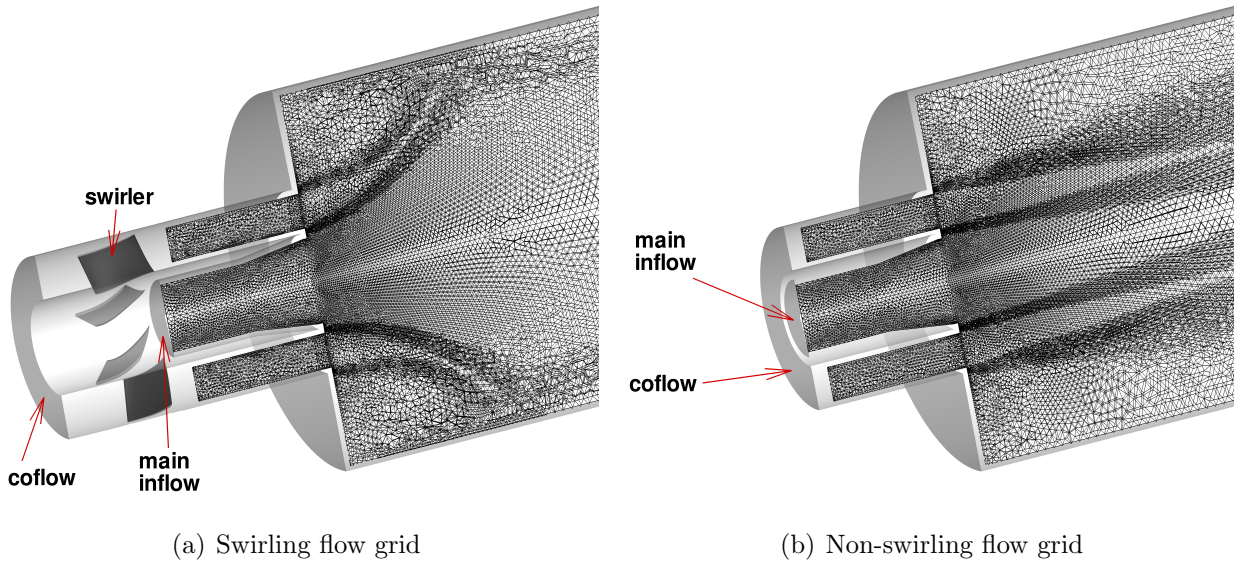


Figure 3.2.2: Inlet region of the computational domain. Tetrahedral elements of the grids comprising 60% less points than used in the present LES calculations are shown.

All calculations were done on polyhedral unstructured adapted grids with hexahedra-layers on the walls (figure 3.2.2). For the case of a swirling flow, the geometry of the swirler was reproduced in the computational grids according to the geometry description given in ref. [104]. The grids are refined in the regions of high velocity gradients based on the results of preliminary RANS calculations. The basic computational grids, on which the LES results presented below were obtained, consisted of approximately 3.5M points. The RANS grids consisted of only around 0.18M points, which is about 18 times less than the basic LES grids. Due to the axial periodicity/symmetry of the considered flows, the angular grid dimension was not 2π as in LES but $\pi/4$ with periodic boundary conditions applied on the xr -planes. The grid independence of the RANS simulations was confirmed. Several additional grid studies were performed for LES to exclude the possibility of large variability of the obtained results with further grid refinement. The computational time step in the LES calculations was chosen in order to ensure maximal CFL numbers of around 5. The temporal convergence of all presented results was confirmed in the computations.

The mean velocity at the coflow inlets in both cases was set by a block profile according to the experimental boundary conditions described in refs. [104, 58]. On the main inflow a fully developed pipe flow velocity profile according to the experimental mass flow rate was imposed. The profile was calculated in a preprocessing step by the SST $k-\omega$ model. In the RANS computations the turbulence data on the jet pipe inlet was also set using the values from the preprocessing pipe flow simulation. In the preliminary LES studies, two different types of the turbulence boundary conditions for both the main inlet and the coflow were investigated. The first approach (less time-consuming) is the setting of steady-state velocity profiles without additional fluctuations. The second approach is the prescription of the unsteady fluctuating boundary conditions according to Klein et al. [69]. Here the turbulent intensities were prescribed according to the values reported in refs. [104, 58]. The application of the latter boundary condition led to a slight increase in the computational cost because at every time step a new velocity field was calculated in a separate routine and then interpolated onto the inlet planes. Since the effect of the fluctuating boundary conditions was rather small, the main results, which required long time averaging, were obtained with the steady-state inlet velocity profiles.

3.2.2 Velocity field modeling

3.2.2.1 Mean and fluctuating velocity field predictions

For the purpose of flow visualization, the time-averaged 2D xy -streamlines from the LES calculations for both test cases are presented in figure 3.2.3. The flow character is clearly different in the swirling and the non-swirling case. In the swirling jet (figure 3.2.3(a)) a vortex breakdown occurs directly after the mixing section expansion, and a large central recirculation zone is formed. A second smaller recirculation zone is located in the corner of the mixing section. In the non-swirling case (figure 3.2.3(b)) the flow is characterized by a long jet core and a long

annular corner recirculation zone.

Figures 3.2.4 - 3.2.9 present the profiles of the mean and fluctuating velocities for both test cases. The experimental profiles are given along with the results of LES and RANS simulations. For the initial comparison of the RANS results, three of the most widespread models were selected: standard $k-\varepsilon$, $k-\omega$ SST, and Wilcox 1988 $k-\omega$. The axial measurement positions of the presented radial profiles are indicated in figure 3.2.3.

Regarding the mean axial flow velocity \overline{U}_x profiles presented in figure 3.2.4, both LES and RANS show a good agreement with the experimental data. The differences between the LES results and the results obtained by different RANS models are barely recognizable. LES shows a slightly better reproduction of the velocity profile form in the swirling case at the axial position $x = 0.051m$ (figure 3.2.4(a)) as well as at the downstream locations in the non-swirling case (figure 3.2.4(b)).

Figure 3.2.5 shows the profiles of the y -velocity component. The experimental data is rather noisy and the absolute level of \overline{U}_y in the non-swirling case appears to be under predicted in all simulations. As in the \overline{U}_x predictions, the differences between RANS and LES can be observed primarily at the position $x = 0.051m$ for the swirling flow (figure 3.2.5(a)) and at $x = 0.152 - 0.203m$ for the non-swirling case (figure 3.2.5(b)). LES again is slightly more accurate than all tested RANS models. The differences in the predictions given by three different RANS models are negligible.

When considering only the mean velocity profiles, no statement can be made about the clear

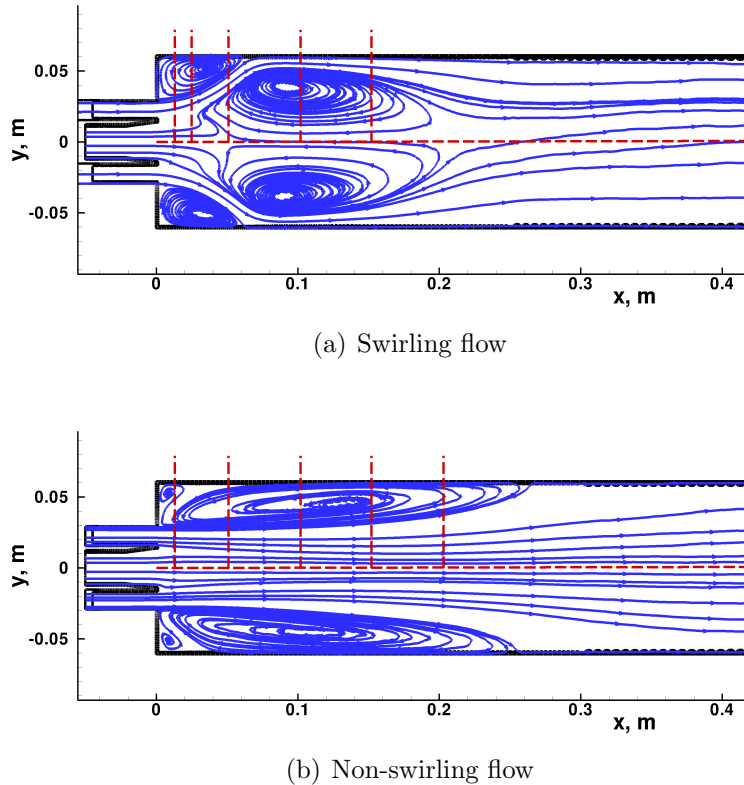


Figure 3.2.3: 2D xy -streamlines and positions of the presented profiles.

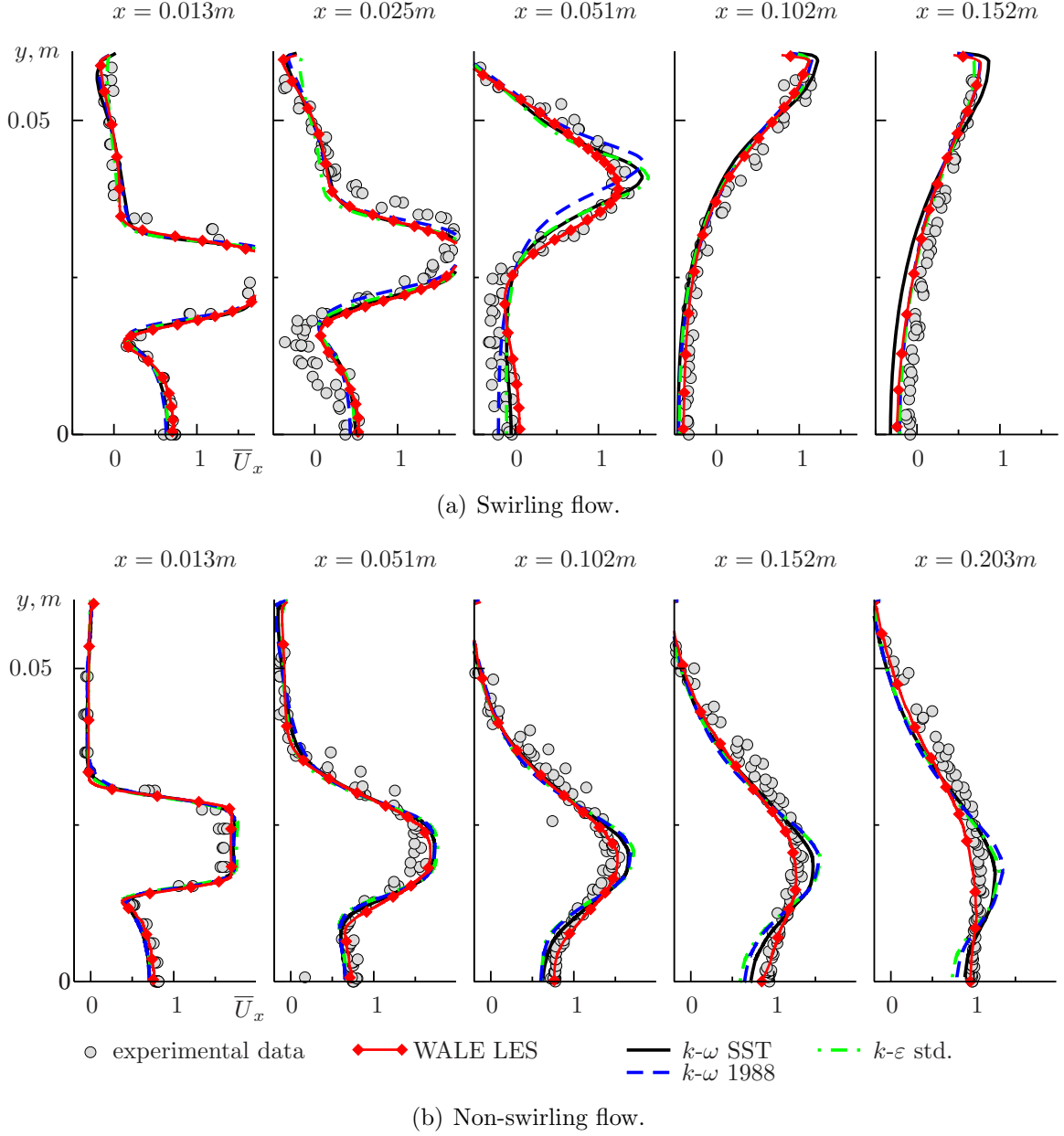


Figure 3.2.4: Axial component of the mean flow velocity \bar{U}_x . Swirling and non-swirling confined jets. RANS and LES in comparison with experimental data.

superiority of LES. RANS also predicts the x - and y -velocities reasonably well at much lower computational cost, in the current simulations at least 120 times more efficient than LES. Only the fluctuating velocity profiles can elucidate the qualitative differences between RANS and LES.

The radial profiles of the turbulent kinetic energy are presented in figure 3.2.6. For the swirling flow, figure 3.2.6(a) reveals a strong underestimation of k in all RANS simulations. In contrast to RANS, LES shows here a much better trend and under predicts the level of the turbulent kinetic energy only slightly. In the non-swirling case (figure 3.2.6(b)), LES even tends to overestimate k , especially in the high shear regions in two first profiles. RANS predicts k reasonably well at the initial measurement stations but further downstream has a tendency

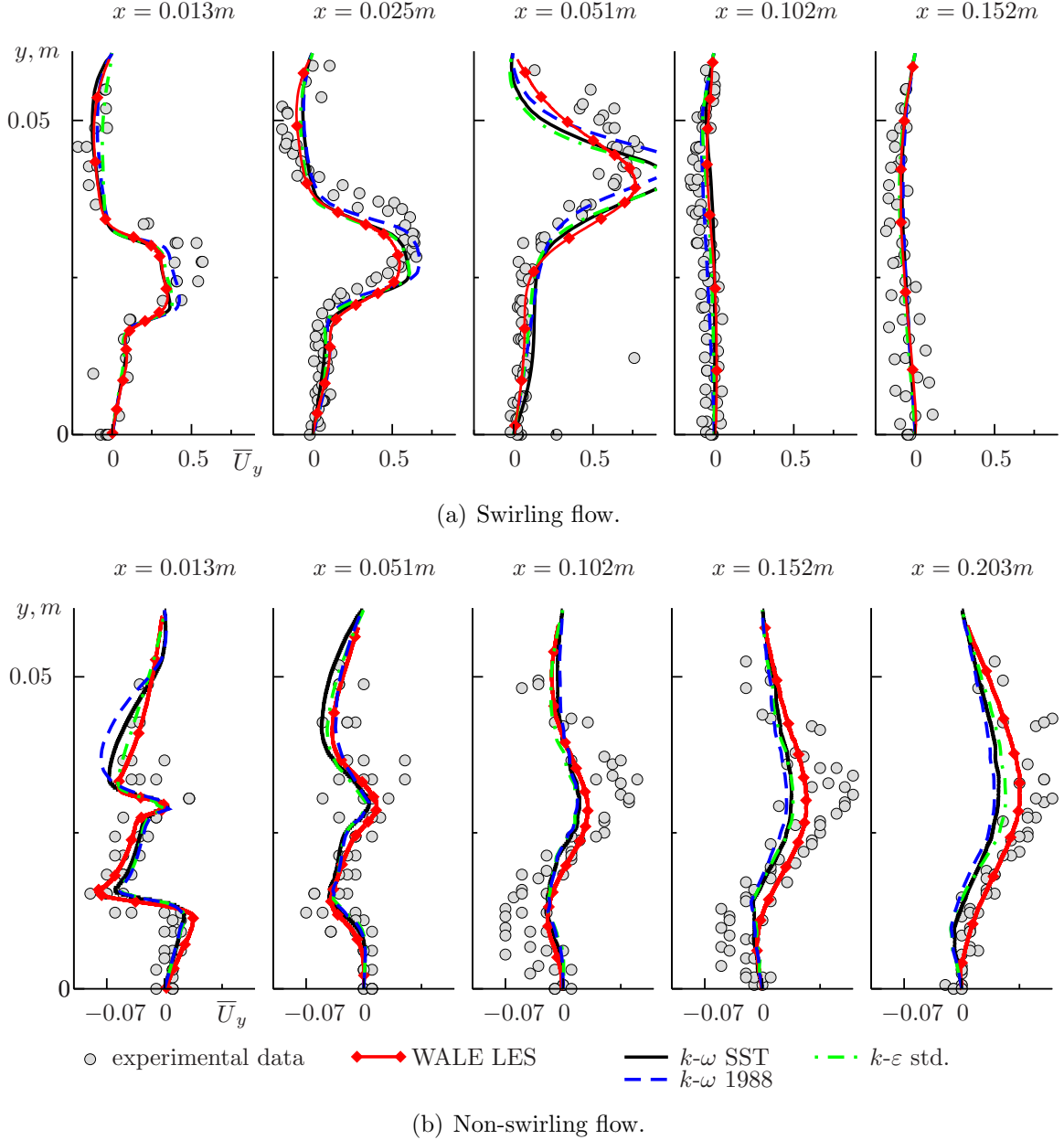


Figure 3.2.5: Vertical component of the mean flow velocity \bar{U}_y . Swirling and non-swirling confined jets. RANS and LES in comparison with experimental data.

to under predict k as in the swirling case. Here again no significant difference between the considered RANS modeling approaches can be observed. The Wilcox 1988 $k-\omega$ model performs slightly worse in the non-swirling case and slightly better in the swirling case. The profiles given by the SST and the standard $k-\varepsilon$ models are almost identical.

Further validation of the fluctuating velocity field predictions can be found in figures 3.2.7 - 3.2.9. The trends observed in the validation of k discussed in the last paragraph are also present here; however, there is a difference in the prediction quality of different fluctuating variables. The variance of the axial velocity $\overline{u_x'^2}$ is for the most part underestimated by RANS in both cases (figure 3.2.7). For $\overline{u_y'^2}$ (figure 3.2.8) this underestimation is seen only in the swirling jet case in the first three locations, and further downstream the fluctuation levels given by RANS

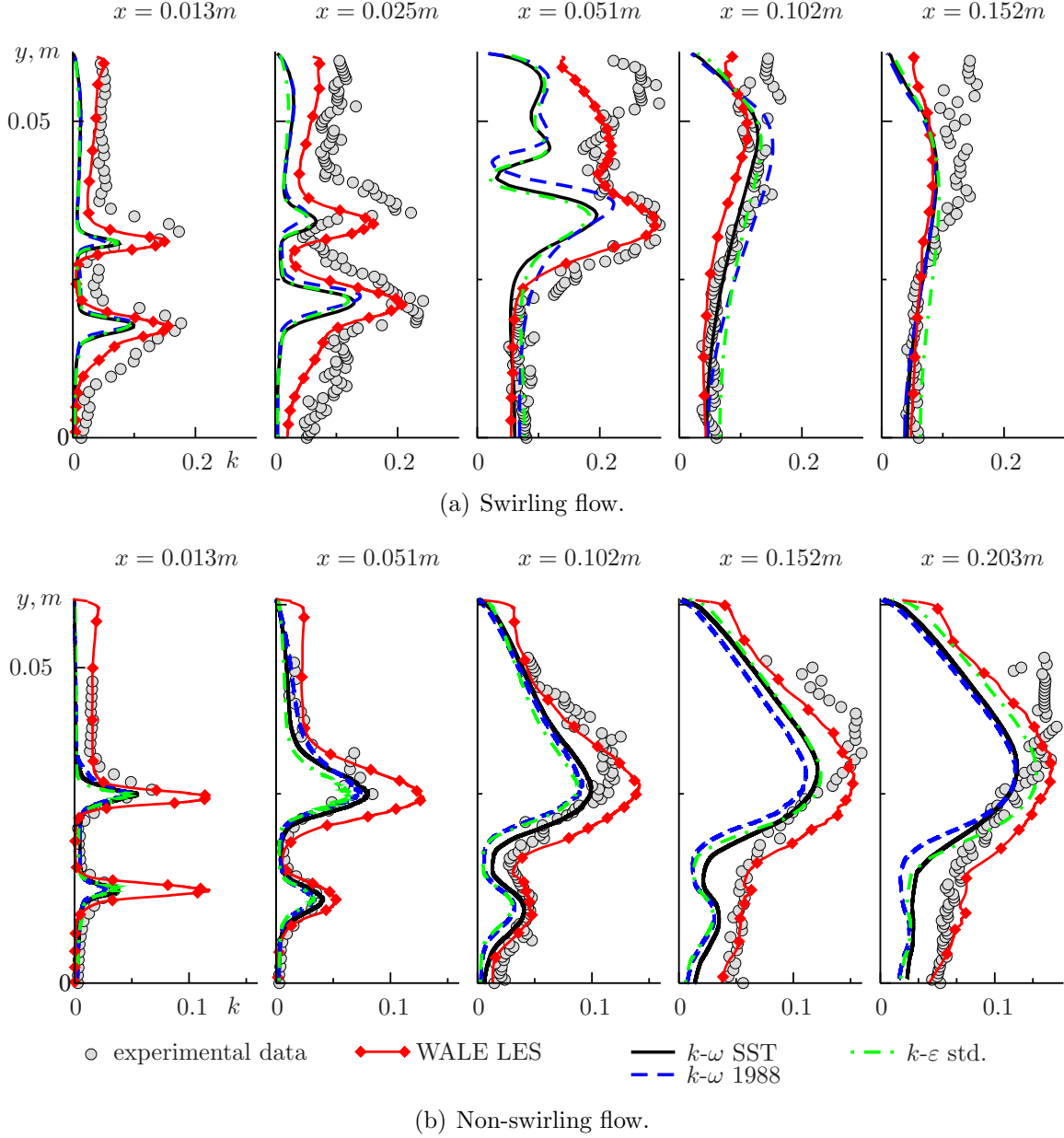


Figure 3.2.6: Turbulent kinetic energy k . Swirling and non-swirling confined jets. RANS and LES in comparison with experimental data.

correspond well with the measured values and exceed the levels predicted by LES. For the non-swirling case the underestimation of $\overline{u_y'^2}$ by RANS can be observed only at $x = 0.152 - 0.203m$ in the regions close to jet centerline. LES over predicts $\overline{u_x'^2}$ in the non-swirling jet, but it shows a high degree of accuracy for $\overline{u_x'^2}$ in the swirling jet and for $\overline{u_y'^2}$ in both cases. The shape of all profiles is well reproduced by LES (better than in RANS). Thus, generally, LES is here again more accurate than RANS; furthermore, fluctuations of U_y are represented by both methods better than fluctuations of U_x .

The validation of the modeled Reynolds shear stresses $\overline{u'_x u'_y}$ is presented in figure 3.2.9. Unfortunately, the statement about the relative quality of different approaches is here rather hard to make due to noisy experimental data, particularly in the swirling jet case. Based on the profiles in the locations near to jet exit, a conclusion can be made that LES data tends

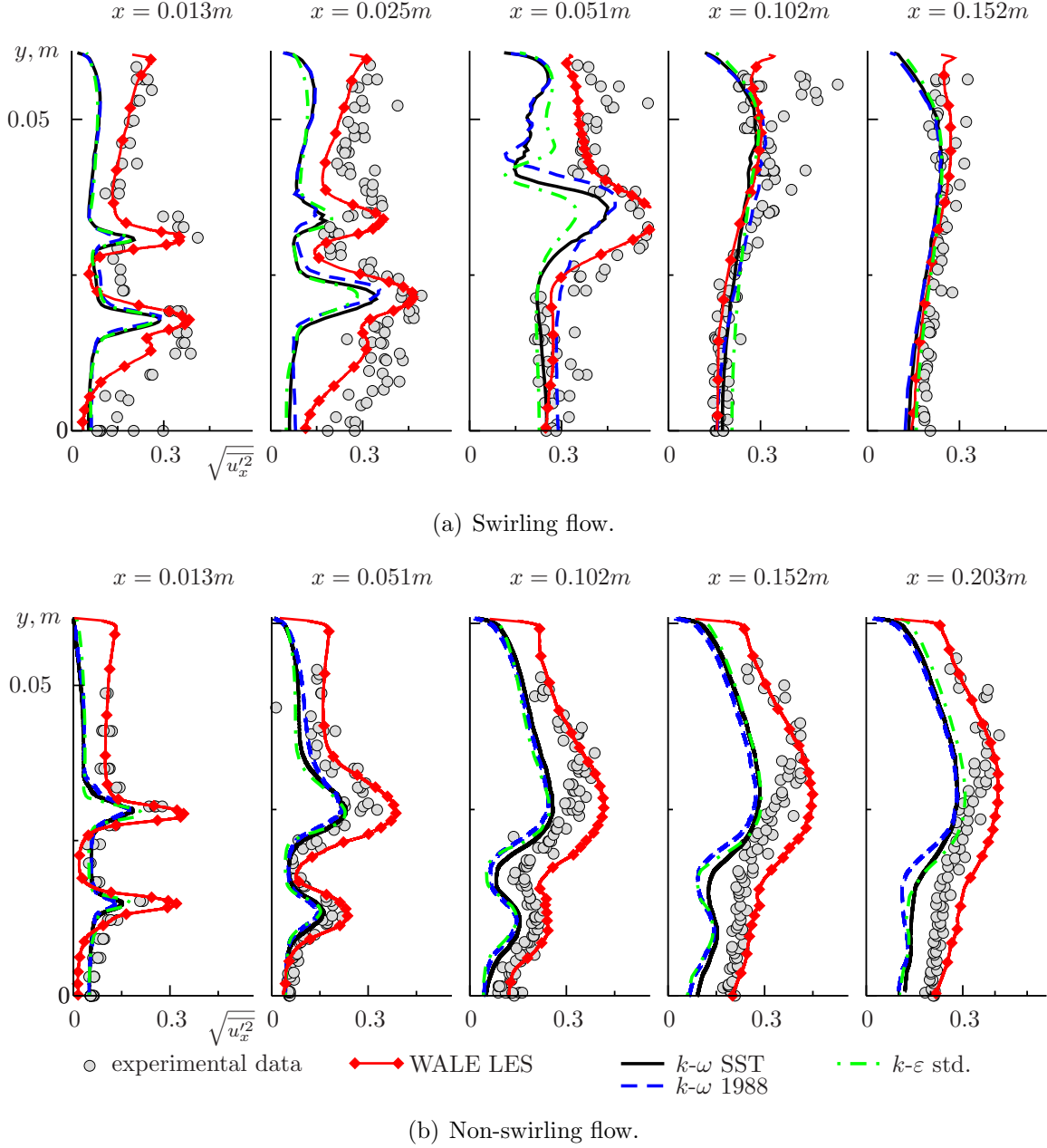
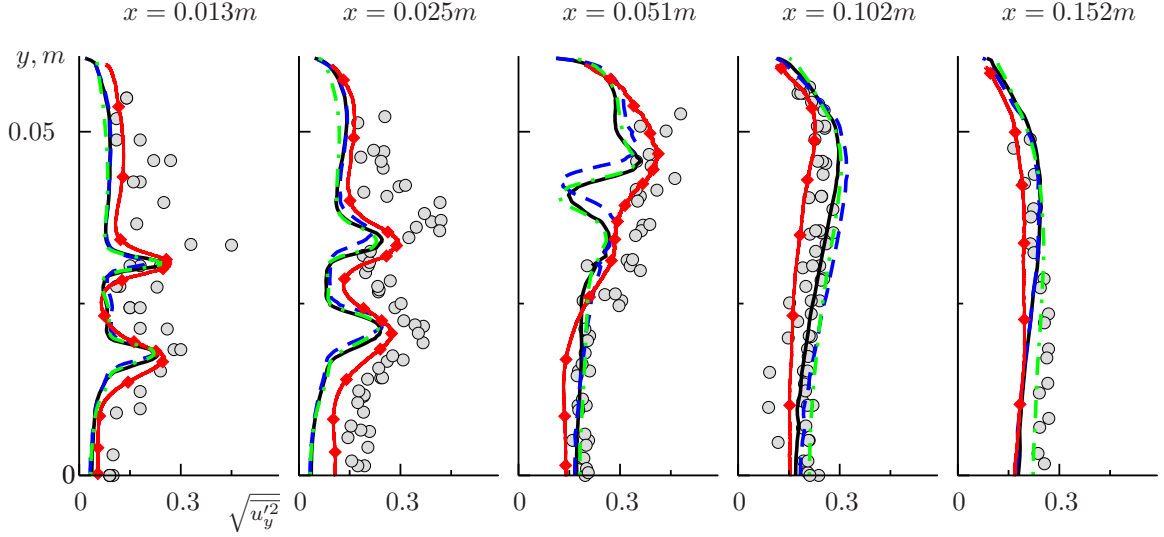


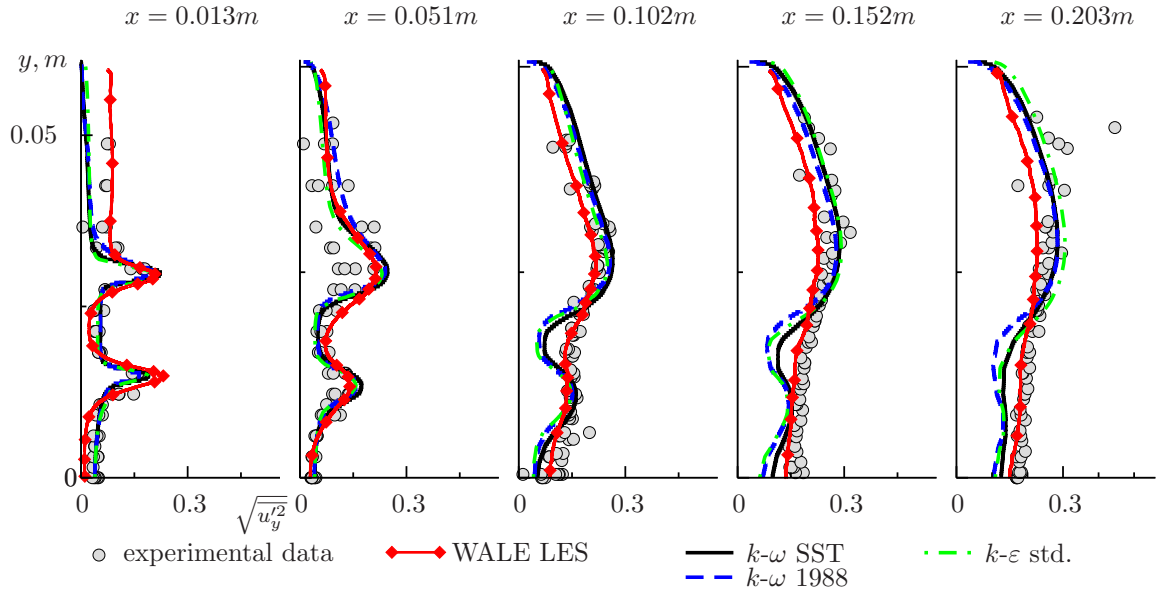
Figure 3.2.7: RMS fluctuations of the axial component of the mean flow velocity $\sqrt{u'^2_x}$. Swirling and non-swirling confined jets. RANS and LES in comparison with experimental data.

to lie above the experimental values of $\overline{u'_x u'_y}$ in the shear regions. This trend is seen especially clear in the non-swirling case and much less for the swirling jet.

Considering all presented data, it is concluded that although the selected RANS models are able to give satisfactorily predictions of the mean velocity field, the overall accuracy given by LES is higher. The main weakness of RANS is a strong under prediction of the turbulent kinetic energy, most clearly revealed for the swirling flow and in the downstream locations of the non-swirling flow. The under prediction of k in the RANS simulations of the swirling jets was also observed by other authors [118] which used different types of the RANS models. In the RANS models used, k is directly linked to the turbulent viscosity ν_t and, consequently, to



(a) Swirling flow.



(b) Non-swirling flow.

Figure 3.2.8: RMS fluctuations of the vertical component of the mean flow velocity $\sqrt{u_y'^2}$. Swirling and non-swirling confined jets. RANS and LES in comparison with experimental data.

the turbulent scalar diffusivity α_t . Thus the failure to capture k accurately can also negatively influence the scalar mixing simulation results. This situation was already pointed out in section 3.1 for the jet in crossflow case. The consequences of the underestimation of k for the mixing modeling in both confined coaxial jet cases will be discussed in section 3.2.3.1.

3.2.2.2 Further studies on the accuracy of RANS models for the velocity field predictions

The profiles presented in the previous section did not reveal any significant differences in the results of three different RANS models. This is in contrast to the jet in crossflow results

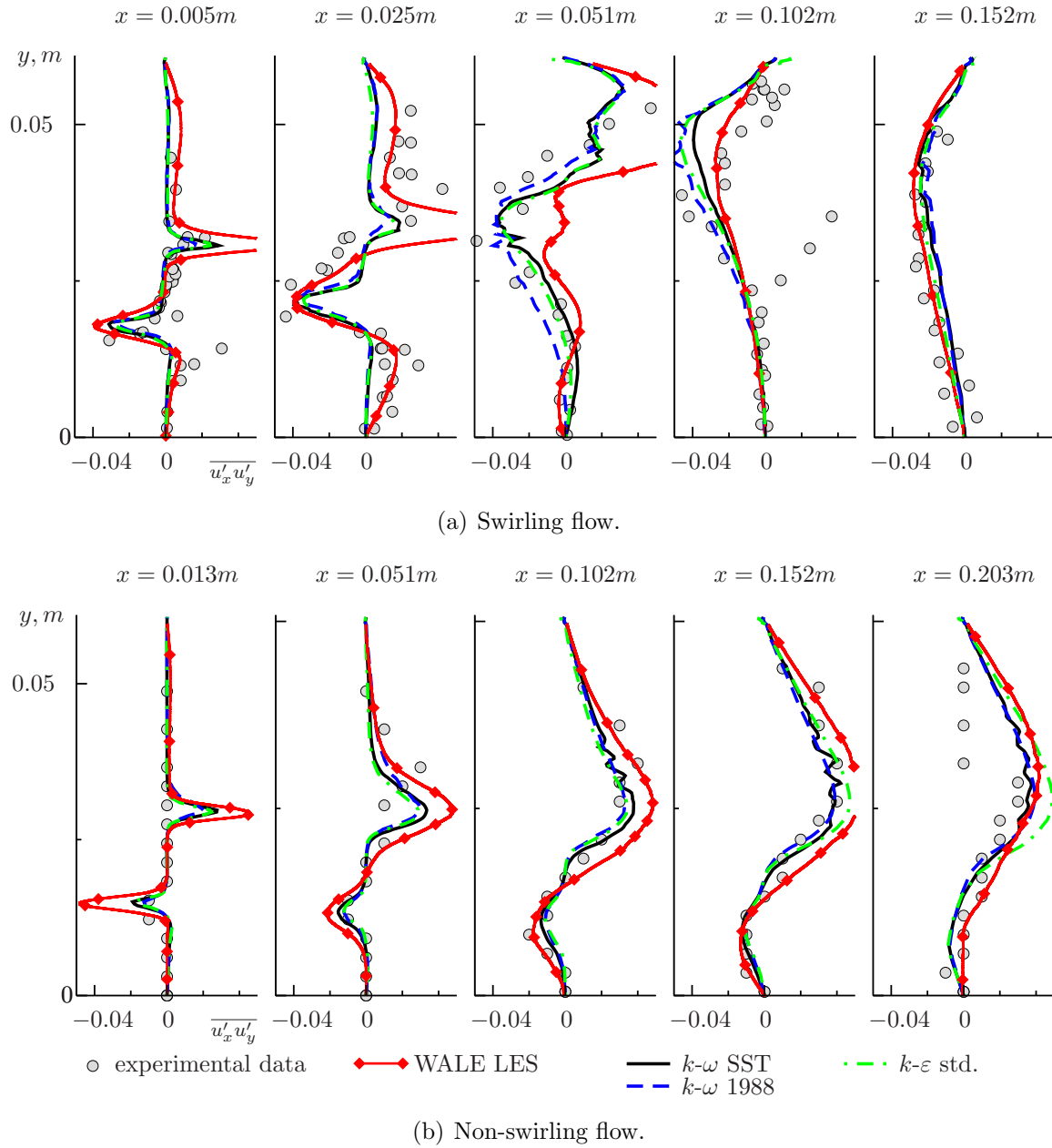


Figure 3.2.9: Reynolds shear stress $\overline{u'_x u'_y}$. Swirling and non-swirling confined jets. RANS and LES in comparison with experimental data.

considered in section 3.1.2.1 where the difference between the predictions given by the standard $k-\varepsilon$ model, the SST $k-\omega$ model of Menter, and the 1988 $k-\omega$ model of Wilcox were quite severe. In this subsection further studies related to the accuracy of different $k-\omega$ -type models are presented. The aim is to gain additional knowledge about the dependence of the RANS results in the considered cases on the various model equation terms and corrections.

3.2.2.2.1 Different variants of the Wilcox $k-\omega$ model First, the 1988, 1998, and 2006 variants of the Wilcox $k-\omega$ model (see sections 2.2.1.4 and 2.2.1.7) are compared. Figures 3.2.10 and 3.2.11 present the profiles of the x -component of the flow velocity vector and of the turbulent kinetic energy given by these approaches for both the swirling and the non-swirling flow. Moreover, the profiles produced by the SST $k-\omega$ model are presented. In both cases the

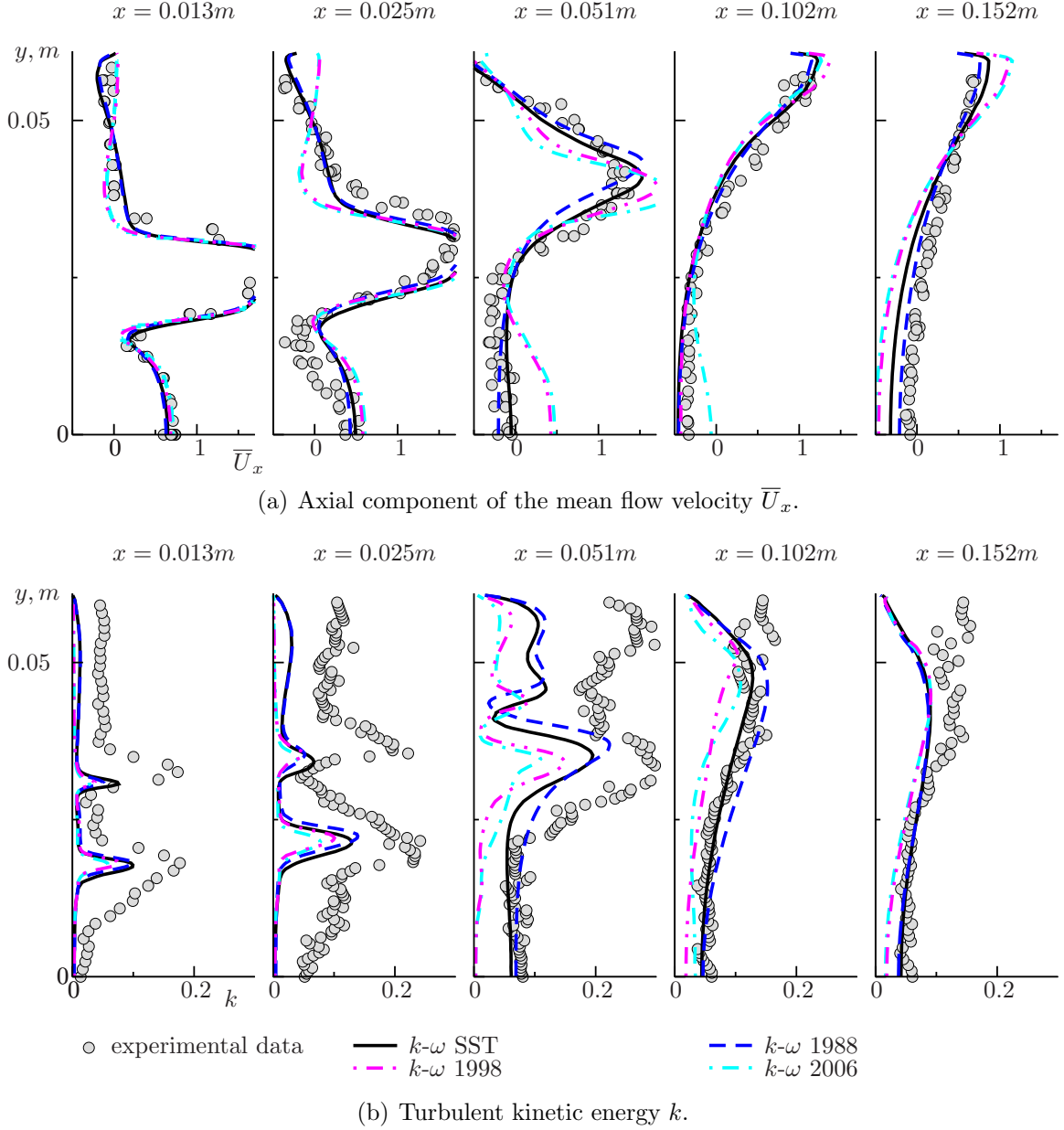


Figure 3.2.10: Swirling flow. Different $k-\omega$ models. Axial component of the flow velocity vector and turbulent kinetic energy.

later versions of the Wilcox model (1998 and 2006) show a more drastic under prediction of turbulence than the 1988 $k-\omega$ model or the SST model. This is clearly seen not only in the turbulent kinetic energy profiles, but for the swirling jet case also in the \bar{U}_x velocity profiles presented in figure 3.2.10(a). The central jet penetration depth is over predicted at $x = 0.051m$. The next sections will present additional investigations on the reasons for such behavior of the 2006 and the 1998 $k-\omega$ models.

3.2.2.2.2 Influence of the round jet correction This section is devoted to the study of the influence of the round jet correction term first introduced by Pope for the standard $k-\varepsilon$ model and later adapted by Wilcox for his 2006 and 1998 $k-\omega$ models (see sections 2.2.1.2 and 2.2.1.7). Figures 3.2.12 and 3.2.13 show for both considered flow configurations in solid lines

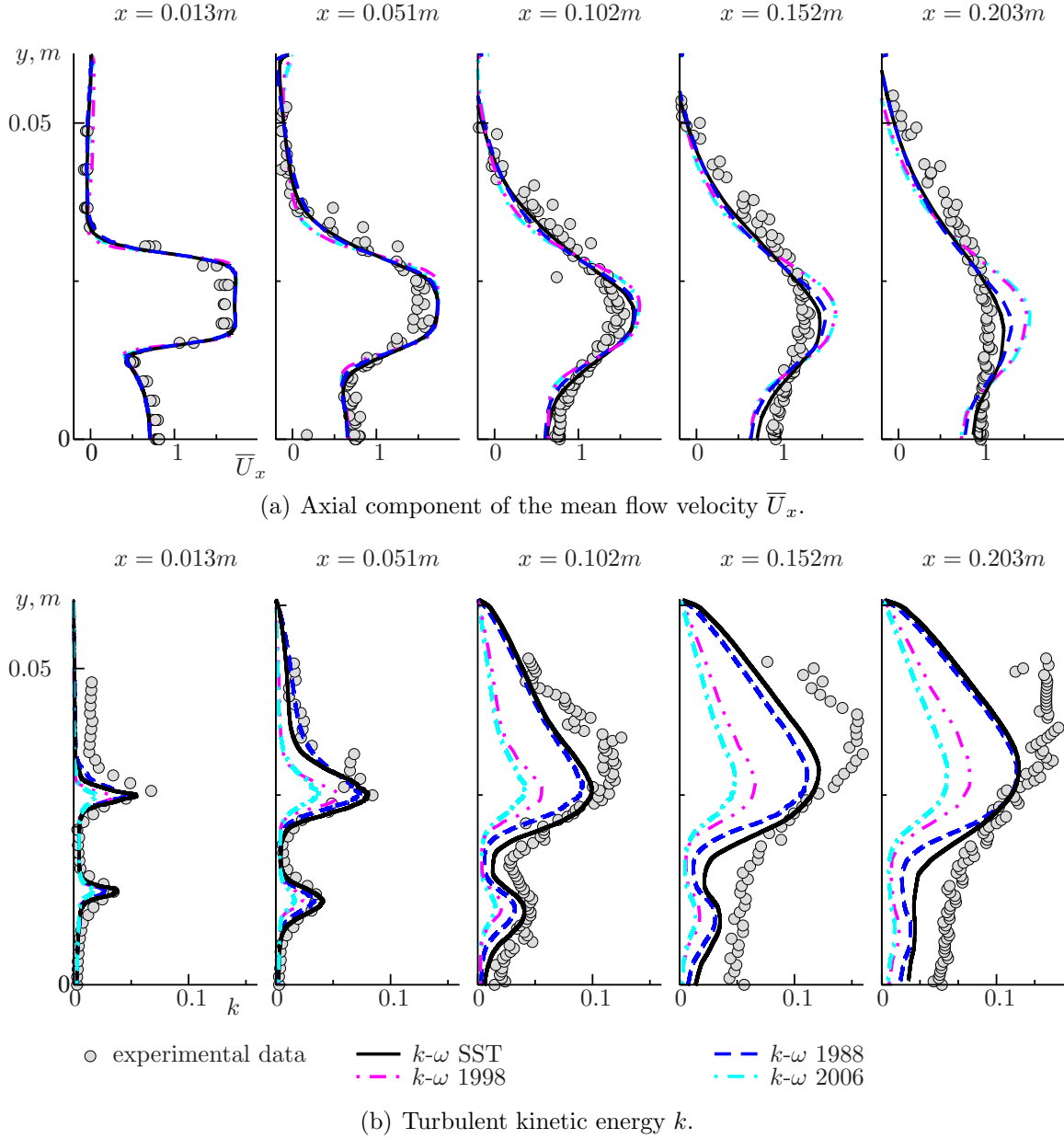


Figure 3.2.11: Non-swirling flow. Different $k-\omega$ models. Axial component of the flow velocity vector and turbulent kinetic energy.

the profiles of the x -component of the flow velocity vector and of the turbulent kinetic energy given by the 1998 and the 2006 $k-\omega$ models of Wilcox as well as by the standard $k-\varepsilon$ model with the limited version of the Pope correction (described in section 2.2.1.2). Dashed lines present the profiles obtained by the same models but without the round jet correction terms (Pope vortex stretching measure χ_ω or χ_p deliberately set to zero values). The absence of the round jet correction increases the level of the turbulent kinetic energy and thus the prediction accuracy for all approaches tested here. For the $k-\varepsilon$ model this effect is much weaker than for both $k-\omega$ models because of the limiter appearing in the correction version used for the present calculations (see section 2.2.1.2).

The results presented in figures 3.2.12 and 3.2.13 are not surprising since, as discussed in section 3.1.2.2.2 for jet in crossflow, the implemented round corrections always act as a sink of

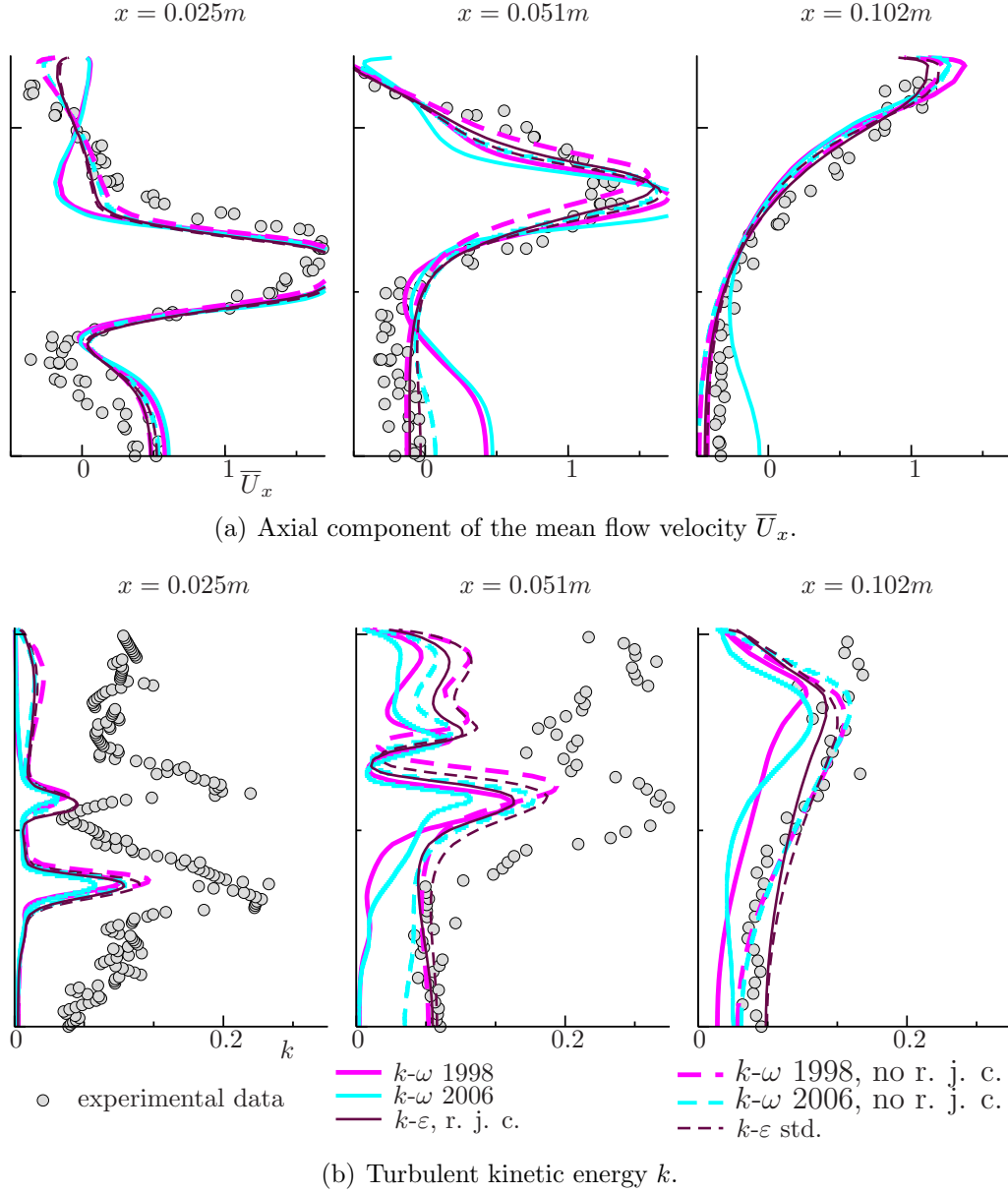


Figure 3.2.12: Swirling flow. Influence of the round jet correction. Axial component of the flow velocity vector and turbulent kinetic energy.

turbulence reacting on the round shape of the jet nozzle. It is clearly seen, however, that even in the absence of the round jet correction the models under consideration tend to underestimate the turbulence. Here, as in the jet in crossflow test case, the assumption can be made that in the considered flows probably additional physical effects not yet accounted for by the studied models play an important role. Even the flow dynamics of the non-swirling confined coaxial jet case studied in this chapter is quite different than the academic free round jet case considered in sections 2.2.1.2 and 2.2.1.7. The coflow velocities in the confined coaxial jet case are higher than the velocities of the central jet. As shown in the experimental work [59], the coflow dominance influences the turbulent momentum and scalar diffusion characteristics in this case (see sections 3.2.3.1.3 and 3.2.3.2.1 for a detailed discussion). This fact, as well as the effects of swirl in the second case considered here, are not replicated by the tested modeling approaches.

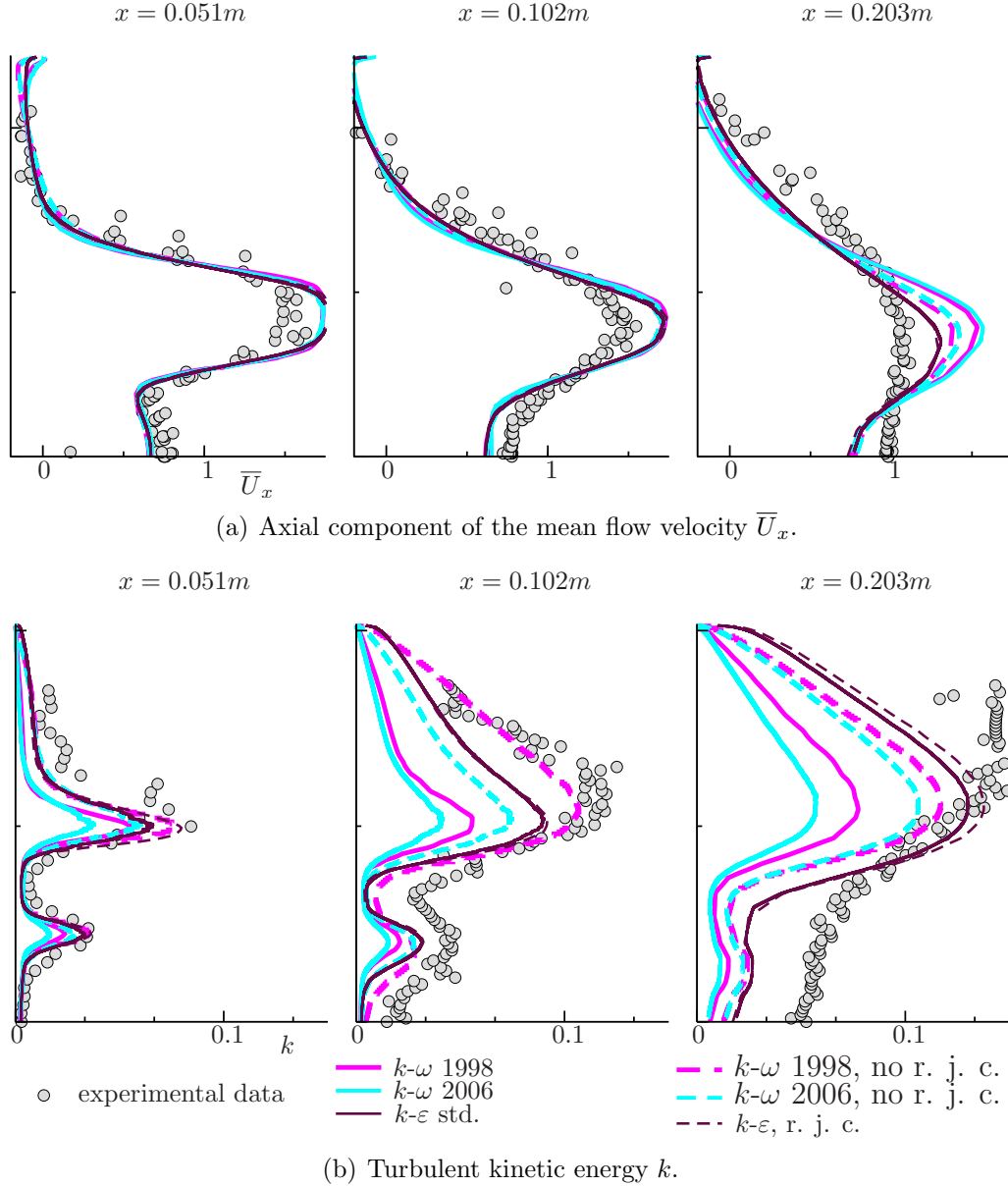


Figure 3.2.13: Non-swirling flow. Influence of the round jet correction. Axial component of the flow velocity vector and turbulent kinetic energy.

A more suitable model has to be developed that can encode these effects in order to improve simulation quality.

3.2.2.2.3 Influence of the streamline curvature correction In this section the influence of the streamline curvature correction developed by Hellsten (ref. [46]) for the SST model of Menter is studied. For the jet in crossflow test case considered earlier (see section 3.1.2.2.3), this correction showed a promising trend by increasing the under predicted level of turbulence. Figure 3.2.14 shows the results obtained after the application of the Hellsten correction to the swirling confined jet case. This correction decreases the level of k near to the jet centerline. In contrast, in the main shear layer region at $x = 0.051m$ the level of turbulence is becoming higher. The overall effect of the SST correction of Hellsten is mixed and no definitive statement about its advantage or disadvantage can be made. Either an improved streamline curvature

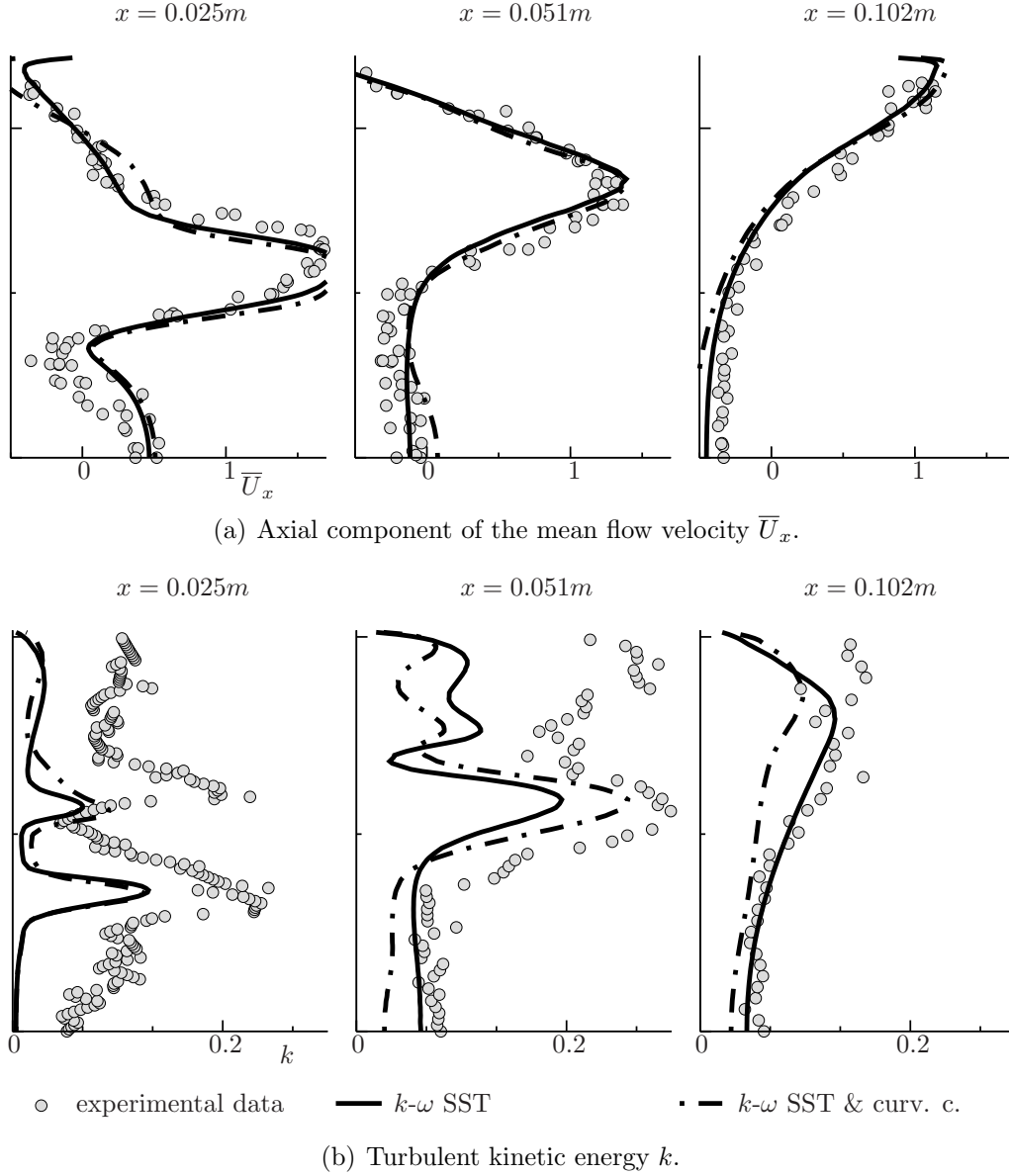


Figure 3.2.14: Swirling flow. Influence of the streamline curvature correction. Axial component of the flow velocity vector and turbulent kinetic energy.

correction is needed or other physical effects should be taken into account in the modeling of this test case. For the non-swirling case the curvature correction did not have any noticeable effect and for this reason the results of its application for this flow are not presented.

3.2.2.2.4 Influence of the shear stress turbulent viscosity limiter In this section the influence of the shear stress turbulent viscosity limiter in the SST k - ω and of the Wilcox 2006 k - ω models is studied. An analogous study was presented in section 3.1.2.2.4 for the jet in crossflow test case. In the jet in crossflow configuration the turbulent viscosity limiter caused a strong ν_t damping in the Wilcox 2006 model. In contrast, for the flows considered in this section the influence of the turbulent viscosity limiter is marginal for both tested k - ω models. Only the turbulent kinetic energy profiles presented for both test cases in figure 3.2.15 show a slight difference in the results obtained with and without limiter (all figure notations are the

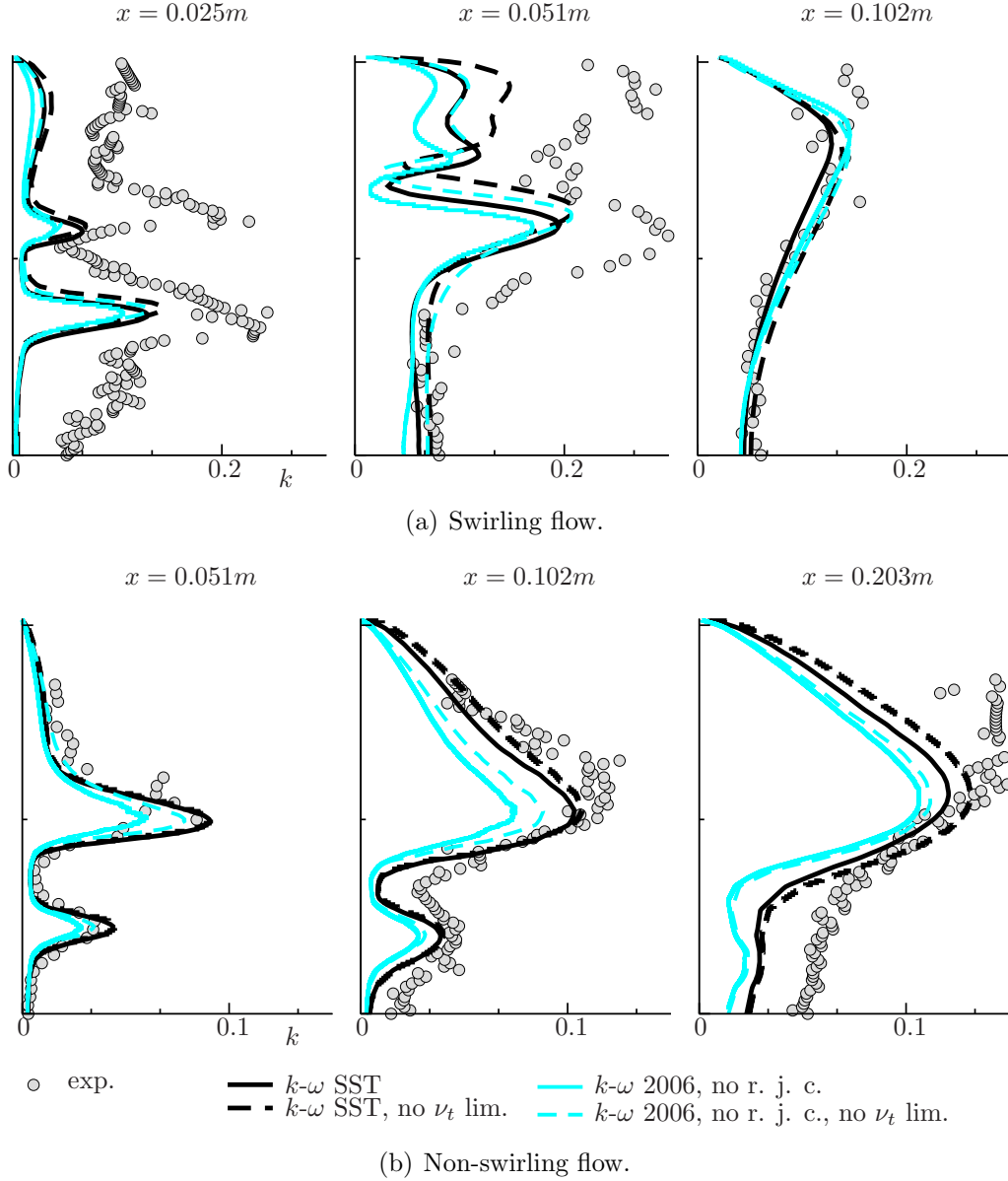


Figure 3.2.15: Swirling jet and non-swirling jet. Turbulent kinetic energy k . Influence of the shear stress turbulent viscosity limiter.

same as used in section 3.1.2.2.4). The mean velocity profiles are not presented since for both models the produced profiles with and without limiter are extremely similar.

3.2.2.2.5 Influence of the cross-diffusion term Figures 3.2.16 and 3.2.17 present a study on the influence of the cross-diffusion term in the SST and the Wilcox 2006 $k-\omega$ models. An analogous study for the jet in crossflow test case can be found in section 3.1.2.2.5. All notations in figures 3.2.16 and 3.2.17 are the same as used in section 3.1.2.2.5. From the analysis presented here, the same conclusions as in section 3.1.2.2.5 can be drawn about the role of the cross-diffusion term in both models. For the Wilcox 2006 model the profiles obtained in the absence of the cross-diffusion term are quite similar to the profiles given when this term is present. This can be explained by the relatively small value of the cross-diffusion term constant (see discussion in section 3.1.2.2.5). For the SST model, where the modeling constant of the cross-diffusion

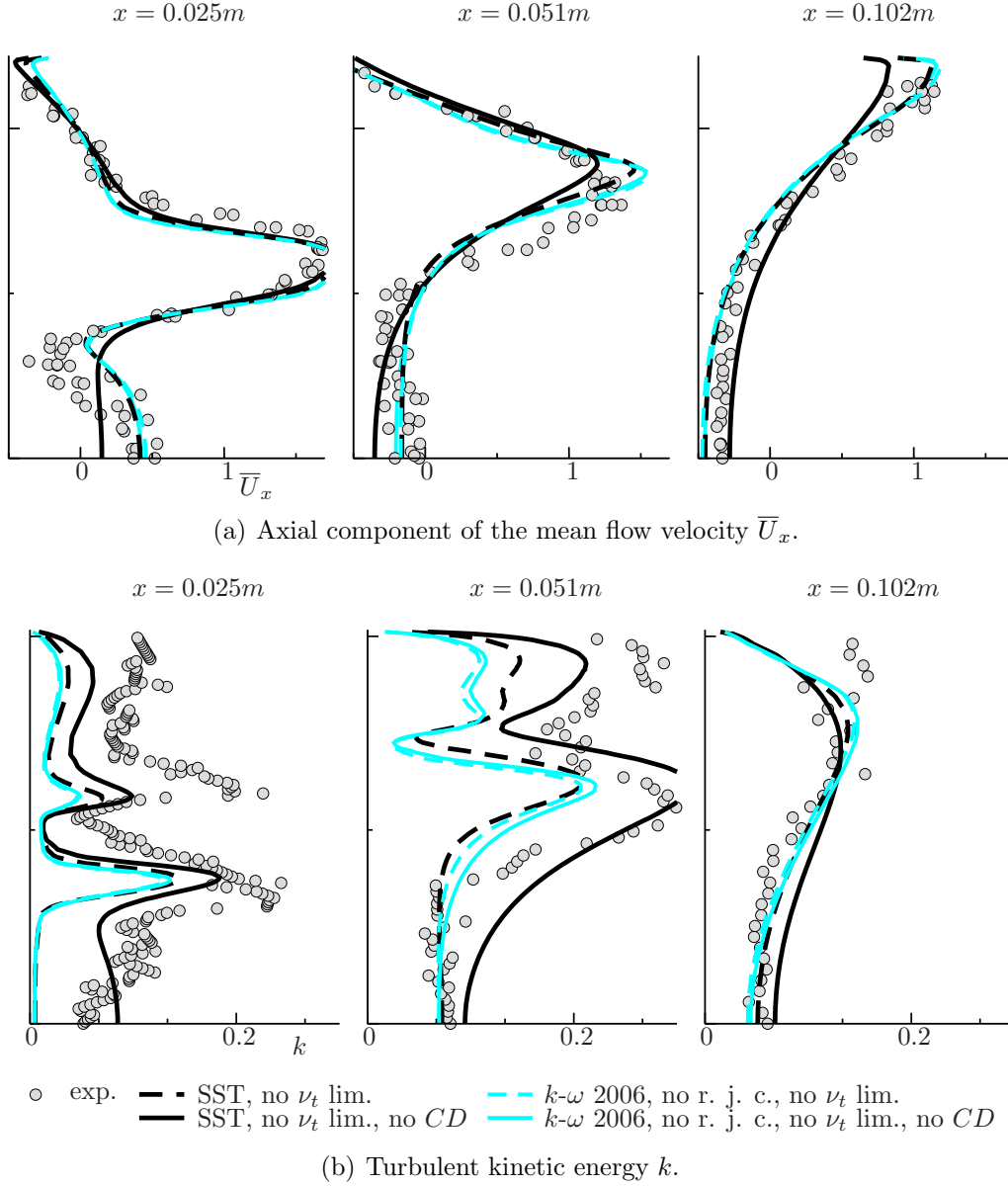


Figure 3.2.16: Swirling flow. Influence of the cross-diffusion term. Axial component of the flow velocity vector and turbulent kinetic energy.

term is more than an order of magnitude higher than in the Wilcox 2006 model, the damping influence of this term is much more evident. All additional conclusions on the influence of the dissipation equation modeling constants reached in section 3.1.2.2.5 for the jet in crossflow case are also applicable here for both confined coaxial jet flows.

Although for the coaxial flows considered in this section, as in the jet in crossflow test case, the absence of the cross-diffusion term partly produces a favorable effect by increasing the under predicted level of turbulence, it does not imply that this term should be generally omitted in the modeling. Many results available in the literature [83, 84, 128] demonstrate the positive effect of the cross-diffusion term for modeling accuracy in a large variety of cases. The elimination of this term or its simple ad hoc adjustment in order to compensate for the under predicted turbulence levels would reduce the model's universality and probably cause unsatisfactory results for other

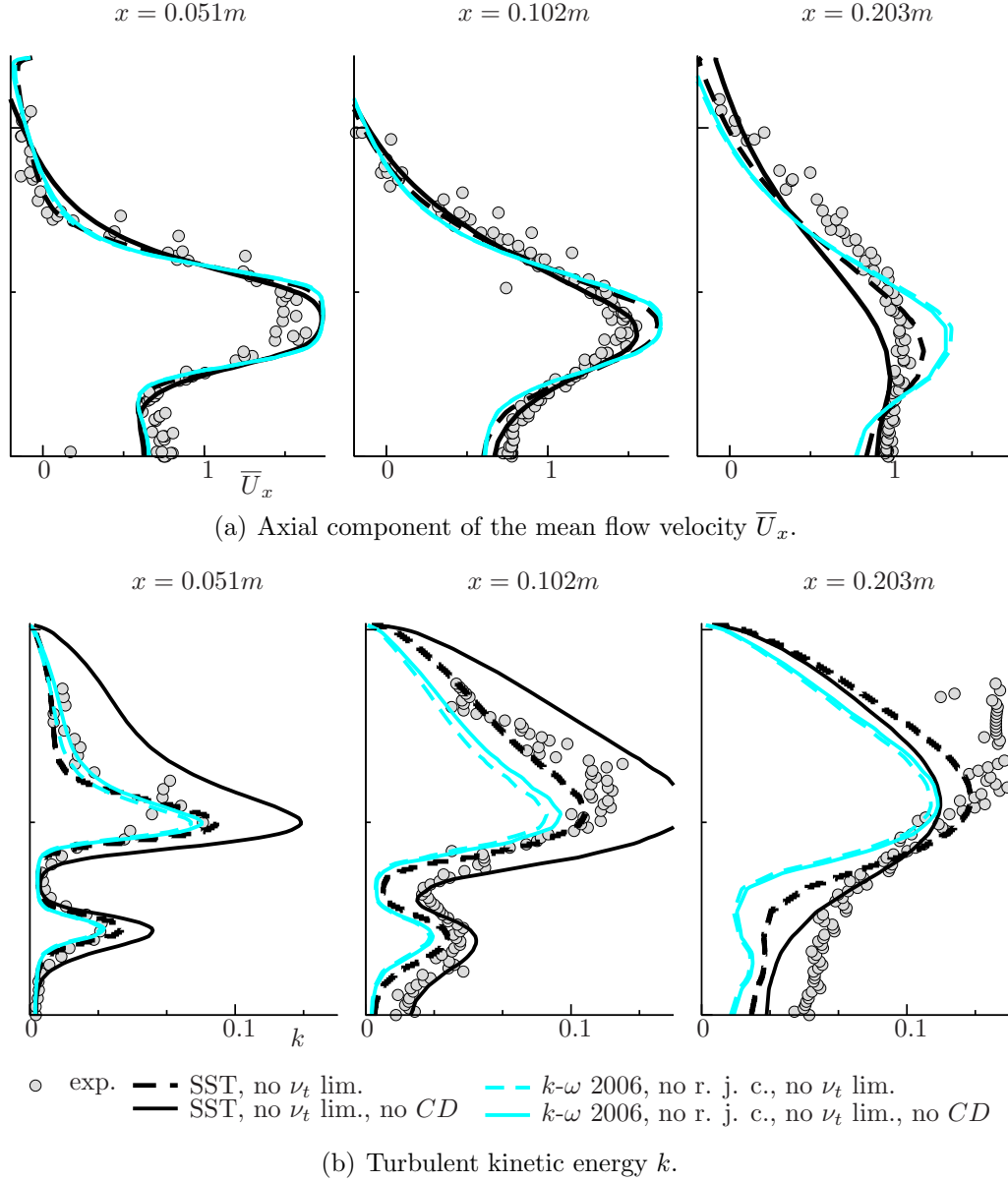


Figure 3.2.17: Non-swirling flow. Influence of the cross-diffusion term. Axial component of the flow velocity vector and turbulent kinetic energy.

applications. A more rigorous approach would be the incorporation of additional corrections reacting to the flow physics specific for the considered flow types.

3.2.2.3 Evaluation of LES data

The validation of the simulation results presented in the previous sections reveals that for both confined coaxial jet cases, as earlier for the jet in crossflow, the LES data reproduces experimentally measured turbulent velocity field statistics more accurately than the RANS models tested in the present work. Thus, additional analysis of LES data regarding the statistical turbulence characteristics can be useful in order to isolate the sources of poor RANS model performance. Such analysis for the jet in crossflow test case was presented in section 3.1.2.3 and will be extended in this section for both considered confined coaxial jet configurations. The turbulent viscosity and the budget terms of the turbulent kinetic energy balance equation are

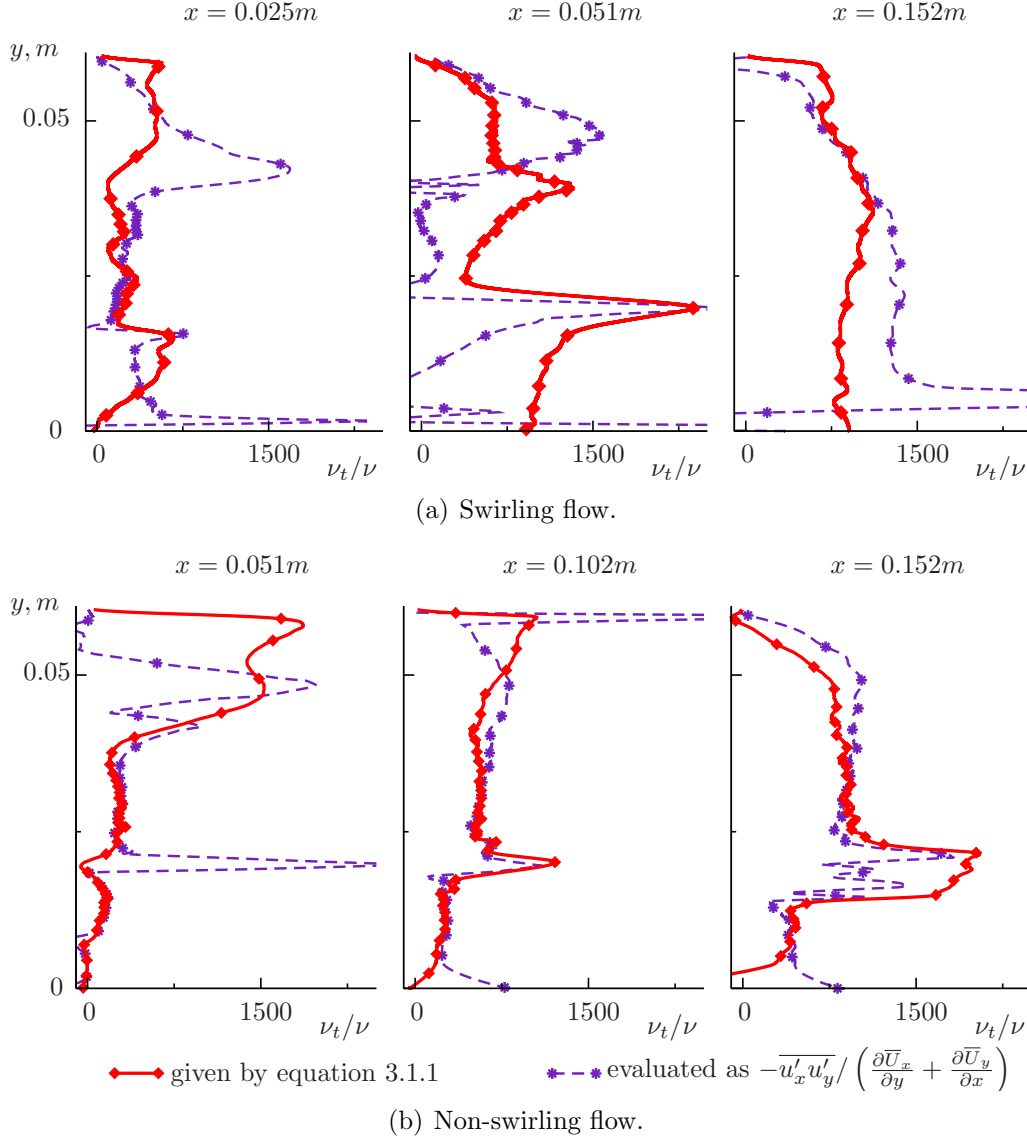


Figure 3.2.18: Dimensionless turbulent viscosity ν_t/ν evaluated from LES data in two different ways.

evaluated from the time-averaged LES data fields and compared with the respective quantities obtained in the RANS modeling.

3.2.2.3.1 Turbulent viscosity

3.2.2.3.1.1 Evaluation from the time-averaged LES data fields First, the turbulent viscosity is evaluated using the time-averaged LES data. This parameter is calculated here in the same way as described in section 3.1.2.3.1.1 (equation 3.1.1), i.e. all components of the Reynolds stress and of the strain-rate tensor are used and a single least-square mean turbulent viscosity value ν_t is obtained. The profiles of this variable evaluated from LES data for both jets are given in figure 3.2.18. Furthermore, a comparison is made with the turbulent viscosity values obtained as $\nu_{txy} = -\overline{u'_x u'_y} / \left(\frac{\partial \overline{U}_x}{\partial y} + \frac{\partial \overline{U}_y}{\partial x} \right)$ using only the $\overline{u'_x u'_y}$ Reynolds stress. This is done to illustrate that for the cases when one particular Reynolds stress can be assumed to be the most important one for the RANS model accuracy (here $\overline{u'_x u'_y}$ for the non-swirling case)

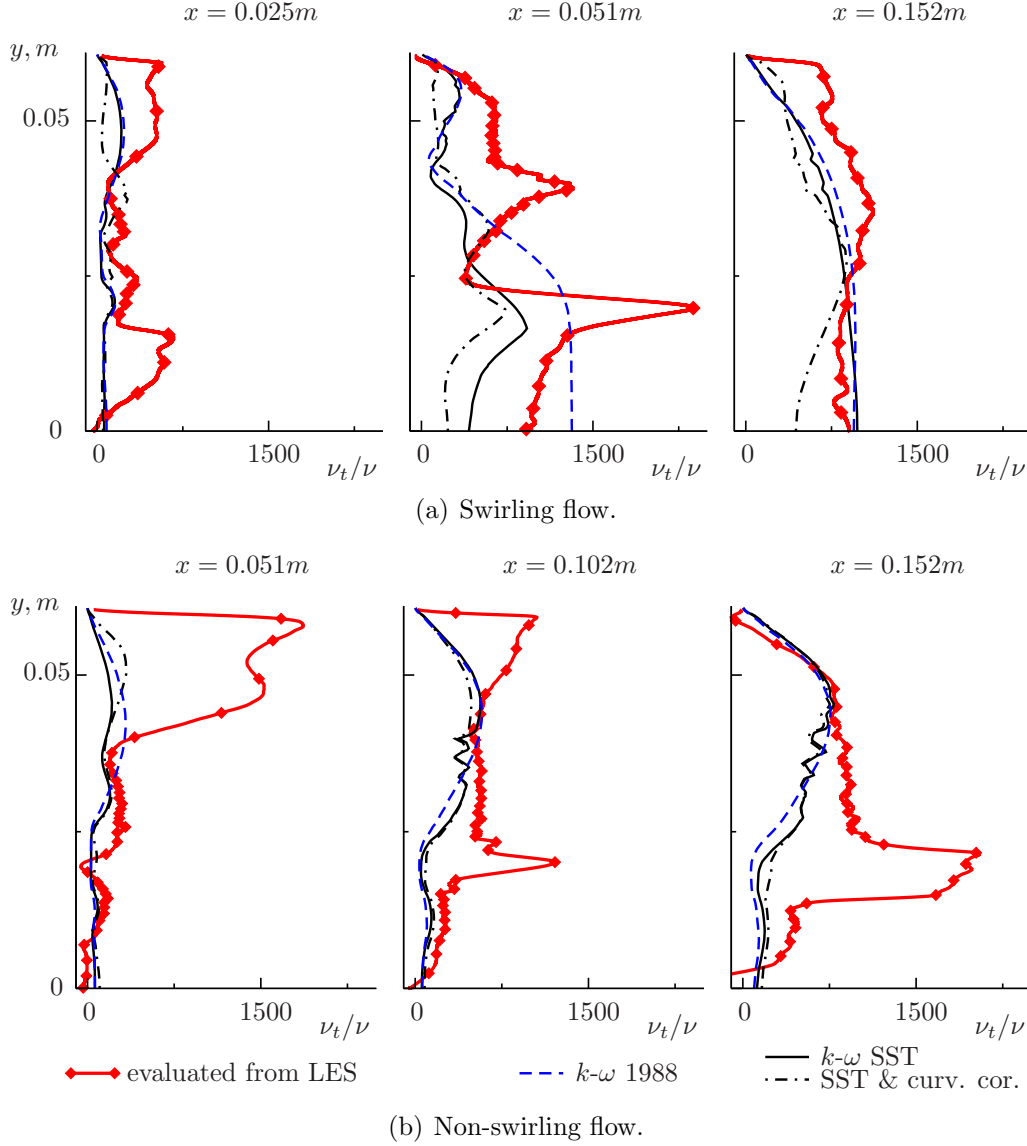


Figure 3.2.19: Dimensionless turbulent viscosity ν_t/ν evaluated from LES data and resulting from RANS modeling.

the mean ν_t evaluated using the least-square fit becomes similar to the ν_t obtained using this dominant Reynolds stress (see discussion in section 3.1.2.3.1.1). In contrast, for the swirling jet case, the evaluation based on just one Reynolds stress gives the turbulent viscosity values quite different from those obtained by equation 3.1.1. Generally, as already discussed in section 3.1.2.3.1.1, for the essentially three-dimensional flow the evaluation based on just one Reynolds stress raises the question on the justification of employing of this particular Reynolds stress to obtain the characteristic ν_t values. Thus, here as for the jet in crossflow test case the evaluation of ν_t using equation 3.1.1 is preferred since it gives a single ν_t value that can be directly compared with the RANS modeling results. These turbulent viscosities will be used for all further investigations presented in the next sections.

3.2.2.3.1.2 Comparison with the RANS modeling results In this section a comparison is made between the results obtained in the LES evaluation of the turbulent viscosity by

equation 3.1.1 and the turbulent viscosities resulting from the RANS modeling. Modeled turbulent viscosities of the Wilcox 1988 $k-\omega$ model, Menter $k-\omega$ SST model, and the SST model employing the curvature correction of Hellsten are presented in figure 3.2.19. This plot reveals that the modeled turbulent viscosities generally tend to be lower than those obtained from the LES data for both test cases. This corresponds with the underestimation of the turbulent kinetic energy in all RANS models used for evaluation.

For the swirling coaxial jets the agreement between ν_t evaluated from LES and modeled by RANS improves towards the end of the mixing section (at the $x = 0.152m$). Unfortunately this location occurs downstream of the critically important region of the flow - the jet breakup location and the edge of the central recirculation zone. Consequently, the quality of the turbulent viscosity reproduction in the downstream regions does not influence the overall model accuracy in this case. The Wilcox 1988 $k-\omega$ model shows the best agreement between the modeled ν_t and the values evaluated from LES (see the $x = 0.051m$ profile); however, the general accuracy is still unsatisfactory

In the non-swirling case, the largest differences between RANS and LES can be observed in the corner recirculation zone at the locations near to the jet injection point and in the shear-layer regions. Figure 3.2.6(b) shows that in the recirculation zones LES results correspond with the experimental turbulence data better than the results of RANS modeling. Thus, it can be also assumed that the turbulent viscosity values obtained from the LES evaluation reproduce the actual physical behavior in these regions better than the RANS models. Slightly higher circumspection is needed regarding the turbulent viscosity values evaluated from LES data in the shear layer regions. As pointed out above in the discussion on figure 3.2.6(b), the LES tends to the over prediction of the turbulence levels in the shear layers in the present case. However, at the locations $x = 0.102m$ and $x = 0.152m$ in figure 3.2.6(b) the agreement between the experimental data and LES is very good. Consequently, the turbulent viscosities evaluated in these locations probably represent the physical reality well. In contrast to LES, RANS at the locations $x = 0.102m$ and $x = 0.152m$ (see figures 3.2.6(b) - 3.2.9) produces rather poor results, which is in agreement with the turbulent viscosity underestimation shown in figure 3.2.19.

The negative values of the turbulent viscosity obtained by post-processing the LES data in the centerline region at $x = 0.152m$ for the non-swirling case (figure 3.2.19(b)) can be explained by the specific eddy structure of the considered confined jet flow discussed in the reference experimental paper of Johnson and Bennett [59]. This specific vortex structure, which is caused by the dominance of the coflow velocity, and its consequences for the momentum and the scalar transport in the present test case are discussed in detail in sections 3.2.3.1.3 and 3.2.3.2.1.

3.2.2.3.2 Turbulent kinetic energy budget

3.2.2.3.2.1 Evaluation from the time-averaged LES data Main budget terms of the exact turbulent kinetic energy transport equation (equation 2.2.11) evaluated from the LES data in the same manner as described in section 3.1.2.3.2 are presented in figure 3.2.20. All terms are non-dimensionalized using the radius of the mixing section R and the mean exit velocity of the

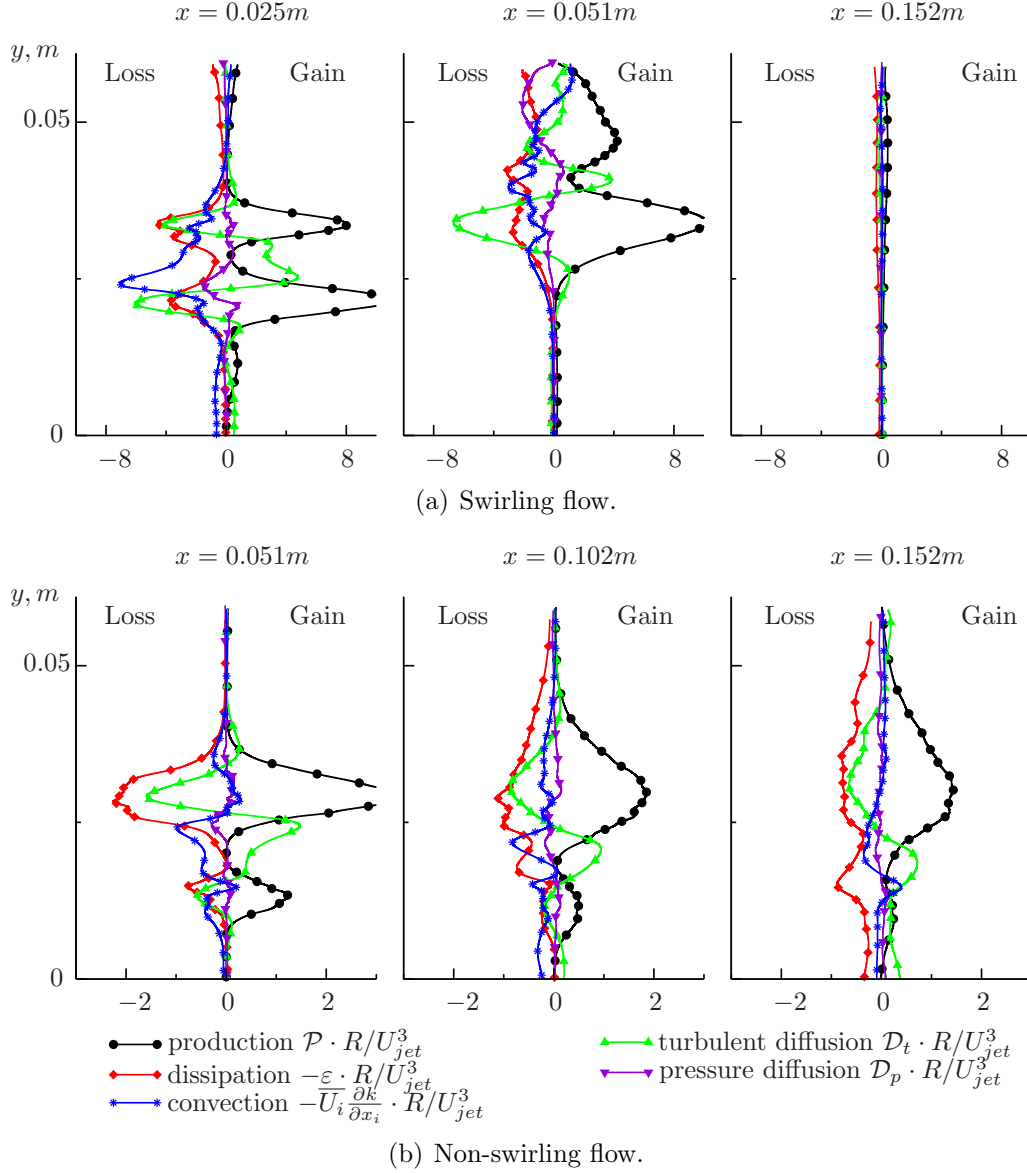


Figure 3.2.20: Main budget terms of the turbulent kinetic energy balance equation evaluated from LES. All terms are non-dimensionalized using the radius of the mixing section R and the mean exit velocity of the inner jet U_{jet} .

inner jet U_{jet} . The form of the budget terms and their spatial evolution are quite different in the swirling and the non-swirling case. In the swirling flow budget terms two main features can be observed: the important role of the turbulent diffusion term $\mathcal{D}_t = -\frac{\partial}{\partial x_i} [\frac{1}{2} \overline{u'_i u'_i u'_l}]$ in the shear layers, and the abrupt drop of the level of all budget terms in the region downstream of the edge of the central recirculation zone ($x > 0.051m$). The turbulent diffusion in the swirling jet partly exceeds the dissipation. Such dominance of the turbulent diffusion term can not be observed in the budgets of other flows considered in this work (2D channel and round free jet shown in the theoretical background section 2.2, jet in crossflow discussed in section 3.1.2.3.2). This fact emphasizes the significant importance of adequately representing the turbulent diffusion term in the RANS modeling of the swirling jets. The exceptionally low magnitude of budget terms downstream of the jet breakup location confirms the hypothesis of the decisive importance of

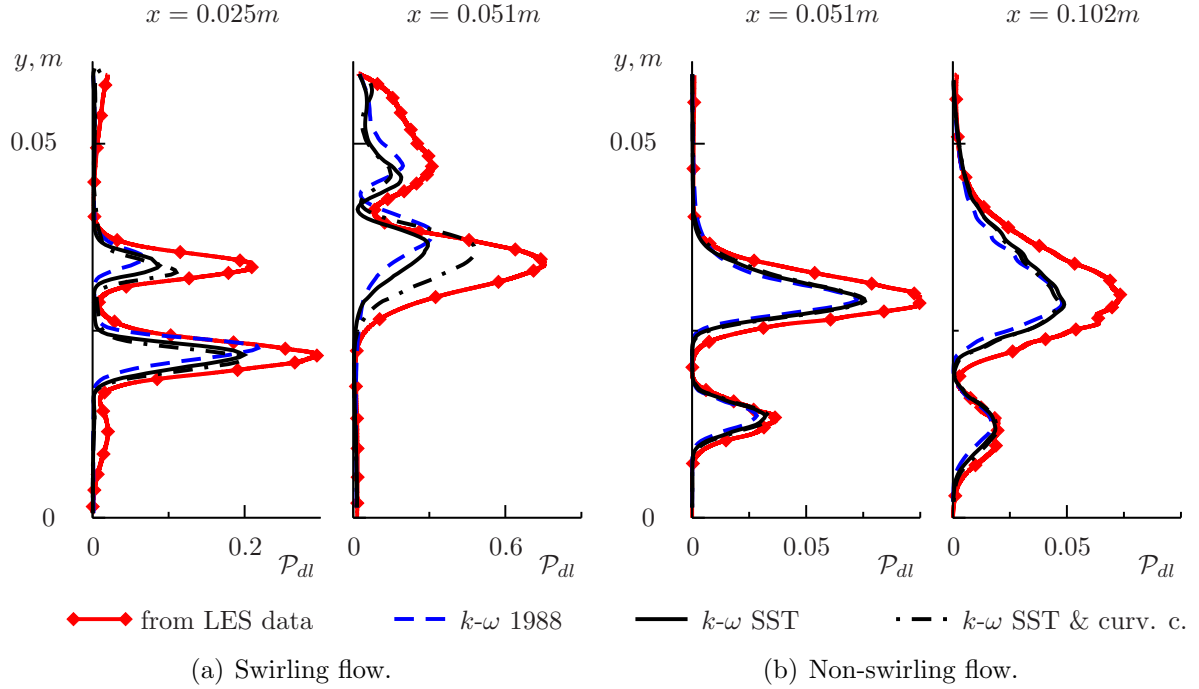


Figure 3.2.21: Dimensionless production of the turbulent kinetic energy \mathcal{P}_{dl} evaluated from LES data and resulting from RANS modeling. All values are non-dimensionalized using the radius of the mixing section R and the respective maximal axial velocities at the extraction planes, $\mathcal{P}_{dl} = \mathcal{P} \cdot R / \bar{U}_{xmax}^3$.

the zone upstream of the jet breakup point for the turbulence and mixing characteristics in the swirling flow. The impact of the pressure-diffusion term is relatively small but not negligible.

The behavior of the budget terms of the non-swirling confined jet is similar to the behavior of the respective terms of other round jet flows (free jet, jet in crossflow). Two peaks can be observed: the first one corresponds to the shear layer between the main jet and the coflow, the second one is located in the shear layer at the outer edge of the coflow. Turbulent diffusion in the non-swirling confined jet, although still relatively large, does not exceed the level of dissipation. The absolute magnitude of all terms decreases slowly in the downstream direction.

3.2.2.3.2 Comparison with the RANS modeling results Direct comparison between the budget terms evaluated from LES data and the respective terms of the modeled k -equation of different RANS approaches is given in figures 3.2.21-3.2.23. For the sake of clarity, all profiles are non-dimensionalized using the radius of the mixing section R and the maximal axial velocity \bar{U}_{xmax} at the respective extraction planes.

In the swirling jet case the production term is highly underestimated by all studied models (see figure 3.2.21(a)), and this can be explained by the underestimation of the turbulent viscosity level by RANS. The curvature correction helps to increase the production level slightly at $x = 0.051m$. That is captured in the k profiles shown in figure 3.2.14. In the non-swirling case (figure 3.2.21(b)) the production is slightly under predicted by RANS at $x = 0.051m$ and the discrepancy grows further downstream.

The turbulent diffusion terms are shown in figure 3.2.22. Here for both the swirling and

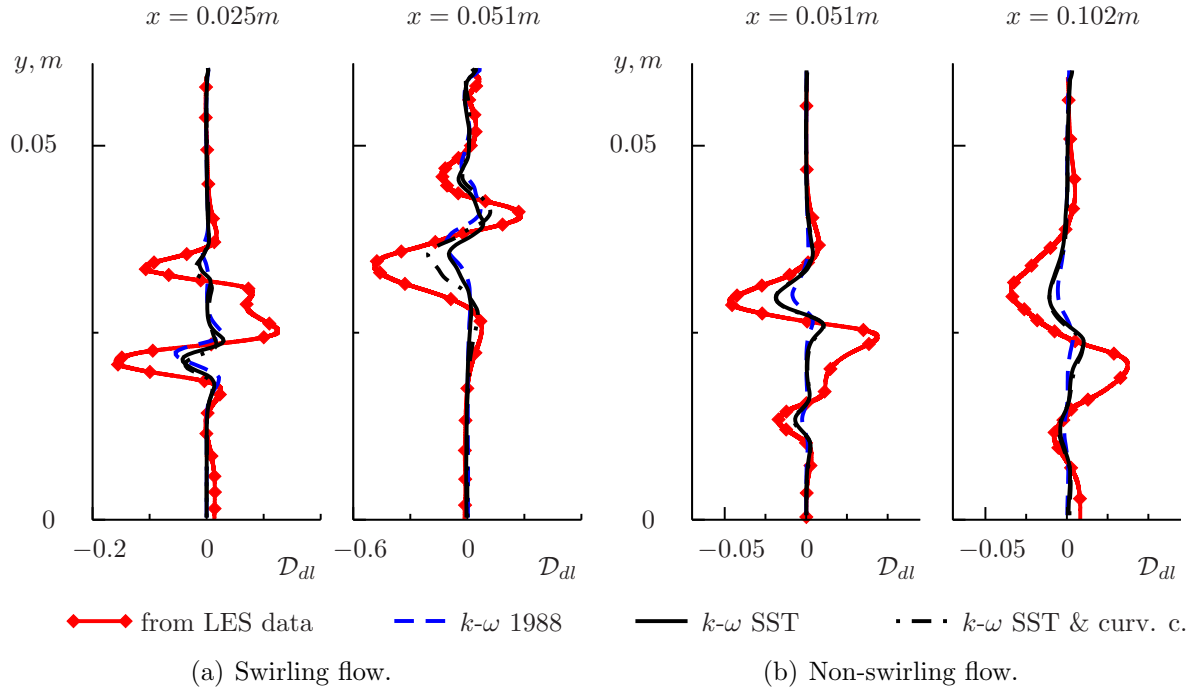


Figure 3.2.22: Dimensionless turbulent diffusion of the turbulent kinetic energy \mathcal{D}_{dl} evaluated from LES data and resulting from RANS modeling. All values are non-dimensionalized using the radius of the mixing section R and $\bar{U}_{x_{max}}$ - the respective maximal axial velocities at the extraction planes, $\mathcal{D}_{dl} = \mathcal{D}_t \cdot R / \bar{U}_{x_{max}}^3$.

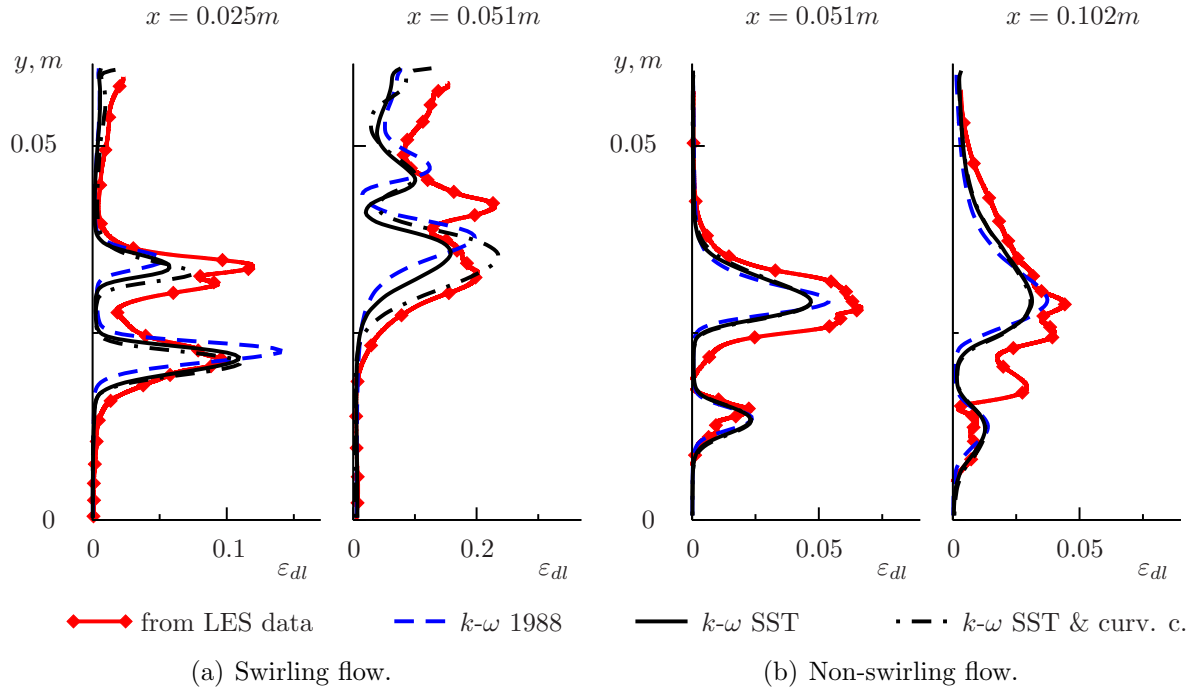


Figure 3.2.23: Dimensionless dissipation of the turbulent kinetic energy ε_{dl} evaluated from LES data and resulting from RANS modeling. All values are non-dimensionalized using the radius of the mixing section R and $\bar{U}_{x_{max}}$ - the respective maximal axial velocities at the extraction planes, $\varepsilon_{dl} = \varepsilon \cdot R / \bar{U}_{x_{max}}^3$.

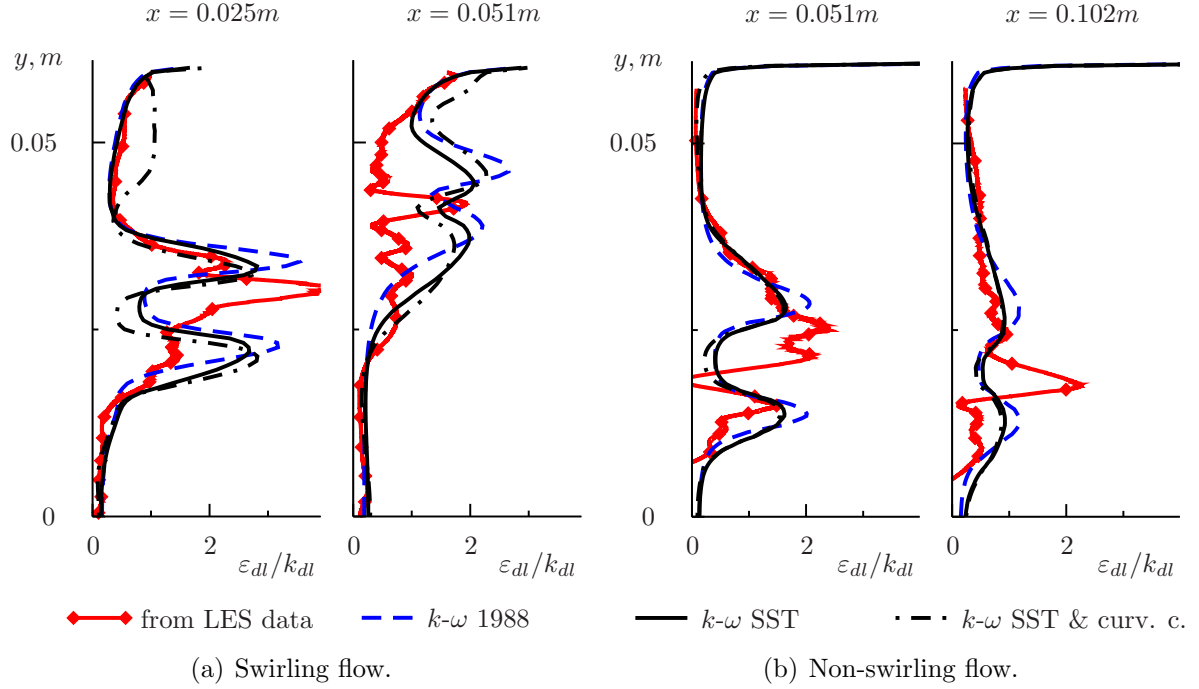


Figure 3.2.24: Dimensionless dissipation per unit turbulent kinetic energy ε_{dl}/k_{dl} evaluated from LES data and resulting from RANS modeling. All values are non-dimensionalized using the radius of the mixing section R the and \bar{U}_{xmax} - the respective maximal axial velocities at the extraction planes.

the non-swirling case the level of the turbulent diffusion is highly underestimated in RANS calculations. Different explanations of this RANS modeling failure are possible. First, it can be a consequence of the underestimation of the turbulent viscosity observed previously in figure 3.2.19. A second possible reason can be the poor choice of the turbulent diffusion modeling constant or potentially the entire modeling approach defined by equation 2.2.13. Further investigations on this subject are needed.

The dissipation profiles are presented in figure 3.2.23. For the RANS $k-\omega$ models used in this study, ε is evaluated according to equation 2.2.53. The absolute level of the dimensionless dissipation is represented by the studied models better than the level of the production and of the diffusion. However, figure 3.2.24 presenting the dimensionless dissipation per unit turbulent kinetic energy shows that for the swirling case at $x = 0.051m$ the level of the dimensionless dissipation is over predicted by all RANS models. That indicates excessive turbulence damping that exists in RANS and implies the necessity of improving the ω -equation for swirling jets.

The next flow quantity evaluated is the production to dissipation ratio shown in figure 3.2.25. The discrepancy between the \mathcal{P}/ε profiles given by RANS and by LES is much larger in the swirling case. In the non-swirling jet \mathcal{P}/ε values fluctuating around 1.0 are observed. These values are very similar to the \mathcal{P}/ε rates employed in the standard $k-\varepsilon$ model closure (see section 2.2.1.9). In contrast, the maximum values of \mathcal{P}/ε obtained for the swirling jet ($\mathcal{P}/\varepsilon > 4$) are much higher. This result can be an important reason of the turbulence modeling deficiencies for this flow because all turbulence models considered here are created assuming lower production

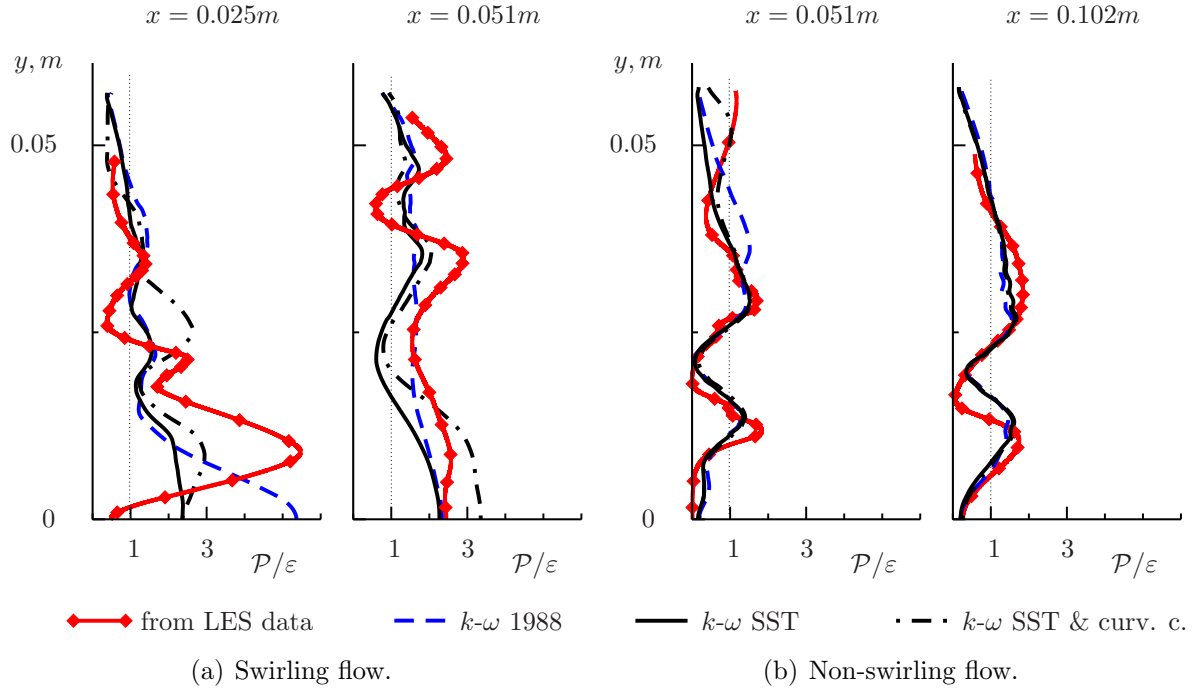


Figure 3.2.25: Production to dissipation ratio evaluated from LES data and resulting from RANS modeling.

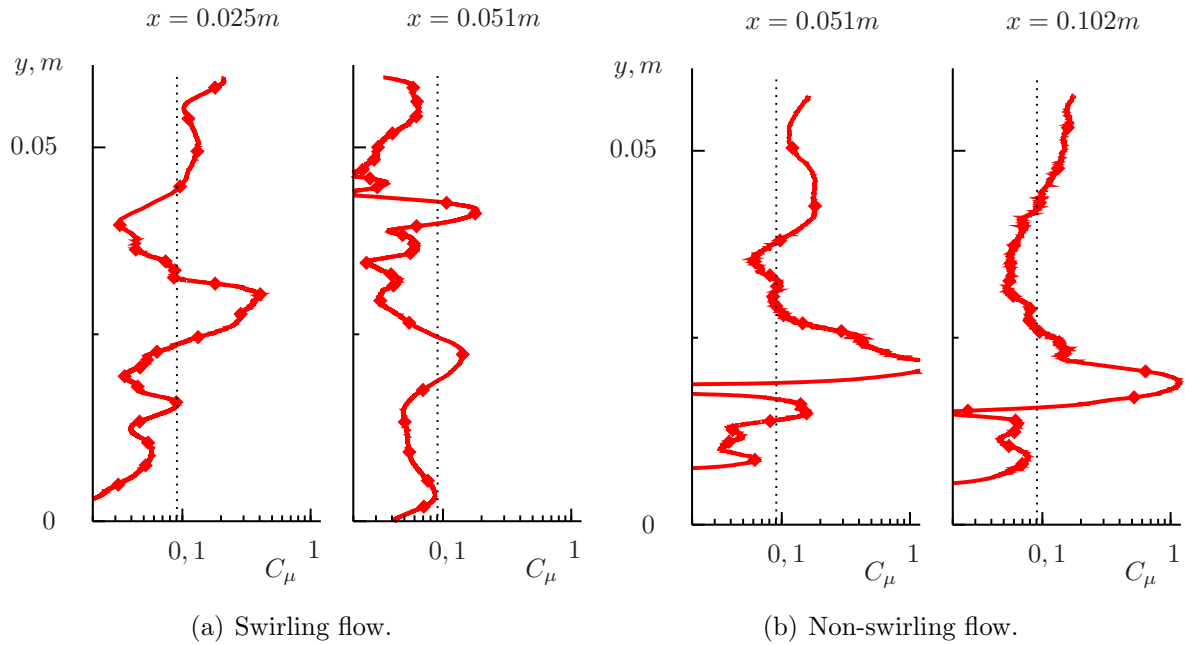


Figure 3.2.26: Turbulent viscosity modeling coefficient C_μ evaluated as $C_\mu = \nu_t \cdot \varepsilon / k^2$ using the LES data. $C_\mu = 0.09$ is indicated by the dotted lines. Note the logarithmic scale on the C_μ axis.

to dissipation ratios (see discussion in section 2.2.1.9).

Finalizing the analysis devoted to the evaluation of the turbulent viscosity and of the budget terms of the turbulent kinetic energy transport equation from LES data, the turbulent viscosity modeling coefficient C_μ is obtained as $C_\mu = \nu_t \cdot \varepsilon / k^2$. Figure 3.2.26 reveals that for both test cases studied here C_μ (or its analog β_k for the $k-\omega$ modeling, see equations 2.2.53 and 2.2.55) is highly variable. In figure 3.2.26 the logarithmic scale on the C_μ axis has to be noted. It can be observed that in the non-swirling case C_μ fluctuates around the value $C_\mu = 0.09$ typically prescribed in the modeling, but for the swirling case C_μ are for the most part lower, especially at $x = 0.051m$. This observation calls additional attention to the deficiencies of the dissipation modeling in the RANS approaches since even using a higher value of the turbulent viscosity modeling coefficient does not correct the under predicted turbulent viscosity in the swirling jet case. Furthermore, a general conclusion can be made that for the confined coaxial jet flows considered here, as in the jet in crossflow test case, the turbulent viscosity models employing a variable C_μ can be useful in order to improve the RANS prediction accuracy.

3.2.3 Scalar mixing modeling

3.2.3.1 Foundational study on the mean and fluctuating scalar field modeling

3.2.3.1.1 Dependence on the turbulent viscosity model The mean radial profiles of the dimensionless transported passive scalar concentration are presented in figure 3.2.27. For the RANS models, the Wilcox $k-\omega$ 1988 model, the SST model, and the SST model with curvature correction are employed in conjunction with the constant turbulent Schmidt number value of $\sigma_t = 1.0$. For the swirling flow the mixing is underestimated in the RANS simulations at $x = 0.013m$ and at $x = 0.025m$. At the position $x = 0.051m$ (at the edge of the central recirculation zone), the mixing intensity suddenly becomes over predicted by RANS. This can be explained by the incorrect position of the central recirculation zone in these simulations. In the non-swirling flow, the mixing is strongly underestimated in the downstream region. A comparison with the turbulent kinetic energy profiles, shown in figure 3.2.6, reveals that the under prediction of the mixing occurs at the same locations where the RANS models produce turbulent kinetic energy levels that are too low. The differences between the mixing predictions given by different RANS models are not significant. The curvature correction of the SST model brings a slight improvement to the swirling jet mixing predictions comparatively to both other models. The Wilcox $k-\omega$ 1988 model underestimates the mixing at the downstream locations of the non-swirling jet slightly more than both variants of the SST model. LES reproduces the experimental values of \overline{C} exceptionally well.

3.2.3.1.2 Dependence on the turbulent scalar transport model It was discussed previously that the variation of the turbulent Prandtl or Schmidt number is a popular method for mixing enhancement in RANS simulations. A study on the influence of this parameter on the mixing predictions in confined jets is presented in figure 3.2.28. For the turbulent viscosity modeling the Wilcox $k-\omega$ 1988 approach is chosen. Three different values of the turbulent Schmidt number

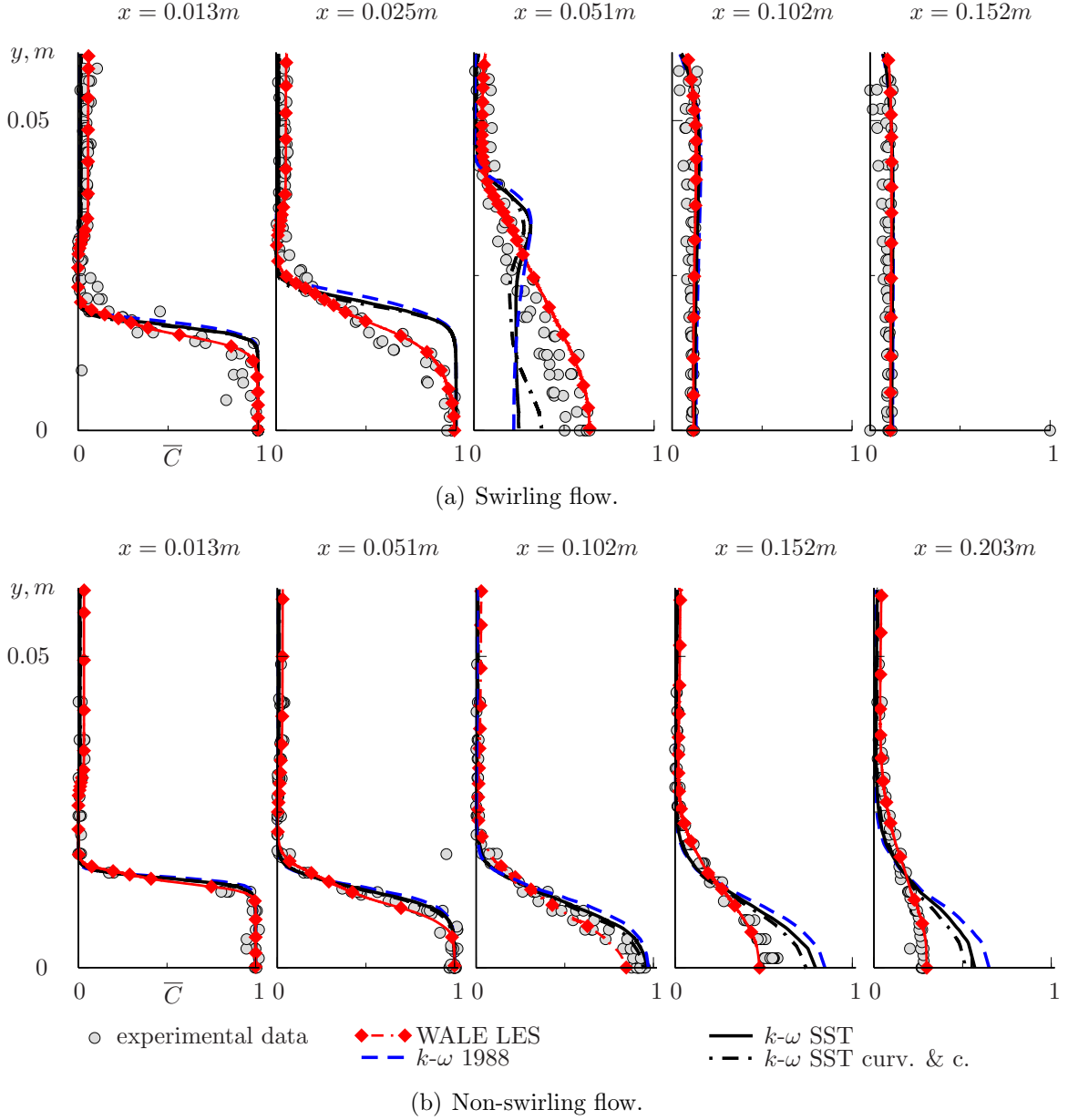


Figure 3.2.27: Dimensionless transported passive scalar concentration. Swirling and non-swirling confined jets. RANS and LES in comparison with experimental data. $\sigma_t = 1.0$.

are applied: $\sigma_t = 1.0$, $\sigma_t = 0.5$, and $\sigma_t = 0.25$. Additionally, the same figure 3.2.28 shows the results given by the $\overline{c^2}-\omega_c$ model of Huang and Bradshaw, which avoids the constant turbulent Schmidt number hypothesis by directly modeling the turbulent scalar diffusivity. The results obtained with the other turbulent scalar diffusivity models considered in this work (AKN, NK, DWX) are not presented since, as for jet in crossflow (see section 3.1.3.1.3), preliminary calculations did not reveal their significant superiority over HB results in the present test cases.

In the swirling flow the variation of σ_t only has a small effect on the mixing at the positions upstream of $x = 0.051m$ (see figure 3.2.28(a)). Further downstream the intensive mixing is caused by the flow field structure rather than by the shear layer vortices, and the variation of the turbulent Schmidt number does not have any influence on the results. It seems to be

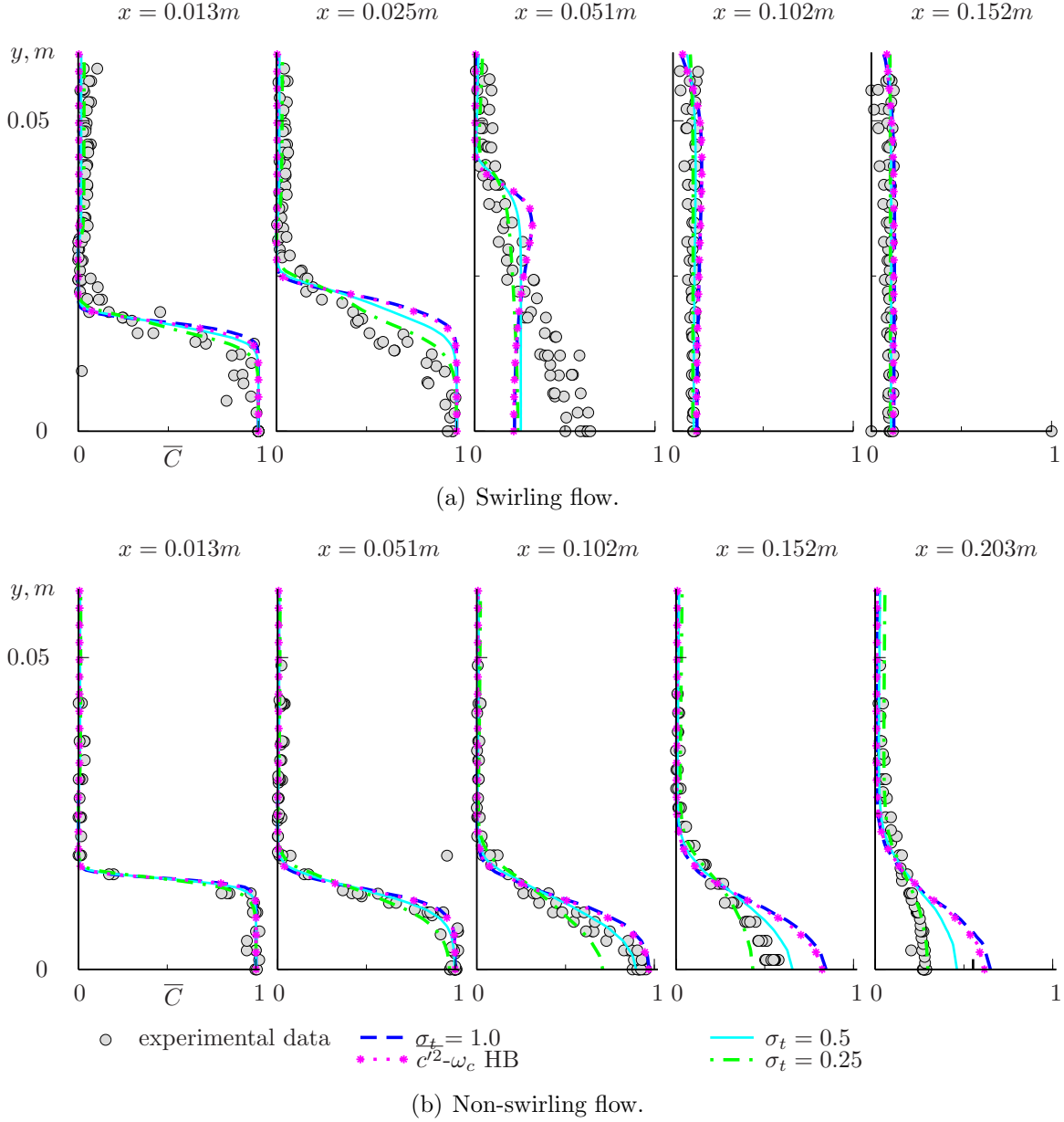


Figure 3.2.28: Dimensionless transported passive scalar concentration. Study on the influence of the turbulent scalar mixing modeling approach. Swirling and non-swirling confined jets. Wilcox $k-\omega$ 1988 used for the turbulent viscosity modeling.

more important here to predict the axial position of the central recirculation zone correctly, which is not achieved in the present RANS turbulent viscosity simulations. In the non-swirling case, the lower values of the turbulent Schmidt number help to increase the mixing, which was underestimated by $\sigma_t = 1.0$. However, depending on the profile position different σ_t values give better predictions. Furthermore, in the downstream region, as it was shown in figure 3.2.6, the level of the turbulent kinetic energy is underestimated by the underlying RANS turbulence model. Thus, the physical eligibility of the low turbulent Schmidt number values is questionable. As in the jet in crossflow case (see section 3.1.3.1.2), the low values of σ_t may only act as an artificial method to compensate for the errors of the turbulence modeling.

The $\overline{c^{j^2-\omega_c}}$ model of Huang and Bradshaw (HB) does not improve the mixing predictions

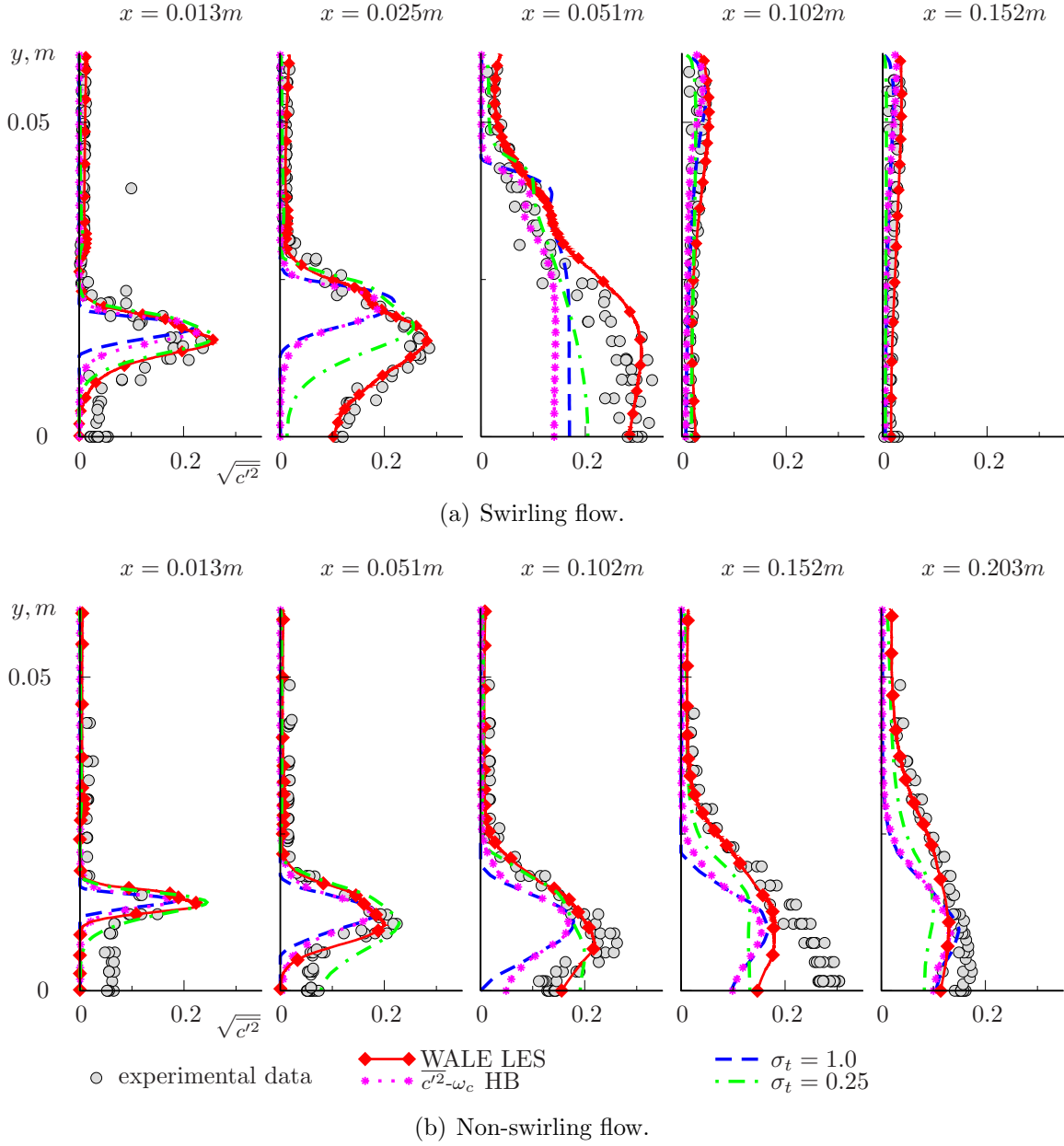


Figure 3.2.29: Turbulent scalar fluctuations $\sqrt{c'^2}$. LES and RANS using different scalar mixing modeling approaches. Swirling and non-swirling confined jets. Wilcox $k-\omega$ 1988 used for the RANS turbulent viscosity modeling. Equation 2.2.116 is used in conjunction with the constant σ_t approach.

comparatively to the constant turbulent Schmidt number approach. As for the jet in crossflow results considered in section 3.1.3.1.3, the HB model gives here the scalar profiles very similar to those achieved by $\sigma_t = 1.0$. The errors in the velocity field modeling, discussed in section 3.2.2.1, probably restrict the potential of the scalar mixing model to improve simulation accuracy. Acknowledging the turbulence model deficiencies, the Huang and Bradshaw approach itself may have some weaknesses responsible for the mixing underestimation.

3.2.3.1.3 Turbulent scalar variance and turbulent scalar fluxes For a better quantification of the scalar mixing prediction accuracy achieved by LES and by different RANS methods, their

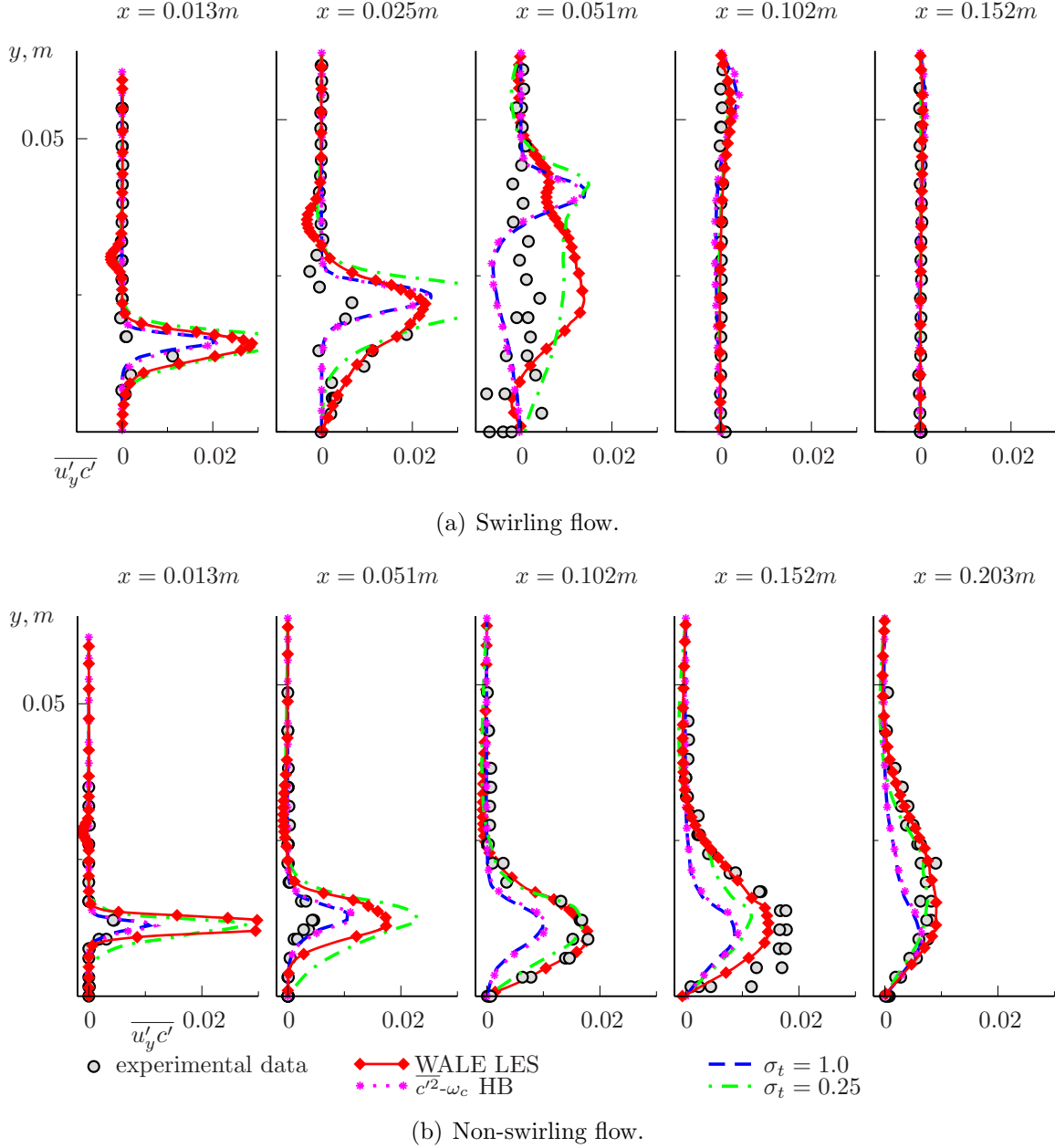
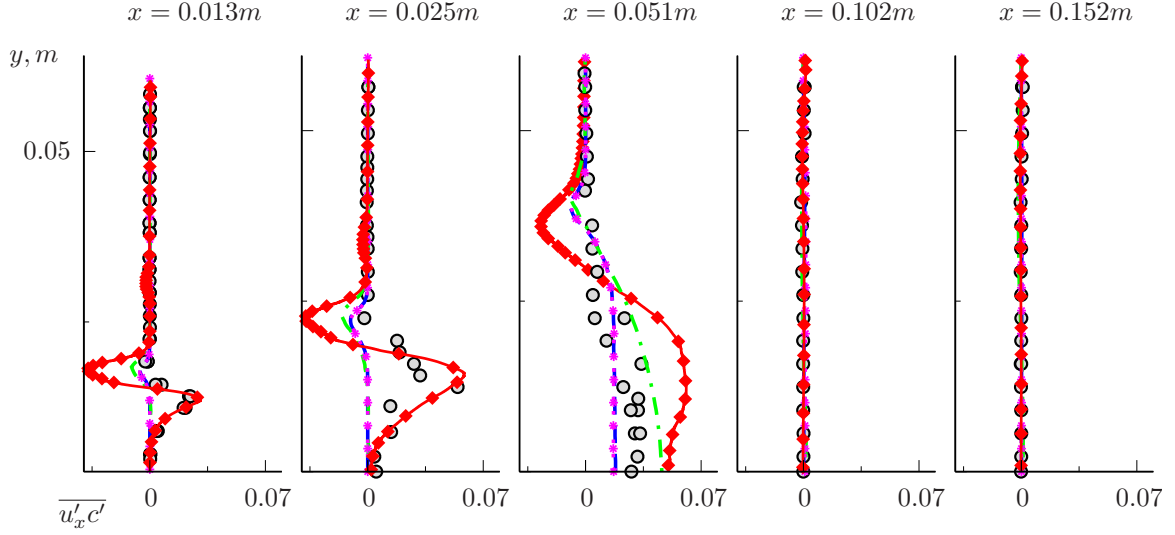
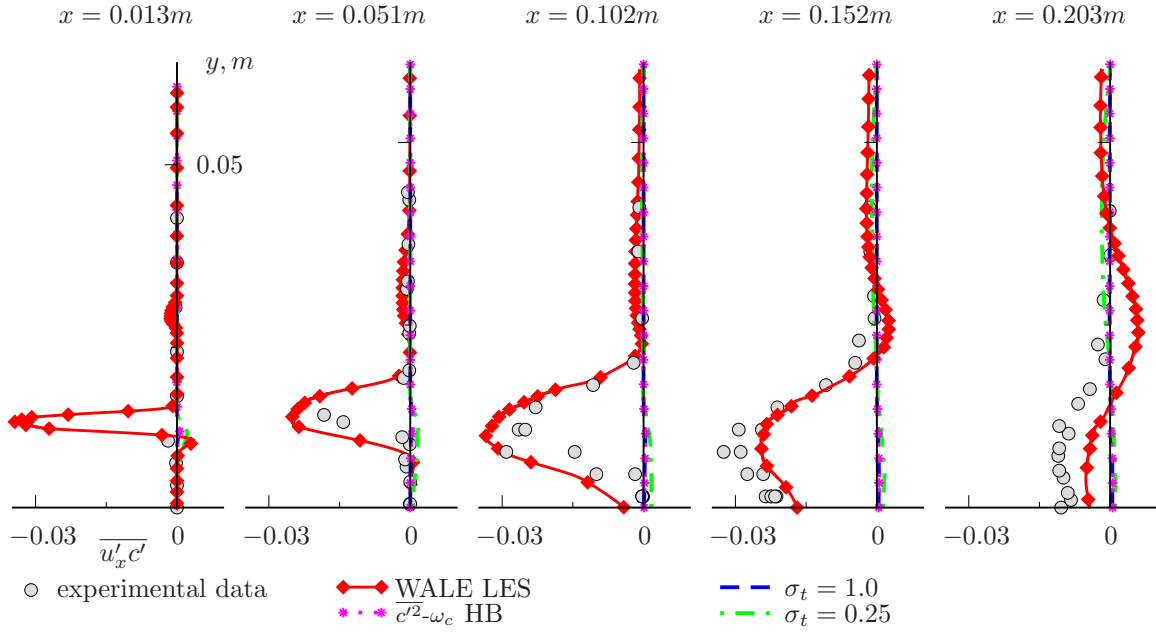


Figure 3.2.30: Turbulent scalar flux in y - direction $\overline{u'_y c'}$. LES and RANS using different scalar mixing modeling approaches. Swirling and non-swirling confined jets. Wilcox $k-\omega$ 1988 used for the RANS turbulent viscosity modeling.

computed scalar variance and turbulent scalar fluxes are validated against experimental data. Figure 3.2.29 presents the profiles of the turbulent scalar fluctuations $\sqrt{c'^2}$. As for the mean scalar field, LES shows good agreement with experimental data and superiority over all RANS results. Here and in all validations presented below, the RANS profiles are obtained using $\sigma_t = 1.0$, $\sigma_t = 0.25$, and the $\overline{c'^2}-\omega_c$ model of Huang and Bradshaw. Calculations employing the turbulent Schmidt number of $\sigma_t = 1.0$ or the $\overline{c'^2}-\omega_c$ model underestimate the RMS values of the transported passive scalar fluctuations. This behavior is in agreement with the trend of the mixing under prediction shown for the confined jets for both approaches. A lower value of the turbulent Schmidt number ($\sigma_t = 0.25$) improves the accuracy; however, the general



(a) Swirling flow.



(b) Non-swirling flow.

Figure 3.2.31: Turbulent scalar flux in x - direction $\overline{u'_x c'}$. LES and RANS using different scalar mixing modeling approaches. Swirling and non-swirling confined jets. Wilcox $k-\omega$ 1988 used for the RANS turbulent viscosity modeling.

agreement with experimental data is still unsatisfactory and worse than for LES. Only one weakness of LES that can be observed in figure 3.2.29 is a slight underestimation of the RMS scalar fluctuations in the jet core region for the non-swirling case.

Figure 3.2.30 shows the turbulent scalar fluxes $\overline{u'_y c'}$ in the (radial) y -direction. As with the scalar variance, $\sigma_t = 1.0$ and the $\overline{c'^2} - \omega_c$ model generally underestimate the scalar flux. A lower value of the turbulent Schmidt number leads to a strong over prediction of the $\overline{u'_y c'}$ scalar flux in the upstream locations in both test cases, but it helps to achieve better agreement with experimental data in the downstream locations of the non-swirling jet.

With regard to the flux in the axial direction, $\overline{u'_x c'}$, the situation with RANS modeling is much worse than for $\overline{u'_y c'}$. Figure 3.2.31 shows the results for this scalar flux component. Particularly in the non-swirling case (figure 3.2.31(b)), the flux values obtained in the RANS post-processing as $\overline{u'_x c'} = -\alpha_t \partial \overline{C} / \partial x$ are not only considerably underestimated but also fail to reproduce the negative direction of the axial scalar flux. This is caused by the fact that the gradients of the scalar in the axial direction are small, about an order of magnitude smaller than the gradients in the y -direction, and negative because scalar concentration is decaying in the downstream direction. Thus according to the gradient diffusion hypothesis (equation 2.2.6), $\overline{u'_x c'}$ scalar fluxes should be positive and about an order of magnitude smaller than the $\overline{u'_y c'}$ fluxes if the same values of the turbulent scalar diffusivity α_t are used for their calculation. However, the experiments of Johnson and Bennett [58, 59] and the present LES data indicate that the axial scalar fluxes are of about the same magnitude as the radial fluxes (at some locations even larger) and additionally are negative, i.e. in this case axial counter-gradient transport is present [59]. The counter-gradient transport in this case is explained in the paper of Johnson and Bennett [59] by the eddy structure associated with the momentum transport. The mean velocity of the annular jet is higher than the mean velocity of the inner jet. Thereby, the inner jet is accelerated by the coflow, and the large eddies in the velocity shear layer near the centerline are “rolling” with the negative fluctuating axial velocities near the inner jet fluid. Thus, the preferred rotational orientation of these large eddies retards the flow and results in $\overline{u'_x c'} < 0$; hence, countergradient mass transport can occur*. This phenomenon cannot be reproduced within the chosen RANS modeling framework and will be discussed again in section 3.2.3.2.1.

In the swirling jet case, the swirl-related effects are dominant, so the flow structure is different. However, at the positions at which a well-defined central jet core is present ($x = 0.013m$ and $x = 0.025m$) the $\overline{u'_x c'}$ flux is largely underestimated due to low scalar gradients in the axial direction. At the location immediately after the jet breakup ($x = 0.051m$) the situation changes and the level of $\overline{u'_x c'}$ in the central recirculation zone region is predicted by RANS better than further upstream. LES at this position tends to overestimate the turbulent scalar flux. In the downstream locations almost no mixing occurs in the swirling case and all scalar fluxes are small.

In summary, significant differences between RANS and LES are evident in the scalar mixing simulations. The assessed RANS models in general poorly represent the jet mixing in the considered cases. Additionally, as a consequence of the gradient diffusion hypothesis, the modeled scalar fluxes in the axial direction are clearly incorrect. Altogether the RANS results, regardless of scalar closure, are not satisfactory. LES, in contrast, despite of some discrepancies between experiment and simulation in the $\overline{c'^2}$ profiles for the non-swirling flow or in the $\overline{u'_y c'}$ profiles in the regions of strong shear is able to give accurate results.

*The two last sentences repeat the explanation from ref. [59].

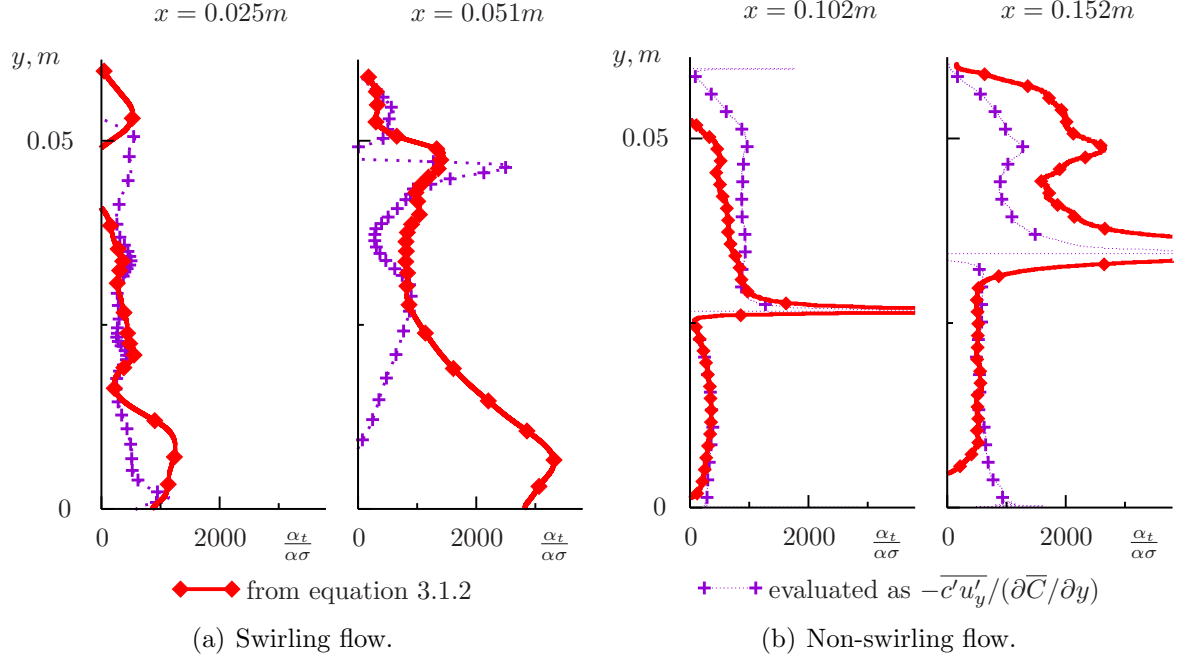


Figure 3.2.32: Dimensionless turbulent scalar diffusivity α_t evaluated from LES data in two different ways. The profiles are non-dimensionalized using the molecular scalar diffusivity and the molecular Schmidt number.

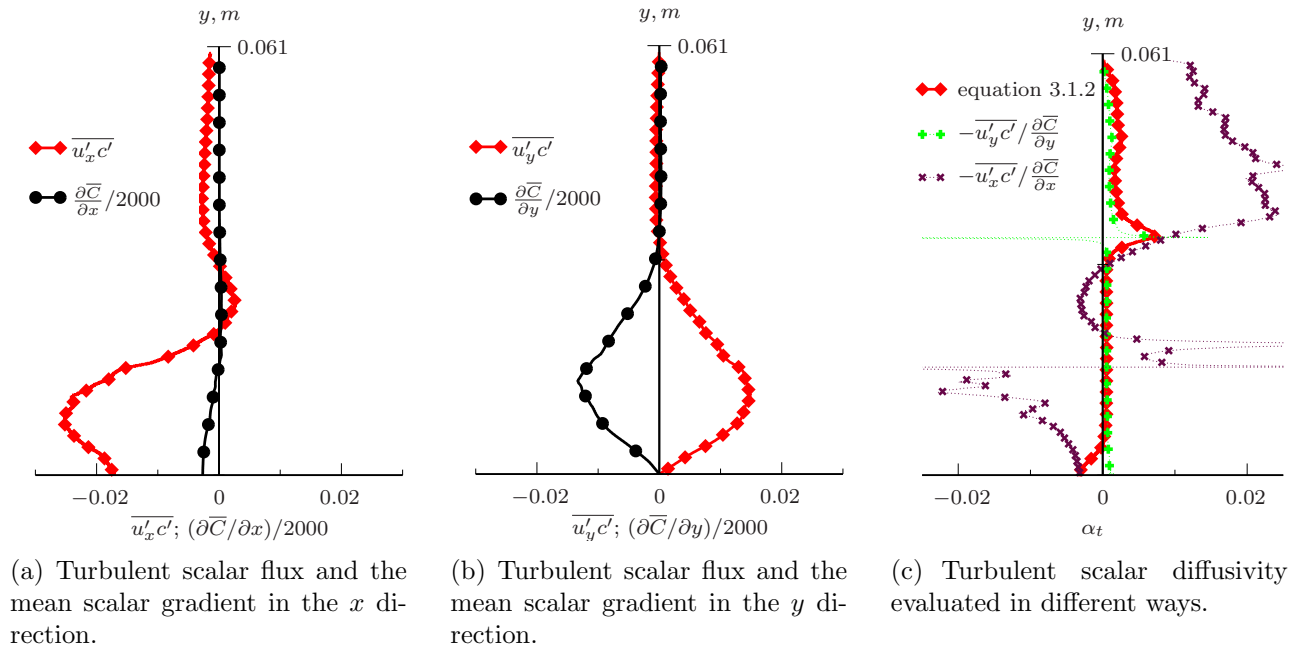


Figure 3.2.33: Evaluation of the turbulent scalar diffusivity for the non-swirling jet case at the position $x = 0.152m$.

3.2.3.2 LES data evaluation for scalar mixing modeling

It was discussed above that the deficiencies of the turbulent mixing modeling in RANS can be caused by both errors of the underlying turbulent viscosity model and the errors of the scalar mixing model. Simple variation of the turbulent Schmidt number cannot be a reliable method for the improvement of the simulation accuracy. This leads to the question regarding the actual turbulent Schmidt numbers in the considered test cases. Answering this question could help to increase the understanding of whether the constant turbulent Schmidt number approximation is justified in the considered flows and which values of σ_t could be optimal for accurately representing turbulent mixing. Moreover, this knowledge can guide future turbulence and scalar mixing modeling improvement. In order to collect such information, the accurate LES data on turbulent scalar mixing for both considered test cases can be post-processed in the same manner as it was done in section 3.1.3.2 for jet in crossflow configuration. Furthermore the LES data can be used in order to gain additional information about the budget terms of the scalar variance transport equation and about the accuracy of their representations by the studied RANS mixing models. All these questions are addressed in the present section.

3.2.3.2.1 Turbulent scalar diffusivity

3.2.3.2.1.1 Evaluation from the time-averaged LES data fields First, the turbulent scalar diffusivity is evaluated from the same approximation as applied in section 3.1.3.2 (least-square fit over all scalar fluxes, equation 3.1.2). The obtained profiles of α_t are shown in figure 3.2.32, and the α_t profiles evaluated from just the $\overline{u'_y c'}$ scalar flux are also presented for comparison. It is seen, that for the non-swirling jet case (figure 3.2.32(b)) where the scalar flux in the y -direction can be assumed to be dominant, the variations between α_t evaluated in different ways are not strong with exception of the recirculation zone regions. The situation changes significantly for the swirling jet case where $\overline{u'_y c'}$ cannot be assumed to be the dominant scalar flux direction. The differences between the least-square mean α_t and α_t obtained from $\overline{u'_y c'}$ are remarkable. The same situation could be observed in the jet in crossflow turbulent scalar diffusivity evaluation presented in section 3.1.3.2 where, as for the swirling jet case, the mixing process does not have a clearly defined dominant direction but is highly three-dimensional.

An additional remark should be made here about the negative turbulent scalar diffusivity values returned by the equation 3.1.2 for the non-swirling case in the centerline region (see figure 3.2.32(b)). The reason for the appearance of negative α_t in this case can be easily explained by the presence of the counter-gradient diffusion in the axial direction, discussed in the previous section. This is illustrated in figure 3.2.33. First, the turbulent scalar fluxes and the mean scalar gradients in the x - and the y -direction evaluated from LES are shown in figures 3.2.33(a) and 3.2.33(b). It is clearly seen that whereas the fluxes and the gradients in the y -direction have different signs, the fluxes and the gradients in the x -directions are negative in the region of intensive mixing. This generates negative values of α_t when evaluated as $\alpha_{tx} = -\overline{u'_x c'} / \frac{\partial \overline{C}}{\partial x}$. Moreover since the gradients in the x direction are much lower than the gradients in the y -direction, the absolute values of α_{tx} obtained from the $\overline{u'_x c'}$ fluxes is about an order of magnitude

larger than the absolute values α_{ty} obtained from the $\overline{u'_y c'}$ fluxes (see figure 3.2.33(c)). Due to scalar gradients of generally small magnitude in the x -direction, α_{tx} does not have much influence on the α_t values obtained using the least-square approximation, and it is important only in the regions where the gradients in the y -direction become comparably small, on the jet centerline and in the near-wall region.

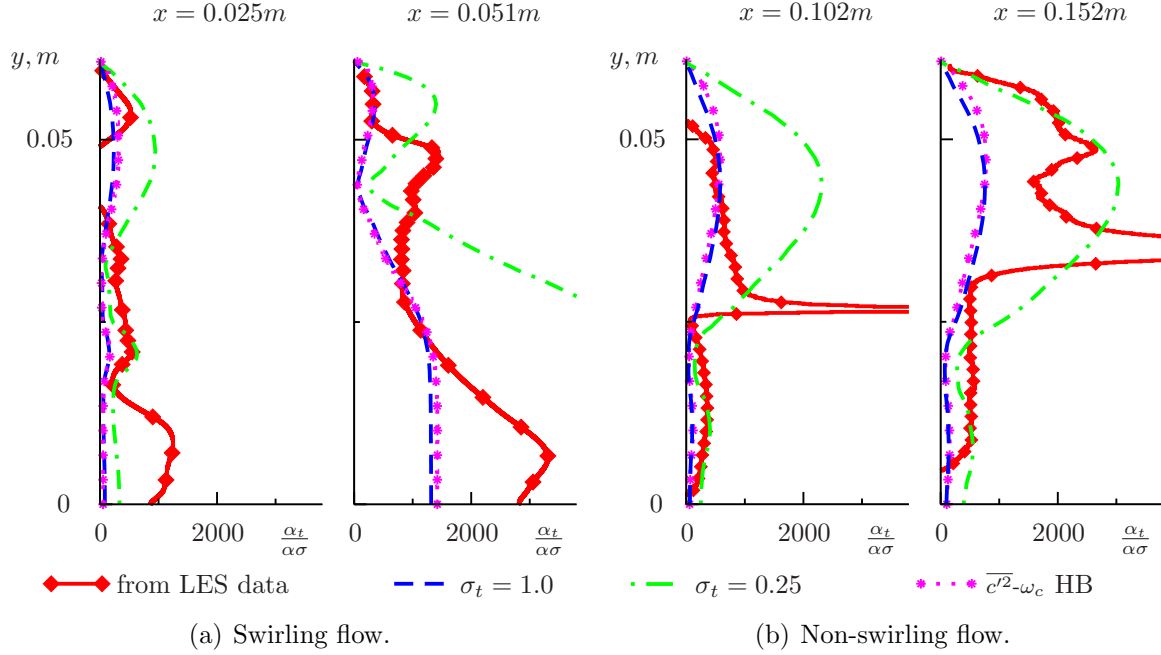
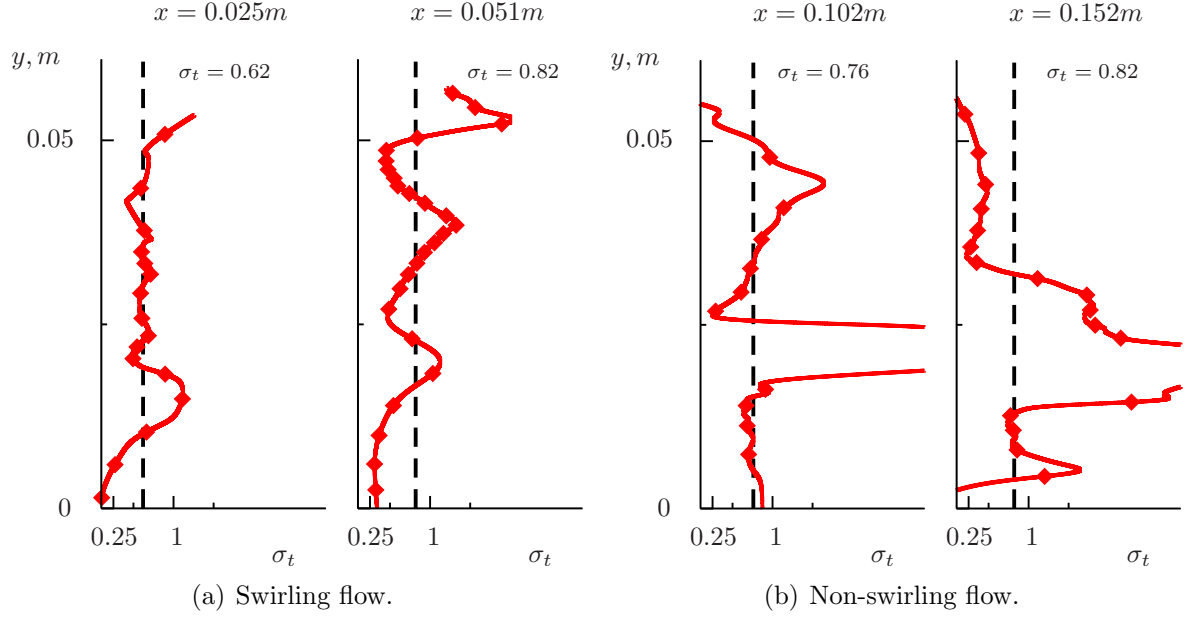
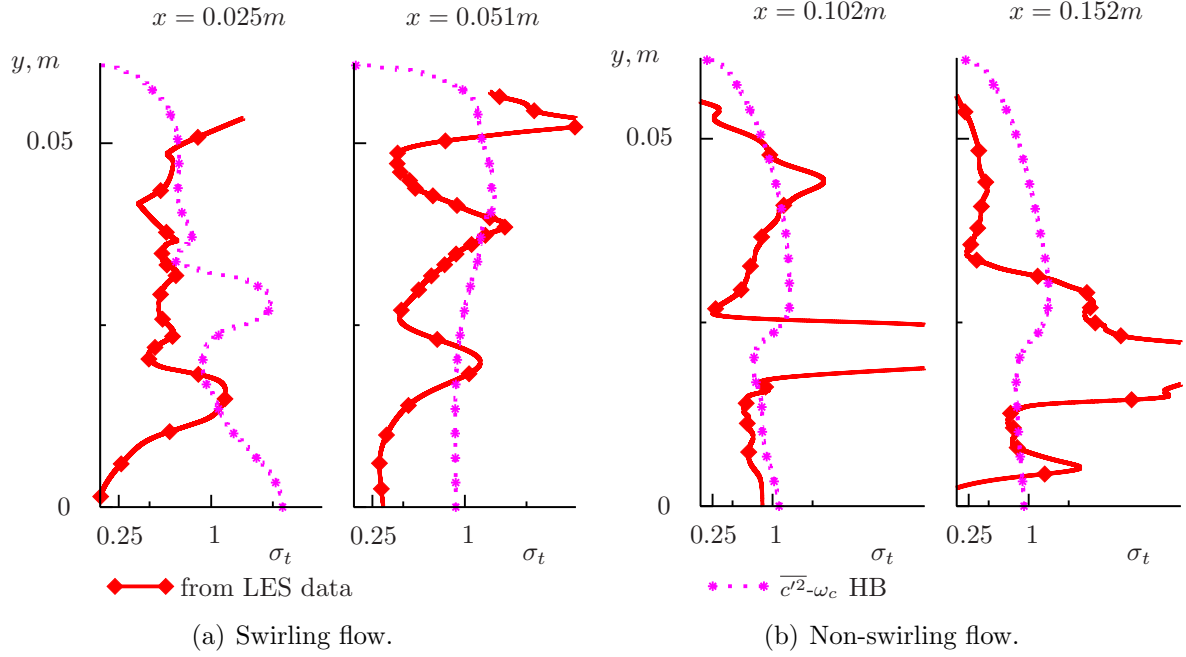


Figure 3.2.34: Comparison of the turbulent scalar diffusivity α_t evaluated from LES data and obtained in RANS modeling. The profiles are non-dimensionalized using the molecular scalar diffusivity and the molecular Schmidt number.

3.2.3.2.1.2 Comparison with the RANS modeling results Figure 3.2.34 compares the least-square mean α_t evaluated from LES data with the values of this quantity given by the different RANS scalar mixing modeling approaches. The underestimation of α_t by both $\sigma_t = 1.0$ and the $\overline{c'^2} - \omega_c$ model in conjunction with the $k - \omega$ 1988 model for the turbulent viscosity is evident. It can also be seen that $\sigma_t = 0.25$ only partly leads to the improvement in the α_t predictions. In some regions this value of the turbulent Schmidt number leads to excessively high values of α_t .

3.2.3.2.2 Turbulent Schmidt numbers The turbulent Schmidt numbers obtained using the least-square mean turbulent viscosities and the least-square mean turbulent scalar diffusivities evaluated from LES data are presented in figure 3.2.35. It can be observed that the actual values of σ_t are far from being constant. Averaging of these turbulent Schmidt numbers over the combustor radius can deliver a number that can be directly compared with the values used in the RANS modeling. The black dashed lines in figure 3.2.35 indicate such averaged σ_t in the presented axial locations. In both cases the values given by the LES data evaluation fluctuate around 0.6-0.8. Furthermore, for both cases a trend of increasing averaged turbulent Schmidt number in the downstream direction is revealed. Similar values of turbulent Schmidt


 Figure 3.2.35: Turbulent Schmidt number σ_t evaluated from LES data.

 Figure 3.2.36: Turbulent Schmidt number σ_t evaluated from LES data and obtained in the RANS modeling.

numbers and their tendency to increase in the downstream direction was also reported in the non-swirling confined jet LES study performed by Dianat et al.[25], in which the radial scalar fluxes were used for the α_t evaluation (in contrast to the least-square averaged α_t employed in the current study). It was shown in the previous section that the radial scalar fluxes and the scalar gradients in the radial direction, with some exception in the jet centerline region, mainly define the characteristic α_t values in the non-swirling confined flow. This fact allowed Dianat et al.[25] to perform their σ_t evaluation based on just one dominant turbulent scalar flux and one dominant Reynolds stress to obtain the turbulent viscosity. For the swirling flow configuration

as well as for the jet in crossflow, where no dominant scalar fluxes and Reynolds stresses can be defined, the evaluation using the least-square mean turbulent scalar diffusivities and turbulent viscosities proposed in the present work is clearly preferable.

Figure 3.2.36 presents the comparison of the turbulent Schmidt number values evaluated by LES and given by the $\overline{c'^2}-\omega_c$ model of Huang and Bradshaw. The $\overline{c'^2}-\omega_c$ model produces σ_t fluctuating around unity. This explains the similarity of the mean and fluctuating scalar profiles given by this approach to the profiles returned by $\sigma_t = 1.0$ (see section 3.2.3.1). It should be noted here that $\sigma_t = 1.0$ is not much higher than the values obtained in the LES data evaluation especially in the downstream locations. Thus probably the under prediction of the turbulent scalar mixing in both considered cases is primarily caused by the deficiencies of the turbulent viscosity modeling and not by a poor choice of the mixing modeling approach.

3.2.3.2.3 Budget terms of the turbulent scalar variance equation

3.2.3.2.3.1 Evaluation from the time-averaged LES data For the further refinement of the $\overline{c'^2}-\omega_c$ model as well as for the improvements in the modeled scalar variance transport equation 2.2.116 used in conjunction with the constant turbulent Schmidt number hypothesis, a validation of the $\overline{c'^2}$ equation terms by their values evaluated from LES is performed. For both confined jet cases, the budget terms of the scalar variance balance equation, obtained from LES data in the same way as for the jet in crossflow case (see section 3.1.3.2), are presented in figure 3.2.37. All presented profiles are non-dimensionalized using the radius of the mixing section R , the exit bulk velocity of the inner jet U_{jet} , and the scalar concentration at the inner jet inlet (here $\overline{C}_{jet} = 1.0$). For the swirling jet, the abrupt drop of the magnitude of all budget terms downstream of the central recirculation zone can be observed. In the non-swirling case, the level of all budget terms decreases slowly in the downstream direction and is generally lower than the peak values for the swirling case.

3.2.3.2.3.2 Comparison with the RANS modeling results Figures 3.2.38 - 3.2.40 present the comparison of the individual terms of the turbulent scalar variance balance equation evaluated from LES data with the same terms modeled by RANS. For the turbulence modeling, here the Wilcox 1988 $k-\omega$ approach is employed, and the scalar mixing models under study are the following: the constant turbulent Schmidt numbers $\sigma_t = 1.0$ and $\sigma_t = 0.25$ with equation 2.2.116 employed for the modeling of the turbulent scalar variance, and the $\overline{c'^2}-\omega_c$ HB model.

In the non-swirling case the production level is given almost correctly by all used models (figure), but in the swirling case the production in the near-centerline region is largely under predicted by RANS (figure 3.2.38(a)). The turbulent diffusion (figure 3.2.39) is reproduced poorly for both test cases by all used RANS approaches. The discrepancies are particularly evident in the swirling case at $x = 0.051m$. In the non-swirling case, $\sigma_t = 0.25$ gives a good prediction at $x = 0.051m$, but its quality drops further downstream. Regarding the turbulent scalar dissipation (figure 3.2.40), in the swirling case the same trends as in the production modeling can be observed. In the non-swirling case the dissipation level given by RANS models is generally higher than evaluated in LES. It can be observed that for all terms studied here

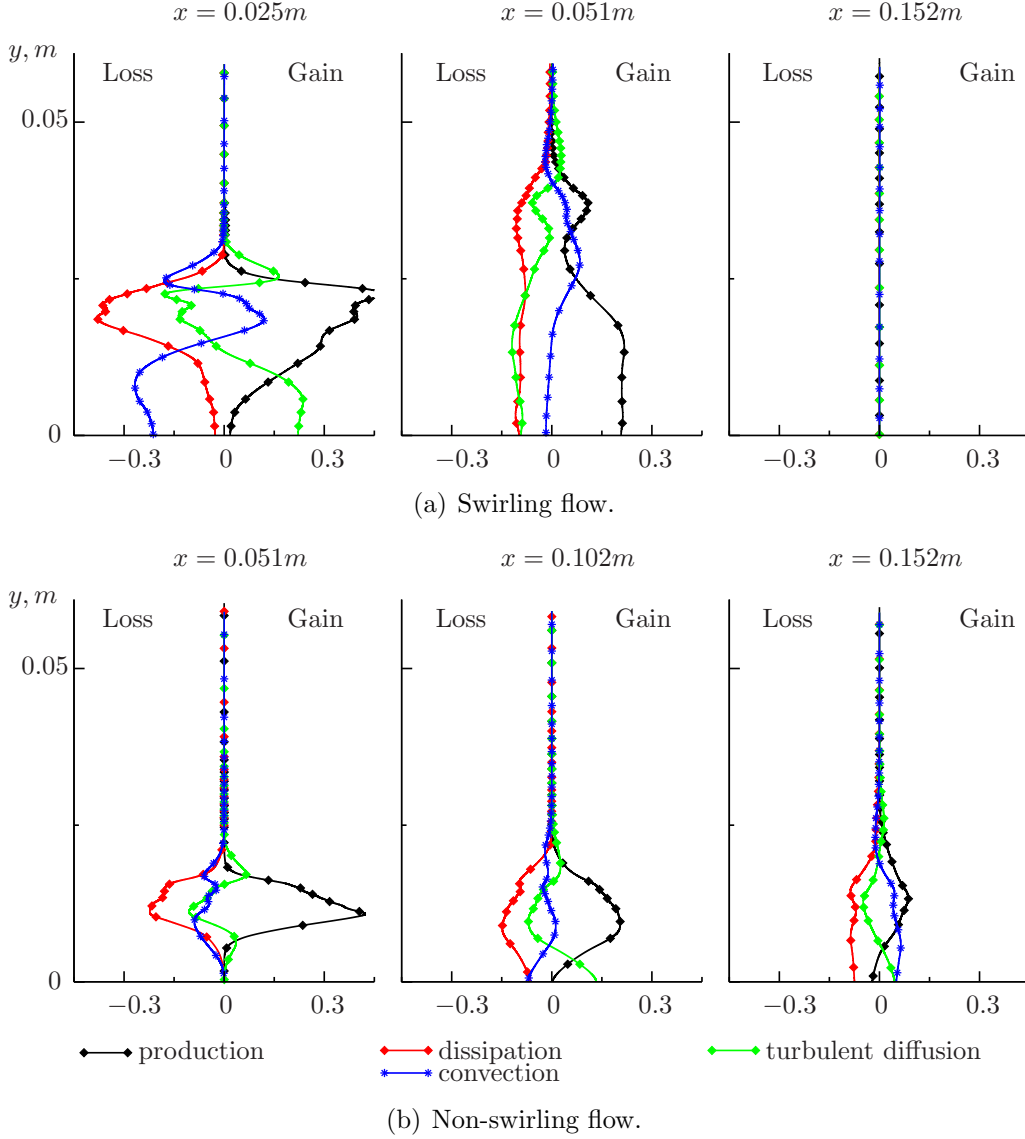


Figure 3.2.37: Main budget terms of the turbulent scalar variance balance equation evaluated from LES. All values are non-dimensionalized using the radius of the mixing section R , the mean exit velocity of the inner jet U_{jet} , and the mean exit scalar concentration of the inner jet (here $C_{jet} = 1.0$).

the profiles given by $\sigma_t = 1.0$ and by the $\overline{c'^2}$ - ω_c HB model are nearly indistinguishable from each other.

The differences between the constant turbulent Schmidt number approach and the HB model are more noticeable in figure 3.2.41. This plot compares the scalar time scales τ_c evaluated from LES, the values of this time scale given by the HB model, and the results obtained employing the constant turbulent scalar to velocity time scale ratio of $\mathcal{R} = \tau_c/\tau_d = 0.5$ with the turbulent velocity time scale τ_d returned by the Wilcox 1988 k - ω model. The assumption of the constant ratio between the turbulent scalar and velocity time scales is applied for the modeling of the turbulent scalar variance dissipation ratio in equation 2.2.116. This equation is employed for the calculation of the turbulent scalar variance in conjunction with the constant turbulent Schmidt number approach; $\mathcal{R} = 0.5$ is the value exceptionally often used in this equation. It

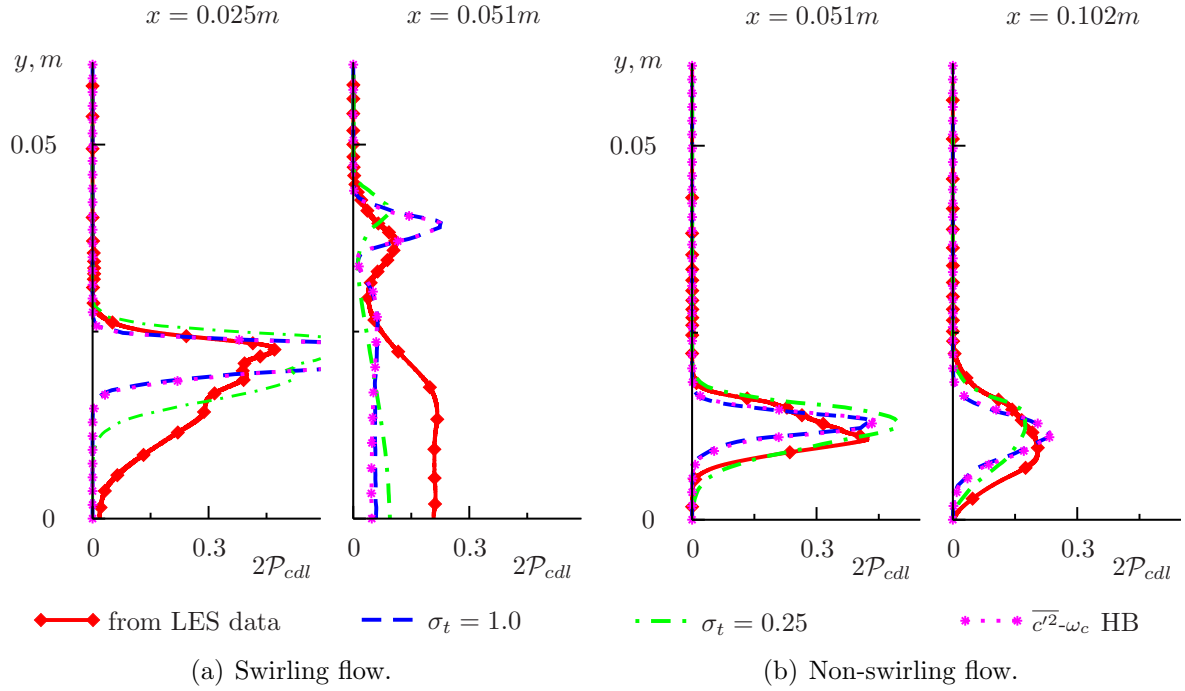


Figure 3.2.38: Dimensionless turbulent scalar variance production evaluated from LES data and resulting from RANS modeling. equation 2.2.116 is used in conjunction with the constant σ_t . All values are non-dimensionalized using the same quantities as in figure 3.2.37.

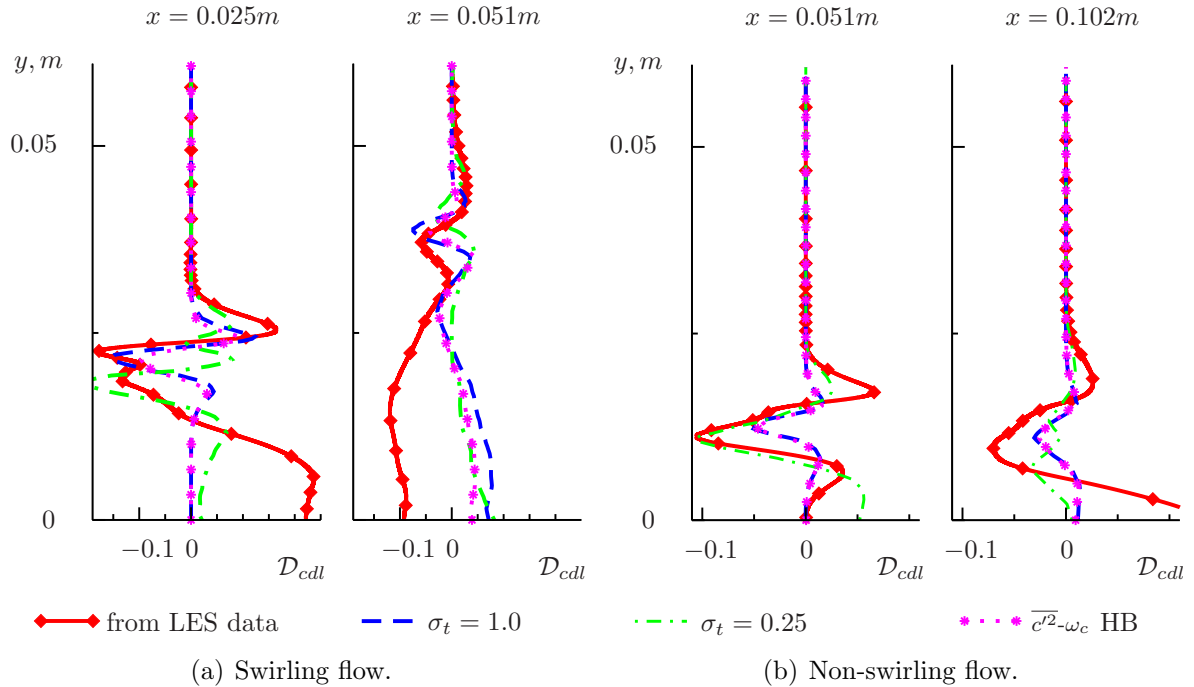


Figure 3.2.39: Dimensionless turbulent diffusion of the scalar variance evaluated from LES data and resulting from RANS modeling. Equation 2.2.116 is used in conjunction with the constant σ_t . All values are non-dimensionalized using the same quantities as in figure 3.2.37.

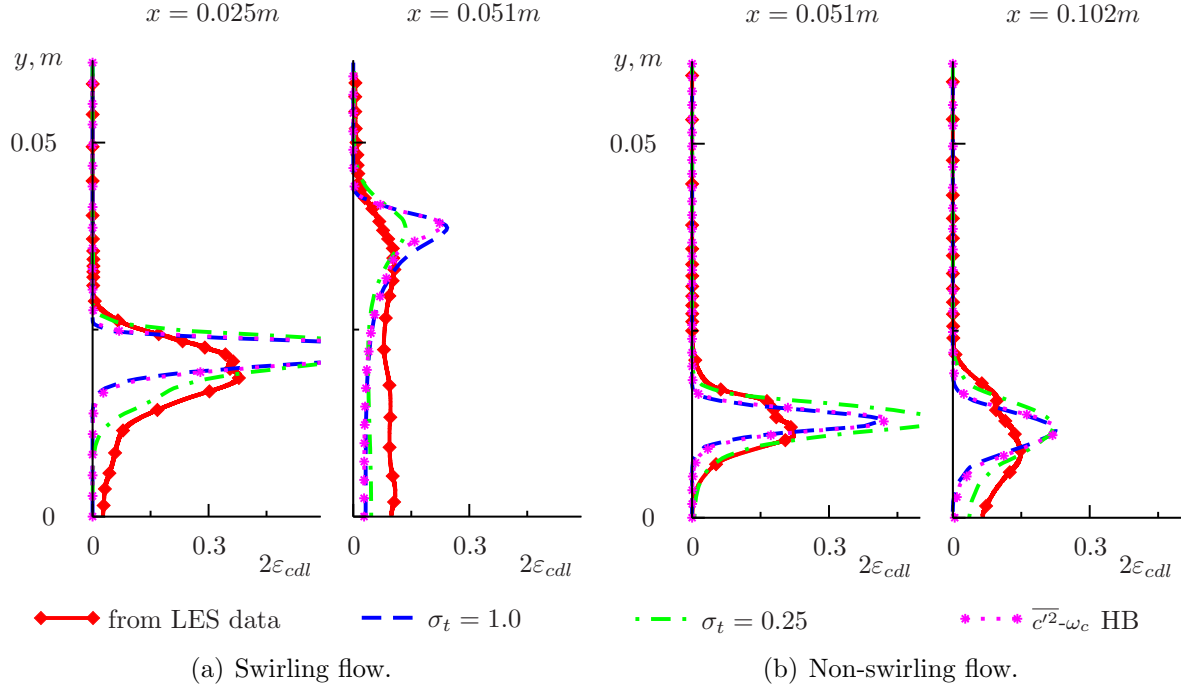


Figure 3.2.40: Dimensionless turbulent scalar variance dissipation rate evaluated from LES data and resulting from RANS modeling. Equation 2.2.116 is used in conjunction with the constant σ_t . All values are non-dimensionalized using the same quantities as in figure 3.2.37.

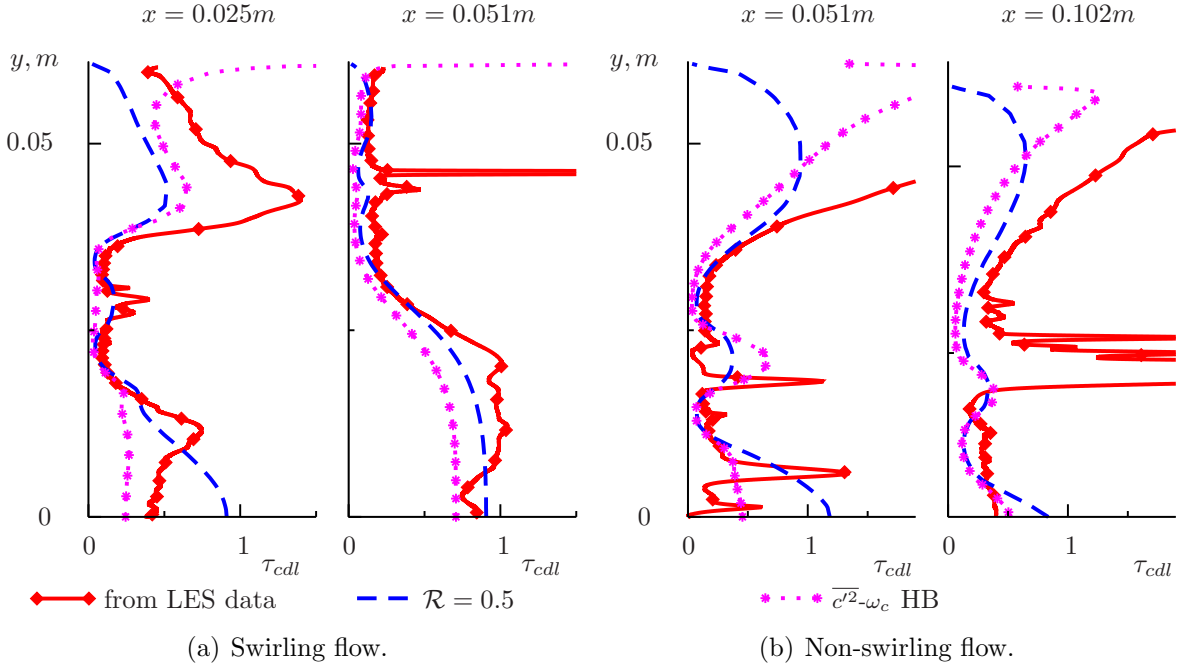


Figure 3.2.41: Dimensionless turbulent scalar time scale evaluated from LES data and resulting from RANS modeling. Wilcox 1988 k - ω model is used for the turbulence modeling. All values are non-dimensionalized using the same quantities as in figure 3.2.37.

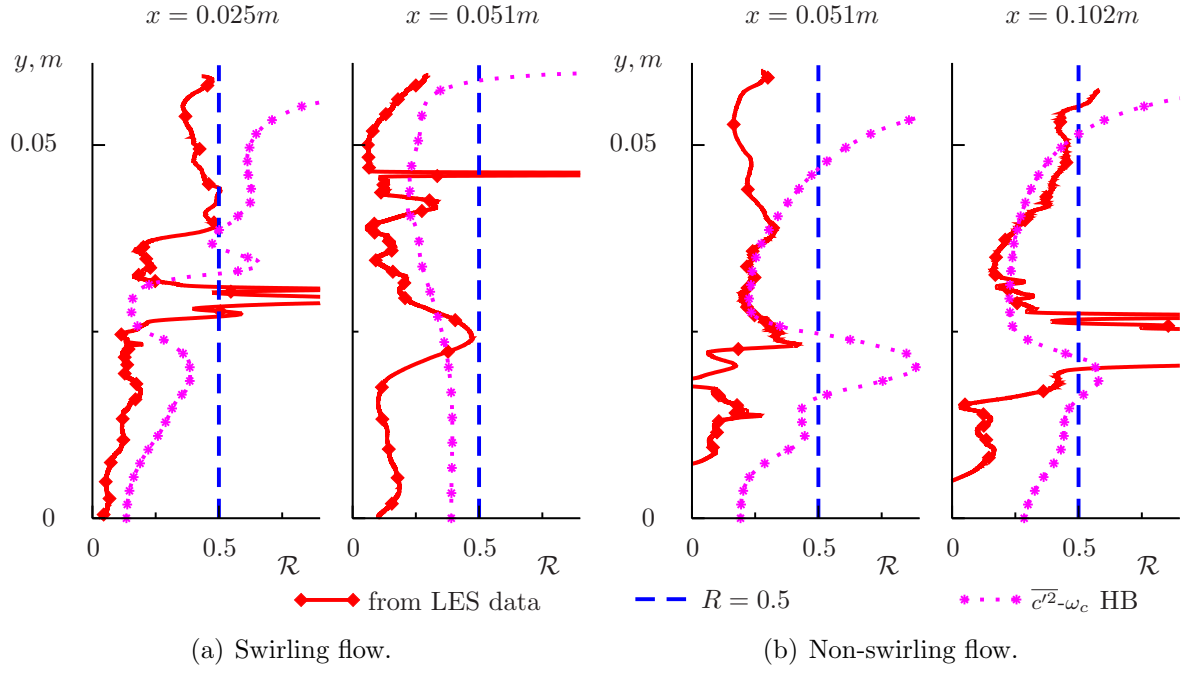


Figure 3.2.42: Turbulent scalar to velocity time scale ratio \mathcal{R} evaluated from LES data and resulting from RANS modeling.

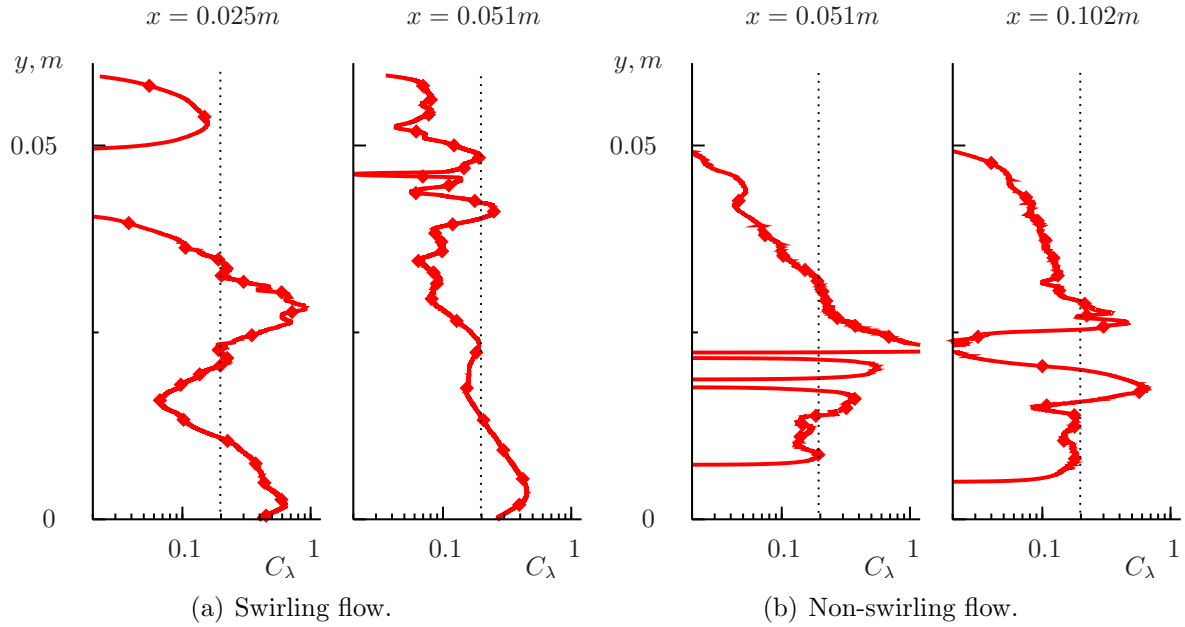


Figure 3.2.43: Turbulent scalar diffusivity modeling coefficient C_λ evaluated as $C_\lambda = \alpha_t / (k\tau_\lambda)$ with $\tau_\lambda = \sqrt{(c'^2/\varepsilon_c)}(k/\varepsilon)$ using the LES data.

can be observed that τ_c given by the HB model lies slightly closer to the LES values than τ_c given by $\mathcal{R} = 0.5$.

Figure 3.2.42 additionally compares the values of the turbulent scalar to velocity time scale ratio \mathcal{R} obtained from LES data and given by the HB model. The popular constant approximation value $\mathcal{R} = 0.5$ used for $\overline{c'^2}$ calculations by equation 2.2.116 is indicated as well by the blue dashed lines. The values of \mathcal{R} obtained from LES are generally lower than $\mathcal{R} = 0.5$. The two-equation turbulent scalar diffusivity HB model reproduces this trend correctly.

The final analysis regarding the two-equation turbulent scalar diffusivity models that is accomplished in this section is the evaluation of the turbulent scalar diffusivity coefficient C_λ from the equation 2.2.106. This evaluation is presented in figure 3.2.43. As with the jet in crossflow test case (see section 3.1.3.2.3.2, figure 3.1.52), C_λ evaluated from LES data is highly variable. Here again a conclusion can be made that either the models not employing the constant C_λ value would be a better choice or an improved formulation of the τ_λ time scale is needed for the more accurate turbulent scalar diffusivity modeling within the two equation $\overline{c'^2}$ - ε_c or $\overline{c'^2}$ - ω_c approach.

3.3 Concluding remarks

The results presented in this chapter revealed several deficiencies of the tested widespread RANS modeling approaches regarding the turbulence and mixing predictions in complex jet flows. A clear trend of the turbulence and mixing underestimation was revealed for the standard k - ε and SST k - ω models as well as for the Wilcox 1998 and 2006 k - ω models. This trend was observed in all test cases considered in this chapter. This is in contrast to the free round jet test case investigated earlier in chapter 2 for which the turbulence was overestimated by the standard k - ε , SST k - ω , and Wilcox 1988 k - ω models, and the vortex-stretching related round jet correction was necessary to improve the accuracy by introducing additional turbulence damping. It can be concluded that, probably, in the complex jet flows considered here physical effects not yet taken into account by the studied models are significant, for example, the streamline curvature, the effects of swirl, and the effects of acceleration of the central jet by the coflow. These effects should be identified and a suitable model developed in order to improve the simulation quality and turbulence model universality.

The evaluation of LES data revealed that the RANS turbulent viscosity modeling coefficient C_μ (or its analog β_k for the k - ω type models, see equation 2.2.53) is not constant in all presented cases and can be much larger or smaller than the value $C_\mu = 0.09$ traditionally used in all considered models. An introduction of a variable turbulent viscosity modeling coefficient would probably seriously improve the results. It should be mentioned here that even the traditional linear eddy-viscosity models often use a variable turbulent viscosity modeling coefficient in order to improve the prediction quality in the near-wall regions (see discussion on the low-Re models in chapter 2). Thus, introduction of an additional flow-type based prefactor function may help to achieve a more accurate representation of C_μ in the model and should be considered in future development. Moreover, the presented investigations on the budget terms of the turbulent

kinetic energy transport equation revealed that improvements in the turbulent kinetic energy dissipation term are necessary, especially in the case of the swirling flow.

Regarding the mixing predictions here further work on the model improvement is also needed. The obtained turbulent Schmidt number profiles show high variability of this parameter in the considered flows. Models not employing the constant turbulent Prandtl or Schmidt numbers should be more intensively studied in the future. The two-equation turbulent scalar mixing models assessed in this dissertation did not show significant improvement over the constant turbulent Prandtl or Schmidt approach predictions. It should be, however, noted that all of these models were initially developed for the near-wall heat transfer predictions; hence, more effort should be devoted to their adjustment for other applications. The correct turbulent Prandtl number trend prediction for the free round jet shown in chapter 2 or the respectable prediction of the turbulent scalar to velocity time scale ratios in the cases considered in this chapter should be viewed as promising results encouraging further investigations of the two-equation turbulent scalar diffusivity models.

Finally, it should be mentioned here that the present data evaluation indicated some phenomena that cannot be reproduced within the Boussinesq hypothesis and the gradient diffusion hypothesis framework. A vivid example of this is the counter-gradient axial transport in the confined coaxial jet test case discussed in sections 3.2.3.2.1 and 3.2.3.1.3 and confirmed by the experiments of Johnson and Bennett [59]. Such phenomena can be captured only by the direct Reynolds stress and scalar flux modeling or by the vortex-resolving methods such as LES or hybrid RANS/LES approaches which are considered in the next chapter.

4 Application of alternative unsteady vortex-resolving methods

Complementing the studies on RANS modeling and the LES data evaluation for complex jet configurations presented in the last chapter, this chapter is devoted to Unsteady RANS (URANS) and Scale-Adaptive Simulation (SAS) calculations of the flows under consideration. The motivation for this study and a short review on previous attempts to apply hybrid unsteady methods for complicated jet flows can be found in section 1.2. Both the URANS and the SAS methods were chosen taking into account the fact that the most computational codes used for industrial applications were historically established as RANS codes. Consequently, URANS and “second-generation URANS”, as SAS may be called, see ref. [41], are a natural choice since these methods require minimal modifications to existing codes. A short description of both methods, and a discussion on their range of applicability as well as on their numerical setup requirements can be found in section 2.3.1.2.

4.1 Scale-Adaptive Simulations (SAS)

In this section the results from applying the SST SAS model to all three main test cases of this work are presented, and direct comparisons are made with the results of RANS and LES calculations discussed in the previous chapter. Computational grids in the SAS were of the same dimensions as used for the LES calculations. Technically, for a comprehensive investigation on the advantages of using hybrid methods comparatively to LES, numerous grid studies have to be conducted and the accuracy of both methods on the grids with different resolutions compared. Since, for example, in the SST SAS calculations two more transport equations have to be solved than in algebraic turbulent viscosity LES models such as the WALE model used here, employment of SST SAS model would only make practical sense if it could give solutions of a better quality than LES on relatively coarse grids. Such a grid study, however, would be relatively computationally expensive and hybrid method development is not the subject of the current work. Instead this study just aims to answer the important question if SAS would give results of at least similar quality as LES on the grids fine enough for LES to obtain an accurate solution.

First, the results obtained for the jet in crossflow test case are presented in figures 4.1.1 and 4.1.2. Mean velocities, turbulent kinetic energy (in SAS reconstructed as a sum of the resolved and the modeled parts), and the mean transported scalar profiles are validated against experimental data and compared with the results of RANS calculations employing the SST

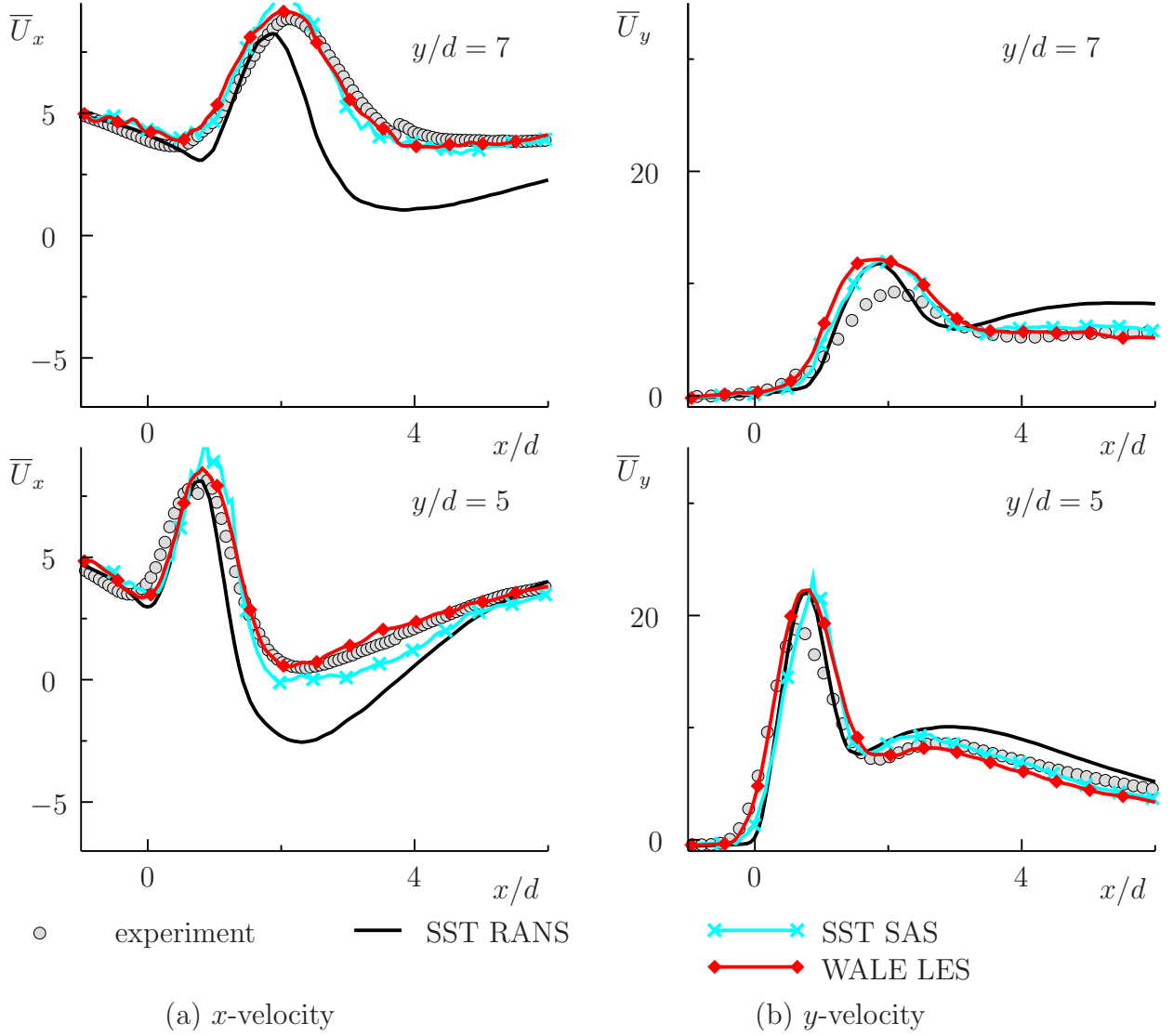


Figure 4.1.1: Jet in crossflow. x - and y -components of the flow velocity vector. $z/d = 0$. RANS, LES, and SAS in comparison with experimental data.

model and of WALE LES. The profiles given by both unsteady methods capture the flow physics more accurately than the SST RANS modeling results. Only small deviations can be observed when comparing the SAS and the LES data. The quality of the predictions given by both methods is approximately equivalent and they reproduce the experimental measurements well. Therefore, the necessary applicability condition of SAS - the ability to produce the results at least as accurate as LES on the same grid is fulfilled for this case, but the computational time on the same grid was about 30% higher with SAS. Hence, additional studies are needed to clarify if the computational time can be strongly reduced in SAS by using coarser grids.

The results for the confined non-swirling jet are presented in figure 4.1.3, and SAS here also gives exceptionally accurate predictions that are comparable to the LES profiles. For the swirling confined jet case (figure 4.1.4), the results obtained by SAS are slightly less satisfactory than for both other configurations. Although the profiles of the mean axial velocity (figure 4.1.4(a)) and the turbulent kinetic energy (figure 4.1.4(b)) do not reveal significant difference

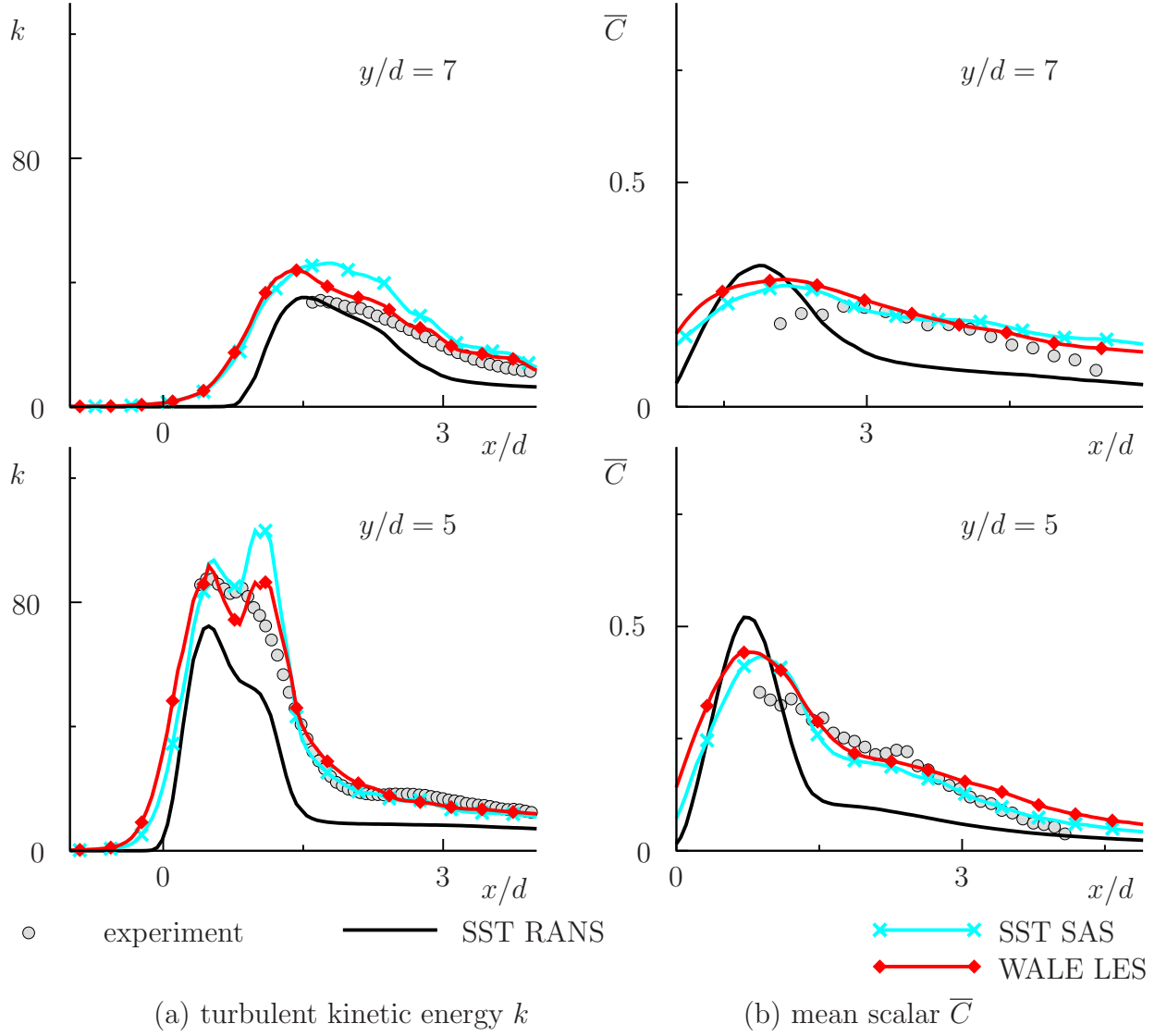
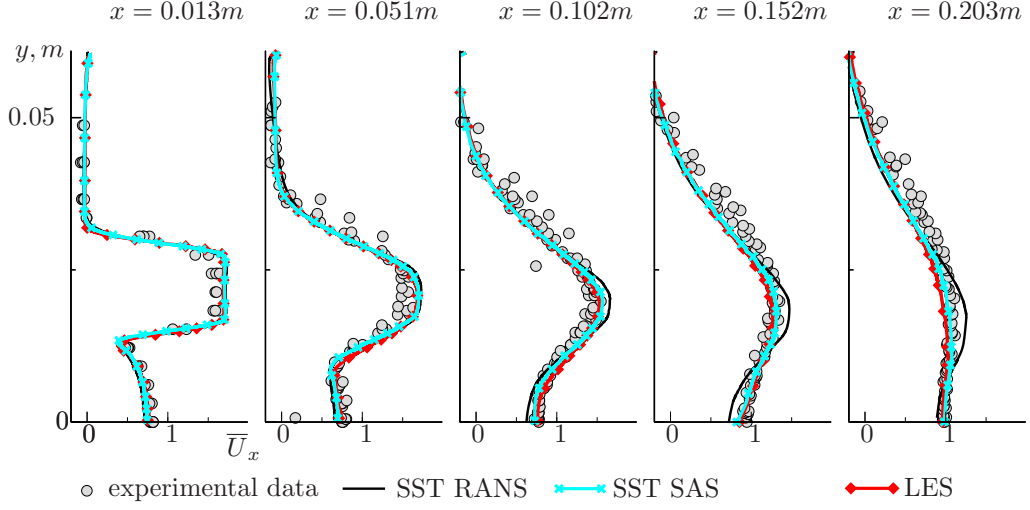
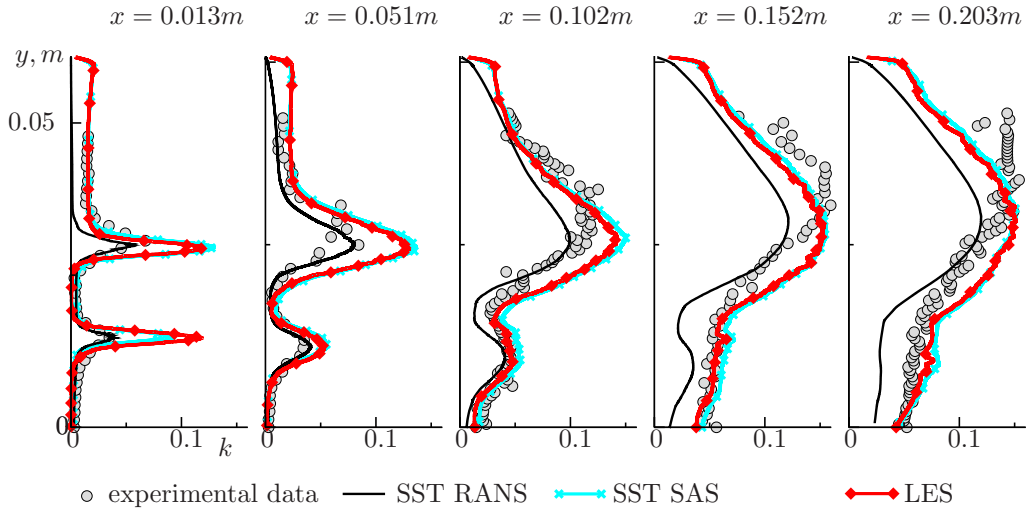
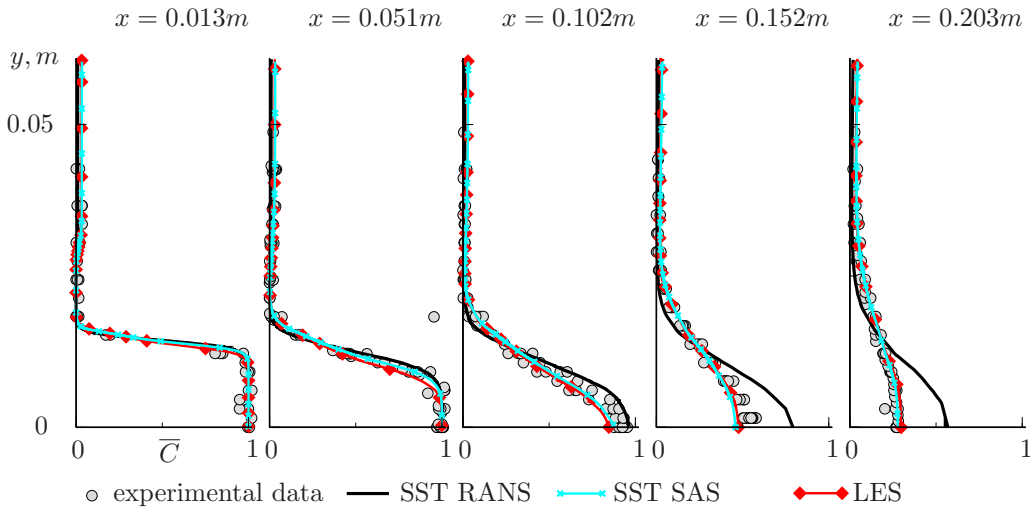


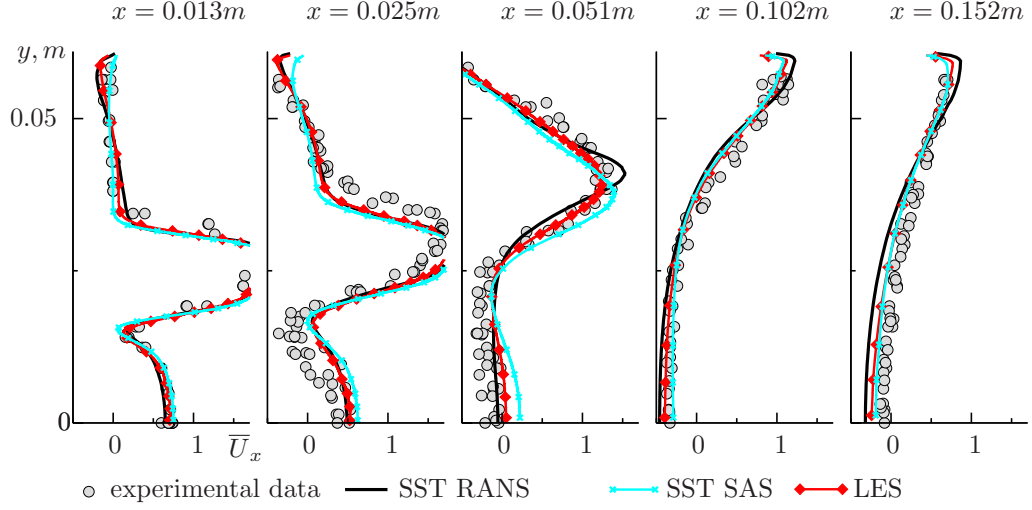
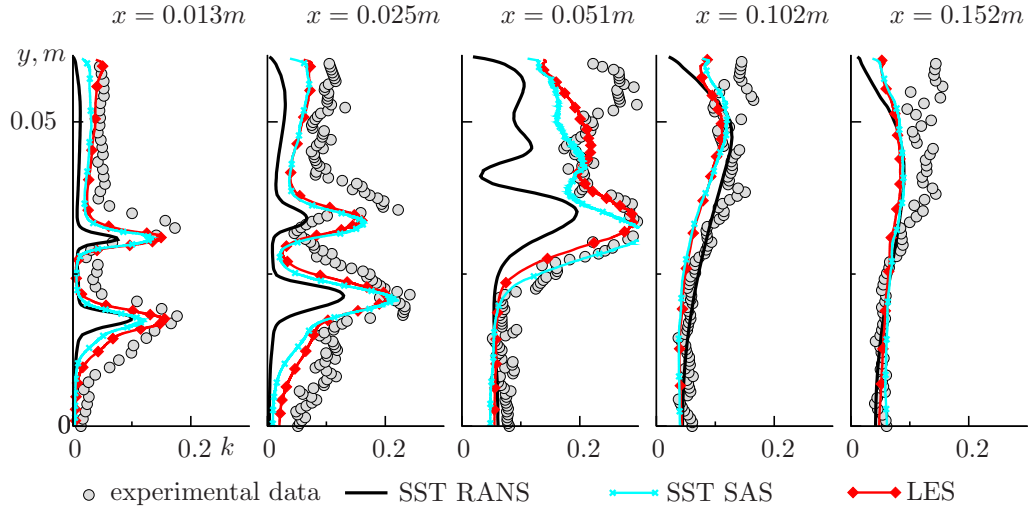
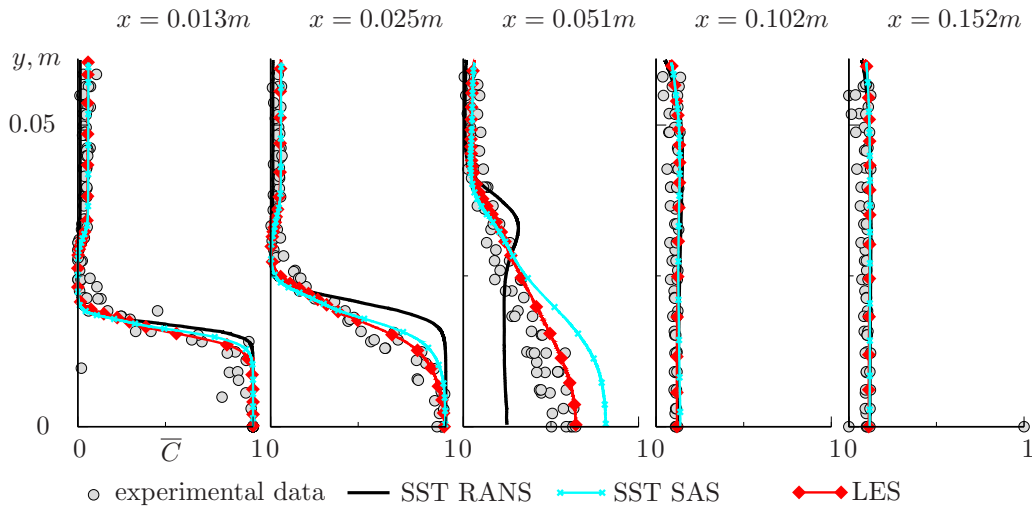
Figure 4.1.2: Jet in crossflow. Turbulent kinetic energy and transported passive scalar. $z/d = 0$. RANS, LES, and SAS in comparison with experimental data. $\sigma_t = 1.0$ is used for the mixing modeling.

between the SAS and the LES results, the mean scalar profiles (figure 4.1.4(c)) show excessive central jet penetration at the edge of the central recirculation zone ($x = 0.051m$), so a considerable under prediction of the mixing occurs in this region. RANS predicts the jet breakup too early in this case and only LES is capable of giving correct results. With further inspection of the \overline{U}_x and k - profiles (figures 4.1.4(a) and 4.1.4(b)), additional indicators of the jet over-penetration can be recognized: a stronger velocity peak at $x = 0.051m$ and the under prediction of k in the jet centerline region at $x = 0.025m$ and $x = 0.051m$. The deficits in the turbulence modeling are more visible in the mean scalar profiles than in the mean velocity profiles. The same trend could be observed earlier in the RANS results for all considered flows. That can be explained by considering the form of the momentum and of the scalar transport equations solved in the simulations. In the scalar transport equation (see equation 2.1.17) the modeled turbulent diffusion term essentially governs the right hand side of the equation. In contrast,


 (a) Axial component of the mean flow velocity \bar{U}_x .

 (b) Turbulent kinetic energy k .


(c) Transported passive scalar.

 Figure 4.1.3: Non-swirling flow. RANS, LES, and SAS in comparison with experimental data. $\sigma_t = 1.0$ is used for the mixing modeling.


 (a) Axial component of the mean flow velocity \bar{U}_x .

 (b) Turbulent kinetic energy k .


(c) Transported passive scalar.

 Figure 4.1.4: Swirling flow. RANS, LES, and SAS in comparison with experimental data. $\sigma_t = 1.0$ is used for the mixing modeling.

the Navier-Stokes equations contain also the pressure term on the right hand side (see equation 2.1.16) which makes the relative impact of the turbulent diffusion term less significant.

To provide additional insight into the nature of differences in the SAS prediction quality in all three test cases, figure 4.1.5 presents the 2D plots of the ratio of the resolved to the total turbulent kinetic energy $k_{res}/(k_{res} + k_{mod})$. According to Pope [102], at least 80% of the turbulent kinetic energy of the flow should be resolved in LES. This criterion of “80% - resolution” can be chosen to identify the “LES” zones of the SAS solutions (see figure 4.1.5). In all cases the jet core regions in the locations directly after injection still remain in the “RANS” mode (i.e. more than 90% of k are modeled). For jet in crossflow and for the non-swirling coaxial jets, the transition from the “RANS” to the “LES” mode takes about one jet diameter (or one coflow annulus height as in the coflow of the non-swirling jet), and for the swirling jet flow in both main jet and the coflow region the transition occurs much faster. This can be explained by the observation that the SAS model automatically decreases the level of the modeled turbulent viscosity if a possible flow unsteadiness is detected (see section 2.3.1.2). Thus for the considered swirling flow on the grid employed here it may “overreact” and start to decrease the modeled turbulent viscosity too quickly. This can lead to a situation in the transitional region where the level of the modeled turbulence drops abruptly, but the resolved fluctuating part is not fully developed yet. This causes an underestimation of the total turbulent kinetic energy of the flow as shown in figure 4.1.4(b) (the total turbulent kinetic energy of SAS has lower values than the resolved turbulent kinetic energy in LES) and, consequently, to the over prediction of the jet penetration depth and to the under prediction of mixing. More investigations on this hypothesis are needed in future.

It can be generally observed that the RANS/LES transition zones in all three cases studied here are relatively short. SAS acts here almost like a zonal model switching from a “full

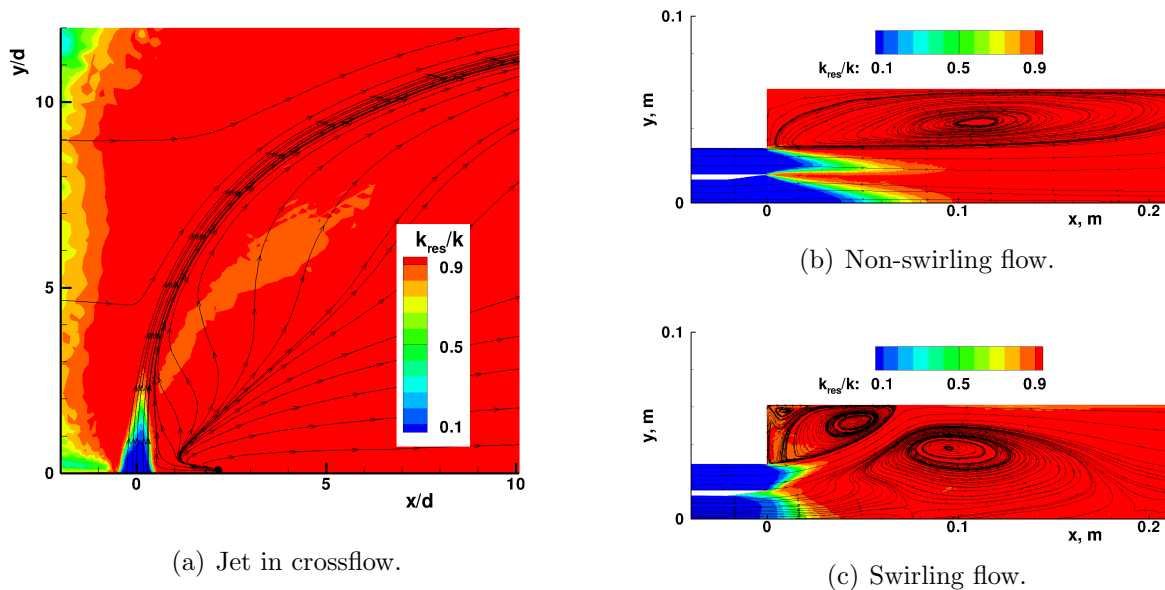


Figure 4.1.5: Ratio of the resolved to the total turbulent kinetic energy in SAS $k_{res}/(k_{res} + k_{mod})$.

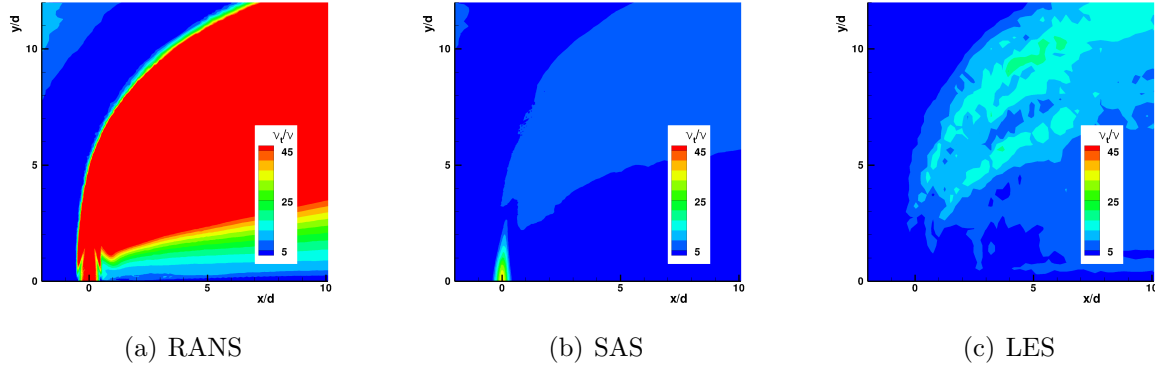


Figure 4.1.6: Jet in crossflow. Ratio of the modeled (SGS for LES) turbulent viscosity to the molecular viscosity ν_t/ν in RANS, SAS, and LES.

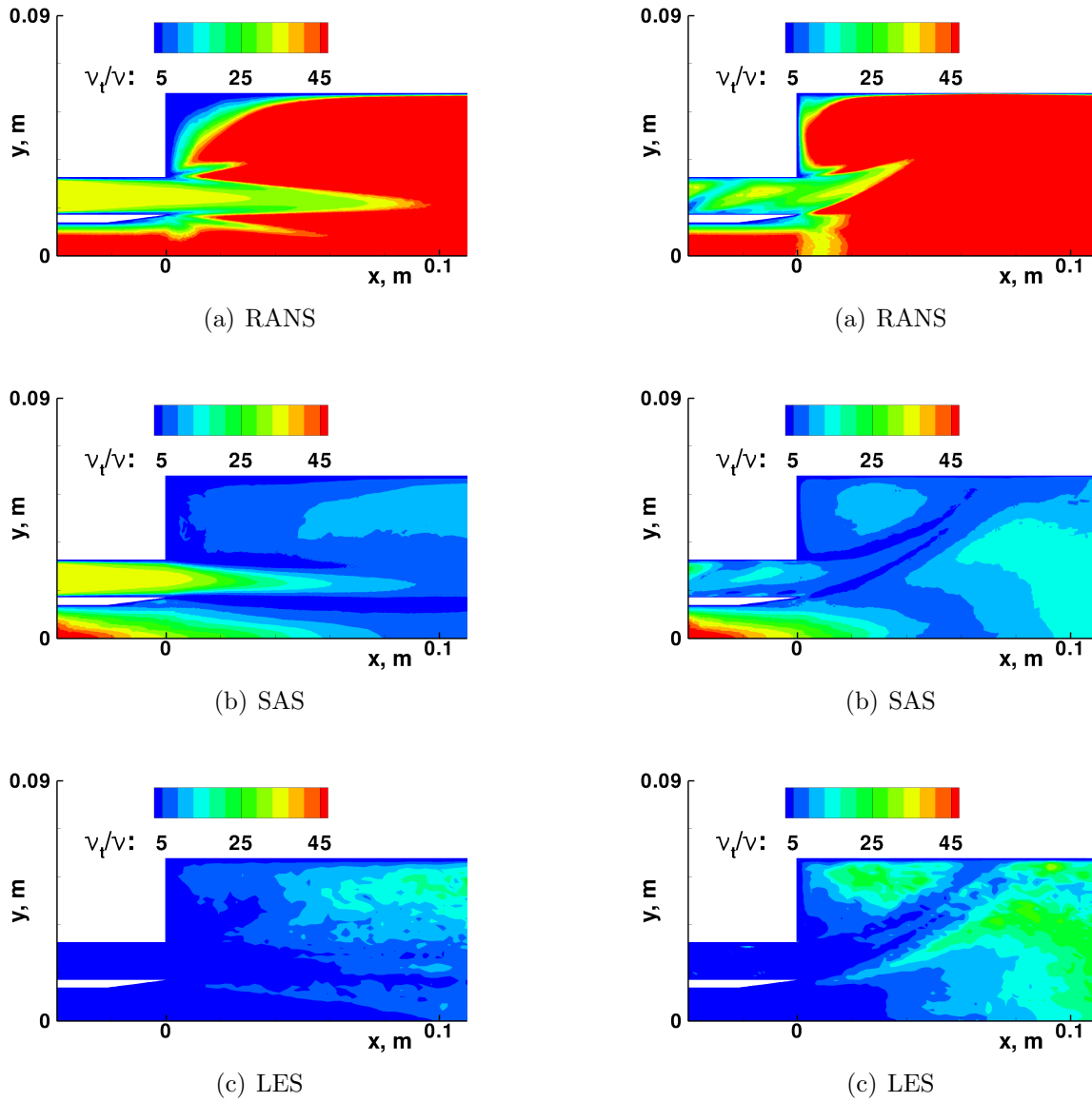


Figure 4.1.7: Non-swirling flow. Ratio of the modeled (SGS for LES) turbulent viscosity to the molecular viscosity ν_t/ν in RANS, SAS, and LES.

Figure 4.1.8: Swirling flow. Ratio of the modeled (SGS for LES) turbulent viscosity to the molecular viscosity ν_t/ν in RANS, SAS, and LES.

RANS” to a “full LES” solution very rapidly. That explains the high similarity of the SAS and the LES solutions for the jet in crossflow and for the confined jet. The main difference with the zonal approaches specially designed to act in such a manner (see examples in ref. [41] and in ref. [108]) is the absence of an algorithm for the generation of the fluctuating turbulent content on the edges of the RANS/LES zones. In the jet in crossflow and in the confined jet case that obviously does not influence the quality of the solution, but in the swirling case it delays the breakup process for the central jet, thereby significantly reducing the accuracy. The advantage of the SAS comparatively to the zonal RANS/LES models is the automatic switching from the RANS to the LES mode which does not require any additional user input.

In addition to the presented plots of the resolved part of the turbulent kinetic energy in SAS, figures 4.1.6, 4.1.8, and 4.1.7 compare the mean turbulent viscosity levels in all simulations. For LES the sub-grid scale (SGS) turbulent viscosities are presented (not to be confused with the Reynolds-averaged turbulent viscosities obtained from the resolved data fields in the previous chapter). RANS, as expected, gives the highest levels. In the SAS simulations the ν_t returned by the model is only slightly lower than in RANS in the jet cores directly after the injection locations, but it drops drastically in the main flow regions when the SAS term comes into effect. In LES simulations the SGS turbulent viscosity level is very low in the jet and in the coflow pipes and only starts to grow with the shear development. In the downstream regions the SGS turbulent viscosities given by LES can even exceed the levels of the SAS ν_t . One possible explanation is the fact that LES explicitly depends on both the velocity gradients and the grid cell size. In the current calculations the grids start to coarsen in the downstream regions, but the velocity gradients may still remain high; hence, the ν_t values given by the model increase. In SAS such explicit dependence on the grid cell size is not present, so the turbulent viscosity levels remain low.

4.2 Unsteady RANS simulations (URANS) of jet in crossflow

Following the SAS investigations of different complex jet flows presented above, the applicability of the unsteady RANS (URANS) method for jet in crossflow simulations is considered in the present section. Theoretical background of this method was discussed in section 2.1.3. Practical experience shows [28, 93] that running the RANS models in an unsteady mode and obtaining a time-dependent solution is possible if the flow is characterized by a presence of the essentially unsteady large-scale coherent vortical structures or periodic flow pulsations. Due to its inner structure, jet in crossflow configuration is perfectly suited for URANS simulations. As discussed in section 1.2, this flow pattern is characterized by the presence of at least four different types of large-scale unsteady coherent vortices. The steady-state solutions presented in section 3.1 were achieved by the application of a symmetry boundary condition in the jet center plane. Such a condition has a stabilizing effect on the RANS solution. If the symmetry boundary condition is removed and the full domain is simulated (as it is done in LES), unsteady flow motions can be resolved by URANS as well.

In the current work, the SST RANS model was applied for the URANS simulations on the

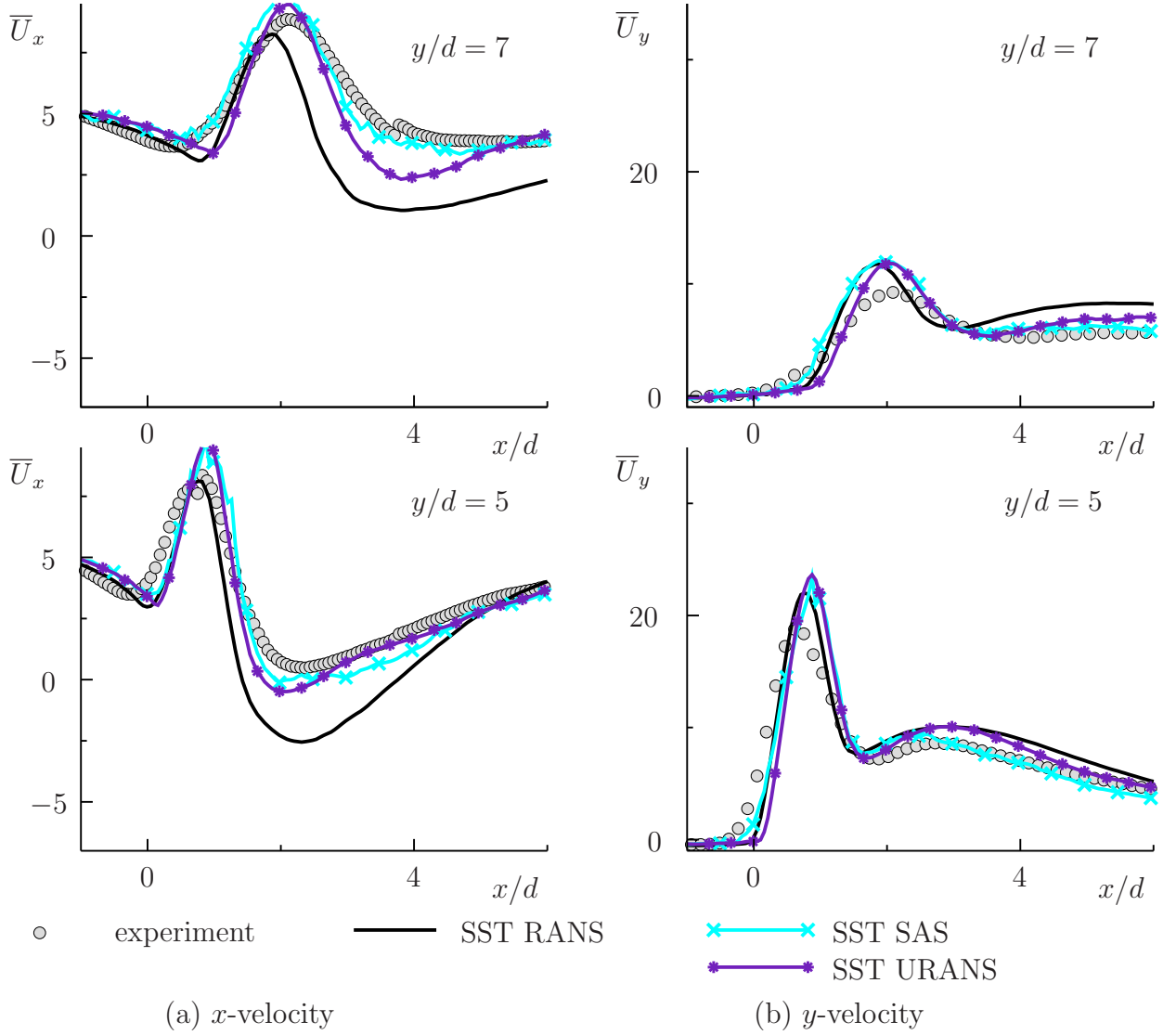


Figure 4.2.1: Jet in crossflow. x - and y -components of the flow velocity vector. $z/d = 0$. SST RANS, URANS, and SAS in comparison with experimental data.

grid with the same resolution as used in the LES and SAS presented in the previous sections. The results of this URANS calculations are presented in figures 4.2.1 and 4.2.2. In the same figures, the profiles obtained in RANS and SAS using the same model are also provided for comparison. Figures 4.2.1 and 4.2.2 show that running the SST model in an unsteady mode noticeably increases the accuracy of jet in crossflow simulations as it was already reported in [54, 51]. The accuracy level of SAS, however, can not be reached by URANS*.

The extent of the turbulent spectrum resolution in URANS is not as deep as in SAS. This is illustrated in figures 4.2.3 and 4.2.4 showing the vortical structures of a different jet in crossflow test case discussed in ref. [54] that was also considered in the framework of this dissertation. In figure 4.2.3 the main vortices resolved in both URANS and SAS calculations are illustrated with isosurfaces of the second invariant of the velocity gradient tensor, $Q = \frac{1}{2}(\|\Omega\|^2 - \|S\|^2)$

*An advantage of URANS over SAS can be a potentially much lower grid resolution demand, but thorough grid dependence studies for both methods are not the focus of this work.

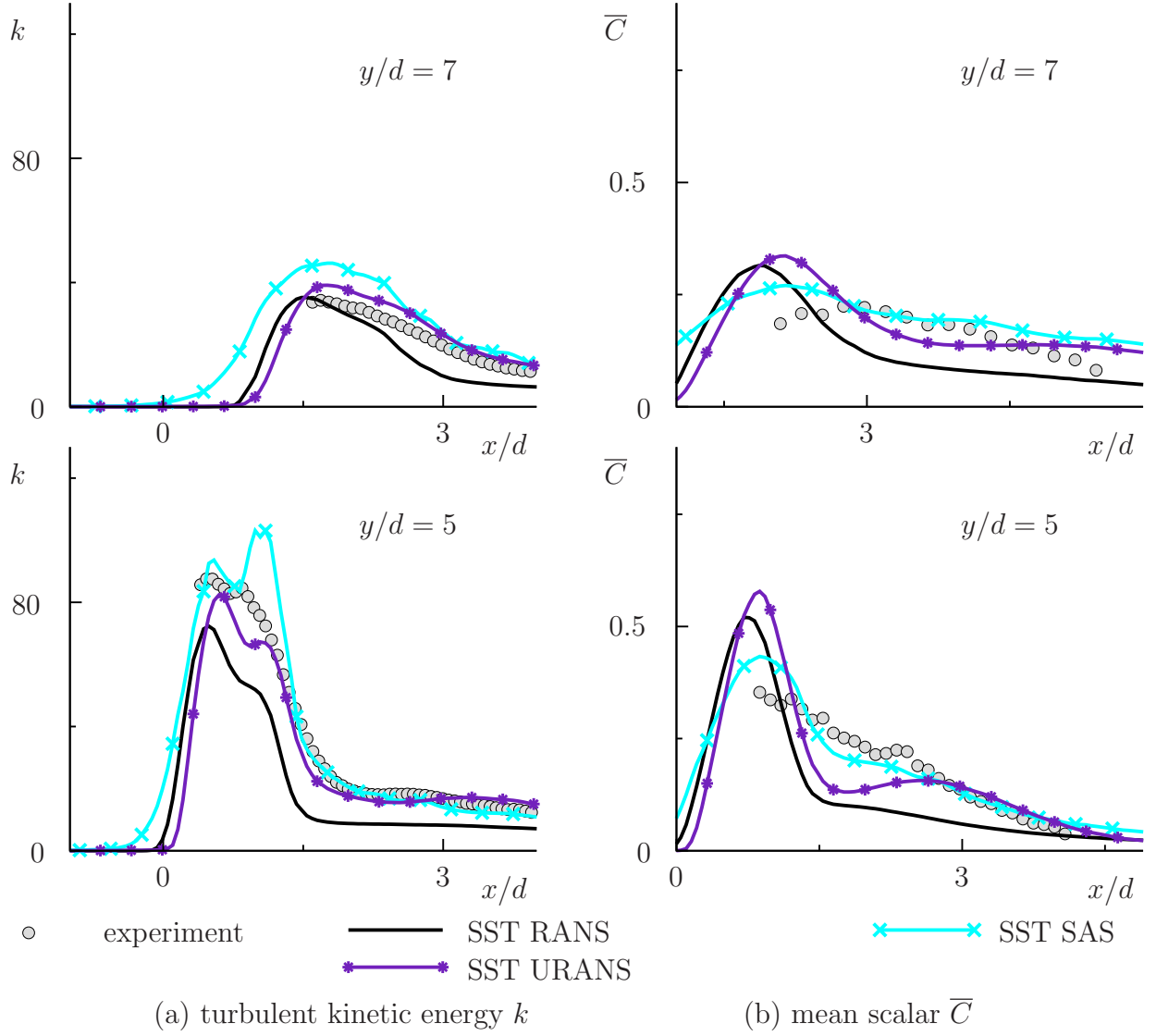


Figure 4.2.2: Jet in crossflow. Turbulent kinetic energy and transported passive scalar. $z/d = 0$. SST RANS, URANS, and SAS in comparison with experimental data. $\sigma_t = 1.0$ is used for the mixing modeling.

where Ω is the vorticity and S is the strain-rate tensor. The positivity of Q is a criterion for the vortex identification according to ref. [49] (see also ref. [39] for the review on the vortex-visualization methods).

The vortical structures obtained in both URANS and SAS show a resemblance to the results of the experimental visualizations given in refs. [38, 75] and to the LES-based visualizations of refs. [130, 111]. All four main types of the jet in crossflow vortices indicated in figure 1.2.1 can be observed in both simulations. The horseshoe vortices are seen in figure 4.2.3 in the main channel boundary layer upstream of the jet injection location. The shear layer vortices are clearly seen in the same figure on the upstream side of the jet but, as further visualization of ref. [54] reveals, are also present on the lee side. The wake vortices are especially clearly seen in the URANS results at the downstream side of the jet (figure 4.2.3(a)). Finally, the counter-rotating vortex pairs are visualized in figure 4.2.4.

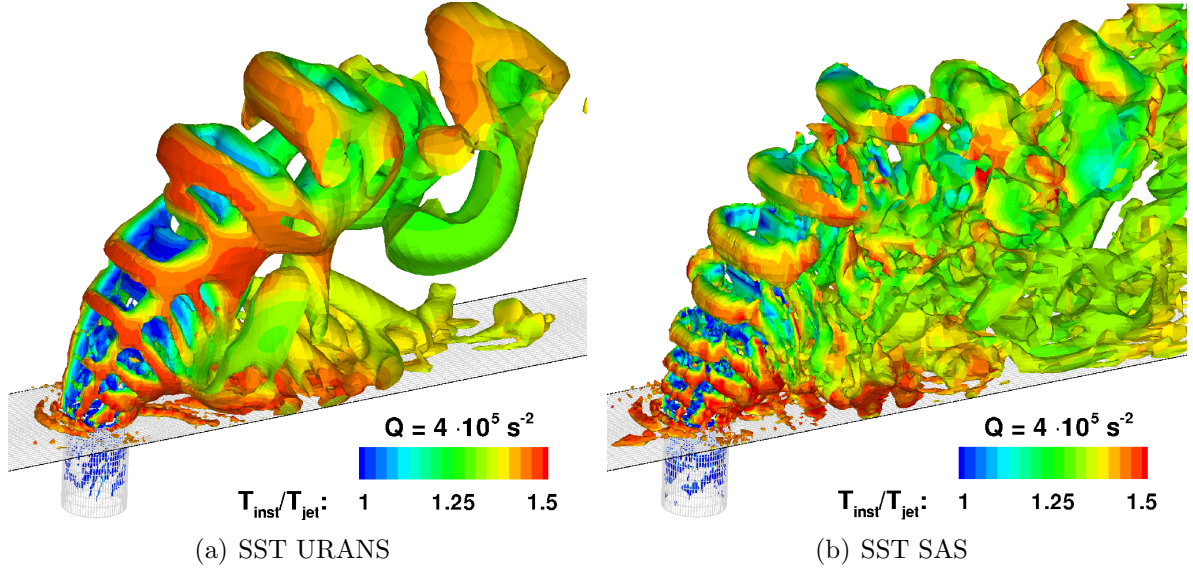


Figure 4.2.3: URANS and SAS of the jet in crossflow test case considered in ref. [54]. Isosurfaces of $Q = 4 \cdot 10^5 \text{ s}^{-2}$

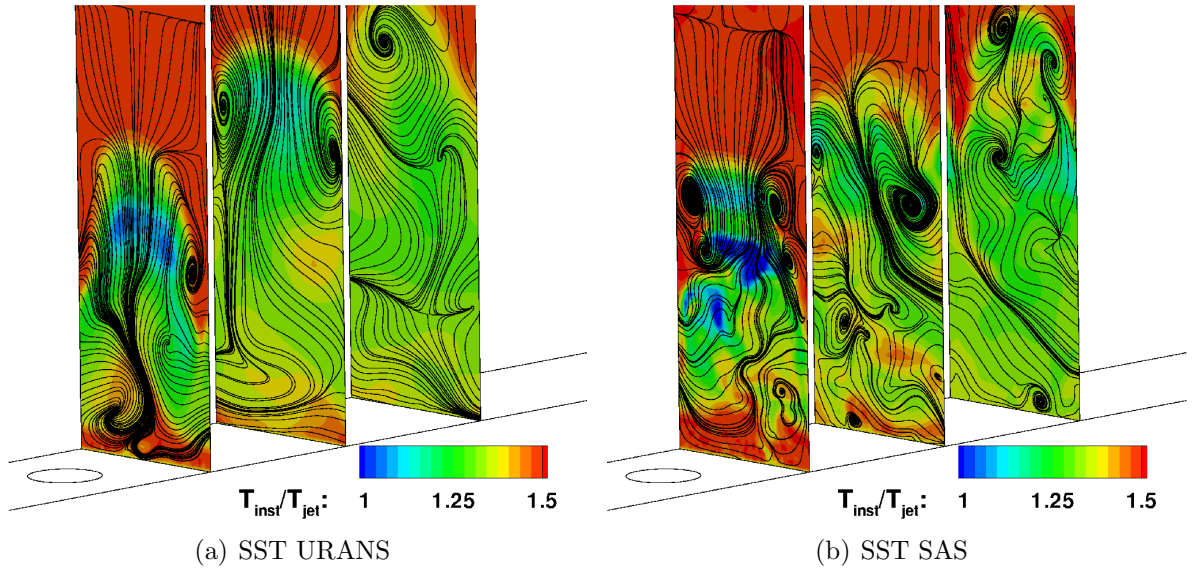


Figure 4.2.4: URANS and SAS of the jet in crossflow test case considered in ref. [54]. 2D streamlines based on instantaneous velocity.

The flow structure given by SAS is much more intricate than in URANS. This can be observed in both figures 4.2.3 and 4.2.4. For example, in figure 4.2.4, URANS shows the counter-rotating vortex pair as two uniform large-scale structures in all presented slices. In the SAS visualization of figure 4.2.4, the first slice near to the jet injection location indicates more the complex characteristic kidney-shaped vortices. As described in the experimental work of ref. [75], this form is typical for the early stage of a counter-rotating vortex pair formation and results from the merge of the side arms of the upstream and the lee side shear layer vortices. This process could not be resolved by URANS.

It should also be mentioned here that the URANS results can also differ in their resolution

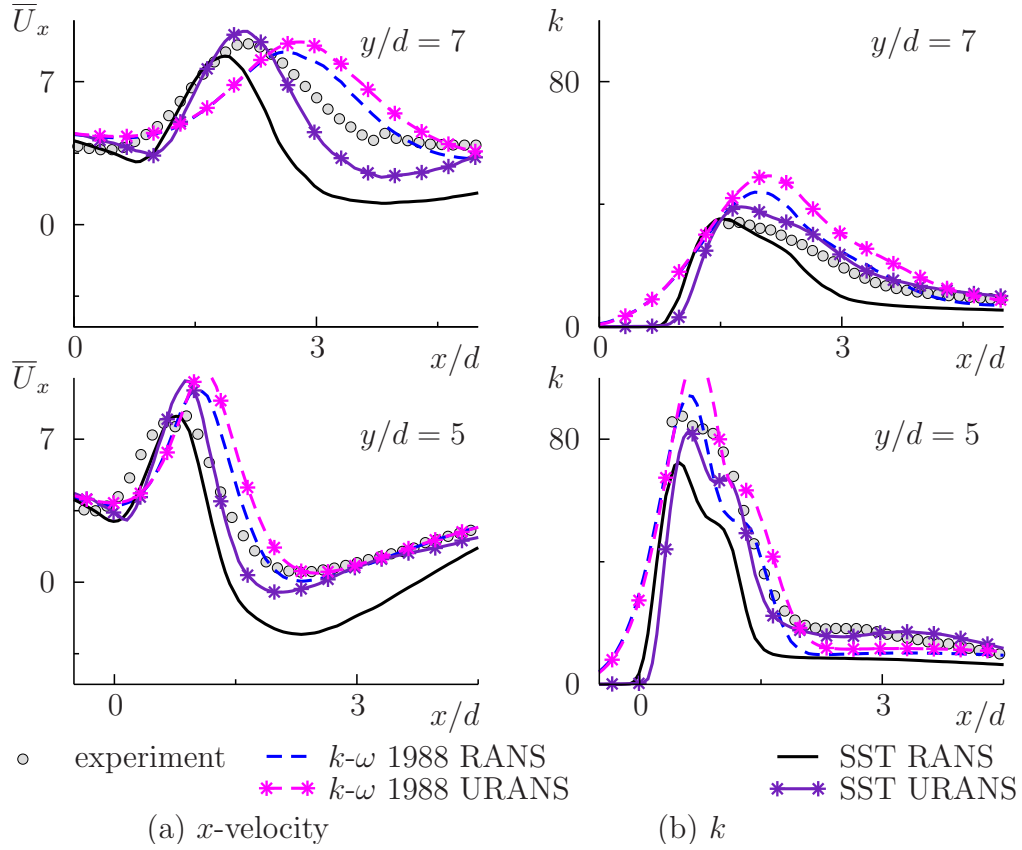
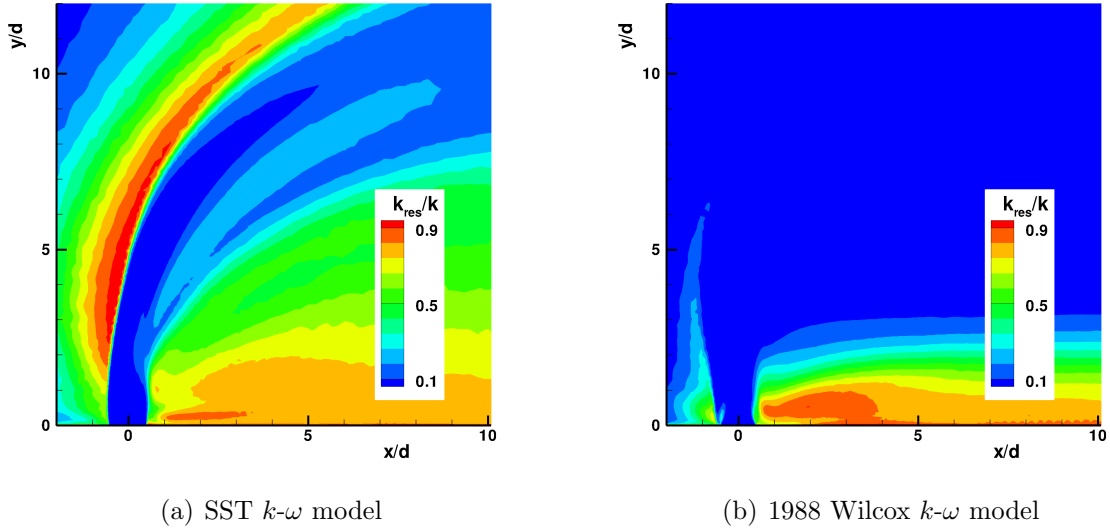


Figure 4.2.5: Dependence of the URANS results on the underlying turbulence model.


 Figure 4.2.6: Ratio of the resolved to the total turbulent kinetic energy $k_{res}/(k_{res} + k_{mod})$ in URANS of jet in crossflow.

depth depending on the underlying RANS model. This is illustrated in figures 4.2.6 and 4.2.5 where the results of URANS employing the SST and the Wilcox 1988 k - ω models are compared. Figure 4.2.5 shows the mean x -velocity and the turbulent kinetic energy predictions. The results of the steady-state RANS calculations with both models are presented as well. Furthermore, figure 4.2.6 shows the ratio of the resolved to the total turbulent kinetic energy in both cases.

It can be observed in figure 4.2.5 that, in contrast to the SST URANS simulations, URANS with the Wilcox 1988 $k-\omega$ model yields worse predictions than its steady-state RANS variant. URANS over estimates the momentum diffusion. The reason is that the Wilcox 1988 $k-\omega$ model when run in an unsteady mode increases the level of the total turbulent kinetic energy, which is already slightly over predicted in the RANS $k-\omega$ simulations. For the SST model, which under predicts the level of k in RANS, additional resolved turbulent kinetic energy has a positive effect.

The magnitude of the resolved kinetic energy k_{res} increase found in URANS depends on the selected RANS momentum closure. Here, for example, the level of the resolved energy k_{res} is different for the Wilcox 1988 $k-\omega$ and the SST model. This can be seen in both figure 4.2.6 and in figure 4.2.5(b). Figure 4.2.6 shows that the resolved part of k in simulations with the 1988 $k-\omega$ model is much less than in simulations with the SST model and both of them are much less than the resolved part of k in SAS, see figure 4.1.5(a). This behavior can be explained easily. Since RANS SST model a-priori tends to have smaller k values, thereby, producing lower ν_t values, the unsteady motions can develop much easier than with the Wilcox $k-\omega$ model which produces more unsteadiness damping turbulent viscosity. In this comparison the main principle of the SAS concept, resolution of the unsteadiness achieved by decreasing ν_t , can be observed. In practical applications, this can lead to the curious result that some models producing poor quality results in steady-state simulations perform better in URANS mode than the more accurate RANS approaches. The high dependence of the URANS results on the employed turbulence model has to be taken into account when applying this method. Studies on the comparative dependence of RANS, URANS, SAS, and LES jet in crossflow scalar mixing predictions on the employed turbulent Schmidt number value were performed in the framework of this dissertation as well. The results are published in refs. [51, 50]. These results also show that, in contrast to LES and SAS, the URANS mixing results decisively depend on the choice of σ_t .

4.3 Practical application: self-ignition simulation in jet in crossflow

This section is devoted to a practical gas turbine combustion application of time-resolving turbulence modeling methods. Unsteady methods are a necessity for the modeling of transient processes like self-ignition and flame propagation. The numerical simulation of a self-ignition process using the SAS and URANS methods was performed in the present work in order to test the applicability of such methods for this problem type.

The test case selected is related to the injection of H_2 -rich fuels in the premixing duct of a lean premixed combustion system. Such fuels introduce special challenges due to a lower autoignition temperature and lower flashback margins compared to natural gas [74]. In the present work the particular case of a reheat, or sequential, combustion system such as ALSTOM's

GT24[®] and *GT26*^{®*} family [62, 44] was considered. This combustion concept is characterized by two fuel injection and energy conversion steps in two separate combustion chambers with an expansion step in a high-pressure turbine stage in between. The mixing zone of the reheat combustor is characterized by high gas temperatures (above 1000 K). Therefore, the ignition delay times, which depend on temperature and on reacting species concentration, are extremely short. Prediction of the ignition delay times as well as of the subsequent flame propagation by numerical simulations presents a significant challenge since such simulations involve a highly complex interplay of turbulence, mixing, and combustion modeling effects. In the present work the influence of the turbulence modeling approach is studied.

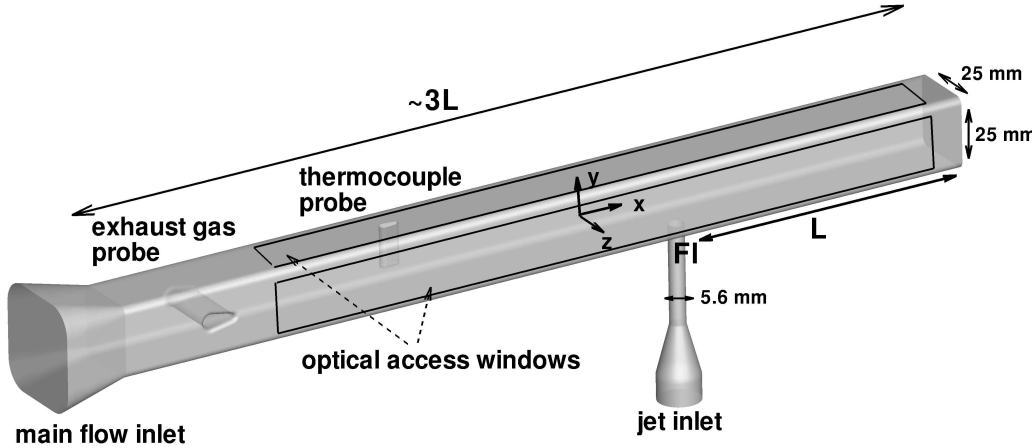


Figure 4.3.1: Computational domain.

4.3.1 Test case description

The computations are performed for the conditions of experiments on a research reheat combustor [36, 35] that were conducted at the Institute of Combustion Technology of the German Aerospace Center (DLR) in Stuttgart. A detailed description of the test rig and of the experimental setup can be found in refs. [36, 35]. For the current simulations the mixing section of the experimental setup is the object of interest, so the mixing section is completely reproduced in the chosen computational domain as shown in figure 4.3.1.

At the inlet of the mixing section the high temperature flue gas from a hot gas generator enters a square duct with a cross-section of $25 \times 25 \text{ mm}$. The description of the hot gas generator operating conditions can be found in [36, 35]. The temperature (above 1000K) and the O_2 content (about 15%vol.) of the hot gas are typical for reheat combustors. The total hot gas mass flow rates on the mixing section inlet are between $260 - 550 \text{ g/s}$, which leads to velocities of above 150 m/s . In the calculations a constant mass flow rate that was identical to the experimental values was set at the mixing section inlet (with a constant velocity distribution over the inlet cross-section). The pressure in the mixing section is 15 bar . The main channel of the mixing section includes an exhaust hot gas emission probe and a thermocouple probe located upstream of the fuel injection. Both are reproduced in the computational domain

**GT24*[®] and *GT26*[®] are registered trademarks of ALSTOM Technology Ltd.

(figure 4.3.1).

The fuel is injected from the lower wall of the mixing section via a jet in crossflow configuration as shown in figure 4.3.1. The diameter of the fuel injector is 5.6mm . A carrier medium (nitrogen) is injected together with the fuel in order to achieve the desired jet to crossflow momentum flux ratio and hence the desired penetration depth. The carrier to fuel mass flow ratios are equal to 1 : 1 in the considered test case, and the fuel/carrier temperature is 313K . In the simulations presented below the fuel is a H_2/N_2 mixture with the hydrogen concentration of $80\%vol.$ which corresponds to the setpoint fuel blend in the autoignition experiments [36]. The jet to crossflow momentum flux ratio in this configuration is about $J \approx 1.4$. It should be noted that in the experiment the setpoint hydrogen concentration has never been reached since the autoignition occurred already at the lower concentrations (about $50\%vol.$) [36]. Furthermore in the presented simulations the crossflow temperature is slightly higher than it was in experiment (around 15%).

In the experiments the optically accessible mixing section parts were convectively air-cooled and the metal parts were water-cooled. The total heat losses in the mixing section were estimated to be about 6% in the experiments [36]. The heat losses were accounted for in the simulation by the application of negative heat fluxes in the respective cooled zones according to the experimental estimation.

4.3.2 Details of the numerical simulation.

The governing equations in the current simulation differ from the form given in the theory section (section 2.1) because of the strongly varying density and temperature due to ignition and flame propagation. Thus, the simplifications related to the constant density assumption can not be made. The form of the governing equations in such case can be found, for example, in refs. [99, 43, 22]. All turbulence and mixing modeling details remain essentially the same. To obtain the results presented below, Menter SST $k-\omega$ model is applied for both URANS and SAS computations. Turbulent Prandtl and Schmidt numbers $\sigma_t = 1.0$ are used for the mixing modeling.

4.3.2.1 Combustion modeling

For the combustion modeling in the reacting flow simulations, a finite-rate combustion model was used in combination with an assumed joint PDF (probability density function) approach. A detailed description of the used combustion modeling technique can be found in ref. [24].

The employed reaction mechanism is the 9-species 21-steps scheme of O’Conaire et al. [94]. It has been validated against experimental data of ignition delay times in the ranges of $0.05 - 87$ bar pressure, $298 - 2700$ K temperature and $0.2 - 6.0$ equivalence ratio in ref. [94]. This mechanism is widely accepted for the combustion simulations at a large range of temperatures and pressures.

4.3.2.2 Computational grids and time stepping

All calculations were performed on polyhedral unstructured grids with hexahedra-layers on the walls (figure 4.3.2). The grid for both URANS and SAS had around 950 000 points (see figure 4.3.2). The grid is refined in the jet shear layer regions based on the results of preliminary calculations using the local velocity differences criterion.

The time step in the current unsteady calculations was about $10^{-7} s$, which leads to maximal CFL numbers of 2. All time-averaged results presented below are obtained after integrating over about 5 residence times ($5L/U_{cf}$).

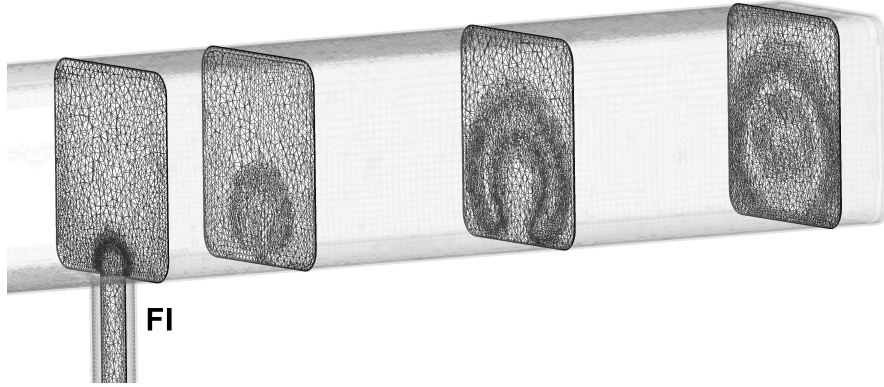


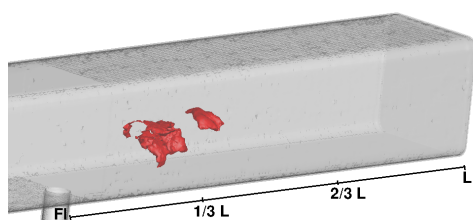
Figure 4.3.2: Computational grid for the SAS simulations. Cross-sections in different positions along the mixing zone of the main channel.

4.3.3 Results

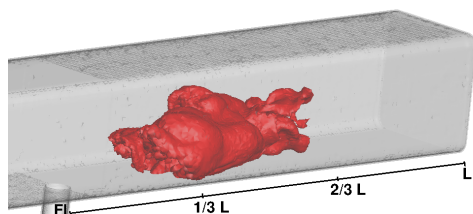
The RANS calculations of the studied mixing and self-ignition arrangement performed in the framework of this dissertation are published in ref. [55]. In the same publication also the direct comparison of the RANS and SAS results against experimental data for a non-reacting fuel mixture is presented. These results again demonstrate the superiority of the SAS method in terms of accuracy over RANS. In the following the differences between the SAS and the URANS predictions in the reacting flow simulations will be elucidated.

In both URANS and SAS autoignition simulations, a pure N_2 jet was injected first into a crossflow with the desired mass flow ratio. After establishing a fully developed turbulent flow field under the given conditions, the pure N_2 was exchanged by the N_2 /fuel blend mixture. From that moment on data “snapshots” were taken in order to observe the autoignition phenomena. Such a procedure is similar to the time-ramping of the H_2 mass flow rate which was applied in the autoignition experiments [36, 35].

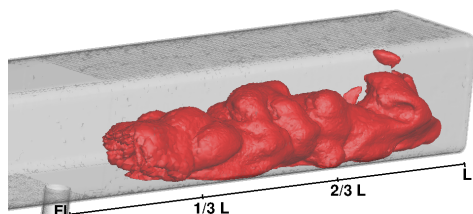
In the present study isosurfaces of the OH mass fraction, Y_{OH} , were selected as the flame front indicator. The isosurface of $Y_{OH} = 0.0001$ at different time instants of the SAS is presented in figure 4.3.3 and the same time instants of the URANS simulation can be seen in figure 4.3.4. The first data snapshots in all figures were taken shortly after the first occurrence of ignition kernels. This time point is chosen to be a reference time point. In both SAS and URANS the ignition starts at the beginning of the second third of the distance L between the jet injection location



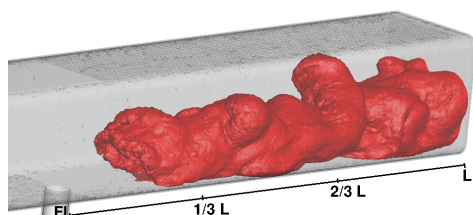
(a) $t = 0ms$



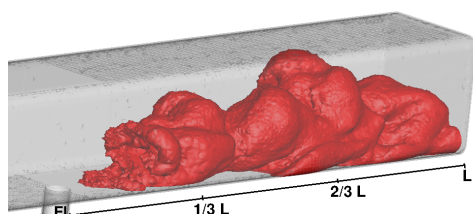
(b) $t = 0.1ms$



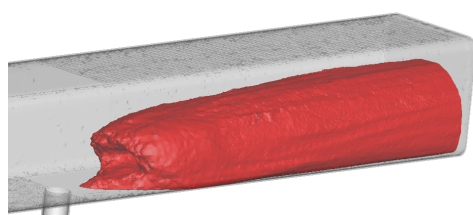
(c) $t = 0.3ms$



(d) $t = 1ms$

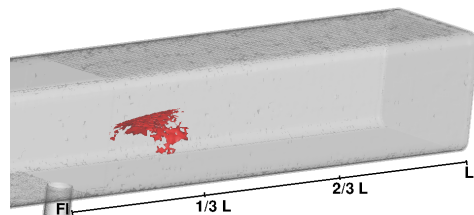


(e) $t = 2.5ms$

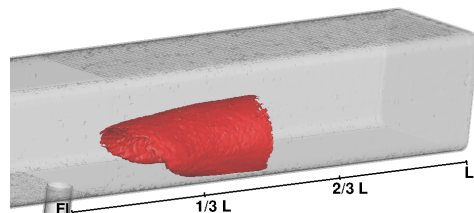


(f) Stable flame isosurface (time-averaged)

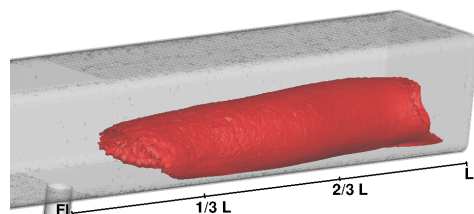
Figure 4.3.3: Isosurfaces of $Y_{OH} = 0.0001$.
Different time points. SAS.



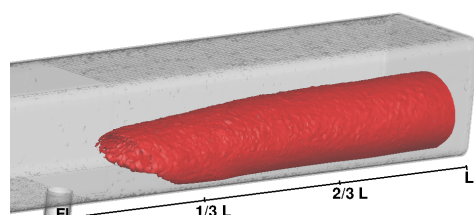
(a) $t = 0ms$



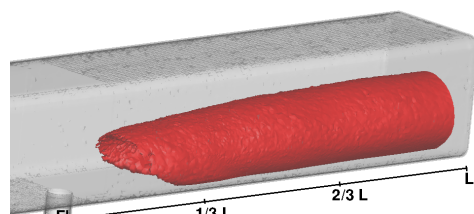
(b) $t = 0.1ms$



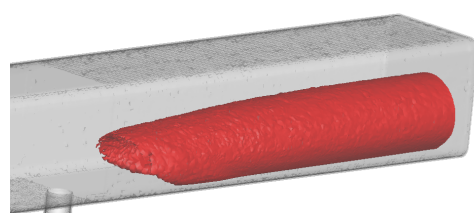
(c) $t = 0.3ms$



(d) $t = 1ms$



(e) $t = 2.5ms$



(f) Stable flame isosurface (time-averaged)

Figure 4.3.4: Isosurfaces of $Y_{OH} = 0.0001$.
Different time points.
URANS.

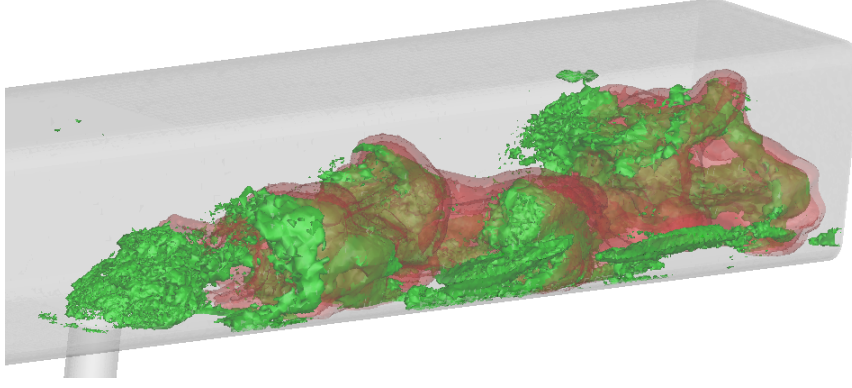


Figure 4.3.5: SAS results. Isosurfaces of $Y_{OH} = 0.001$ (red) and of $U' = 0.15 \cdot \bar{U}_{crossflow}$ (green).

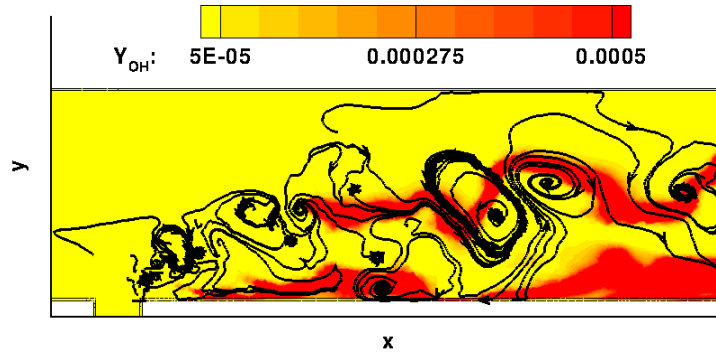


Figure 4.3.6: SAS results. Instantaneous 2D xy -streamlines and OH mass fractions on the symmetry plane of the considered configuration.

and the end of the mixing section. Similar axial positions of the ignition kernels were reported in the experimental study by Fleck et al. [36]. Next the flame starts to propagate downstream along the jet shear layer as seen in both figures 4.3.3 and 4.3.4. In the SAS simulations the flame shape is much more wrinkled than in URANS, but the characteristic times of the downstream propagation given by both methods are similar. At the time $t = 0.1ms$, the flame is located almost entirely between $1/3L$ and $2/3L$ in both cases. The same situation was observed in the experiments [36] at the same time point.

Not only downstream but also upstream flame propagation can be observed here. This fact becomes evident in the SAS calculations at a later point in time between 1 and $2.5ms$ (figures 4.3.3(d) and 4.3.3(e) respectively). Here the flame propagation upstream of the initial ignition location can be observed especially near to the lower wall of the mixing section. This behavior has also been observed in the experiments[36]; however, in the experiments, this phenomenon could not be described in detail because of the limited optical access in the boundary layer region. The present SAS simulation reveals the upstream transport of the flame in the boundary layer. The reasons for the upstream near-wall flame propagation could not be clarified in the present work. A possible explanation can be the transport of the flame along the complex vortical structures formed in the jet in crossflow configuration [38] and their interaction with the wall boundary layer.

The hypothesis of the vortex-related flame propagation is supported by figures 4.3.5 and 4.3.6. The first one shows that the SAS isosurfaces of $Y_{OH} = 0.001$ are perfectly aligned with the large-scale vortices of the flow which in this case are visualized by the instantaneous absolute velocity fluctuation isosurface $U' = 0.15 \cdot \bar{U}_{crossflow}$. In the second figure, where also the SAS data are analyzed, the instantaneous xy -streamlines indicate the transfer of the flame surfaces.

Such a tight dependence of the flame front on the resolved vortical structures is probably the main reason of the differences between the flame shapes given by SAS and by URANS (see figures 4.3.3 and 4.3.4). In URANS, the near-wall flame is never present in the first third of the mixing section (figure 4.3.4). However, the experimental investigations have reported the existence of the flame in this region in the stabilized combustion phase have been reported in the experimental investigations [36], and the flame in this upstream region is clearly seen in the time-averaged SAS results (figure 4.3.3(f)). Therefore, the results given by the SAS method, providing a deeper resolution of the present spatiotemporal complexity than URANS, resemble the physical flow field better.

4.4 Concluding remarks

The results presented in this chapter show that especially SAS or similar hybrid URANS/LES methods have great potential for unsteady gas turbine combustion simulations. In two of three basic test cases the SST SAS model showed the same degree of accuracy as WALE LES. Furthermore, in the self-ignition simulations accurate reproduction of the upstream and the downstream flame propagation processes was achieved with SAS.

Two main directions of further SAS-related investigations can be identified here. The first one are the grid dependence studies. These studies are needed to clarify the potential of SAS to get accurate time-resolved solutions at the computational costs lower than in LES. The second main effort should focus on a thorough study and improvement of the SAS mode switching mechanism, from RANS to scale-resolving mode, which can be potentially a cause of the less than optimal results obtained here in the confined swirling jet case.

Regarding URANS, it can be stated that this method also deserves its niche in the industrial computations. Jet in crossflow simulations presented here show that in such cases, indeed, improvement over RANS results can be achieved. However, it is also determined that URANS cannot be the method of choice for a thorough analysis of the flow structure and furthermore high attention has be payed to its strong turbulence and mixing model dependence.

5 Summary and conclusions

In the present work a comprehensive study is accomplished regarding several aspects of turbulence and mixing modeling in complex jet flows relevant for gas turbine combustion applications. The results of RANS, LES, URANS, and SAS computations were compared for three different flow types: jet in crossflow, confined swirling coaxial jets, and confined non-swirling coaxial jets. Furthermore, RANS results obtained for two standard academic test cases (plane channel flow and free round jet flow) are presented for the purposes of model validation and a more complete model assessment.

The results presented for the RANS velocity field simulations employing a variety of widespread modeling approaches reveal serious weaknesses of all models tested. The models exceptionally often used for applied computations - the standard $k-\varepsilon$ model and the SST $k-\omega$ model of Menter, underestimate the turbulent kinetic energy of the flow in all complex jet test cases considered. The 1988 $k-\omega$ model of Wilcox performs better in the jet in crossflow test case but not in the confined coaxial jets. Moreover, additional studies reveal that the better accuracy of the Wilcox 1988 model in the jet in crossflow case originates mainly from the absence of the cross-diffusion term in the ω -equation. The lack of the cross-diffusion term in the Wilcox 1988 $k-\omega$ approach causes several issues in the modeling of free shear flows, as pointed out by Menter in ref. [83]. Furthermore, the validation of the turbulent viscosity profiles obtained in the Wilcox 1988 $k-\omega$ model computations of jet in crossflow against LES data shows that the location of the turbulent viscosity peaks is represented inaccurately by the Wilcox 1988 $k-\omega$ model. This issue can be also explained by the absence of the cross-diffusion term in this RANS model. Thus, none of three tested, most widespread, two-equation turbulence models can guarantee a satisfactory degree of accuracy in the simulations of complex jet flows.

The analysis of various corrections often implemented in RANS two-equation modeling provides additional practically important information. The corrections attempting to reduce the turbulent viscosity or the turbulent kinetic energy, such as shear stress turbulent viscosity limiter or the round jet correction of Pope, resulted in a decrease of accuracy for three main test cases. It should be pointed out that these corrections have been initially developed for the free shear flows where the flow physics and the model challenges can be different from those of the applications considered here. For example, the round jet correction of Pope applied for the standard $k-\varepsilon$ model or in the 1998 and 2006 $k-\omega$ models of Wilcox indeed helps to achieve more accurate predictions for the academic test case of a free round jet. The reason is that in the absence of the round jet correction the tested models would overestimate the level of the turbulent kinetic energy in this free shear flow. A different situation can be observed

in three complex jet cases. The turbulent content of these flows is obviously influenced by their complicated structure which is not taken into account in the standard models (streamline curvature, effects of swirl, effects of acceleration of the central jet by the coflow). Neglecting these effects leads to the underestimation of the turbulence level in the studied flows even by the models not employing the round jet correction and to worse results in the presence of this dissipation-increasing term. The curvature correction of Hellsten for the SST model shows a positive trend by increasing the turbulence in the jet in crossflow simulations. However, further work on refinement of this technique is needed. In the form implemented in the present work, the correction tends to “overreact” to the curvature of a jet in crossflow that then causes a strong over prediction of turbulent kinetic energy.

Regarding the LES results presented in this dissertation, their overall accuracy, as anticipated, was higher than in RANS simulations, but the computational costs were more than 150 times higher than the costs of RANS. In the present work LES was applied to collect additional validation data for RANS and for a thorough study of the legitimacy of different RANS modeling assumptions in the considered jet flows. The Reynolds-averaged turbulent viscosities and the budget terms of the turbulent kinetic energy balance equation were evaluated from LES data fields and compared to the respective turbulent quantities resulting from the RANS modeling. A method to obtain representative values of turbulent viscosities from an overdetermined system of the Boussinesq approximation equations using the least-square fit over all stress directions is proposed in the present work. The value obtained from the LES data using the least-square fit is consistent with the idea of the RANS turbulent viscosity modeling where a unique ν_t is used to model all Reynolds stresses. Especially in complex three-dimensional flows where no dominant Reynolds stress can be determined, the turbulent viscosity estimated using the least-square fit is much more suitable for the comparison with the RANS output than the values obtained in the LES data evaluation using just one Reynolds stress in a certain direction.

A direct comparison of the evaluated turbulent viscosity with the results of RANS modeling helps further to reveal the advantages and weaknesses of different models. The magnitudes and the curve trends in the evaluated and the modeled ν_t profiles are mostly comparable. The profiles evaluated from LES data show larger variability in space. For jet in crossflow, a relatively large region of negative turbulent viscosities along the shear layer on the lee side of the jet was revealed by evaluation of LES data. For the confined non-swirling jet, negative turbulent viscosities were observed in the narrow region near to the jet centerline. In both cases the appearance of such regions can be explained by the complex vortical structure and its corresponding influence on the momentum transport discussed in the respective result sections. These negative turbulent viscosities cannot be reproduced by the existing two-equation RANS models which represents one of the possible sources of modeling uncertainty. Furthermore, the evaluation of the turbulent viscosity modeling coefficient C_μ using LES data shows that this coefficient is highly variable in all considered flows and can be sufficiently higher or lower than $C_\mu = 0.09$ used in all tested RANS models. This implies a probable advantage of using the turbulent viscosity approaches which do not employ the concept of the constant turbulent

viscosity coefficient for the modeling of considered flows.

In addition to the turbulent viscosity evaluation, the budget terms of the turbulent kinetic energy balance equation were recovered by post-processing the LES data. A comparison with the budget terms of the k equation of the studied RANS models is presented. Production to dissipation ratios and the reciprocal dynamic turbulent time scales were evaluated and compared as well. This study helped to further assess the advantages and weaknesses of different RANS modeling approaches and their correlation with the actual trends of different budget terms.

Another focus of the present work is the modeling of turbulent scalar mixing. Dependence of the RANS mixing predictions on the dynamic turbulence model, turbulent Schmidt number values, two-equation turbulent scalar diffusivity modeling approaches were investigated. Furthermore, the turbulent scalar diffusivity and the budget terms of the turbulent scalar variance transport equation were evaluated from the scalar fields given by LES. The turbulent scalar diffusivity was obtained from an overdetermined system of the gradient diffusion hypothesis equations using the least-square fit over all scalar flux directions. As in the study on the turbulent viscosity, a comparison of the least-square profiles with the turbulent scalar diffusivity profiles obtained using just one scalar flux in any particular direction reveals that the least-square based evaluation has to be performed for a direct comparison with the RANS model results.

The RANS mixing results show that the scalar mixing modeling quality is highly dependent on the underlying dynamic turbulence modeling approach. Scalar profiles react to the weaknesses of the turbulent viscosity models more sensitively than the velocity profiles. Scalar mixing in the RANS simulations was underestimated everywhere in the regions of under prediction of k and of the turbulent viscosity. Artificially decreasing the turbulent Schmidt numbers as a method to enhance the mixing in RANS simulations was found to be without physical justification. The LES data evaluation demonstrated that the averaged turbulent Schmidt number values in the considered flows vary in the range $0.5 - 0.9$ and not $0.2 - 0.3$, which are the values commonly used to improve the mixing predictions in RANS calculations.

The turbulent Schmidt number profiles obtained in the LES data evaluation show the high variability of this parameter. For this reason the application of the models not employing the constant turbulent Prandtl or Schmidt number approach can be potentially favorable for the mixing modeling accuracy. Unfortunately, the two-equation turbulent scalar diffusivity models tested in the present work on the complex jets gave predictions close to those with a fixed turbulent Schmidt number of 1.0. No significant improvements over the constant turbulent Schmidt number calculations could be observed. However, it was shown that these models are able to represent the turbulent scalar time scale more accurately than the constant scalar to dynamic time scale ratio $\mathcal{R} = 0.5$. Thus, the two-equation turbulent scalar diffusivity models show some potential to improve the mixing predictions but further intensive development work is needed, and their refinement for the modeling of mixing in complex flows cannot be accomplished without an accurate underlying turbulent viscosity model.

In the final chapter of this dissertation the scale-adaptive simulation (SAS) and the unsteady RANS (URANS) methods were applied to the considered test cases. The SAS results for the jet in crossflow and the confined non-swirling jet were of similar accuracy as the data obtained from LES, but for the swirling jet the accuracy of SAS was worse than that of LES. URANS applied for jet in crossflow simulations showed less accurate results than SAS. This could be observed not only in the non-reacting flow predictions, but also in the reproduction of the flame front propagation in autoignition simulations. The flame front shape could not be correctly reproduced in URANS in contrast to the SAS calculations. It was also observed that the results of URANS, in general, are extremely dependent on the turbulence model used. From the SAS autoignition simulations accomplished in this dissertation, a conclusion can be drawn that such unsteady vortex-resolving methods represent a promising technique for the applied studies of the unsteady flame propagation mechanisms. Capable of capturing the inner vortical structure of the flow, the SAS method in the present application was able to reproduce the upstream flame propagation phenomenon not displayed in the URANS simulations but observed in experiments.

In summary, it can be concluded that the further development of turbulence and mixing modeling approaches should comprise the improvement of all simulation methods considered in the present dissertation. The knowledge gained in the present work regarding the advantages and weaknesses of several RANS models in complex jets can be used for the further refinement of RANS modeling in gas turbine applications. Also extremely beneficial for practical applications are the results regarding the turbulent Schmidt numbers and the statistical turbulence and mixing fields characteristics obtained in the present work using LES. The vortex-resolving methods, such as LES and hybrid URANS/LES, should be also further developed in order to increase their accuracy and time-efficiency. Such methods are indispensable when a thorough physical analysis of the flow and mixing processes is needed or fundamentally transient processes have to be reproduced in the simulation.

Bibliography

- [1] K. Abe, T. Kondoh, and Y. Nagano. A new turbulence model for predicting fluid flow and heat transfer in separating and reattaching flows - I. Flow field calculations. *International Journal of Heat and Mass Transfer*, 37(1):139–151, 1994.
- [2] K. Abe, T. Kondoh, and Y. Nagano. A new turbulence model for predicting fluid flow and heat transfer in separating and reattaching flows - II. Thermal field calculations. *International Journal of Heat and Mass Transfer*, 38(8):1467–1481, 1995.
- [3] S. A. Ahmed and R. M. C. So. Concentration distributions in a model combustor. *Experiments in Fluids*, 4:107–113, 1986.
- [4] K. Akselvoll and P. Moin. Large-eddy simulation of turbulent confined coannular jets. *J. Fluid Mech.*, 315:387–411, 1996.
- [5] J. Alvarez, W. P. Jones, and R. Seoud. Predictions of momentum and scalar fields in a jet in cross-flow using first and second order turbulence closures. In *AGARD Conf. Proc. Computational and Experiment Assessment of Jets in Cross Flow*, pages 24–1 – 24–10, April 1993.
- [6] J. E. Bardina, P. G. Huang, and T. G. Coakley. Turbulence modeling validation, testing, and development. NASA Technical Memorandum 110446, NASA Ames Research Center, 1997.
- [7] C. Beguier, I. Dekeyser, and B. E. Launder. Ratio of scalar and velocity dissipation time scales in shear flow turbulence. *Physics of Fluids*, 21(3):307–310, March 1978.
- [8] C. Bogey and C. Bailly. Turbulence and energy budget in a self-preserving round jet: direct evaluation using large eddy simulation. *J. of Fluid Mech.*, 627:129–160, 2009.
- [9] A. Brancovic, Jr. Ryder, R. C., and S. A. Syed. Mixing and combustion modeling for gas turbine combustors using unstructured CFD technology. *34th AIAA/ASME/SAE/ASEE Joint Propulsion Conference and Exhibit*, July 1998. AIAA 98-3854.
- [10] K. W. Brinckman, W. H. Jr. Calhoon, S. J. Mattick, J. Tomes, and S. M. Dash. Scalar variance model validation for high-speed variable composition flows. AIAA 2006-715, Reno, NV, January 2006. 44th AIAA Aerospace Sciences Meeting and Exhibit.

- [11] K. W. Brinckman, D. C. Kenzakowski, and S. M. Dash. Progress in practical scalar fluctuation modeling for high-speed aeropropulsive flows. AIAA 2005-508, Reno, NV, January 2005. 43rd AIAA Aerospace Sciences Meeting and Exhibit.
- [12] W. H. Jr. Calhoon, K. W. Brinckman, J. Tomes, S. J. Mattick, and S. M. Dash. Scalar fluctuation and transport modeling for application to high speed reacting flows. AIAA 2006-1452, Reno, NV, January 2006. 44th AIAA Aerospace Sciences Meeting and Exhibit.
- [13] C. Cardenas, R. Suntz, J. Denev, and H. Bockhorn. Two-dimensional estimation of reynolds-fluxes and -stresses in a jet-in-crossflow arrangement by simultaneous 2D-LIV and PIV. *Applied Physics B: Lasers and Optics*, 88:581–591, 2007.
- [14] N. Chidambaram, S. M. Dash, and D. C. Kenzakowski. Scalar variance transport in the turbulence modeling of propulsive jets. AIAA 99-0235, Reno, NV, January 1999. 37th AIAA Aerospace Sciences Meeting and Exhibit.
- [15] A.J. Chorin. Numerical solution of Navier-Stokes equations. *Mathematics of Computation*, 22(104):745, 1968.
- [16] L. P. Chua and R. A. Antonia. Turbulent Prandtl number in a circular jet. *Int. J. Heat Mass Transfer*, 33(2):331–339, 1990.
- [17] G. Comte-Bellot and S. Corrsin. Simple Eulerian time correlations of full- and narrow-band velocity signals in grid-generated isotropic turbulence. *J. Fluid Mech.*, 48:273–337, 1971.
- [18] T. Daris. *Etude des modeles de turbulence a quatre equations de transport pour la prevision des ecoulements turbulents faiblement chauffes*. PhD thesis, École nationale supérieure de l’aéronautique et de l’espace ("SUPAERO"), 2002.
- [19] D. Davidenko. *Contribution au developement des outils de simulation numerique de la combustion supersonique*. PhD thesis, Universite d’Orleans, 2005. In French.
- [20] A. Dejoan and M. A. Leschziner. Large eddy simulation of a plane turbulent wall jet. *Physics of Fluids*, 17(025102), 2005.
- [21] B. Deng, W. Wu, and S. Xi. A near-wall two-equation heat transfer model for wall turbulent flows. *International Journal of Heat and Mass Transfer*, 44:691–698, 2001.
- [22] M. Di Domenico. *Numerical Simulation of Soot Formation in Turbulent Flows*. PhD thesis, University of Stuttgart, 2007.
- [23] M. Di Domenico, P. Gerlinger, and B. Noll. Numerical simulations of confined, turbulent, lean, premixed flames using a detailed chemistry combustion model. In *Proc. ASME Turbo Expo 2011, Power for Land, Sea and Air, 06-10.06.2011, Vancouver, Canada*, number GT2011-45520, 2011.

- [24] M. Di Domenico, P. Kutne, C. Naumann, J. Herzler, R. Sadanandan, M. Stoehr, B. Noll, and M. Aigner. Numerical and experimental investigation of a semi-technical scale burner employing model syntetic fuels. In *Proc. ASME Turbo Expo 2009: Power for Land, Sea and Air, Orlando, Florida, USA*, June 2009. GT2009-59308.
- [25] M. Dianat, D. Jiang, Z. Yang, and J.J. McGuirk. Simulation of scalar mixing in co-axial jet flows using an LES method. In *Proceedings of GT2005 ASME Turbo Expo 2005: Power for Land, Sea and Air*, 2005. GT2005-69010.
- [26] M. Dianat, Z. Yang, D. Jiang, and J. J. McGuirk. Large Eddy Simulation of Scalar Mixing in a Coaxial Confined Jet. *Flow, Turbulence and Combustion*, 77(1-4):205–227, 2006.
- [27] P. E. Dimotakis. Turbulent mixing. *Annual Rev. Fluid Mech.*, 37:329–356, 2005.
- [28] P. A. Durbin. A perspective on recent developments in RANS modeling. In W. Rodi and N. Fueyo, editors, *Engineering Turbulence Modelling and Experiments 5*, 2002.
- [29] P. A. Durbin and B. A. Petterson-Reif. *Statistical theory and modeling for turbulent flows*. John Wiley and Sons, LTD, 2001.
- [30] F. Durst. *Grundlagen der Strömungsmechanik (Basics of Fluid Mechanics)*. Springer, Berlin Heidelberg, 2006. in German.
- [31] Y. Egorov and F. Menter. Development and application of SST-SAS turbulence model in the DESIDER project. In S.-H. Peng and W. Haase, editors, *Advances in Hybrid RANS-LES Modelling*, pages 261–270. Springer Verlag Beriln Heidelberg, 2008.
- [32] S. E. Elgobashi and B. E. Launder. Turbulent time scales and the dissipation rate of tempeature variance in the thermal mixing layer. *Physics of Fluids*, 26(9):2415–2419, 1983.
- [33] T. Esch and F. R Menter. Heat tranfer prediction based on two-equation turbulence models with advanced wall treatment. In K. Hanjalic, Y. Nagano, and M. Tummers, editors, *Turbulence, Heat an Mass Transfer 4*, 2003.
- [34] J. H. Ferziger and M. Peric. *Computational Methods for Fluid Dynamics*. Springer, 3rd edition, 2010.
- [35] J. Fleck, P. Griebel, A. M. Steinberg, M. Stöhr, M. Aigner, and A. Ciani. Autoignition limits of hydrogen at relevant reheat combustor operating conditions. In *Proc. ASME Turbo Expo 2011: Power for Land, Sea and Air, Vancouver, Canada*, June 2011. GT2011-46195.

- [36] J. M. Fleck, P. Griebel, A. M. Steinberg, M. Stöhr, and M. Aigner. Experimental investigation of a generic, fuel flexible reheat combustor of a gas turbine relevant operating conditions. In *Proc. ASME Turbo Expo 2010: Power for Land, Sea and Air, Glasgow, UK*, June 2010. GT2010-22722.
- [37] M. Freitag, M. Klein, M. Gregor, D. Geyer, C. Schneider, A. Dreizler, and J. Janicka. Mixing analysis of a swirling recirculating flow using DNS and experimental data. *Int. J. Heat and Fluid Flow*, 27:636 – 643, 2006.
- [38] T.F. Fric and A. Roshko. Vortical structure in the wake of a transverse jet. *J. Fluid Mech.*, 279:1–47, 1994.
- [39] J. Fröhlich. *Large Eddy Simulation turbulenter Strömungen (Large eddy simulation of turbulent flows)*. Teubner, 2006. In German.
- [40] J. Fröhlich, M. García-Villalba, and W. Rodi. Scalar mixing and large-scale coherent structures in a turbulent swirling Jet. *Flow Turbulence Combustion*, 80:47–59, 2008.
- [41] J. Fröhlich and D. von Terzi. Hybrid LES/RANS methods for the simulation of turbulent flows. *Progress in Aerospace Sciences*, 44:349 – 377, 2008.
- [42] F. C. C. Galeazzo, G. Donnert, P. Habisreuther, N. Zarzalis, R. J. Valdes, and W. Krebs. Measurement and simulation of turbulent mixing in a jet in crossflow. *Journal of Engineering for Gas Turbines and Power*, 133:061504–1 – 061504–10, June 2011.
- [43] P. Gerlinger. *Numerische Verbrennungssimulation (Numerical combustion simulation)*. Springer, Berlin Heidelberg, 2005. In German.
- [44] F. Güthe, J. Hellat, and P. Flohr. The reheat concept: the proven pathway to ultralow emissions and high efficiency and flexibility. *J. Eng. Gas Turbines Power*, (131):021503 1–7, 2009.
- [45] G. He, Y. Guo, and A. T. Hsu. The effect of Schmidt number on turbulent scalar mixing in a jet-in-crossflow. *International Journal of Heat and Mass Transfer*, 42:3727–3738, 1999.
- [46] A. Hellsten. Some improvements in Menter’s $k-\omega$ SST turbulence model. In *29th AIAA Fluid Dynamics Conference*, 1997. AIAA-98-2554.
- [47] A. T. Hsu, G. He, and Y. Guo. Unsteady simulation of jet in crossflow. *Int. Journal of Computational Fluid Dynamics*, 14(41 - 53), 2000.
- [48] P. G. Huang and P. Bradshaw. Law of the wall for turbulent flows in pressure gradients. *AIAA Journal*, 33(4):624 – 632, 1995.

- [49] J. C. R. Hunt, A. A. Wray, and P. Moin. Eddies, streams and convergence zones in turbulent flows. 1988. Center for Turbulence Research. Proceedings of the Summer Programm 1988.
- [50] E. Ivanova, B. Noll, and M. Aigner. Unsteady simulations of turbulent mixing in jet in crossflow. In *40th AIAA Fluid Dynamics Conference and Exhibit*, 2010. AIAA 2010-4724.
- [51] E. Ivanova, B. Noll, and M. Aigner. Computational modelling of turbulent mixing of a transverse jet. *J. Eng. Gas Turbines Power*, 133(2):021505–1 021505–7, 2011.
- [52] E. Ivanova, B. Noll, and M. Aigner. RANS and LES of Turbulent Mixing in Confined Swirling and Non-Swirling Jets. In *Proc. 6th AIAA Theoretical Fluid Mechanics Conference*, number AIAA 2011-3934, 2011.
- [53] E. Ivanova, B. Noll, M. Di Domenico, and M. Aigner. Improvement and assessment of RANS scalar transport models for jets in crossflow. In *46th AIAA Aerospace Sciences Meeting and Exhibit, Reno, NV, USA*, 7 January 2008. AIAA-2008-565.
- [54] E. Ivanova, B. Noll, M. Di Domenico, and M. Aigner. Unsteady simulations of flow field and scalar mixing in transverse jets. In *Proc. ASME Turbo Expo 2009: Power for Land, Sea and Air, Orlando, Florida, USA*, June 2009. GT2009-59147.
- [55] E. Ivanova, B. Noll, P. Griebel, M. Aigner, and K. Syed. Numerical simulations of turbulent mixing and autoignition of hydrogen fuel at reheat combustor operating conditions. In *Proc. ASME Turbo Expo 2011: Power for Land, Sea and Air, Vancouver, Canada*, June 2011. GT2011-46264.
- [56] R. Jester-Zürker, S. Jakirlic, and C. Tropea. Computational modelling of turbulent mixing in confined swirling environment under constant and variable density conditions. *Flow, Turbulence and Combustion*, (75):217–244, 2005.
- [57] C. Jiménez, F. Ducros, B. Cuenot, and B. Bédát. Subgrid scale variance and dissipation of a scalar field in large eddy simulations. *Physics of Fluids*, 13(6):1748–1754, 2001.
- [58] B. V. Johnson and J. C. Bennett. Mass and momentum turbulent transport experiments with confined coaxial jets. 1981. NASA contractor report 165574.
- [59] B. V. Johnson and J. C. Bennett. Statistical characteristics of velocity, mass transport, and momentum transport for coaxial jet mixing in a confined duct. *J. of Engineering for Gas Turbines and Power*, 106:121–127, 1984.
- [60] W. P. Jones and P. Musonge. Closure of the Reynolds stress and scalar flux equations. *Physics of Fluids*, 31(12):3589–3604, 1988.
- [61] W.P. Jones and B.E. Launder. The prediction of laminarization with a two-equation model. *Int. J. Heat Mass Transfer*, 15:301–314, 1972.

- [62] F. Joos, P. Brunner, B. Schulte-Werning, K. Syed, and A. Eroglu. Development of the sequential combustion system for the ABB GT24/GT26 gas turbine family. 1996. ASME Paper 1996-GT-315.
- [63] J-C. Jouhaud, L. Y. M. Gicquel, and B. Enaux. Large-eddy-simulation modeling for aerothermal predictions behind a jet in crossflow. *AIAA Journal*, 45(10):2438–2447, 2007.
- [64] M. Karcz and J. Badur. An alternative two-equation turbulent heat diffusivity closure. *International Journal of Heat and Mass Transfer*, 48:2013–2022, 2005.
- [65] N. Kasagi, Y. Tomita, and A. Kuroda. Direct numerical simulation of passive scalar field in a turbulent channel flow. *ASME Transactions Journal of Heat Transfer*, 114:598–606, August 1992.
- [66] H. Kawamura, H. Abe, and K. Shingai. DNS of turbulence and heat transport in a channel flow with different Reynolds and Prandtl numbers and boundary conditions. In Y. Nagano, K. Hanjalic, and T. Tsuji, editors, *Turbulence, Heat and Mass Transfer 3*, pages 15–32, 2000.
- [67] D. C. Kenzakowski. RANS modeling improvements for jets using scalar variance equations. AIAA 2006-491, Reno, NV, January 2006. 44th AIAA Aerospace Sciences Meeting and Exhibit.
- [68] D. C. Kenzakowski, J. Papp, and S. M. Dash. Evaluation of advanced turbulence models and variable Prandtl/Schmidt number methodology for propulsive flows. AIAA 2000-0885, Reno, NV, January 2000. 38th AIAA Aerospace Sciences Meeting and Exhibit.
- [69] M. Klein, A. Sadiki, and J. Janicka. A digital filter based generation of inflow data for spatially developing direct numerical or large eddy simulations. *Journal of Computational Physics*, (186):652–665, 2003.
- [70] A. N. Kolmogorov. Equations of turbulent motion of an incompressible fluid. *Bulletin of the Academy of Sciences USSR: physical series*, 6(1-2):56–58, 1942.
- [71] C. K. G. Lam and K. A. Bremhorst. Modified form of the k - ε model for predicting wall turbulence. *ASME Journal of Fluids Engineering*, 103:456–460, 1981.
- [72] B. E. Launder. Heat and mass transport. In P. Bradshaw, editor, *Turbulence*, volume 12 of *Topics in Applied Physics*, pages 232–287. Springer, Berlin, 1976.
- [73] A. H. Lefebvre. *Gas turbine combustion*. Taylor and Francis, 1999. 2nd ed.
- [74] T. Lieuwen, V. McDonnel, E. Petersen, and D. Santavicca. Fuel flexibility influences on premixed combustor blowout, flashback, autoignition and stability. *J. Eng. Gas Turbines Power*, (130):011506 1–10, 2008.

- [75] T. T. Lim, T. H. New, and S. C. Luo. On the development of large-scale structures of a jet normal to a cross flow. *Physics of Fluids*, 13(3):770 – 775, March 2001.
- [76] M.M.C.L. Lima and J.M.L.M. Palma. Mixing incoaxial confined jets of large velocity ratio. In *Proc. of 11th Int. Symp. on Appl. of Laser Techniques to Fluid Mechs.*, 2002.
- [77] C. A. Lin. Modeling a confined swirling coaxial jet. *Center for Turbulence Research: Annual Research Briefs 1998*, pages 211 –219, 1998.
- [78] T. Lischer, G.D. Donnert, F.C.C. Galleazzo, P. Habisreuther, N. Zarzalis, R. Valdes, and W. Krebs. Simultaneous velocity and concentration measurements using laser-optical measurement methods in comparison with Reynolds-Averaged Navier-Stokes models. In *The 12th International symposium on Transport Phenomena and Dynamics of Rotating Machinery*, February 2008. ISROMAC12-2008-20112.
- [79] P. Majander and T. Siikonen. Large-eddy simulation of a round jet in a crossflow. *Int. J. Heat and Fluid Flow*, 27:402–415, 2006.
- [80] R. E. Malecki and et al. Application of an advanced CFD-based analysis system to the PW6000 combustor to optimize exit temperature distribution - Part 1: Description and validation of the analysis tool. In *Proceedings of ASME Turbo Expo 2001: Power for Land, Sea and Air, New Orleans, Louisiana, USA*, June 2001. 2001-GT-0062.
- [81] N. N. Mansour, J. Kim, and P. Moin. Reynolds stress and dissipation rate budgets in turbulent channel flow. *Journal of Fluid Mechanics*, 194:15–44, 1988.
- [82] R.J. Marganson. Fifty years of jet in cross flow research. In *Computational and Experimental Assessment of Jets in Cross Flow*, volume 534 of *AGARD Conference Proceedings*, pages 1.1 – 1.41, UK, 1993.
- [83] F. R. Menter. Two-equation eddy-viscosity turbulence models for engineering applications. *AIAA Journal*, 32(8):1598–1605, 1994.
- [84] F. R. Menter. Review of the shear-stress transport turbulence model experience from an industrial perspective. *International Journal of Computational Fluid Dynamics*, 23(4):305–316, 2009.
- [85] F. R. Menter and Y. Egorov. A scale-adaptive simulation model using two-equation models. 2005. AIAA Paper 2005-1095.
- [86] F. R. Menter, M. Kuntz, and R. Langtry. Ten years of industrial experience with the SST turbulence Model. In K. Hanjalic, Y. Nagano, and M. Tummers, editors, *Turbulence, Heat and Mass Transfer 4*, 2003.
- [87] S. Muppidi and K. Mahesh. Passive scalar mixing in jets in crossflow. AIAA 2006-1098, Reno, NV, January 2006. 44th AIAA Aerospace Sciences Meeting and Exhibit.

- [88] S. Muppidi and K. Mahesh. Direct numerical simulation of round turbulent jets in cross-flow. *J. Fluid Mech.*, 574:59–84, 2007.
- [89] Y. Nagano and C. Kim. A two-equation model for heat transport in wall turbulent shear flows. *Journal of Heat Transfer*, 110:583–589, 1988.
- [90] Y. Nagano, M. Tagawa, and T. Tsuji. An improved two-equation heat transfer model for wall turbulent shear flows. In *ASME/JSME Thermal Elgineering Proceedings*, volume 3, 1991.
- [91] G. R. Newman, B. E. Launder, and J. L. Lumley. Modelling the behaviour of homogeneous scalar turbulence. *Journal of Fluid Mechanics*, 111:217–232, 1981.
- [92] F. Nicoud and F. Ducros. Subgrid-scale stress modelling based on the square of the velocity gradient tensor. *Flow, Turbulence and Combustion*, 62(3):183 – 200, 1999.
- [93] B. Noll, H. Schütz, and M. Aigner. Numerical simulation of high-frequency flow instabilities near an airblast atomizer. *Proceedings of ASME TURBO EXPO 2001*, June 2001. 2001-GT-0041.
- [94] M. O’Conaire, H.J. Curran, J.M. Simmie, R.W. Pitz, and C.G. Westbrook. A comprehensive modeling study of hydrogen oxidation. *International Journal of Chemical Kinetics*, (11):602–622, 2004.
- [95] N. R. Panchapakesan and J. L. Lumley. Turbulence measurements in axisymmetric jets of air and helium. Part I. Air jet. *J. Fluid Mech.*, 246:197–223, 1993.
- [96] S. V. Patankar. *Numerical heat transfer and fluid flow*. Series in Computational Methods in Mechanics and Thermal Science. Hemisphere Publishing Corporation, 1980.
- [97] V. C. Patel, W. Rodi, and G. Scheuerer. Turbulence models for near-wall and low reynolds number flows: a review. *AIAA Journal*, 23(9):1308–1319, 1985.
- [98] C.D. Pierce and P. Moin. Large eddy simulation of a confined coaxial jet with swirl and heat release. *29th AIAA Fluid Dynamics Conference*, June 1998. AIAA 98-2892.
- [99] T. Poinso and D. Veynante. *Theoretical and numerical combustion*. R. T. Edwards, Inc., 2005.
- [100] S. B. Pope. An explanation of the turbulent roind-jet/plane-jet anomaly. *AIAA Journal*, 16(3):279–281, 1978.
- [101] S. B. Pope. *Turbulent Flows*. Cambridge University Press, 2000.
- [102] S. B. Pope. Ten questions concerning the large-eddy simulation of turbulent flows. *New Journal of Physics*, 6(35), 2004.

- [103] A. J. Reynolds. The variation of turbulent Prandtl and Schmidt numbers in wakes and jets. *International Journal of Heat and Mass Transfer*, 19:757–764, 1976.
- [104] R. Roback and B. V. Johnson. Mass and momentum turbulent transport experiments with confined swirling coaxial jets. 1983. NASA contractor report 168252.
- [105] G. P. Rodebaugh. *Large eddy simulation of variable density jets: Investigation of numerical, resolution, and subgrid-scale model effects on predictive quality*. PhD thesis, The Johns Hopkins University, Baltimore, MD, USA, 2011.
- [106] D. B. Rusch. *Turbulence model validation for fire simulation by CFD and experimental investigation of a hot jet in crossflow*. PhD thesis, Swiss Federal Institute of Technology, Zurich, 2007. Diss. ETH No. 16966.
- [107] P. Sagaut. *Large eddy simulation for incompressible flows*. Springer, 2004.
- [108] P. Sagaut, S. Deck, and M. Terracol. *Multiscale and multiresolution approaches in turbulence*. Imperial College Press, 2006.
- [109] M. Salewski, D. Stankovic, and L. Fuchs. Mixing in circular and non-circular jets in crossflow. *Flow Turbulence Combust*, 80:255–283, 2008.
- [110] J. Schlüter, T. Schönfeld, T. Poinso, W. Krebs, and S. Hoffmann. Characterization of confined swirl flows using large eddy simulations. In *Proceedings of ASME Turbo Expo 2001*, 2001. 2001-GT-0060.
- [111] J. U. Schlüter and T. Schönfeld. LES of jets in cross flow and its application to a gas turbine burner. *Flow, Turbulence and Combustion*, 65:177–203, 2000.
- [112] T. P. Sommer, R. M. C. So, and Y. G. Lai. A near-wall two-equation model for turbulent heat fluxes. *International Journal of Heat and Mass Transfer*, 35(12):3375–3387, 1992.
- [113] T. P. Sommer, R. M. C. So, and H. S. Zhang. Heat transfer modeling and the assumption of zero wall temperature fluctuations. *J. of Heat Transfer*, 116:855 – 863, 1994.
- [114] P. R. Spalart. Strategies for turbulence modelling and simulations. *International Journal of Heat and Fluid Flow*, 21:252 – 263, 2000.
- [115] O. S. Sun. *Analysis of subgrid scale modeling approaches for large-eddy simulation of turbulent mixing in spatially developing round jets*. PhD thesis, The Johns Hopkins University, Baltimore, MD, 2008.
- [116] I. Tkachenko, N. Kornev, S. Jahnke, G. Steffen, and E. Hassel. Performances of LES and RANS models for simulation of complex flows in a coaxial jet mixer. *Flow Turbulence and Combustion*, 78:111–127, 2007.

- [117] E. G. Tulapurkara, R. A. Antonia, and L. W. B. Browne. Optimisation of a $\overline{\theta^2} - \varepsilon_\theta$ model for a turbulent far wake. Proc. 7th Symposium on Turbulent Shear Flows, pages 29.2.1–29.2.6. Stanford University, August 1989.
- [118] K. Van Maele, B. Merci, and E. Dick. Comparative study of k- ε turbulence models in inert and reacting swirling flows. 2003. AIAA 2003-3744.
- [119] Z. Warhaft and J. L. Lumley. An experimental study of the decay of temperature fluctuations in grid-generated turbulence. *Journal of Fluid Mechanics*, 88:659–684, 1978.
- [120] B. Wegner, Y. Huai, and A. Sadiki. Comparative study of turbulent mixing in jet in cross-flow configurations using LES. *International Journal of Heat and Fluid Flow*, 25:767–775, 2004.
- [121] B. Wegner, A. Maltsev, C. Schneider, A. Sadiki, A. Dreizler, and J. Janicka. Assessment of unsteady RANS in predicting swirl flow instability based on LES and experiments. *International Journal of Heat and Fluid Flow*, 25:528–536, 2004.
- [122] D. Wennerberg. *Entwicklung eines vorhersagefähigen Berechnungsmodells für stark verdrahlte Strömungen mit Verbrennung*. PhD thesis, University of Erlangen-Nürnberg, Germany, 1995.
- [123] A. Widenhorn, B. Noll, and M. Aigner. Numerical Characterisation of a Gas Turbine Model Combustor Applying Scale-Adaptive Simulation. In *Proc. ASME Turbo Expo 2009, Power for Land, Sea and Air, 08.-12.06.2009, Orlando, Florida*, GT2009-59038, 2009.
- [124] A. Widenhorn, B. Noll, and M. Aigner. Numerical Study of a Non-Reacting Turbulent Flow in a Gas Turbine Model Combustor. In *Proc. 47th AIAA Aerospace Sciences Meeting, 05.-08.01.2009, Orlando, Florida*, number AIAA 2009-0647, 2009.
- [125] D. C. Wilcox. Reassesssment of the scale determining equation for advanced turbulence models. *AIAA Journal*, 26(11):1299–1310, 1988.
- [126] D. C. Wilcox. Simulation of transition with a two-equation turbulence model. *AIAA Journal*, 32(2):247–255, 1994.
- [127] D. C. Wilcox. *Turbulence modeling for CFD*. DCW Industries, 1998. 2nd ed.
- [128] D. C. Wilcox. *Turbulence modeling for CFD*. DCW Industries, 2006. 3rd ed.
- [129] M.S. Youssef, Y. Nagano, and M. Tagawa. A two-equation heat transfer model for predicting turbulent thermal fields under arbitrary wall thermal conditions. *International Journal of Heat and Mass Transfer*, 35:3095–3104, 1992.

- [130] L. L. Yuan, R. L. Street, and J. H. Ferziger. Large-eddy simulations of a round jet in crossflow. *J. Fluid Mech.*, 379:71–104, 1999.
- [131] O. Zeman and J. L. Lumley. Modeling buoyancy driven mixed layers. *J. Atmos. Sci.*, 33:1974–1988, 1976.
- [132] V. Zhdanov, N. Kornev, E. Hassel, and A. Chorny. Mixing of Confined Coaxial Flows. *Intern. J. Heat Mass Transfer*, pages 3942–3956, 2006.